UNIVERSITÀ DEGLI STUDI DELL'INSUBRIA
Scuola di Dottorato in Scienze Esatte ed Alta Tecnologia

Tesi di Dottorato di Ricerca in:
ASTRONOMIA E ASTROFISICA
XXVIII Ciclo

The hidden complexity of stellar population properties in high-redshift early-type galaxies

Supervisore:
Dr. Marcella Longhetti

Tesi di dottorato di:
Ilaria LONOCE
Matr. 720551

Anno Accademico 2014/2015

Contents

Chapter 1

Introduction

The principal aim of this PhD thesis is the investigation of the formation and evolution of galaxies during the cosmic epochs. The followed approach is the observational analysis of the stellar population properties of high redshift galaxies directly in their early phases of evolution in order to catch a picture of their possible origin and of the subsequent processes which have brought them toward the local Universe, where we observe their descendants.

In particular this thesis is focused on elliptical galaxies which, as it will be presented in Section 1.1, are ideal candidates to probe the evolution of most of the stellar mass in the local Universe, and on their stellar properties: age (Section 1.4) and metallicity (Section 1.5). All the work is based on spectroscopic data coming from the 8m ESO-VLT telescopes (Section 4) and on the potentiality of spectral indices (Section 2) in the comparison with the updated and mostly used stellar population models (Section 3).

1.1 Elliptical galaxies

Elliptical and lenticular galaxies, i.e. Early-Type Galaxies (ETG), constitute a well-defined class of objects thanks to which we can trace back the evolution of most of the stellar mass of the Universe. In this section I will briefly describe the characteristics of this family of galaxies in the well-studied local Universe.

First of all, ETGs, for definition, share their regular elliptical morphology. An example of the regular morphology of ETGs is shown in Fig. 1.1 with the HST images of the sample of 15 high redshift ETGs that will be analyzed in Chapter 5. Many studies in the local Universe, as for example those based on the Sloan Digital Sky Survey (SDSS), tell us that ETGs include about the 80% of the baryonic mass belonging to stars, and that more than the 80% of the stellar mass enclosed in ETGs belongs to the most massive galaxies with $M_* > 3\text{x}10^{10} M_\odot$ (Renzini 2006 [96]). As it can be seen in Fig. 1.2, indeed, the total stellar mass contribution of the ETGs (top panel) with respect to their number, is much more than that of the spiral and/or star-forming galaxies (called Late-Type Galaxies)(bottom panel).

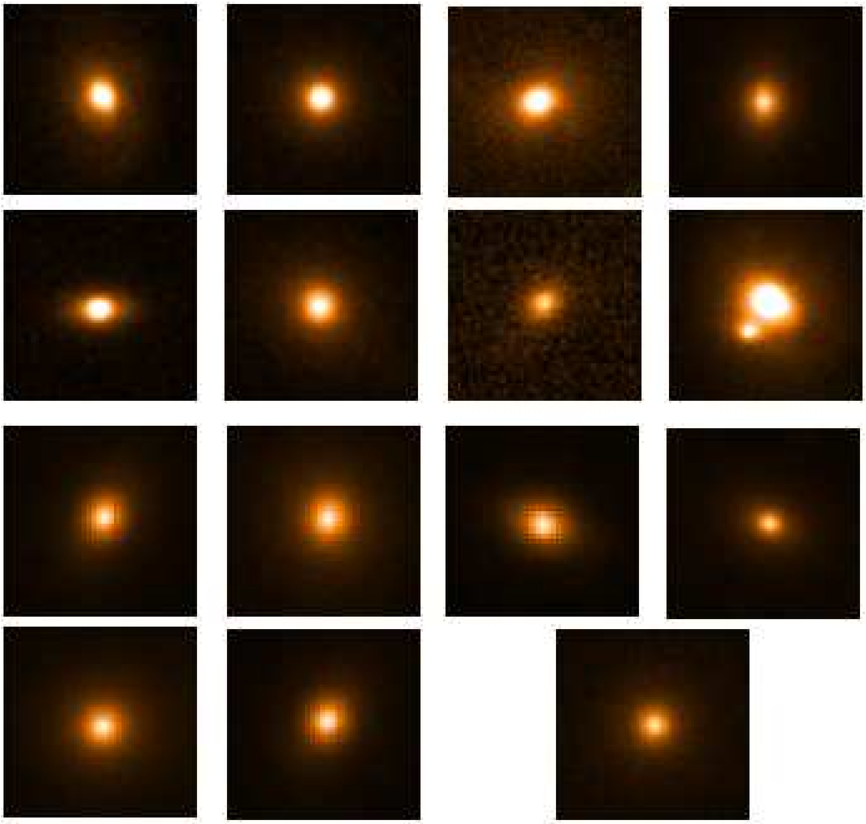

Figure 1.1: HST images of 15 high redshift ETGs analyzed in Chapter 5.

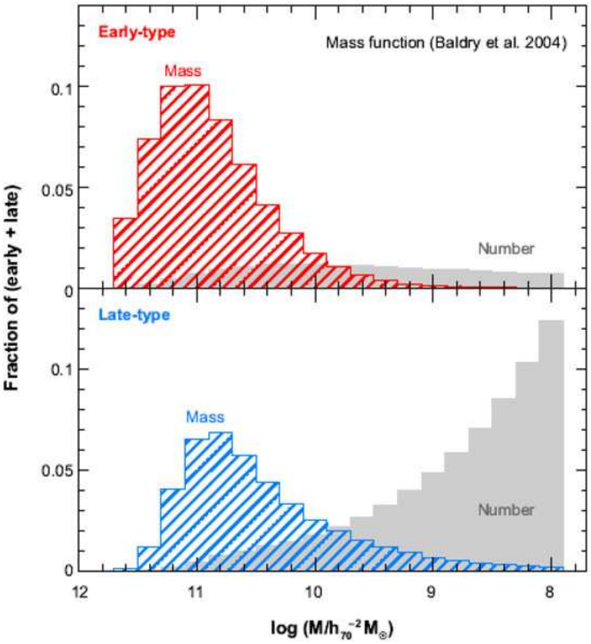

Figure 1.2: Mass distributions in the local Universe of early-type galaxies (top panel) and late-type galaxies (bottom panel). [96].

Furthermore, these galaxies constitute an homogeneous class in terms of colors and stellar population content, displaying always red colors and evolved (i.e. old) stellar populations. Generally their spectra show only absorption lines (see for example Fig. 5.1) since the most of the star formation is already quenched.

The homogeneity of ETGs is confirmed also by the numerous scaling relations observed in the local Universe. In particular, these scaling relations involve both their structural parameters, as the effective radius, and their colors and mass. In particular, the Mass-age, Mass-metallicity, and Mass-α/Fe will be scaling relations involved in the studies presented within this thesis, as it will be discussed in the next sections (in particular in Section 1.5). All these relations demonstrate the presence of a clear correlation between the mass and the stellar population properties implying important constraints on their formation and evolution processes.

The class of ETGs and their study thus appear as the more powerful tool to investigate the formation and evolution history of galaxies in the Universe. We have seen that in the local Universe on one hand they are a class of well recognizable objects, and on the other hand they include the most of the baryonic mass, even enclosed in the most luminous and thus easier to be analyzed systems.

Most of these favourable characteristics are a strong point also in the more distant Universe at least until $z \sim 1$, even if with some difference and with some more observative difficulties. For example in the earlier cosmic epochs, galaxies host younger stellar populations, thus their colors are slightly bluer and/or could be obscured by dust due to the very recent star formation events. Moreover, exists the observational problem of the morphology (as discussed in Tamburri et al. 2014 [113]), due to the faintness of these distant objects which prevents a certain morphological classification. Finally, we do not know if the observed scaling relation are the product of the evolution of ETGs during the cosmic epochs, or of the formation mechanisms. This latter possibility would imply that these relations still hold at any redshift with the same characteristics.

For all these reasons, exploring the formation and evolution of ETGs both in the local and in the distant Universe is a powerful tool to shed light on the issue of the formation of the structures as they appear in the Universe that we observe. In the next section I will introduce the main proposed scenarios for the star formation and assembly histories of ETGs together with the observational evidences so far collected.

1.2 Formation and evolutionary scenarios

Since the 1960s, many theories on the formation and evolution of this special class of galaxies, the ellipticals, have been formulated to explain the observational evidence that ETGs show the remarkable uniformity in their photometric and chemical properties discussed in the previous section. These models not only have to fully describe what is observed in the local and distant galaxies, but also to match the constraints imposed by the studies on the formation of dark matter halos structures, in a wider cosmological framework.

One of the first models proposed to describe the formation of the ETGs was the so-called monolithic collapse scenario. In this framework, ellipticals are assumed to have formed at high redshift ($z > 5-7$) as a result of a rapid collapse of a gas cloud. This gas is then quickly converted into stars by means of a very strong burst followed by a rapid quenching of the star formation activity due to the galactic wind powered by supernovae explosions and stellar winds which carry out the residual gas (Eggen et al. 1962 [24], Larson 1974 [54], van Albada 1982 [126]).

The numerous observational works which have revealed the presence of old stellar populations in ETGs and the recent finding of a population of massive and passive galaxies already in place at high redshift, when the Universe was only a few Gyr old (Cimatti et al. 2004 [14], Saracco et al. 2005 [103]), are in agreement with this scenario.

However, both the detection of residual star formation activity in ETGs at $z < 1$ (Kauffmann et al. 1993 [43], Trager et al. 2000 [120]), and the problem that the monolithic model cannot be easily included in a global cosmological framework, have lead to the formulation of a *revised* monolithic model (Kobayashi 2004 [46], Pipino et al. 2010 [91]). In this new scenario, now placed in the cosmological context of the Cold Dark Matter (CDM) model which is successful in reproducing the anisotropies of the cosmic microwave background, the massive ETGs would assemble most of their mass at $z > 2-3$ by means of merging events with small substructures comoving in the same potential well. The following evolution is mainly characterized by the ageing of the stellar populations, with new small star formation events at $z < 1$, connected for example with merging events with smaller satellite galaxies.

An alternative scenario of galaxy formation is the hierarchical model, based on the hierarchical clustering scenario for the formation of dark matter haloes in the CDM cosmological framework. This model suggests that massive galaxies are the final product of several gas-rich merging (called "wet") episodes of disc galaxies at high redshift ($z \sim 4 - 5$) which form most of the final galaxy mass (Kauffmann et al. 1993 [43], De Lucia et al. 2006 [23]). Observational evidences in favour of this scenario are the sharp increasing of the merging rate with redshift (see Patton et al. 1997 [86]) and the observed relation between the colors and the structures complexity of galaxies, with colors tending to bluer wavelengths with the increasing of the complexity. Finally, this scenario is well supported by numerical simulations of the merging interaction among galaxies which successfully reproduce also the kinematic and photometric properties of massive ellipticals (Naab et al. 2006 [79]).

On the other hand, the number density of elliptical galaxies does not decrease with increasing redshift at least until $z \sim 2$, with the fraction of ETGs being constant at $20 - 30\%$ (Tamburri et al. 2014 [113], Im et al. 1996 [38]), contrary to what is foreseen by the hierarchical scenario.

A further model of galaxy formation, the so-called dry merging view, predicts merging events without gas (called "dry") from which very luminous ETGs are formed by the union of quiescent galaxies, i.e. without ongoing star formation. This scenario is supported by the evidence of an almost-null evolution of the ETGs luminosity from $z \sim 1$, while a strong decrease would be expected due to the ageing of stars. This effect could be thus explained assuming an increasing of mass not followed by new star formation, i.e. dry merging (Bell et al. 2004 [4]).

In the last years, a new scenario called "inside-out growth" has become under discussion. In this scenario, ETGs formed at high redshift ($z \sim 4 - 5$) as single *compact* spheroids from gas-rich merging event. This initial wet merging event must have happened at high redshift where the progenitors galaxies still have residual gas, while at lower redshift the compact ETGs will experience consecutive dry minor merging events which involve low mass systems. The main effect of the dry merging events is the adding of an external envelope at low density to the compact ETG, which is able to leave unchanged the stellar mass while the total effective radius is enlarged. This model has been formulated because of the observation of elliptical galaxies at $1 < z < 2.5$ with an effective radius a factor $\sim 2 - 5$ smaller with respect to the mean radius of local ETGs with the same stellar mass (Daddi et al. 2005 [20], Longhetti et al. 2007 [62], Cimatti et al. 2008 [17], Saracco et al. 2009 [105]). This mechanism should expand the galaxy dimension, but not the total mass, until the values of the effective radius match those of the ETGs with the same mass observed in the local Universe (Naab et al. 2009 [80], Bezanson et al. 2009 [5]).

Actually, this scenario shows some limitations as for example the unlikely number of minor dry merging events necessary to expand the ETGs and the lack of a mechanism able to justify the presence of a number of non-compact ETGs observed at high redshift equivalent to that of the compact ones (Saracco et al. 2010, 2011 [106], [107]). These last results suggest that the processes that drive the mass assembly of ETGs are probably not universal within the whole class of galaxies and which could be the factors that determine different formation histories remain an open issue.

In conclusion, the origin and the assembly history of the ETGs still remains an open issue up to now, and the way to discriminate among the different proposed scenarios is offered by the studies of high redshift galaxies. For example, the wet merging scenario predicts that ETGs are formed by composite stellar populations with the inner population younger than the outskirts. On the contrary, dry merging events, mixing the stellar populations of the progenitors should dilute the age radial variation, forming a rather flat stellar population distribution. In the inside-out growth scenario, instead, the gas-rich merging events which should have formed the compact ETGs, suggests a stellar population highly coeval in the center, to which there will be added and redistributed in the outer regions the contributions of the following dry merging events, preserving the absence of strong gradients.

This picture of formation models of ETGs thus highlights the possible presence of multiple stellar populations within this class of objects but with some differences depending on the way mass has been accreted. Up to now, studies on ETGs based on photometric analysis have allowed to identify them also in the distant Universe, but only recently the available spectroscopic data for some of these distant objects with high signal to noise ratios has opened a new possibility of studying these composite populations at high-redshift as it will be detailed in the work of Chapter 5.

1.3 Observational approach

In the previous section the still debated scenarios of ETGs formation have been presented. All the possible tests aimed at verifying which is the most realistic model to describe the formation and evolution of ETGs must pass through the comparison with the observations. From the observational point of view, two different but complementary approaches exist for the studying of galaxy formation. In this section I present these two mostly adopted approaches together with their main observational results obtained so far in the local and high redshift Universe.

The so-called "archaeology" approach (Thomas et al. 2005, 2010 [116], [117]) studies in details the properties of *local* galaxies, trying to trace back their past star formation history. The studies on local ETGs have the advantage of dealing with a huge quantity of data (e.g. complete samples) with high signal to noise ratio and with high spectral and spatial resolution. In particular, this approach has been pioneered by the analysis of slopes and scatter of the main ETGs scaling relations (Renzini 2006 [96]) and followed by detailed studies of absorption-line indices (Longhetti et al. 2000 [60], Trager et al. 2000 [120], Thomas et al. 2005, 2010 [116], [117]). The main challenge in the archaeology of stellar populations of ETGs is the disentanglement of age and metallicity, whose effects are degenerate in old ($>$ 5 Gyr) stellar populations. Moreover, in the local Universe the stellar properties of old ETGs could have been mixed up by many possible evolutionary events (like merging events), that could have led to the same final result. As a consequence they have lost the faculty of bringing information on the origin of their star content.

A more direct approach is of course that of following the evolution of the stellar properties of ETGs with redshift by means of direct observations at each cosmic epoch. In this case the main difficulty is the lower quality (i.e. signal to noise ratio) and quantity (e.g. lack of complete samples) of the obtained data with increasing redshift, that consequently result more difficult to be reduced and interpreted. An other complication is the so-called “progenitor bias”, which implies that ETGs observed at low and high redshift are not necessarily extracted from the same sample (van Dokkum et al. 2000 [129]). Only in the last years, testing the high redshift ($z > 1$) Universe is beginning possible thanks to the advent of new technologies and instrumentations that allow to obtain the necessary high quality data. The work described in this thesis, in particular, adopted this second approach exploiting new available spectroscopic data in the $z > 1$ Universe.

In the local Universe ($z \sim 0$), as already mentioned, ETGs constitute a family of stellar systems mainly characterized by rather old stellar populations. Most of the recent works based on samples of ETGs at $z < 0.1$, are in agreement in considering the mass assembly of ETGs completed at $z \sim 0.8$. Indeed, from the results on the evolution of the stellar mass function, which describes the galaxy density as a function of mass, we know that means that the number of massive ETGs remains constant from the local Universe to $z = 1$ (Fontana et al. 2004 [28]). Moreover, the observation of the evolution of the galaxy luminosity function, which provides the number of galaxies in different luminosity bins, which shows a shape variation in the range of the brightest galaxies, is consistent with a pure passive evolution of ETGs (Saracco et al. 2006 [104]). Other observational evidences in agreement with these findings are that the number density of ETGs observed at $z \leq 1$ is consistent with that at $z = 0$ (Saracco et al. 2005 [103], Cimatti et al. 2006 [15]) and that the evolution of the scaling relations that ETGs follow, in particular size-mass and size-luminosity, is consistent with a passive evolution of their luminosity. Finally, from the evolution of the Fundamental Plane, empirical sharp relation (Treu et al. 2001 [121]) which involves the main characteristics of ETGs (effective radius, superficial brightness and velocity dispersion), we know that its scatter is invariant until $z \sim 0.7$ (Treu et al. 2002 [122]) and that the offset observed at $z \sim 1$ with respect to the local relation is consistent with a pure passive evolution of the stellar population (van Dokkum et al. 2003 [130]).

A fundamental role in the evolution of ETGs at $z < 1$ is played by mass. Indeed, many observational evidences support the hypothesis of the so-called “downsizing”, which suggests that galaxy evolution is strongly affected by mass, i.e. that more luminous and massive systems complete their formation first, while less massive systems prolong their star formation activity for a longer time. For example, it is found that the possible new star formation episodes at low redshift $z < 1.2$ in ETGs would involve mass fractions $< 1\%$ for massive galaxies, and up to about 40% for those less massive (M< $10^{11}M_{\odot}$) (Treu et al. 2005 [123]). An other evidence of properties connected with mass is the color-magnitude relation (Kodama et al. 1998 [47]) which shows that ETGs are composed mainly by coeval stellar populations, but being the more massive more metal rich (see Section 1.5).

An other important factor in the evolution of ETGs is the environment where they have formed. Indeed, for example scaling relations of ETGs are invariant with respect to the density of their environment, but in low-density environments they show a more significant scatter with respect to more dense regions or clusters. The main result obtained within the analysis of local sample of ETGs, is that galaxies in low-density environments are $\sim 1-2$ Gyr younger with respect to cluster counterparts (Thomas et al. 2005 [116]). This could be explained as a consequence of a more complex and prolonged mass assembly and stellar evolution of field ETGs with respect to those in denser environments. However, the environment seems to be less determinant for the ETGs evolution than the effects related to their mass, as suggested by the work of Thomas et al. 2010 [117] that will described in Section 1.5.

In conclusion, on the one hand the agreement among these results has lead to a clear comprehension of the properties and evolution of ETGs at $z < 1$, but on the other hand it has not added any strong constraint on the mechanisms responsible of their mass assembly, thus opening the necessity of focusing on the higher redshift ETGs analysis.

The situation in the redshift range $1 < z < 2$ is far from being clear and homogeneous like that at $z < 1$, firstly because of the difficulties in finding numerical significant samples of ETGs at high redshift. Moreover, the spectral characteristics that provide information on this class of galaxies are located in the spectral optical region, which at $z \sim 1$ is redshifted toward the near infrared, where the observations are greatly disturbed by the atmospheric emissions and absorptions. Therefore, the first step to study the stellar populations of ETGs at $z > 1$ is that of finding an appropriate sample of ETGs with spectroscopic redshift determination, spectral classification and morphological characteristic similar to those of local ETGs (Tamburri et al. 2014 [113]). Up to now, only few pioneering works (Ziegler et al. 2005 [139]; Cimatti et al. 2008 [17]; Onodera et al. 2012 [81]; Jorgensen & Chiboucas 2013 [40]; Lonoce et al. 2014 [63]; Gallazzi et al. 2014 [29]; Jorgensen et al. 2014 [41]) have been devoted to the analysis of spectroscopic data of high-z ETGs and they are mostly based on very low resolution data and/or in some cases performed on stacked spectra (Onodera et al. 2015 [82]). From these analysis we know that the population of ETGs at $z \sim 1-2$ is composed by stellar populations formed in a strong and short burst of star formation happened at $z > 3$ (Cimatti et al. 2004 [14], Longhetti et al. 2005 [61]), and characterized by red colors (R-K $> 5-6$) typical of an old population passively evolved, with age within $1-4$ Gyr, with only small dust extinction and with a typical stellar mass M $\geq 10^{11}$ $M_{\odot}$ (Cimatti 2008 [16]).

Next two sections will describe the two main stellar population properties, i.e. age and metallicity, that have been investigated in this thesis, which are the main tools to constrain the evolution of ETGs.

1.4 Age

The age of the stellar populations is the first stellar property that must be explored if we want to know the evolutionary stage of ETGs at high redshift. Indeed, knowing the distribution of the ages among the high-z ETGs population and consequently the epochs of the formation of their stars allows to put strict constraints on the formation of the ETGs themselves. Age is also the easiest parameter to be determined thanks to the strong dependence of colors and absorption lines (e.g. Balmer lines) on the evolutionary phase of stars. In particular, the determination of ages in the higher redshift Universe is even simplified because galaxies are younger and the effects of small age variations on the observables are more evident than in the local Universe, even if a residual age-metallicity degeneracy still holds. Moreover, obtaining a solid measure of the stellar population age of ETGs is of fundamental importance to derive solid constraints also on the other stellar population parameters, as the stellar metallicity (see next section).

It has been already mentioned in the previous section that recent observations have revealed a population of massive and passive galaxies already in place at high redshift (Cimatti et al. 2004 [14], Glazebrook et al. 2004 [33], Saracco et al. 2005 [103]), as shown in the example of Fig. 1.3. This makes important to move the investigation of ETGs ages to even higher redshift ($z > 2 - 3$) to explore the phase of their stronger evolution that was previously expected in the lower redshift range between 1 and 2. However, the $z > 3$ Universe exploration is still challenging for ETGs due to their faintness. Thus, the only actual possibility now is studying in more details the fossil records of $z \sim 1$ ETGs trying to extract information on the active processes of their recent formation. Indeed, any recent event as dry/wet mergers or gas inflows that could have changed the mean age of the original stellar population thanks to new added stars or as a result of new star formation events, can be detected in the analysis of the age of the stellar populations.

The analysis of ages is generally performed by means of photometric data and colors analysis since we have seen that they are sensitive to age variations (Longhetti et al. 2005 [61], Cimatti et al. 2008 [17], Maraston et al. 2010 [71]). In fact, this is also due to the great availability of multiband photometric data on a large number of objects also at high redshift, collected by many deep galaxy surveys as GOODS (Great Observatories Origins Deep Survey, see Santini et al. 2009 [102] for a complete catalogue) and COSMOS (Cosmological Evolution Survey, McCracken et al. 2010 [76]), which usually include also high-quality HST (Hubble Space Telescope) deep images. The derivation of the age of high redshift ETGs is performed through the comparison of their colors with a wide range of stellar population models (see Section 3), providing a mean value of their global stellar population. In fact, this method apart from being easily applied to large quantities of data has the disadvantage that cannot be used to detect different stellar components with different ages, but it allows only the estimate of an average global value. Moreover, colors could be biased by dust absorption which can influence all the photometric analysis.

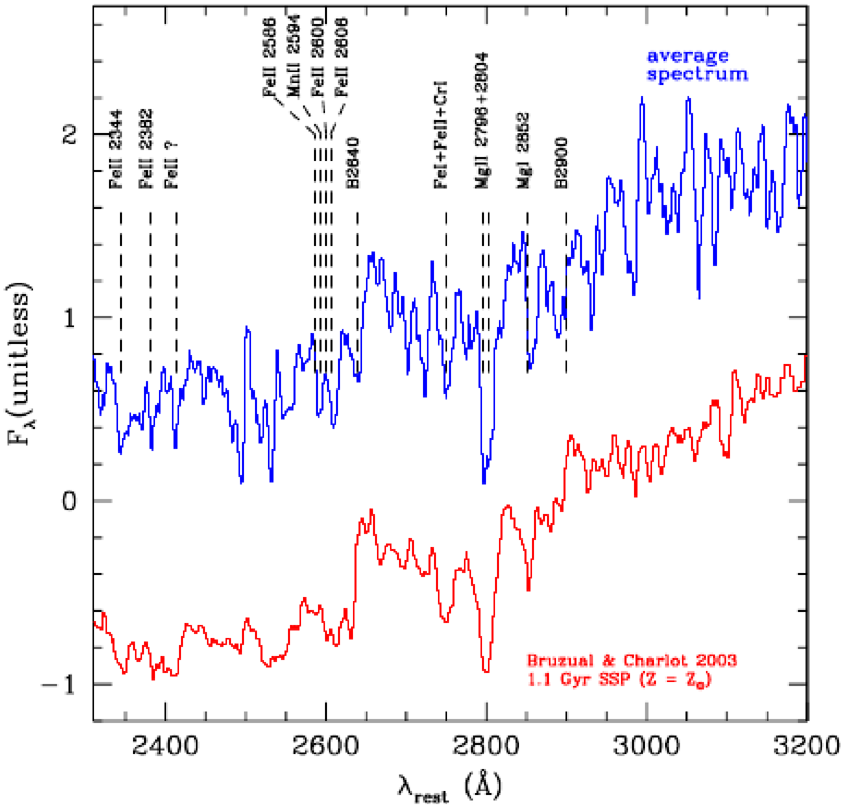

Figure 1.3: A zoom of the average UV spectrum of the four ETGs found in the range $1.4 < z < 1.9$ (blue line) compared with the synthetic spectrum of a 1.1 Gyr old simple stellar population (red line) with solar metallicity and Salpeter initial mass function (Bruzual & Charlot 2003 [7] models, see Section 3.3). Formation redshift $z_{form} > 2.7$. (Cimatti et al. 2004 [14])

As it will be extensively seen later within the here presented work, more sensitive age-indicators exist: the spectral indices. As colors, absorption lines are strongly affected by the evolutionary stage of stars, but they are first of all less sensitive to dust absorption. Well studied spectral indices are able to provide very detailed information on the stellar population content of ETGs as it will be described in Chapter 2, and demonstrated by numerous works in the local Universe (Longhetti et al. 2000 [60], Poggianti et al. 2001 [92], Thomas et al. 2010 [117]) and intermediate Universe (Jorgensen & Chiboucas 2013 [40], Gallazzi et al. 2014 [29]). Moreover, some particular combinations of indices can help to detect multiple stellar components, even when involving few percentages of the total stellar mass (Section 2.1), giving precious constraints on the recent star formation history of ETGs. As already said, however, at the moment spectroscopic analysis can be performed only on small samples of ETGs, and up to now no statistical analysis have been possible.

A large part of the work presented in this thesis is devoted to the analysis of the age of high redshift ETGs, both looking for multiple components (at $0.7 < z < 1.2$) and trying a solid determination of its average value at $z > 1.4$.

1.5 Metallicity

The metallicity characterizing the stars of a galaxy is an important parameter because it gives information both on the origin of the galaxy itself (i.e. the original gas from which its stars formed) and on the processes which have contributed to its early evolution (i.e. the gas enrichment related to the star formation activity). Furthermore, it is sensitive to processes as the gas infalls and outflows, i.e. to feedback processes and to the interplay between the galaxy and the intergalactic medium. This is for example connected with the still unclear mechanisms of star formation quenching in elliptical galaxies.

From the 1970s it has been historically known the existence of a clear correlation between luminosity and metallicity of galaxies (Lequeux et al. 1979 [58]). The fact that the most massive galaxies are also the most metal-rich was interpreted by Larson (1974, [54]) as a result of the galactic winds that occur later in the most massive objects, thus allowing the star formation process to continue for a longer period than in less massive galaxies. Indeed, outflows are expected to be more important in low-mass galaxies where the gravitational potential is lower and a smaller fraction of gas is retained. This could explain why the higher is the mass of the galaxy, the larger is the chemical enrichment and the redder are the colours.

It is now clear that local galaxies follow a well-defined *mass-metallicity relation*. However, the above interpretation based on the galactic winds has been changed in the last years due to the observed α-elements (e.g. Magnesium) enhanced abundance with respect to Iron (α/Fe ratio) compared to the solar abundances in the central parts of ellipticals which shows a trend with mass (Faber, Worthey & Gonzalez 1992 [25]), suggesting that the star formation lasted for a period shorter than the time at which the numbers of type Ia Supernovae becomes important. Indeed, an overabundance of α-elements relative to Iron is a clear sign that a short process of galaxy formation occurred before than a substantial number of type Ia Supernovae could explode and contribute to lower the α/Fe ratio (see Matteucci 2001 [75], Thomas et al. 2005 [116]). The observed increasing of the α/Fe ratio in the core of elliptical with mass indicates, among other possibilities, that the star formation lasted for a shorter period in the more massive systems, on the contrary of the classical wind scenario of Larson [90].

Other possible explanations exist, for example a variable initial mass function that changes systematically with mass (Koppen, Weidner & Kroupa 2007 [48]) and/or a decrease of the dark matter content again as a function of the mass (Matteucci, Ponzone & Gibson 1998 [74]). These effects have a significant impact on galaxy evolution, and the knowledge of their relative contributions is of crucial importance. Different models have been built to reproduce the mass-metallicity relation in the local Universe (Pipino & Matteucci 2004 [90]) and it has been possible to test their predictions directly in the first phases of evolution as *gas* metallicity can be measured at high redshift in star-forming galaxies, in particular in Lyman-break galaxies (Pettini et al. 2001, 2002 [88], [89]). Gas metallicity at high redshift could be obtained

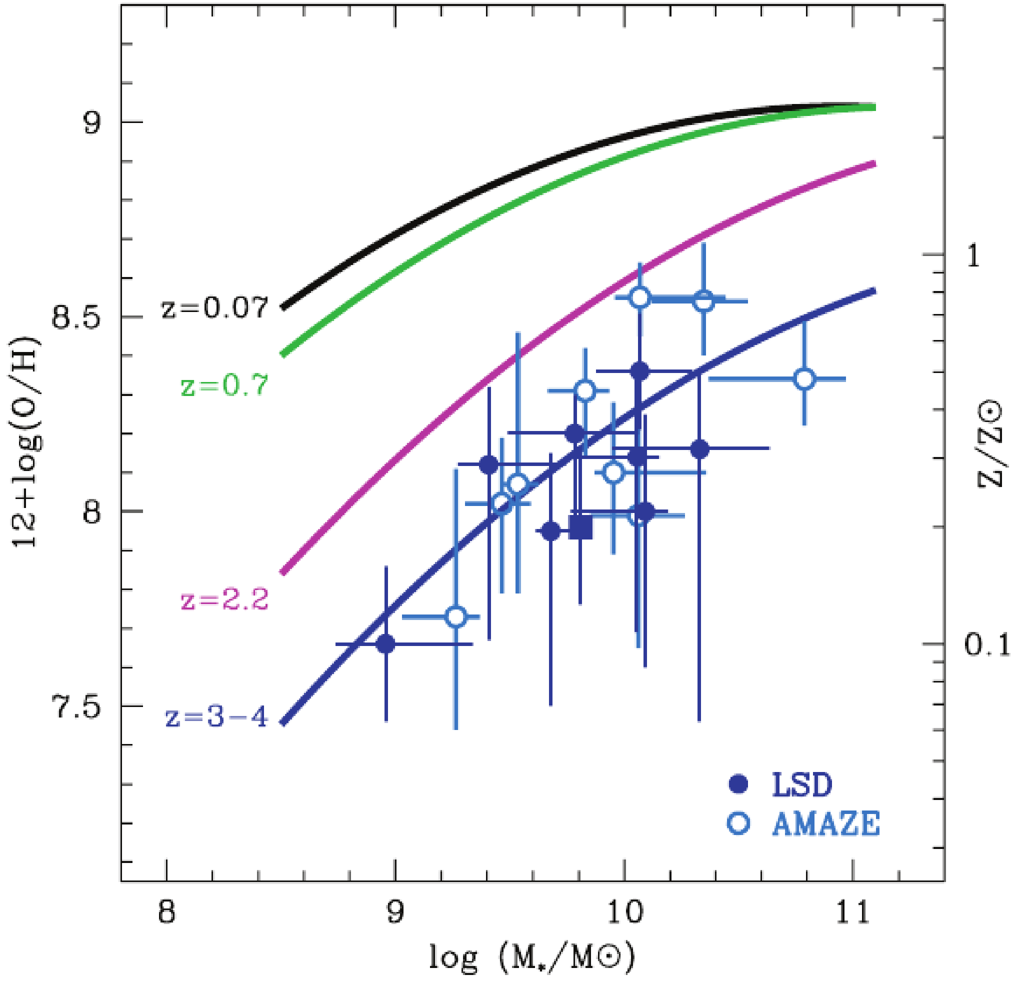

Figure 1.4: Mass-metallicity relation from the *gas* in Lyman Break Galaxies at high redshift. At higher redshift the ISM is observed to be more metal-poor. [67].

by measuring the fluxes of the main optical emission lines ([O II]λ3727, Hβ, [O III] λ5007, Hα) that in this kind of galaxies are prominent (Mannucci et al. 2009 [67]). As shown in Fig. 1.4 several works have observed the mass-metallicity relation in the distant Universe, around $z = 0.7$ (green line), between 0.5 and 1.2, at $z \sim 2$ (Purple line) and $z \sim 3-4$ (blue line) (See references in [67]). It is found a clear evolution with cosmic time of this relation, with metallicity decreasing with increasing redshift, for a given stellar mass. This evidence could be the expected behaviour if the metal enrichment of the interstellar medium increases during the early cosmic epochs as a consequence of the metal production in stars.

In contrast, deriving the *stellar* metallicity of high-redshift galaxies, in particular of the most quiescent, is much more challenging because it is obtained from

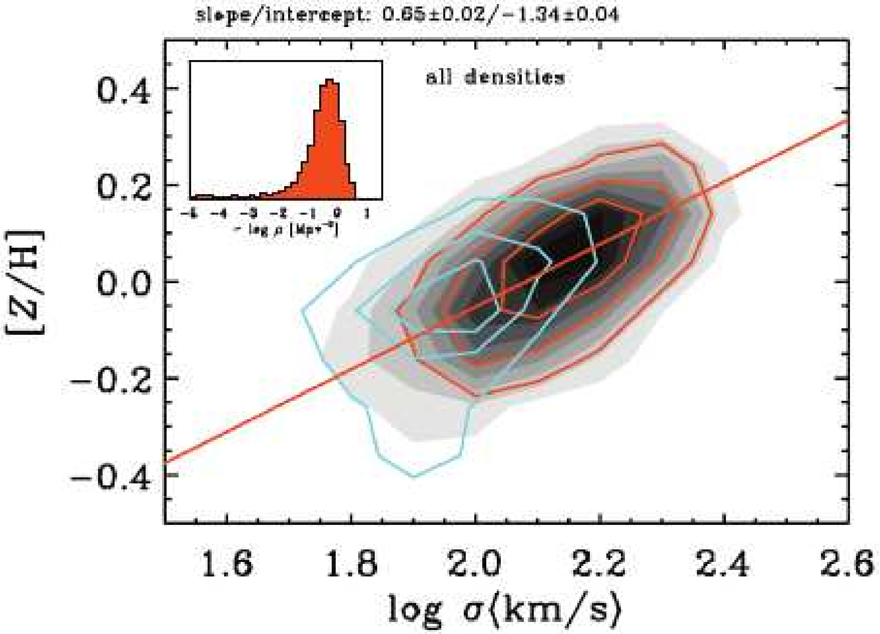

Figure 1.5: *Stellar* mass-metallicity relation in the local Universe [117].

absorption lines which require high S/N of the spectroscopic data to be detected and measured. It is important to note that *gas* and *stellar* metallicity (both showing the mass-metallicity relation) are related, but the information that they contain is different because the gas fraction which effectively turns into stars during the star formation must be considered. Moreover, it is still hardly debated if the high-z Lyman-break galaxies are the real progenitors of the $z \sim 1$ and local ellipticals population (see de Mello et al. 2004 [77], Williams et al. 2014 [134]), thus a “progenitor bias” must be taken into account when comparing the two galaxy populations.

Up to now, the analysis of the stellar mass-metallicity relation is based on local sample of elliptical galaxies following the so-called “archaeology approach” to derive information about their star formation histories. Many works have studied this relation helped also by the α-elements abundances measures to disentangle the important age-metallicity degeneracy affecting the local studies (Thomas et al. 2005, 2010 [116], [117]). An example taken from Thomas et al. 2010 [117] is shown in Fig. 1.5: a large sample of local elliptical galaxies exhibits a clear correlation between the stellar metallicity and the velocity dispersion which is a tracer of the stellar mass.

This evidence, combined with the observed α/Fe-velocity dispersion relation [117], has lead to the discovery of the fundamental role of the mass in determining the star formation history of ellipticals. Indeed, the chemical content of the sample of galaxies, as already discussed, provides the star formation time-scale. In Fig. 1.6 the specific star formation rate as function of look-back time (or redshift) of

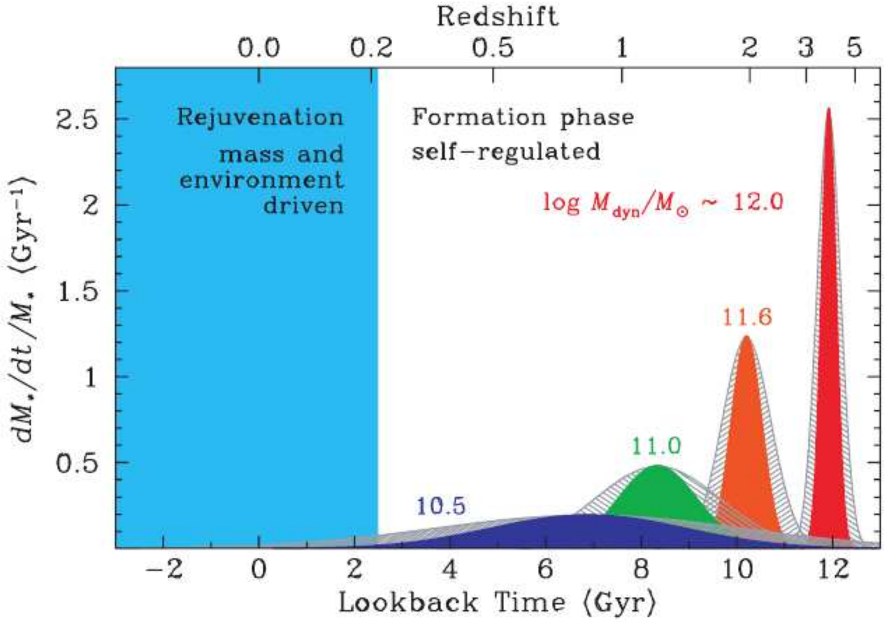

Figure 1.6: Specific star formation rate as function of look-back time for early-type galaxies of various masses as indicated by the labels.[117].

ETGs of various masses is shown, indicating that the more massive galaxies formed at earlier cosmic epoch and on a shorter time-scale than the less massive ones.

The previous important relations and finding have been found and measured in the local Universe, even if local galaxies are the result of a very long evolution from the formation of the first stars to what is observed at $z = 0$, so that their stellar properties could have been mixed up by possible evolutionary processes or events, like prolonged gas inflows that trigger new star formation or merging events with external systems. Indeed, line indices and colour gradients are observed in local ellipticals (Carollo et al. 1993 [10], La Barbera et al. 2012 [53], Spolaor et al. 2008 [110]) and they can be reproduced by means of a variation in the mean metallicity of the stellar population as a function of the radius. This evidence could be explained both as an indicator of a common formation process, or as the product of evolutionary events, since at higher redshift colour gradients are also observed but with different characteristics (Gargiulo et al. 2012 [31]).

So it is of fundamental importance to derive these scaling relations also directly at higher redshift to complete our knowledge on the formation scenario. Up to now, only few spectroscopic works have been devoted to the analysis of the mass-metallicity relation at intermediate redshift (e.g. Sanchez-Blazquez et al. 2009 [101], Jorgensen & Chiboucas 2013 [40]), mainly focused on cluster samples of ellipticals. These works confirm the trend of the local scaling relations observing the same slope at redshift $z \sim 0.5 - 0.8$, with the more massive galaxies being the more metal rich, but the main difficulty found is the observed larger scatter in metallicity and α-enhancement which actually prevents the determination of the scaling relation itself. At higher redshift in the field the analysis is at the moment based on stacked spectra due to the even lower quality of spectroscopic data (de Mello et al. 2004 [77], Schiavon et al. 2006 [109], Onodera et al. 2015 [82]), so that the apparent consistent results with the local scaling relations could be only the product of the stacking process. Indeed, the metallicity values, being a mean of the stacked galaxies, actually hide the underlying scatter that can be a sign of non homogeneous properties of the high-redshift stellar populations.

In general, it is found that the high redshift ($z > 1$) quiescent galaxies host *high stellar metallicity* populations, which is in agreement with what is found in the local massive ellipticals, at least in their inner cores. This could be explained with a simple passive evolution toward $z = 0$. As it will discussed in next section, in this thesis new clues on the metallicity measures of high redshift ellipticals will be shown, which will in part confirm this trend but also open to a non homogeneous scenario with the consequent suggestion of a variety of evolutionary paths for this class of objects which appear more and more complex than thought before.

1.6 This thesis

As it has been detailed in the previous sections, different galaxy formation scenarios suggest different star formation histories. Gaining information on the stellar population content, in particular age and metallicity, of ETGs is thus of great importance to shed light on their origin. In this thesis I will present my contribution to this investigation studying the age and metallicity of $z > 1$ ETGs, that has been possible thanks to new available spectroscopic data which allowed to exploit the great potentiality of measuring many combinations of spectral indices.

As far as the *age*, in Chapter 5 the analysis of a sample of 15 ETGs at $z \sim 1$ for which, by means of a specific combination of spectral indices sensitive to young stars, I detected the presence of minor younger components superimposed on the old bulk of stars will be presented. As will be argued in Chapter 5, this evidence tells us that new, although minor, episodes of star formation must have occurred after their formation later during their evolution, implying new constraints on the evolutionary models.

As discussed in the previous Section 1.5, the estimate of the stellar *metallicity* of individual high redshift ellipticals is at the moment an observational challenge, because it requires high S/N spectroscopic data covering large spectral window, but it would be fundamental to shed light on the star formation histories of ETGs. The contribution of this thesis to this topic will be presented in Chapters 6 and 7. Thanks to spectroscopic data collected with the VLT/X-Shooter spectrograph, which offer the possibility of exploring many metallicity indicators, I was able to derive for the first time an estimate of the stellar metallicity of 4 individual elliptical galaxies at $z > 1.4$, together with some hints on their α/Fe enhancement. These observations show different values of the metallicity among the sample galaxies, including both super and sub solar values.

The three works performed during my PhD, discussed in Chapter 5, 6, 7, have been built on three important elements: *i*) the spectral indices (i.e. the main tool of the analysis), *ii*) the synthetic stellar population models (needed to derive stellar parameters from data), *iii*) the spectral data useful for the proposed analysis. The three elements will be described in details in the following Chapter 2, 3 and 4 respectively.

Chapter 2

Spectral indices

Spectral indices are powerful instruments to get information on the stellar population properties of galaxies, in particular age and metallicity. Indeed, they provide, thanks to their definitions, the measure of the strength of many absorption lines or features, which are related both to the age of the stellar populations (by means of their dependence to the stellar temperature) and to its chemical content (by means of their dependence on the abundance of metals in the stellar atmospheres). Obviously, this double dependence leads to some degeneracy between these two parameters, but as it will become clear in the following sections, in some cases this deficiency can be exceeded by choosing the right set of indices.

One of the great advantage of working with the line indices is that absorption lines are less affected by dust reddening than continuum or emission lines, which is a well-known issue for younger stellar populations. This fact helps the analysis of the stellar population properties, deleting de facto one parameter, i.e. dust, which is degenerative with age and metallicity. Indeed, these three factors (age, metallicity and dust) act in same way on the spectrum shape, increasing the emission in the redder wavelength.

The mostly known and used spectral indices are the so-called Lick/IDS indices, defined by Worthey et al. 1994 [135] in the optical region around 5000 Å (see the following Sec. 2.2). This important set of indices has being exploited by many works based on local sample of galaxies (Longhetti et al. 2000 [60]). However, in the last years, many works focused on the analysis of the stellar population properties of galaxies are approaching medium and high redshift ranges in order to study the stellar content of more and more distant galaxies, closer to their formation epochs. Thanks to the cosmological redshift, this has meant that the restframe spectral region that is analysed with optical observations, is moving to shorter wavelength, toward the extreme UV region. From this fact, the necessity of exploring new sets of spectral indices in the region from 4000 Å to 2000 Å has raised. Thus now, besides the Lick/IDS indices, we have the possibility of dealing with a very wide set of solid spectral indices defined and tested by e.g. Ponder et al. 1998 [93], Maraston et al. 2009 [70] (and references therein) covering a large spectral range.

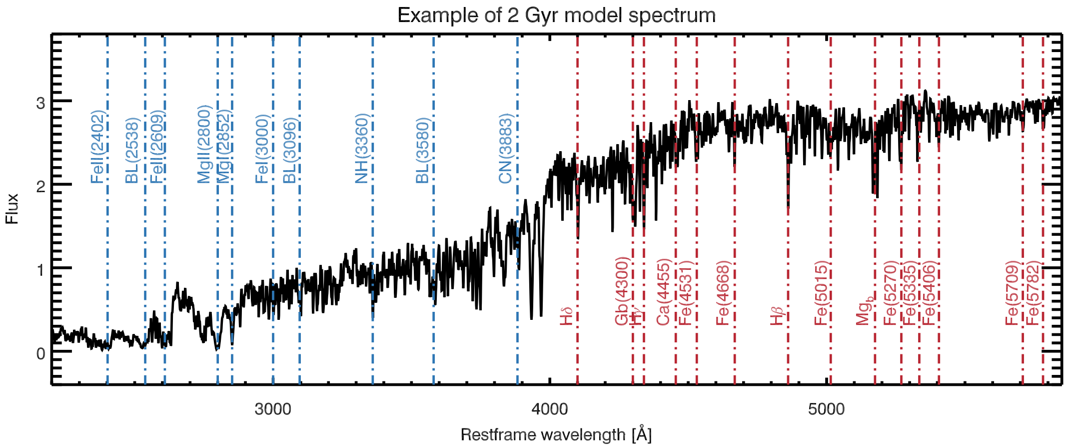

Figure 2.1: Example of a 2Gyr synthetic spectrum in the spectral region around 2500 − 6000 Å. UV and Lick/IDS indices are highlighted in blue and red respectively.

The work of this thesis is principally based on spectroscopic data in the observed spectral range from UV to the near-Infrared (see next sections) of ETGs in the redshift range from $z \sim 0.6$ to $z \sim 2.0$, therefore the following sections are dedicated to a brief description of the main and most important spectral indices used in this work. In particular, the first section is focused on the 4000 Å region exploited in the analysis discussed in Chapter 5; in the second section there is the description of the Lick/IDS indices together with the peculiarity of some important indices used in the analysis of Chapter 6; and in the third section I will present the main characteristics of the new UV indices (in the 2000 − 3000 Å region), which are the basis of the work described in Chapter 7. Finally, the last section is focused on the error analysis followed by this work, giving particular emphasis to the MonteCarlo simulations.

In Fig. 2.1 the spectral features of many indices are shown on a representative synthetic spectrum in the spectral region around 2500 − 6000 Å restframe.

All the spectral band-passes involved in the indices definitions are listed in Table 2.1.

2.1 D4000 and H+K(CaII)

The two most important age-dependent spectrophotometric indices around the 4000Å range are the D4000 and H+K(CaII) index. The D4000 index was defined by Bruzual 1983 [6] and Hamilton 1985 [36] as the ratio between mean fluxes in two different wide spectral ranges

$$D4000 = \frac{\bar{F}_\nu(\lambda_1 - \lambda_2)}{\bar{F}_\nu(\lambda_3 - \lambda_4)} \tag{2.1}$$

with $\lambda_1 - \lambda_2 = [4050\text{Å}{-}4250\text{Å}]$, $\lambda_3 - \lambda_4 = [3750\text{Å}{-}3950\text{Å}]$ (see also Table 2.1);

Table 2.1: Band-passes for the indices definitions. UV indices from Maraston et al. 2009 [70] (and references therein), Blue indices from Ponder et al. 1998 [93] (and references therein) and Lick indices from Trager et al. 2000 [120].

Index	Blue band-pass [Å]	Index band-pass [Å]	Red band-pass [Å]	notes
BL(1617)	1577.0 - 1597.0	1604.0 - 1630.0	1685.0 - 1705.0	UV
BL(1664)	1577.0 - 1597.0	1651.0 - 1677.0	1685.0 - 1705.0	UV
BL(1719)	1685.0 - 1705.0	1709.0 - 1729.0	1803.0 - 1823.0	UV
BL(1853)	1803.0 - 1823.0	1838.0 - 1868.0	1885.0 - 1915.0	UV
FeII(2402)	2285.0 - 2325.0	2382.0 - 2422.0	2432.0 - 2458.0	UV
BL(2538)	2432.0 - 2458.0	2520.0 - 2556.0	2562.0 - 2588.0	UV
FeII(2609)	2562.0 - 2588.0	2596.0 - 2622.0	2647.0 - 2673.0	UV
MgII(2800)	2762.0 - 2782.0	2784.0 - 2814.0	2818.0 - 2838.0	UV
MgI(2852)	2818.0 - 2838.0	2839.0 - 2865.0	2906.0 - 2936.0	UV
Mg_{wide}	2470.0 - 2670.0	2670.0 - 2870.0	2930.0 - 3130.0	UV
FeI(3000)	2906.0 - 2936.0	2965.0 - 3025.0	3031.0 - 3051.0	UV
BL(3096)	3031.0 - 3051.0	3086.0 - 3106.0	3115.0 - 3155.0	UV
NH(3360)	3320.0 - 3350.0	3350.0 - 3400.0	3415.0 - 3435.0	Blue
BL(3580)	3500.0 - 3540.0	3540.0 - 3600.0	3620.0 - 3650.0	Blue
CN(3883)	3760.0 - 3780.0	3780.0 - 3900.0	3900.0 - 3915.0	Blue
H+K(CaII)	3926.0 - 3940.0	-	3961.0 - 3975.0	Blue
D4000	3750.0 - 3950.0	-	4050.0 - 4250.0	Blue
CN(4170)	4082.0 - 4118.0	4144.0 - 4178.0	4246.0 - 4284.0	Blue
$\mathrm{H}\delta_A$	4041.60 - 4079.75	4083.50 - 4122.25	4128.50 - 4161.00	Lick
$\mathrm{H}\delta_F$	4057.25 - 4088.50	4091.00 - 4112.25	4114.75 - 4137.25	Lick
Ca(4227)	4211.00 - 4219.75	4222.25 - 4234.75	4241.00 - 4251.00	Lick
$\mathrm{H}\gamma_A$	4283.50 - 4319.75	4319.75 - 4363.50	4367.25 - 4419.75	Lick
$\mathrm{H}\gamma_F$	4283.50 - 4319.75	4331.25 - 4352.25	4354.75 - 4384.75	Lick
Gband(4300)	4266.375 - 4282.625	4281.375 - 4316.375	4318.875 - 4335.125	Lick
Fe(4383)	4359.125 - 4370.375	4369.125 - 4420.375	4442.875 - 4455.375	Lick
Ca(4455)	4445.875 - 4454.625	4452.125 - 4474.625	4477.125 - 4492.125	Lick
Fe(4531)	4504.250 - 4514.250	4514.250 - 4559.250	4560.500 - 4579.250	Lick
Fe(4668)	4611.500 - 4630.250	4634.000 - 4720.250	4742.750 - 4756.500	Lick
$\mathrm{H}\beta$	4827.875 - 4847.875	4847.875 - 4876.625	4876.625 - 4891.625	Lick
Fe(5015)	4946.500 - 4977.750	4977.750 - 5054.000	5054.000 - 5065.250	Lick
Mg_b	5142.625 - 5161.375	5160.125 - 5192.625	5191.375 - 5206.375	Lick
Fe(5270)	5233.150 - 5248.150	5245.650 - 5285.650	5285.650 - 5318.150	Lick
Fe(5335)	5304.625 - 5315.875	5312.125 - 5352.125	5353.375 - 5363.375	Lick
Fe(5406)	5376.250 - 5387.500	5375.500 - 5415.000	5415.000 - 5425.000	Lick
Fe(5709)	5672.875 - 5696.625	5696.625 - 5720.375	5722.875 - 5736.625	Lick

The D4000 index is known to be a solid *age* estimator for galaxies stellar populations. In effect, thanks to the wide (200 Å) spectral ranges involved in its definition (Eq. 2.1) and to its strategic position at the boundary from UV and optical range, this index takes care of the balance between young UV-emitter stars and more evolved population. And for the same reasons, it provides an age-indication of the *global* stellar population (as it will be used in Chapter 5). Unfortunately, it is also dependent on the stellar metallicity of the main stellar population thus creating the well known age-metallicity degeneracy, even if the metallicity dependence is much less pronounced for ages < 5 Gyr (upper limit for the age of the Universe at $z\sim 1.4$). Its dependence to age and metallicity can be visualized in Fig. 2.8 (bottom panel).

The H+K(CaII) index was defined by Rose 1985 [98] as the ratio between minimum fluxes of the two CaII absorption lines H and K

$$H + K(Ca\text{II}) = \frac{F_{min}(\lambda_3, \lambda_4)}{F_{min}(\lambda_1, \lambda_2)} \tag{2.2}$$

with $\lambda_1 = 3926$, $\lambda_2 = 3940$, $\lambda_3 = 3961$, $\lambda_4 = 3975$ (see also Table 2.1).

The ratio between the intensity of the two CaII lines would be almost constant over a wide range of stellar population ages, but the spectral resolution usually adopted in the observations causes the blend between the Balmer Hϵ line and the H(CaII) line. Thus the resulting apparent ratio between the two lines is very sensitive to the presence of small mass fractions of young stars, as deeply discussed in Chapter 5. Indeed, it is the blend of H(CaII) with Balmer Hϵ which actually determines the index value. In particular, the effective ratio between H(CaII)+Hϵ and K(CaII) becomes < 1 only for hot stars of type earlier than F5 which have strong Balmer series absorptions, with a minimum value for A-type Balmer-dominated stars [98]. Its dependence to age and metallicity can be visualized in Fig. 2.8 (bottom panel).

In Fig. 2.2 an example of the behaviour of the H+K(CaII) feature for a pure 5 Gyr template spectrum (upper panel) to which a younger stellar component with age 0.5 Gyr is added with increasing mass fractions (1% middle panel, 2% bottom panel) is shown: from these plots it is clear how this index is highly sensitive to the presence of the added younger stars; indeed with only 2% of a younger component, the H+K(CaII) index is significantly changed.

Another peculiarity of this index, similar to that of the Balmer lines, is its sensitivity to the presence of even very modest residual star formation activity. Indeed, in case of the presence of a young stellar component, younger than 0.2 Gyr (see Fig. 2.3), a nebular emission Hϵ line is expected, and even in case of small intensity it can fill the whole H(CaII) line. The behaviour of this index can be followed both in Fig. 2.3 where the H line feature (red vertical line) is plotted for different young stellar populations, and in Fig. 2.4, where, similar to Fig. 2.2, I show a 5 Gyr template spectrum (upper panel) to which is added a very young component 0.05 Gyr old in very small fractions (0.1% and 0.2%) which shows signs of recent star formation activity revealed by the change in the H+K(CaII) feature.

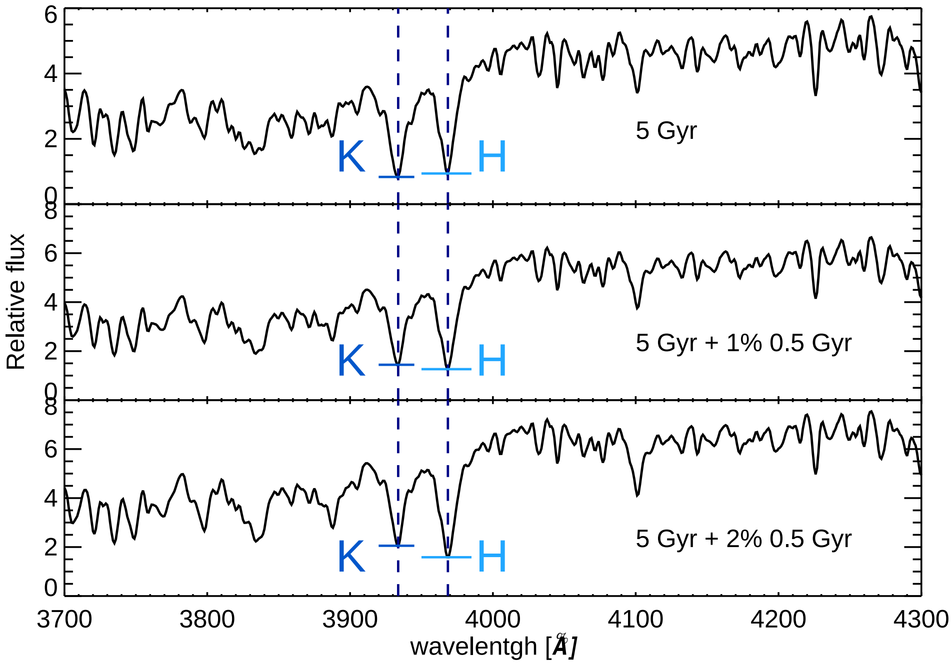

Figure 2.2: The variation of the H+K(CaII) feature on a template composed by a main stellar population of 5 Gyr and increasing mass fractions of a 0.5 Gyr stellar population.

In conclusion, thanks to the above described mechanism, the H+K(CaII) index is a very powerful tool to reveal the presence of multiple stellar population, as it will be widely discussed in Chapter 5.

2.2 Lick/IDS system indices

The Lick/IDS system indices are a well known set of optical indices, and they measure the strength of many absorption lines (with respect to the spectral continuum) produced by various elements or blends of elements, including Balmer lines, Iron, Magnesium and Calcium features. Thanks to the variety of traced elements, the Lick indices are very sensitive to both age (thanks mainly to the Balmer lines) and the metallicity of the stellar population. Furthermore, they have been exploited also to give constraints on the abundances of each specific element. In particular the Mg_b index and many Irons lines indices are good indicators of the balance between α-elements (those produced by Type II supernovae events) and Fe peak elements (produced by Type Ia supernovae events), the so-called α-enhancement. The dependence of these indices on the α-enhancement will be a key point in the work discussed in Chapter 6.

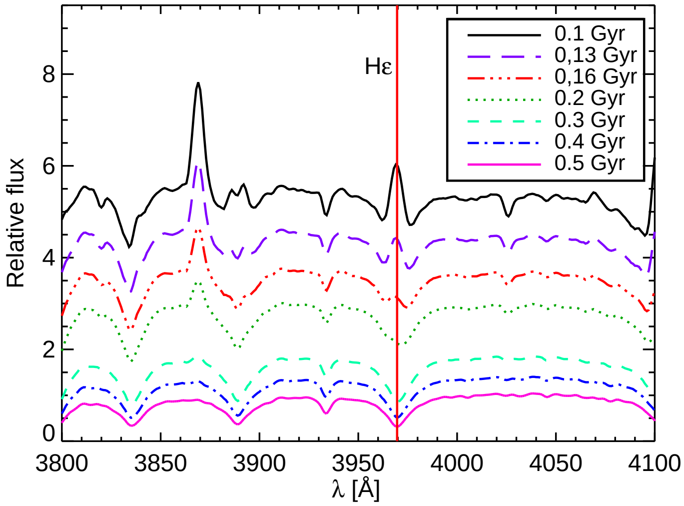

Figure 2.3: Trends of the Hϵ in the H(CaII) line (red vertical line) for stellar population with different ages. From ages younger than 0.2 Gyr the Hϵ emission line starts to be predominant over the absorption.

The set of Lick indices I have used in this work are all defined as *atomic* indices and they are expressed as line equivalent width:

$$I_{atomic} = \int_{\lambda_1}^{\lambda_2} \left(1 - \frac{F_{I\lambda}}{F_{C\lambda}}\right) d\lambda \tag{2.3}$$

where λ_1 and λ_2 are the wavelength limits of the feature band-pass, $F_{I\lambda}$ is the flux per unit wavelength of the feature and $F_{C\lambda}$ is the value of the pseudo-continuum obtained interpolating the mean values of the blue and red band-passes. The used band-passes for both feature and continuum (blue and red) are shown in Table 2.1, and come from Trager et al. 2000 [120].

To visualize the dependence of the Lick indices with respect to age and metallicity, in Fig. 2.5 some examples of the Lick indices trends (following the models of Maraston & Strömbäck 2011 [72]) are plotted as a function of the age of the stellar population (truncated at the age of the Universe at $z\sim 1.4$) for three stellar metallicities: subsolar (blue lines), solar (black lines) and supersolar (red lines). It can be easily noticed that some of these indices are pure *age* indicators. In particular the Hβ index is only very slightly affected by the metallicity degeneracy, because as all the Balmer transitions is mainly determined by the temperature of the stars, being strongly pronounced in very hot/young stars [49]. Similarly, also the Balmer Hγ index is an age-dependent index too, but this index is more affected by the stellar metallicity and by α-enhancement because of the presence of Fe lines in its pseudo-continua windows [115]. Furthermore, both these two indices could be contaminated by the presence of also small contributions of nebular emissions, due to possible

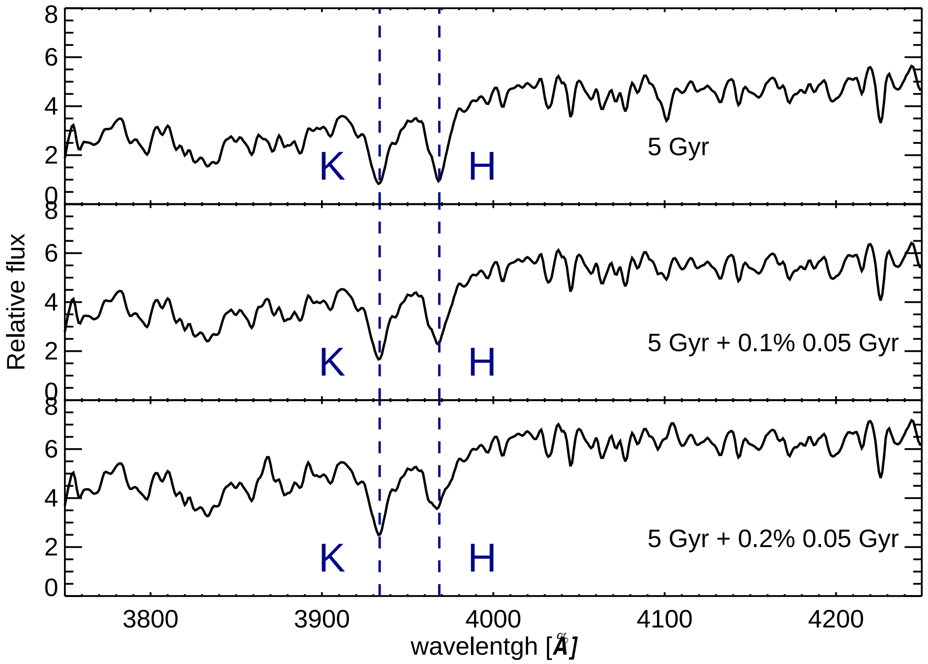

Figure 2.4: The variation of the H+K(CaII) feature on a template composed by a main stellar population of 5 Gyr and increasing mass fractions of a 0.05 Gyr stellar population with residual gas Hϵ emissions.

residual of recent star formation activity. For this reason, when analysing the stellar populations of galaxies, it must be taken into account always this possibility and eventually correct the indices values for this effect.

On the other hand, solid *metallicity* indicators among Lick indices are the Iron lines (e.g. Fe(4668), Fe(5015), Fe(5270), Fe(5335), Fe(5406), Fe(5709)), whose trends with age appear almost constant for ages > 1 Gyr (see Fig. 2.5), and the Mg$_b$, that, with its wide and depth feature around 5175 Å, is the best *metallicity* and *abundance* dependent index in the region of 5000 Å restframe. Indeed, the feature related to this index contains both Mg (α-element) and Fe (Korn et al. 2005 [49]), whose abundances affect its value much more than the age of the stellar population. For this reason it has been widely used to derive the chemical composition of the ETGs stellar population both in the local Universe (Longhetti et al. 2000 [60]) and at intermediate redshift (Ziegler et al. 2005 [139]). In my work, it will be used for the first time to derive the stellar metallicity and an α-enhancement estimate of the stellar content of an early-type galaxy at $z \sim 1.4$, as it will be described in Chapter 6.

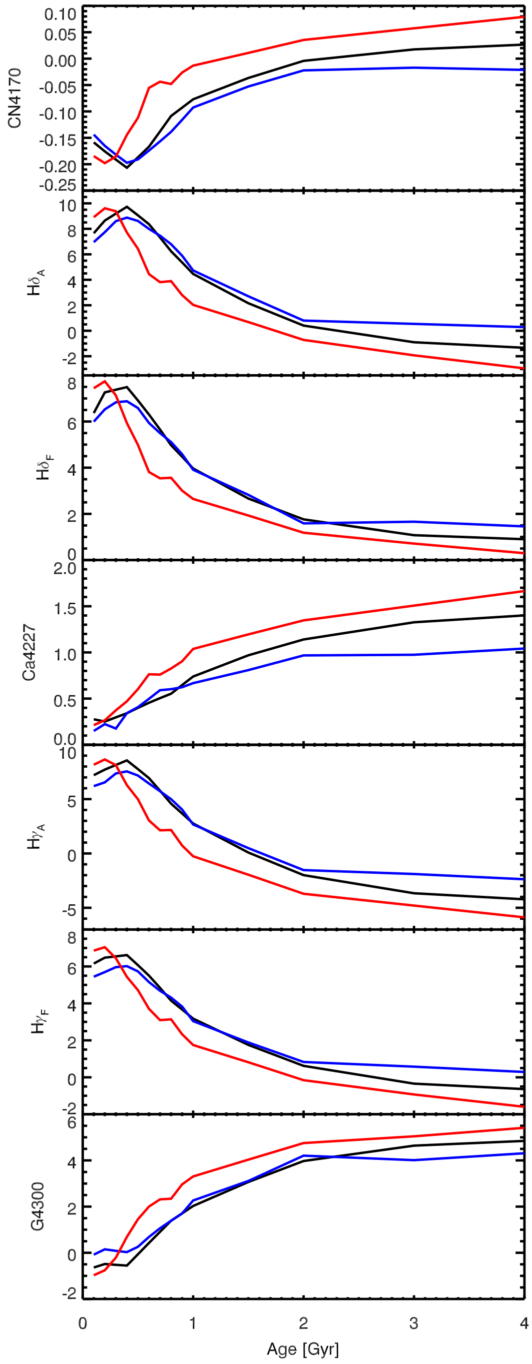

Figure 2.5: Trends of some of the Lick indices as a function of the age of the stellar population (truncated at the age of the Universe at $z\sim 1.4$) for three representative stellar metallicities, subsolar (blue lines), solar (black lines) and supersolar (red lines). Models of Maraston & Strömbäck 2011 [72], see Sec. 3.4.

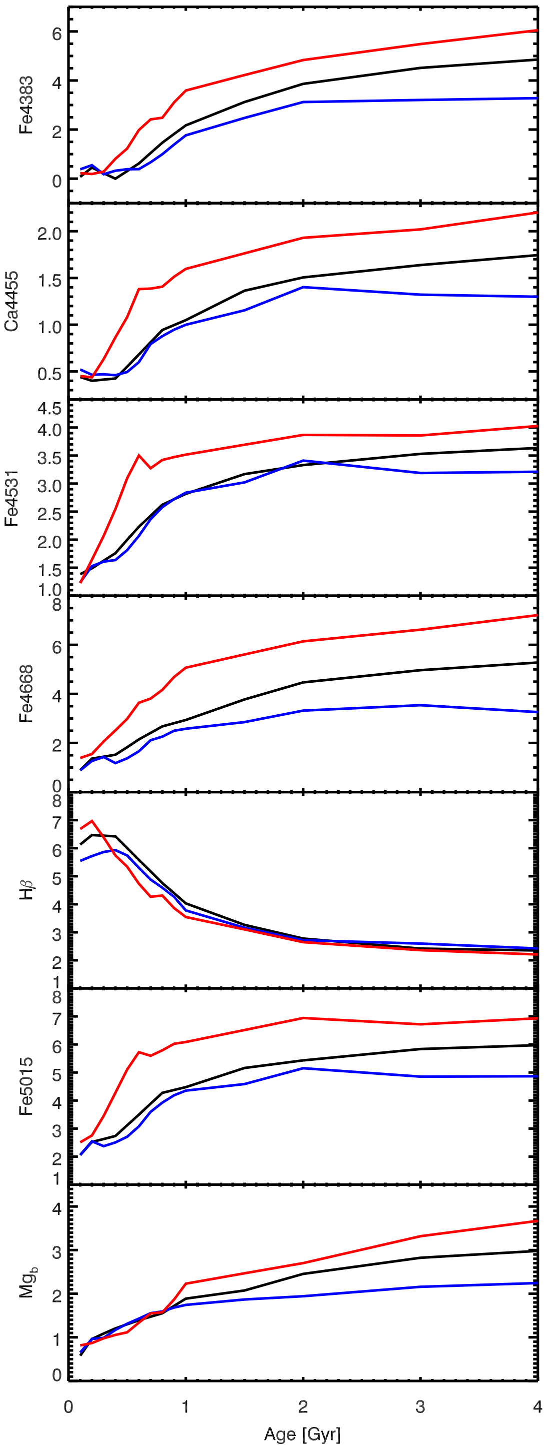

Figure 2.6: Continued.

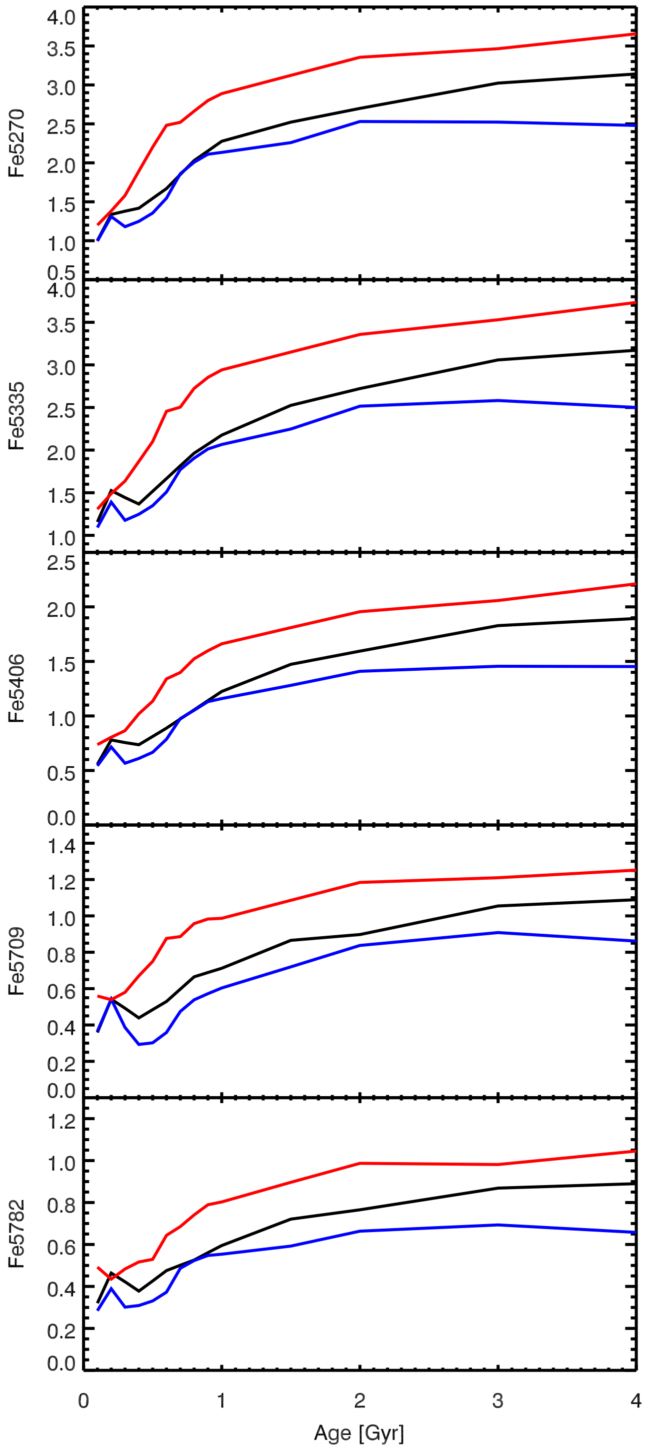

Figure 2.7: Continued.

2.3 UV indices

As already mentioned, with the most recent studies focused on high-redshift galaxies, thus dealing with younger stellar populations, the UV range becomes the most relevant because it is the most convenient to be observed by means of optical spectroscopy. The most used line index system in the UV was defined by Fanelli et al. 1987, 1990 and 1992 [26] and Davidge & Clark 1994 [21] (all summarized in the paper of Ponder et al. 1998 [93]). Within this system, some indices are defined following the Eq. 2.3, while other ones are defined as *molecular* indices:

$$I_{molecular} = -2.5 \log \int_{\lambda_1}^{\lambda_2} \left(\frac{F_{I\lambda}}{F_{C\lambda}} \right) d\lambda \tag{2.4}$$

where again λ_1 and λ_2 are the wavelength limits of the feature band-pass, $F_{I\lambda}$ is the flux per unit wavelength of the feature and $F_{C\lambda}$ is the value of the pseudo-continuum. Again the definitions of the band-passes are listed in Table 2.1.

Due to the spectral region covered by the observations on which this work is based and to the redshift of the analyzed samples, I focus my attention on the UV indices at $\lambda > 1600$ Å, in particular to the BL(1617) index, neglecting in this description all the extreme far-UV indices. Like all the "BL" lettering in the UV-indices list, the BL1617 is a blend of elements (including in particular FeIV and FeV lines). The principal absorption lines included in these blends in the range of $\lambda \sim 1600 - 1800$ Å are: AlII, CI, NIV, SiIV, FeIV, FeII, and AlIII.

In the mid-UV, the most prominent absorptions features are the MgII(2800), the FeI(3000), the two Iron lines FeII(2402) and (2609) and the MgI(2852). All these indices show a similar behaviour as a function of the stellar parameters, being monotonically increasing with age and moderately dependent on the stellar metallicity (see Fig. 2.8), with higher metallicities corresponding to stronger equivalent widths. BL(2538) is a blend of FeI and MgI, and BL(3096) a blend of FeI and AlI lines. In particular this last index is less dependent on metallicity with respect to the other UV-indices, thus it is a potential age estimator (Maraston et al. 2009 [70]).

Finally, the blue wavelength region, around the 4000 Å, contains prominent signatures of molecules such as CN(3883 and 4170) and NH(3360), which are potential indicators of the chemical evolution of the stellar populations of ETGs. Furthermore in this blue region, there is another important blend of elements, BL(3580), mostly due to Fe peak elements and CN molecule that is rather sensitive to the chemical content of the stellar population (Davidge & Clark 1994 [21]).

All the trends of the described indices with age and metallicity are shown in Fig. 2.8 for synthetic models of Maraston & Strömbäck 2011 [72].

2.4 Measurements and errors

The minimum requirement to have the possibility to measure reliable spectral indices on a spectrum is that its signal to noise ratio (S/N) is not lower than 5 per dispersion

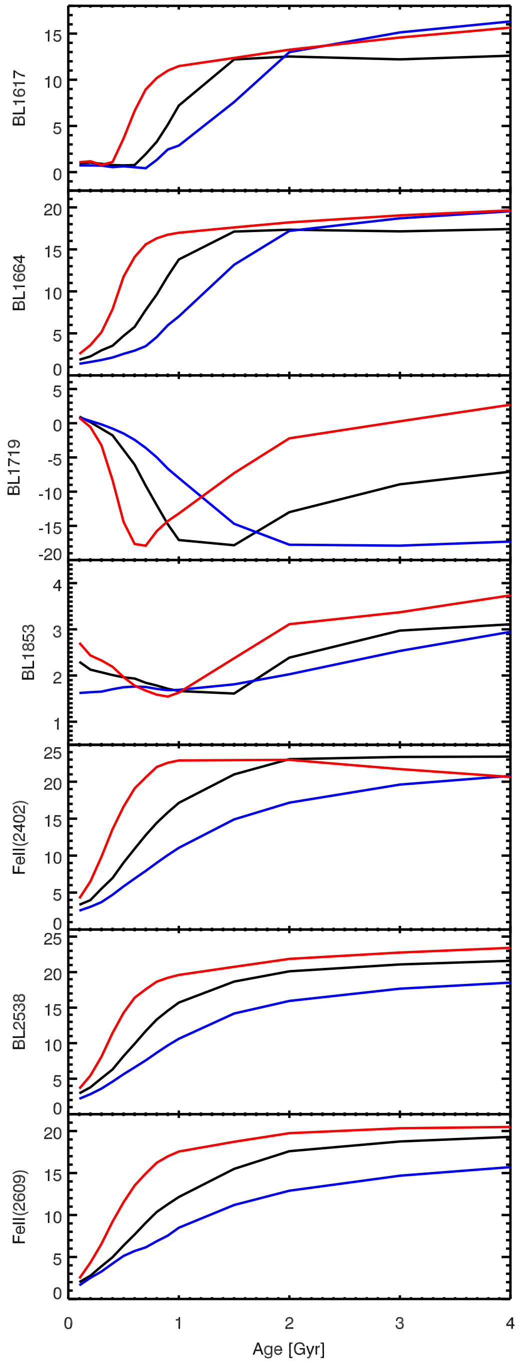

Figure 2.8: Trends of the UV-Blue indices as a function of the age of the stellar population (truncated at the age of the Universe at $z \sim 1.4$) for three representative stellar metallicities: subsolar (blue lines), solar (black lines) and supersolar (red lines). Models of Maraston & Strömbäck 2011 [72], see Sec. 3.4.

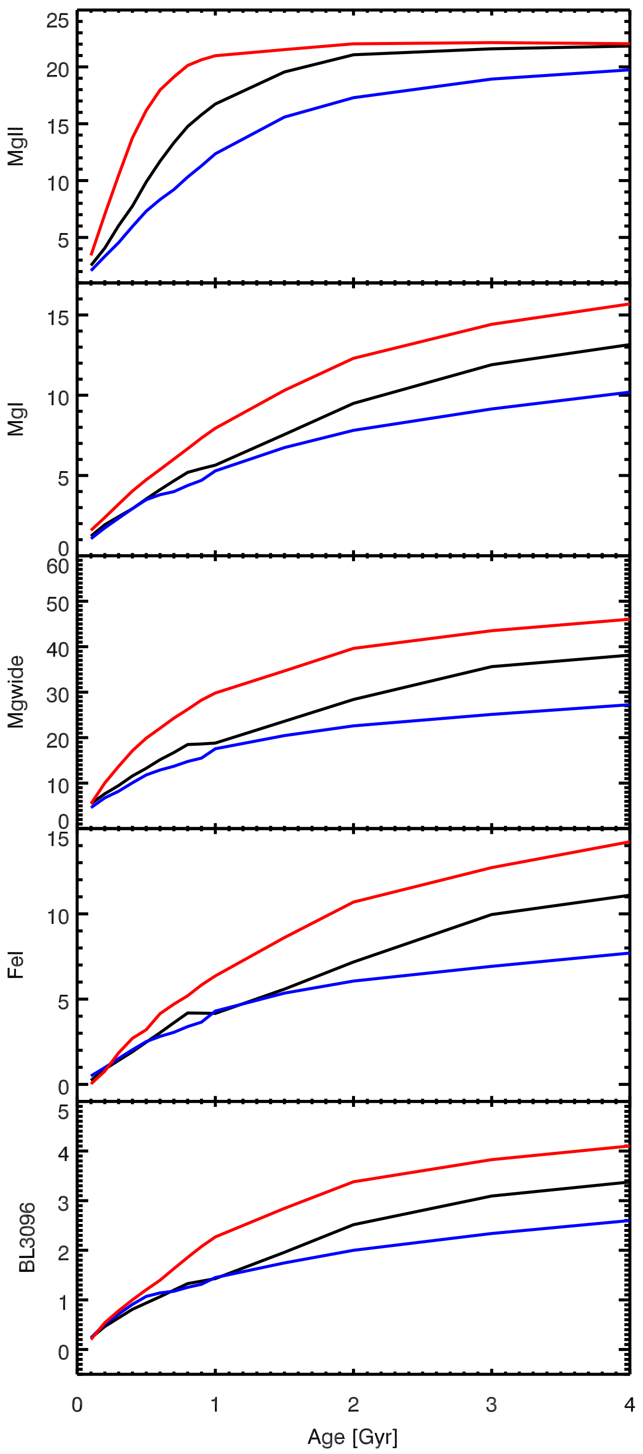

Figure 2.9: Continued.

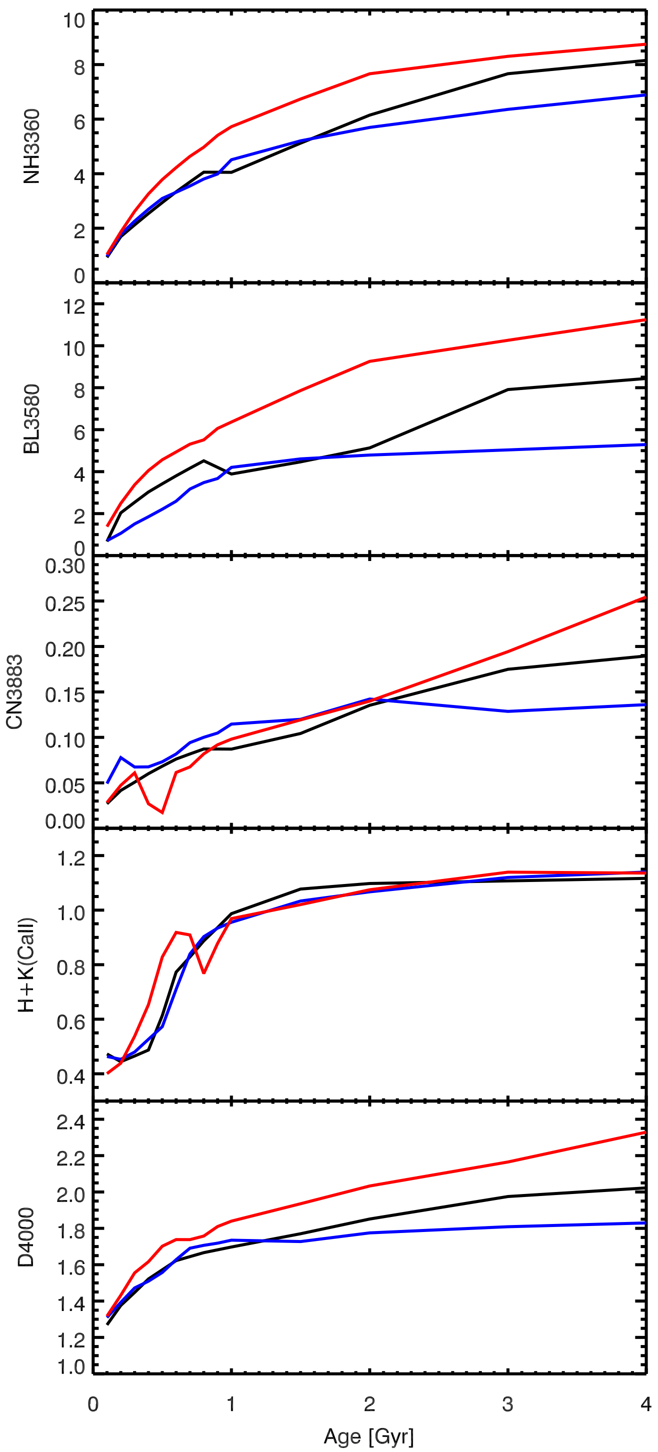

Figure 2.10: Continued.

element, even at moderate spectral resolution (i.e., R$= 1000 - 2000$) and only in the last years these measurements have been possible also on high-redshift galaxies ($z > 1$).

More in details, many indices require higher S/N ratios (> 10) spectra to appreciate, in very small spectral windows, the feature flux value with respect to the continuum one. This is particularly true for those indices related to weak absorption lines, like many Iron lines mainly in the 5000 Å region. On the other hand, there are also some indices defined on larger spectral windows, like the Mg_{wide} and D4000, that can be measured also on lower-quality spectra like those which can be achieved when observing the high redshift Universe. Furthermore, in some lucky cases (as the one of COSMOS-307881 described in Chapter 6), the combinations of indices and the particular extreme values of the parameters (e.g. the metallicity), allow to get information also from spectra at S/N lower than those needed in the analysis of galaxies in the local Universe.

The quantitative measurement of the spectral indices has been performed by a F77 code which computes the integrals of eq. 2.3-2.4 in the index band-passes shown in Table 2.1 on the observed spectrum flux de-redshifted to the restframe system. A check of possible noisy spikes in the spectrum flux is set in each index measurements in order to avoid spurious index values. In all the cases, thanks to the small number of objects in the analysed sample, it has been possible to verify by eye the computed values of both feature and pseudocontinuum in each index measure, thus feeling if it were solid.

With the aim of comparing the index values with the previsions of stellar population models (see Chapter 3), it is important to take care of two aspects: the instrumental spectral resolution of the analyzed spectrum and the intrinsic velocity dispersion characterizing elliptical galaxies. Both this two elements act on the broadening of the absorption (and emission) lines being thus able to modify the index values (with respect to the ones strictly related to the stellar population properties). In some cases it can happens that the instrumental spectral resolution is so low that the effect of the velocity dispersion is negligible (e.g. Chapter 5); indeed, the measurement of the intrinsic velocity dispersion of the galaxies can be performed only on spectra with sufficient high resolution, e.g. as in the case of X-Shooter data (see Sec. 4.3). To correct for these effects, I have reproduced them starting from a template spectrum downgrading it with a `IDL` code. This code, at each wavelength convolves the flux with a Gaussian kernel whose amplitude is connected with the simulated velocity dispersion (or resolution). Indices measured on the wide range downgraded spectra allow to estimate the corrective factor (for each index) to be applied on the real index measurement before comparing them with model previsions. These corrective factors slightly depend also on the stellar population parameters (in particular age), so this effect can be better corrected if the properties of the analysed stellar population are known (at least within a narrow range of values).

The analysis of the errors associated to the indices measurements has been performed in two different, but consistent, ways. The first one consists in the analytical propagation of the errors on the basis of the instrumental errors derived from the flux uncertainties; and the second one exploits the MonteCarlo simulations by means of a numerical approach. This second method will be described in the next Sec. 2.4.1, and it has been principally adopted in the works discussed in Chapters 6 and 7. In all the cases, I have verified that both approaches lead to the same results.

If no other known systematic uncertainties are present, the errors associated to the measured indices are the propagation of the residual noise in the observed spectrum. The flux uncertainties, which depend on the wavelength range, are extracted from the bidimensional spectrum in the data reduction phase before the extraction of the monodimensional spectrum. The noise spectrum is extracted from the bidimensional one from the same number of rows of the source spectrum, in a physical region away from the scientific object. In this way, the noise spectrum represent the pure residuals spectrum which affects the scientific data, providing a tool for extracting at each wavelength the poissonian error of the correspondent flux. Once the flux error is known, the well-known formula of the propagation of errors can be applied following the index definition. In this computing, it is worthy to take into account the effect on the errors of all the manipulations done on the scientific spectrum after the extraction, as for example binning, convolution, etc... . In some cases, as described for example in Chapter 5, for some indices, together with the poissonian errors, also a further uncertainty derived by the flux calibration process, must be quadratically added.

In all the tables showing the measured indices values, the errors are reported at the 1σ level (Tables 5.3, 5.7, 6.2 and 7.3).

2.4.1 MonteCarlo simulations

An alternative and solid method to derive the uncertainties of the measured indices is following a *MonteCarlo* approach. It consists on repeating the same index measurement on a wide set (~ 5000) of mock spectra, built on a basis of the observed one with the adding of random noise. Measuring the same index on this wide sample of mock spectra leads to the distribution of the possible index values, peaked to the real mean value and with a standard deviation resulted from the original poissonian noise.

Following this idea, I made a code which firstly uploads the original observed spectrum and derives the values of the S/N ratios in different spectral regions (the ones involved with the indices that are meant to be measured). The determination of the noise level is done comparing the observed spectrum with a synthetic template (with similar characteristics), and extracting the mean quadratic deviations from it. Once the S/N ratios are known, the code starts generating mock spectra starting from the observed and adding randomly at each wavelength the respective noise. The results is a set of mock spectra of equal quality to the original observed one. As last step, the code performs the index measurements on all the obtained spectra.

The result is the distribution of the index values from which the program compute its standard deviation, i.e. the error of the measure.

As examples of this process, in Fig. 2.11-2.12 are shown the distributions of two measured spectral indices (taken from the analysis described in Chapter 6) with the obtained mean values and standard deviations.

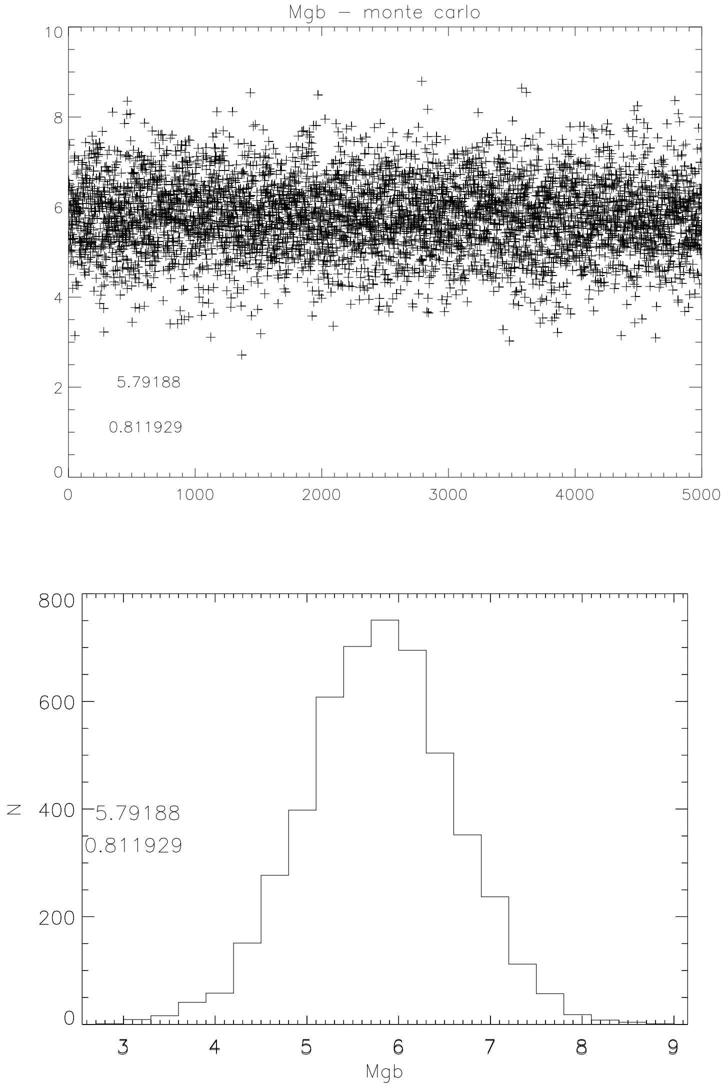

Figure 2.11: Distributions of the values of Mg_b obtained from 5000 mock spectra built on the observed spectrum of COSMOS-307881 at $z = 1.426$ (see Chapter 6). Top panel: index values for each mock spectrum; bottom panel: distributions of the index values.

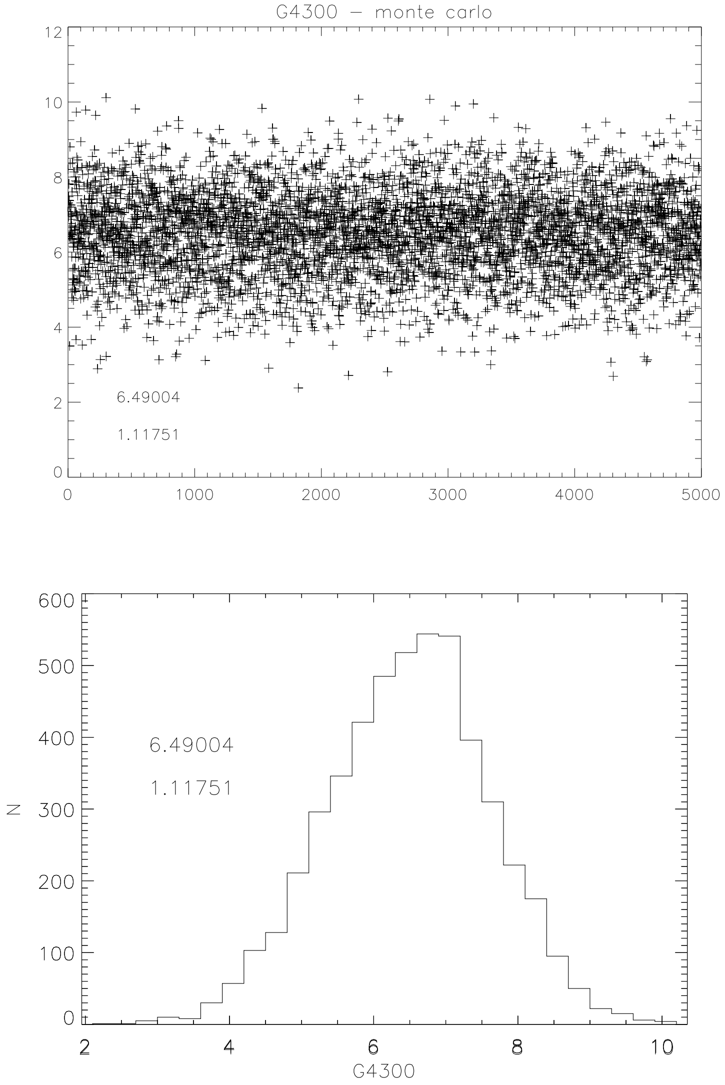

Figure 2.12: Distributions of the values of G4300 obtained from 5000 mock spectra built on the observed spectrum of COSMOS-307881 at $z = 1.426$ (see Chapter 6). Top panel: index values for each mock spectrum; bottom panel: distributions of the index values.

Chapter 3

Stellar population synthesis models

The analysis of the properties of the galaxies stellar content, e.g. age and metallicity, is usually based on the comparison between their spectro-photometric characteristics and the expectations of stellar population synthesis models. Indeed, these models are able to reproduce the observed spectrum basing on a set of initial parameters. In this chapter it will be presented: *i)* a wide description of these initial parameters essential to the building of stellar population models; *ii)* how the models can be adapted to the galaxies stellar population, in particular to elliptical galaxies; *iii)* the last sections are dedicated to the description of the two main and mostly used family of models, the Bruzual and Charlot 2003 models [7] and Maraston et al. models ([69], [72] and [118]).

3.1 Simple Stellar Population

The simplest modelling of a stellar population is the so-called "Simple Stellar Population" (SSP), which describes a generation of stars formed at the same time and from the same nebular cloud; this population has thus the characteristic of being homogeneous, that means that at each fixed age all stars of the model are coeval and have the same metallicity.

The synthetic spectrum of a SSP is obtained by the stellar population synthesis models by simply summing up all the spectra of its stars. The stars that compose the SSP as a function of the age and their relative number are expressed by the so-called "*isochrones*".

In the following I will present all the parameters that must be fixed in the stellar population model in order to obtain the expected SSP spectrum as a function of the age.

- Isochrones. As already hinted, the spectrum of a stellar population is the sum of the stellar spectra that, at each epoch, compose that generation of stars.

Therefore the *isochrones* are a “snapshot” of the stellar population at a fixed age, indicating how many and which stars are present at each epoch. The characteristic of the stellar spectra change in every phase of their evolution, and their mass is a fundamental parameter in determining their evolution; The mass distribution of the stars born in a single star forming event is described by the *Initial Mass Function* (IMF). The IMF will be described in the next point.

- Initial Mass Function. The IMF is one of the factors that mostly determines the evolution of the spectro-photometric characteristics of a stellar population. Very massive stars (M > 2 $M_{\odot}$) burn rapidly, leaving quickly (within less than 1 Gyr) the main sequence and in a short time they do not contribute any more to the total light of the stellar system. On the contrary, low-mass stars ($M < 1M_{\odot}$), burn very slowly and in the evolution of the SSP their contribution to the total radiation is predominant over the longer time-scales. The difference between high and low mass stars is visible also on their expected spectrum; indeed, high-mass stars have a predominant emission in the blue/ultraviolet region, instead low-mass stars emit principally in the optical/infrared region.

  Nowadays, the local direct star counts have shown that the IMF is approximately constant throughout the disk of the Milky Way and it can be described by two declining power laws

  $$\frac{dN}{dm} \propto m - s \tag{3.1}$$

  one with slope $s \simeq 2.35$ for stars with mass $m > 1M_{\odot}$, as originally suggested by Salpeter (1955) [99], and the other, flatter, for lower masses stars (e.g. Kroupa 2001 [50]; Chabrier 2003 [12]). This form, measured in the Milky Way disk, is then assumed to be universal, i.e. invariant both throughout the wide population of galaxies, and across the cosmic time. Nonetheless, both theoretical arguments and recent observational evidences cast strong doubts on IMF universality (see Bastian et al. 2010 [3]; Kroupa et al. 2013 [51], for complete reviews). At the same time, the lack of reliable information on this parameter makes unavoidable an a-priori assumption of this important ingredient in the stellar population models.

- Metallicity. An other parameter of the model is the *metallicity* of the initial nebular cloud from which the stellar population has formed that strongly influences both the continuum shape and the depth of some absorption lines in the resulting synthetic spectrum. In particular, more metal stars have slightly redder spectral continua than low metallicity stars. The net effect on the global properties of a stellar population is that the increasing metallicity produces the reddening of its continuum. At the same time, as it will more clear in the next chapters, the same effect is produced by the ageing of the stellar population itself, causing the well known age-metallicity degeneracy.

- Stellar library. The last "ingredient" for the construction of stellar population synthesis models is the *stellar library*, a collection of stellar spectra which co-added together following the model recipe will give the expected stellar population spectrum. The spectra collected in these libraries can be both *theoretical* and *empirical* (observed).

  The spectra of *theoretical* stars are built for any combination of the physical stellar parameters, i.e. surface temperature, chemical composition and gravity, on the basis of the stellar evolution theory. These theoretical spectra have the advantage of well reproducing the spectral continuum, covering all the wavelength range in which stars emit their light. However, they are mostly produced at low resolution, lacking of all the spectral details which cannot be properly reproduced.

  An alternative is the use of stellar libraries of *observed* spectra, composed by spectra of real stars. In this case, models are produced at high spectral resolution and thus including all the observed spectral features. The disadvantage of these libraries is the lack of the total wavelength coverage caused by unavoidable observational limits. Moreover, observed stellar spectra are not available for all the parameters values, in particular for extreme metallicity values.

3.2 Models for elliptical galaxies

The so far described simple stellar population model is an approximation of the stellar populations in galaxies, which are generally more complex structures. To study the spectral properties of galaxies, the use of a modelling with a more complex star formation history is more appropriated.

In the stellar population synthesis models it is generally assumed a star formation history with a Star Formation Rate (SFR) exponentially declining with a time-scale τ:

$$SFR(t) = SFR_0 e^{-t/\tau} \tag{3.2}$$

where SFR_0 is the initial star formation rate. The longer is the time-scale τ, more the star formation is spread on a wide period tending to a null SFR only for $\tau \to \infty$. On the contrary, if the τ value is very small, the initial star formation event is very short, reproducing the SSP for $\tau \to 0$.

The stellar population synthesis model, given the SFR(t) and the IMF(m), creates the synthetic spectrum S_λ at each time T, following:

$$S_\lambda(T) = \int_0^T SFR(t) S_\lambda^{SSP}(T-t)dt \tag{3.3}$$

where $S_\lambda^{SSP}(T-t)$ is the spectrum of a SSP with age ($t' = T - t$) given by:

$$S_\lambda^{SSP}(t') = \int_{M_{min}}^{M_{max}(t')} IMF(m) f_\lambda(m, t')dm \tag{3.4}$$

where the product of IMF(m) times the monochromatic flux of a star with initial mass m and age t' ($f_\lambda(m, t')$), is integrated over the correspondent isochrone between the minimum mass (M_{min}) and the maximum one existing at the time t' ($M_{max}(t')$), i.e. the maximum mass of stars in the evolutionary phase more advanced that still significantly contributes to the total luminosity.

Typically, elliptical galaxies in the local Universe are low SFR systems, i.e. passive systems composed mainly by low-mass stars which evolve slowly. The recent detection of quiescent elliptical galaxies also at high redshift ($z > 1$), suggests that the star formation history of these systems is well described by an initial burst of star formation at redshift $z > 2-3$ followed by a rapid quenching of the star formation, i.e. well reproduced by small τ values. Indeed, the comparison with models shows that data coming from elliptical galaxies are well described by $\tau < 1$ Gyr.

3.3 BC03 models

One of the mostly used family of stellar population synthesis models is the last published version of the Bruzual & Charlot 2003 models (BC03) [7]. In this thesis, these models have been used in the work described in Chapter 5, for the modelling of the two measured spectral indices (D4000 and H+K(CaII)) and in the comparison with the observed SEDs. Indeed, they provide the template spectra in a very wide spectral range, from 91 to 1600000 Å, at very low resolution with the exception of the blue/optical region in which a moderate resolution $R = 1500 - 2000$ is available. For this reason, in the other analysis discussed in Chapter 6 and 7, which include the measurements of UV indices, BC03 models could not be used for most of the comparison due to their too low resolution at wavelength below ~ 3000 Å.

The BC03 models adopted within this thesis work are based on the following assumptions:

- Isochrones. The isochrones are the "Padova 2000" from Girardi et al. 2000 [32], which cover the metallicity range $Z = 0.0004 - 0.03$.
- Initial mass function. The chosen IMF is the Chabrier [12], but when needed it has been verified that the choice of another IMF (e.g. Salpeter) would have not changed the obtained results.
- Metallicity. The allowed values of the stellar metallicity are in the range of $Z = 0.008 - 0.04$, where the solar value is $Z_\odot = 0.02$. In many cases, galaxies at high redshift have not secure metallicity estimate, so that the solar value is a priori assumed (as it is the case of Chapter 5).
- Stellar library. Among the available set of BC03 models, I have selected those based on an empirical stellar library, providing a high enough spectral resolution ($R = 2000$) at least in the blue/optical spectral range. The used stellar library is called "STELIB" [56], and it has a spectral resolution of about $R = 2000$ in the wavelength range $3200 - 9500$ Å.

Together with the standard BC03 models described above, as mentioned in Chapter 5, I have introduced also another set of models, derived from the BC03 ones but including the nebula emission components (Charlot & Longhetti 2001 [13]). In particular, the emission contribution is important for very young ages when the star formation is still active or recently dimmed. In Fig. 5.7 it will be presented the difference between standard BC03 models and these emission models, where it can be noticed that this difference arises only below 1 Gyr at least for $\tau < 1$ Gyr. The main spectral lines involved in the emission contribution are: all the Balmer lines (Hα, Hβ, Hγ, Hδ, Hϵ etc...), OII(λ3727), OIII(λ5007), NII(λ6583), SII($\lambda\lambda$6717,6731), etc... . In Chapter 5, the emission line that will be particularly exploited is that of the Hϵ line blended with the Ca(H) line, which will be of fundamental importance to detect the presence of a second younger component in the stellar content of ETGs.

3.4 Maraston models

The second family of models used in this work is that of Maraston & Strömbäck 2011 [72] and Thomas, Maraston and Johansson (TMJ) [118] (all based on the first version described in Maraston 2005 [69]). One of the advantages of dealing with these models is that they provide the template spectra covering also the UV region at high resolution.

In the following I present all the "ingredients" at the basis of the Maraston & Strömbäck 2011 models:

- Isochrones. These evolutionary population synthesis models assume a stellar evolution prescription, based on the isochrones and stellar tracks by Cassisi, Castellani & Castellani (1997) [11] for ages larger than ~ 30 Myr and by Schaller et al. (1992) [108] for younger populations. Sets of models have been also computed with the "Padova 2000" isochrones (as before, [32]).

- Initial mass function. All these models are based both on a Salpeter [99] and Kroupa [50] IMF. For the purpose of this thesis, I have assumed a Salpeter IMF.

- Metallicity. For the assumed stellar library (see next point), the available values of the metallicity are: $Z = 0.01, 0.02, 0.04$. The number of available ages depends on the metallicity: 31 for subsolar, 47 for solar and 22 for supersolar metallicity.

- Stellar library. This set of models includes templates based on many stellar libraries (both empirical and theoretical). The four popular libraries of empirical stellar spectra, are those of Pickles, ELODIE [95], STELIB [56] and MILES [100], all at intermediate resolution around $R = 2000$. Models at very high spectral resolution ($R = 20000$) are provided based on the MARCS library. For the purpose of this work, the selected models are those based on the

MILES library, providing a FWHM= 2.54 Å in the spectral range $3500 - 7430$ Å, and extended in the UV region by means of a concatenation with the SSP models of Maraston et al. (2009a) [70], which are based on the fully theoretical UVBLUE/Kurucz library [52] at high-resolution ($R = 10000$) in the region between $1000 - 4700$ Å.

The main difference between BC03 and Maraston models is the method applied to compute the SSPs. Indeed, there are two techniques which differ depending on the integration variable adopted in the post main sequence evolutionary phase: isochrone synthesis and fuel-consumption-based algorithms. In the first one, the properties of the stellar population are computed by integrating the contributions to the flux in the various passbands of all mass bins along the isochrone, assuming a specific IMF. Usually, isochrones are calculated until the end of the early asymptotic giant branch phase. Later stellar phases, like the thermally pulsing asymptotic giant branch, are added following individual recipes. On the other hand, in the fuel-consumption approach, the integration variable in the post main sequence is the so-called *fuel*, that is the amount of Hydrogen and/or Helium that is consumed via burning during each phase. The advantages of this second method are that the fuel as integration variable is very stable because it is directly proportional to the contributions of the various phases to the total luminosity; and, very important, that there are several relevant stellar phases (blue horizontal branch, thermally pulsing asymptotic giant branch, very old stars...) whose theoretical modelling is uncertain because of mass loss and for which complete stellar tracks are not available. This approach provides useful analytical relations that link the main sequence to the post main sequence evolution, by means of which one can include into the synthesis the energy contribution of these uncertain phases (Maraston 2005 [69]). BC03 models follow the first path, while all the Maraston models the second one.

The consequence of following these two different approaches can be appreciated mainly in the resulting shape of the continuum in the red wavelength region and for stellar population younger than 2 Gyr, principally affecting the analysis of the whole SEDs, which thus results to be model-dependent. The two models differ also in the expected values of some indices, even if the effect is less dramatic than for the continuum. In Fig. 3.1 an example of the behaviour of the two analyzed spectral indices (H+K(CaII) and D4000) in both models (Maraston with black line and BC03 with red line) is shown. As declared also in Chapter 5, differences in the indices values between the two models do exist, but the discrepancies are well within the error bars obtained for the high-z sample.

3.4.1 TMJ models

Even if based on the Maraston models, some more details on the Thomas, Maraston and Johansson 2011 (TMJ) [118] models are needed because these models will be widely used in the works of Chapter 6 and 7, and mainly because they contain a further ingredient very important for the purposes of this thesis. This new element is

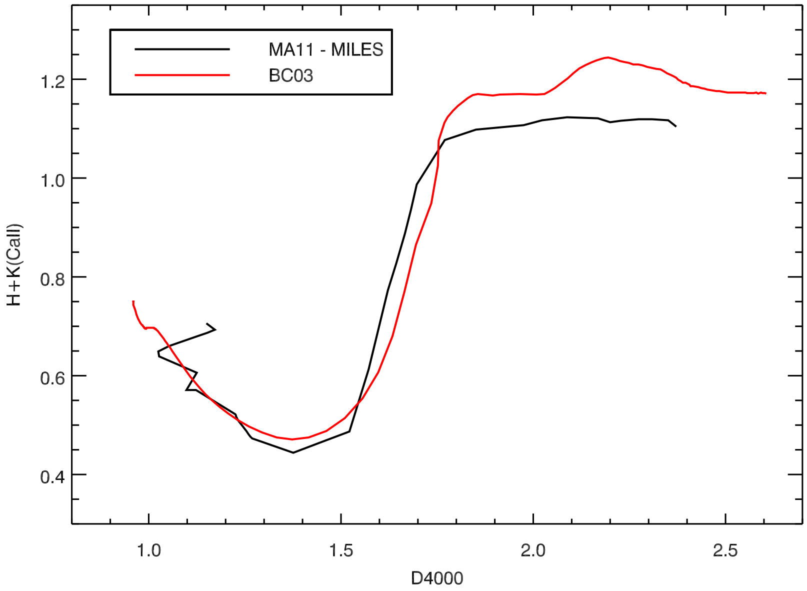

Figure 3.1: Comparison between Maraston & Strömbäck 2011 (MA11 (MILES)) models (black line) and BC03 models (red line) for the expectations of H+K(CaII) and D4000 index values.

the dependence of the expected spectrum of a stellar population on a variable *element abundance ratio*. The information enclosed in the element abundance balance is a key point in the study of stellar population properties, in particular of high-z ETGs. Indeed, as it will be explained in Chapter 6, the α/Fe ratio (called α-enhancement) is related to the time-scale of the star formation. Thus obtaining this information on the chemical content of ETGs, leads to information on how the formation of these systems has occurred.

The TMJ models are based on the evolutionary synthesis code of Maraston 2005 [69], with Cassisi et al. 1997 [11] stellar evolutionary tracks, Salpeter IMF, and the MILES stellar library. The explored metallicity values are wider with respect to the other models, in particular: [Z/H] $= -2.25, -1.35, -0.33, 0.0, 0.35, 0.67$ (where the notation [Z/H] means the logarithmic ratio between the metallicity value Z and the reference solar value $Z_\odot$). While the allowed α-enhancement values are [α/Fe] $= -0.3, 0.0, 0.3, 0.5$ (again [α/Fe] means the logarithmic ratio between the α-elements on Fe peak elements balance and the reference solar value of the α-enhancement).

These models provide directly the values of all the Lick/IDS absorption-line indices (see Sec. 2.2) for different abundance elements ratio, neglecting the behaviour of the stellar continuum. Indeed, differently from the other described models, they do not provide the template SED of each parameters combination, but they are focused only on the optical absorption features. In particular, Lick absorption-line indices have been computed through their empirical calibrations as a function of each stellar parameters combination. In this widely adopted approach, first of all absorption-line indices are measured on the stellar spectra of an empirical library, then analytical dependence of these indices values from stellar parameters are derived (fitting functions), which are then included in the evolutionary population synthesis code (Thomas, Maraston and Johansson 2011 [118]). More in details, in the work of Thomas, Maraston and Johansson 2011, the authors have calculated new empirical fitting functions for the 25 optical Lick absorption-line indices based on the new stellar library MILES [100], so in the TMJ models Lick indices are available at the higher spectral resolution of 2.5 Å (FWHM) and flux calibrated. This advantage allows to compare directly the Lick indices values measured on observed flux calibrated spectra at the same MILES resolution.

Chapter 4

Spectroscopic data

Most of the work described in this thesis is based on the information extracted by spectroscopic data of very distant objects. Spectra of galaxies contain the precious informations detailed in the previous chapter, and offer the possibility to derive details on their stellar content. At the same time, obtaining high S/N spectra of high redshift galaxies is very time demanding. Indeed, in order to reach high signal to noise ratios (S/N) of $z > 1$ galaxies, very long exposure time (t $\geq$ 5 hours) and very large ground based telescopes (D $\geq$ 8 m) are required. And despite the acquisition of many hours of exposure, faint objects spectra remain mostly dominated by the residual sky emission (see Fig. 4.6).

An important parameter characterizing the spectroscopic data is the spectral resolution combined with the dispersion. The spectral resolution $R = \Delta\lambda/\lambda$ (where $\Delta\lambda$ is the FWHM in Å of a line as will be obtain through the instrument, and λ is the wavelength of the line itself) represents how much close can be two lines and/or features to be discriminated as separate lines. The spectral dispersion quantifies the wavelength range involved in one detector pixel. The two quantities are related each other, being the spectral bin small enough that $\Delta\lambda = 6-8$ pixels. When dealing with high redshift galaxies, resolution, and consequently the spectral dispersion, is usually selected to be not very high (i.e., $R = 1000-3000$) helping to obtain high S/N. At the same time, higher resolution spectra (i.e., $R > 5000$) is sometime adopted in order to obtain a better definition of the sky emission lines which can be consequently better subtracted from the object background.

All the data reduction process in case of distant galaxies must be accomplished with extreme care, starting from the raw bidimensional spectrum to the monodimensional calibrated one. In particular the main steps are:

- Residuals removing such as cosmic rays, dark pixels, CCD defects...;
- CCD distortions correction;
- Wavelength calibration;
- Background subtraction;

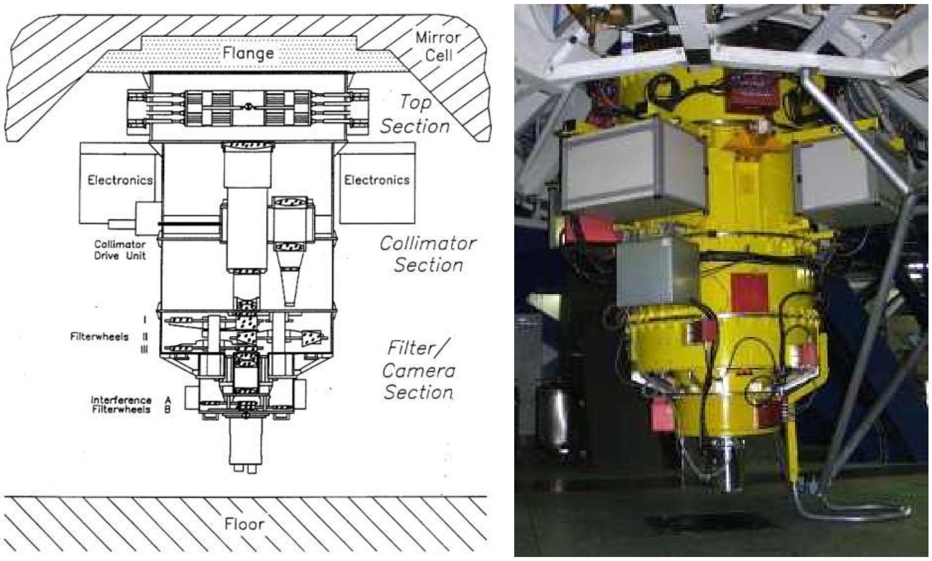

Figure 4.1: Schematic view of FORS instruments.

- Monodimensional spectrum extraction;
- Flux calibration (by means of standard stars).

The spectroscopic data used in the works of Chapters 5, 6 and 7 come all from one of the largest world telescopes, i.e. the Very Large Telescope (VLT) of ESO (European Southern Observatory) at Paranal (Chile), but from three different spectrographs. The work of Chapter 5 exploits the optical data coming from FORS2 (Sec. 4.1) and VIMOS (Sec. 4.2) and the other two works those coming from one of the most efficient spectrograph, X-Shooter (Sec. 4.3). Next sections are dedicated to the detailed descriptions of these instruments.

4.1 FORS

FORS is the visual and near-UV "FOcal Reducer and low dispersion Spectrograph" at the VLT (see Fig.4.1) and it is designed as an all-dioptric instrument for the wavelength range 3300 – 11000 Å. Two versions of FORS have been built, upgraded and moved to different telescopes in the past years, called FORS1 and FORS2. In 2009, FORS1 was dismounted so only FORS2 is now in operation. Indeed, the FORS1 observations analysed in Chapter 5 have been carried out before 2002.

FORS1 has been used for our purposes in Chapter 5 in the MOS mode, i.e. Multi-Object Spectroscopy with Movable Slitlet. In this configuration up to 19 objects can be observed simultaneously by means of slitlets which are formed each by two blades mounted on opposite carriers. The slitlets can be moved by linear guides to any position along the dispersion direction in the field of view and each single MOS slit

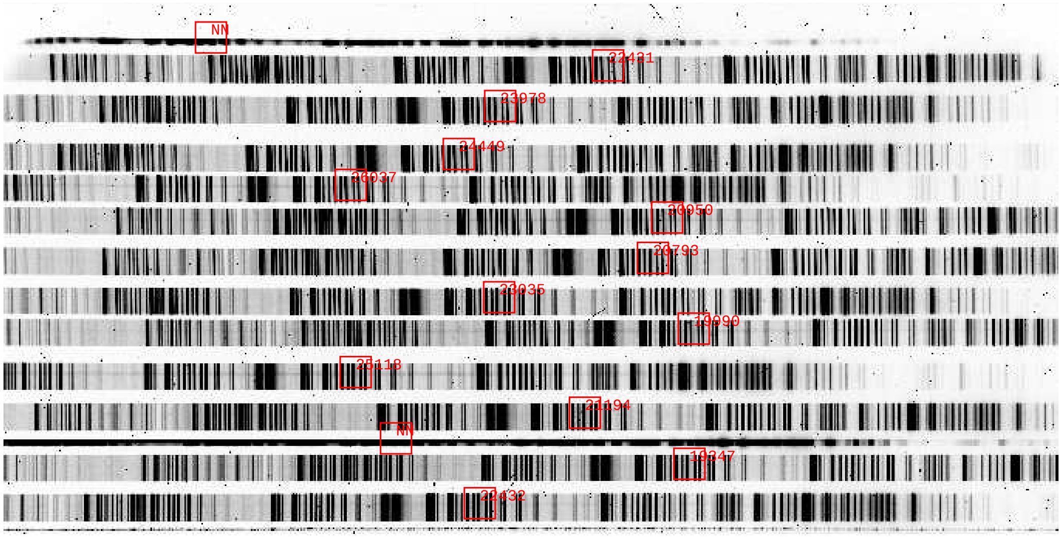

Figure 4.2: Example of raw spectroscopic data from a multi-object mask of FORS2. The horizontal axis is the dispersion direction and different rows are bidimensional spectra of different sources. Red squares indicate the physical position of the slit during the observation.

width can be adjusted by the user. By combining the linear positioning of the slitlets in the focal area with a rotation of the FORS instrument around its optical axis a wide variety of object configurations can be realized.

FORS2 works in many modes including the MXU mode, i.e. Multi-Object Spectroscopy with Exchangeable Masks. The MXU mode allows to get the spectra of many sources in the same exposure time thanks to user-designed masks composed by many slits. These masks are inserted in the focal plane of the telescope after being cut by a laser machine that can shape slit with different length, width and shape. Up to 10 masks can be mounted in a mask unit inside the instrument and each mask can have up to 470 slits, depending on the grism and filter used. The spectroscopic data exploited in this work made use of this mode, and an example of an image obtained with this instrument is shown in Fig. 4.2; the dispersion direction is the x-axis and in each horizontal row the physical position of the slit can be seen, highlighted by red squares.

4.2 VIMOS

VIMOS is a visible (3600 − 10000 Å) wide field imager and multi-object spectrograph mounted on the Nasmyth focus of UT3 (Melipal)(Fig. 4.3). The instrument is made of four identical arms with each a field of view of $7'$x$8'$ with a 0.205" pixel size. Each arm is equipped with 6 grisms providing a spectral resolution range $\sim 200 - 2500$ and

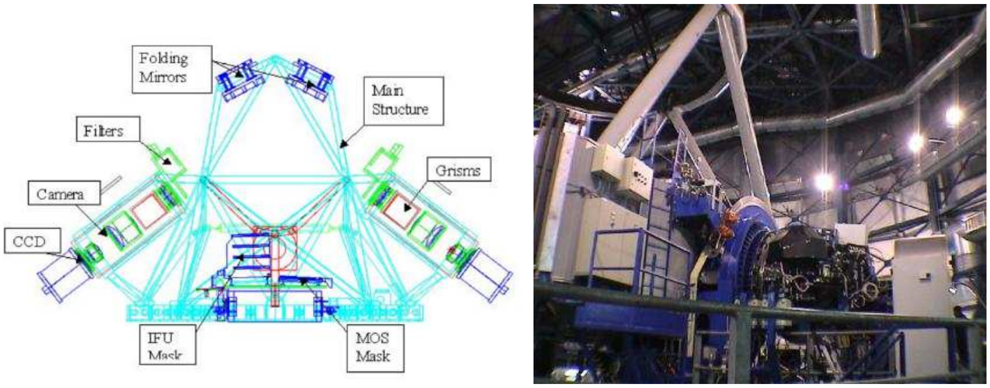

Figure 4.3: Schematic view of VIMOS instruments.

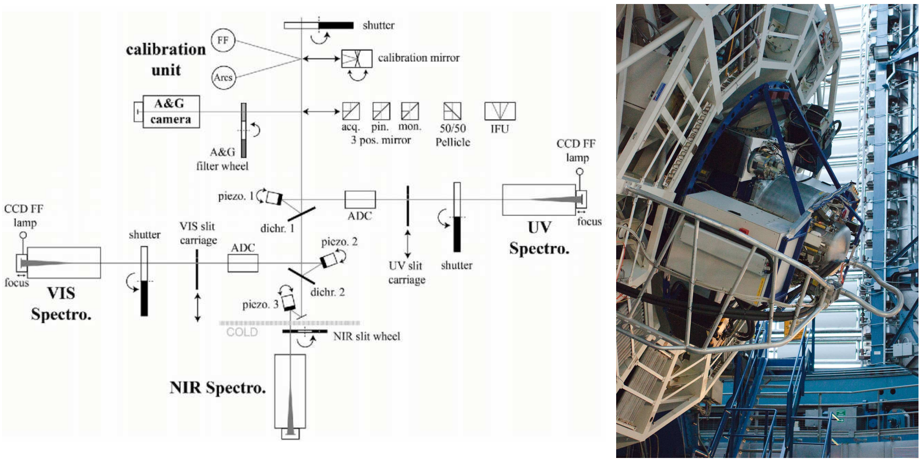

Figure 4.4: Schematic view of X-Shooter instruments.

with a CCD of $4k$x$2k$. VIMOS operates in three different modes: Imaging (IMG), Multi-Object Spectroscopy (MOS), and with Integral Field Unit (IFU). Again, my data have been acquired in the MOS mode (see Chapter 5).

4.3 X-Shooter

X-Shooter is a multi wavelength (3000 – 25000 Å) medium resolution spectrograph mounted at the UT2(-UT3) Cassegrain focus at VLT (see Fig.4.4). The great advantage of this instrument is its capability of acquiring in a single exposure the source's spectrum on a very wide spectral window (wider than those provided by the other mostly used spectrographs, like FORS and VIMOS, previous Sec. 4.1 and 4.2). Indeed, it consists of 3 independent spectroscopic arms (UVB, VIS and NIR), each with optimized optics, dispersive elements and detectors:

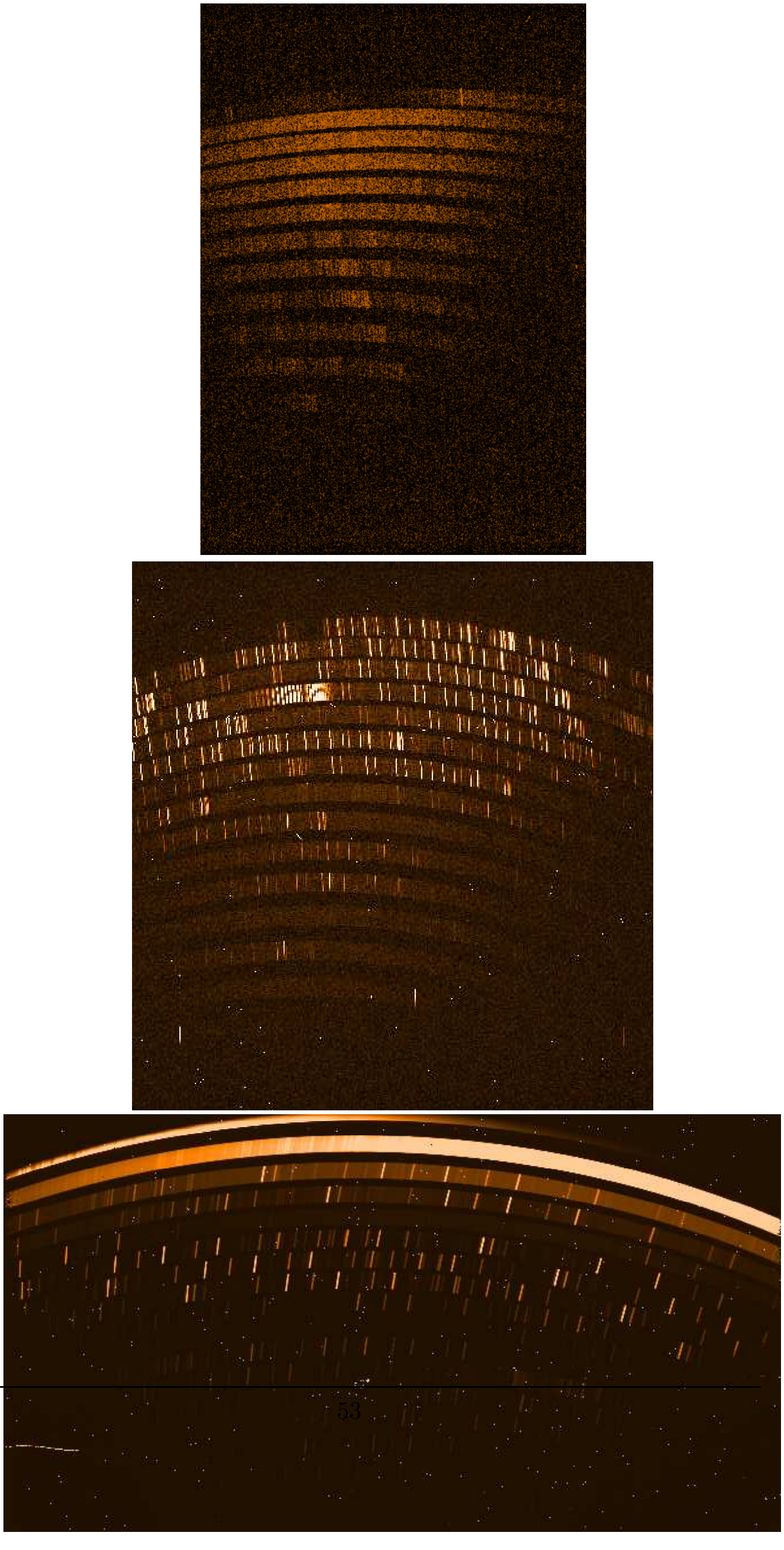

Figure 4.5: Raw data from the three spectroscopic arms of X-Shooter: UVB (upper panel), VIS (middle panel) and NIR (bottom panel).

UVB, covering the wavelength range 300 – 559.5 nm
VIS, covering the wavelength range 559.5 – 1024 nm
NIR, covering the wavelength range 1024 – 2480 nm

Each arm is an independent cross dispersed *Echelle* spectrograph completed with its own shutter and/or slit mask. In particular, an Echelle spectrograph disperses the light in two perpendicular directions, consequently it can be designed to give simultaneously high spectral resolution and large spectral band-pass. In this way the spectral orders are physically separated on the CCD area, as it can be seen in Fig. 4.5: each horizontal line is the bidimensional spectrum of each spectral order, from the redder orders on the top to the bluer orders on the bottom.

The incoming light is split into the three different spectrographs/arms through 2 dichroics (cut off wavelengths of 5595 Å and 10240 Å for the separation of the UVB-VIS light and VIS-NIR light, respectively). For each arm the spectral format is fixed. The orders in each detector are highly curved and the sky/arc lines within each order are highly tilted, as it can be seen again in Fig. 4.5. Three piezo controlled mirrors, located in front of each arm, guarantee that the optical path is maintained aligned against instrument flexure and correct for differential atmospheric refraction between the telescope guiding wavelength and each arm central wavelength. The Acquisition and Guiding system consists of a $1.5'$x$1.5'$ FoV technical CCD for the target acquisition. The five positions slide, located before the UVB, VIS and NIR spectrograph, allows to insert an image slicer in the optical path and perform IFU spectroscopy of a 1.8"x4" FoV. IFU mode observations are an alternative to slit mode observations, but I will focus only on the slit mode since it has been used in the works described in Chapters 6 and 7. An internal calibration unit, equipped with [Ar, He, Neand Xe], Th-Ar, Halogen and D2 lamps, is used to produce the necessary calibration frames (flats, arcs, order definition, etc...) for the data reduction.

The reduction process of the data obtained with X-Shooter is slightly different from the standard one adopted for examples for FORS and VIMOS data. Indeed, as just mentioned, raw data appear in a very complicated configuration, with curved and separated spectral orders from which the light must be collected to obtain the integrated single bidimensional spectrum. Once this single bidimensional spectrum is obtained, thanks to the merging of the separated orders, the standard data reduction analysis can be performed, taking care of the higher spectral resolution of X-Shooter and of its wider spectral range. These first delicate steps of the data reduction can be performed thanks to the ESO pipeline for the X-Shooter data reduction, applied individually on UVB, VIS and NIR. Actually, the pipeline is able to perform all the data reduction chain, until the production of the final monodimensional spectrum, but in the works described in Chapters 6 and 7, only the first steps made use of the pipeline and all the other parts of the process have been performed by hands using

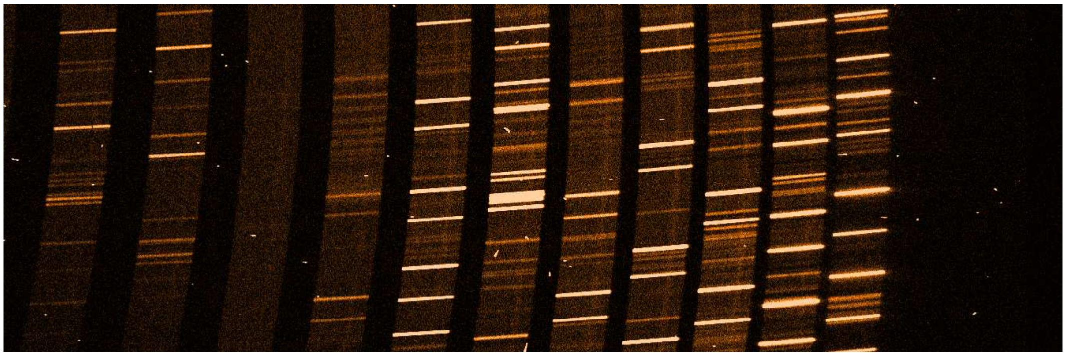

Figure 4.6: Particular of raw data from the VIS spectroscopic arm of X-Shooter. The vertical light colour lines (in the dispersion direction) are the source in the different spectral order split by the echelle configuration of X-Shooter. Instead horizontal light colour lines are the bright sky lines emissions.

`IRAF` tools. Indeed, in that works the sources are very faint due to their high redshift, and most of the work in this case is to extract more signal as possible from the noisy sky residuals (see Fig. 4.6 for a concrete example).

A concrete example of dealing with X-Shooter data can be found in Chapters 6 and 7, where the results of the data reduction, i.e. the monodimensional spectra, will be presented (see Fig. 6.1 and 7.1-7.4).

In the following chapters (5, 6, 7), the most important results obtained from the exploitation of the available high-quality spectroscopic data by means of all the tools I have described in the previous chapters, i.e. spectral indices (Chapter 2) and stellar population synthesis models (Chapter 3), are presented.

As it will be clear in the reading, this kind of spectroscopic analysis of $z > 1$ ETGs is challenging because of the inevitable lower quality of the data with respect to those used in the same analysis in the local Universe. To compensate for this difficulty, it has been necessary to use appropriate strategies in the analysis, like for examples using peculiar sets of indices, to constraints the stellar population parameters as age and metallicity. The obtained solid results open the way to this kind of analysis and to further investigations on the stellar content of the most distant ETGs.

These works have been published on the astronomical journal "Monthly Notices of the Royal Astronomical Society" (MNRAS):

- Lonoce et al. 2014: *Spectral detection of multiple stellar populations in* $z \sim 1$ *early-type galaxies.* [63]
- Lonoce et al. 2015: *Old age and super-solar metallicity in a massive* $z \sim 1.4$ *early-type galaxy from VLT/X-Shooter spectroscopy.* [64]
- Lonoce et al., in preparation: *Individual stellar metallicity measure in* $z > 1.4$ *ETGs.*

Chapter 5

Evidence of multiple stellar populations in $z \sim 1$ ETGs

In this chapter it will be described a spectroscopic analysis based on measurements of the two mainly age-dependent spectrophotometric indices in the 4000Å rest frame region, i.e. H+K(CaII) and D4000, for a sample of 15 early-type galaxies (ETGs) at $0.7 < z_{spec} < 1.1$, morphologically selected in the GOODS-South field.

The important goal to be reached through the analysis of the stellar population properties of galaxies observed at $z \sim 1$ in their critical state of evolution, is to understand if all of their stars are coeval and still passively evolving, as they are usually modelled with $z_{form} > 2 - 3$ (Renzini 2006 [96]), or there are some pieces of evidence of later star forming episodes or minor merging events which led to composite stellar populations already at $z \sim 1$.

The hidden complexity of the star formation history of ETGs has been revealed by many works on local ETGs (Coccato et al. 2010 [18], Panuzzo et al. 2011 [85], Kaviraj et al. 2012 [44], Rocca-Volmerange et al. 2013 [97]), and at intermediate redshift (Treu et al. 2002 [122]), where different kinds of signature suggest that elliptical galaxies have possibly undergone rejuvenation episodes in their recent history. Also at high redshift, with both archaeological and direct measurements, the necessity of introducing multiple stellar populations, with different stellar properties, in their modelling has been found (Gargiulo et al. 2012 [31], Huang et al. 2013 [37]). The main stellar properties involved in the discrimination of stellar components are age and metallicity. However, age is surely the first stellar parameter which should be investigated on high-z ETGs. In fact, direct spectroscopic measurements of stellar metallicity on high-z ETGs are still a hard issue (as discussed in Chapters 6 and 7); moreover, Gargiulo et al. 2012 [31] found that age gradients are necessary to reproduce the majority of the observed high-z colour gradients.

Coexistent different stellar populations in ETGs are expected from the theoretical models on galaxy formation and evolution: minor mergers and small accretion events instead of major mergers, in fact, are predicted to be frequent until $z = 0$ (Naab et al. 2009 [80], Oser et al. 2010, 2012 [83], [84]). This inside out formation scenario, however, predicts that for high mass galaxies, accreted stars have been formed in the same epoch of "*in situ*" stars (Oser et al. 2010 [83]), assembling thus composite stellar populations of rather coeval stellar content, though the minor mergers have occurred at different times.

So the attention now should be focused on finding some observables which allow one to understand how homogeneous are the stellar populations of elliptical galaxies and how important are the mass fraction and the age of the accreted stars. A spectroscopic analysis on a sample of high-z ETGs reveals precious details on their stellar properties, shedding light on the composition of the stellar populations of galaxies in their earlier phases of evolution. Previously, other pioneer works (Onodera et al. 2012 [81], Jorgensen & Chiboucas [40]) have been devoted to the analysis of spectroscopic high-z data, revealing many differences in the stellar properties of $z > 1$ objects with respect to local ETGs, such as the presence of extreme values of spectral indices not foreseen by models (Onodera et al. 2012 [81]).

In this spectroscopic analysis of a small sample of ETGs based on some of the first high quality optical spectroscopic data at $z \sim 1$, I found that ages derived from the two different indices by means of the comparison with stellar population synthesis models, are not consistent with each other for at least 9 galaxies (60% of the sample), while for the remaining 6 galaxies, the ages derived from their global spectral energy distribution (SED) fitting are not consistent with those derived from the two indices. I then hypothesized that the stellar content of many galaxies is made of two stellar components with different ages. The double-component analysis, as it will be described in the following sections, performed by taking into account both the index values and the observed SED, fully explains the observational data and improves the results of the standard one-component SED fitting in 9 out of the 15 objects, i.e. those for which the two indices point towards two different ages. In all of them, the bulk of the mass belongs to rather evolved stars, while a small mass fraction is many Gyr younger. In some cases, thanks to the sensitivity of the H+K(CaII) index, it is found that the minor younger component reveals signs of recent star formation. The distribution of the ages of the younger stellar components appears uniformly in time and this suggests that small amounts of star formation could be common during the evolution of high-z ETGs. It is argued the possibility that these new star formation episodes could be frequently triggered by internal causes due to the presence of small gas reservoir.

5.1 The sample and the spectroscopic data

The sample consists of 15 ETGs at $0.7 < z_{spec} < 1.1$ morphologically selected from a catalogue complete to $K \simeq 22$ (Tamburri et al. 2014 [113]), in the southern field of the Great Observatories Origins Deep Survey (GOODS-South v2). The selection criterion of this sample was basically the availability of sufficient high-quality (S/N > 5) spectroscopic data to perform the measurements of the main spectrophotometric indices in the 4000Å break region, which is the aim of this analysis. Thus, starting from the complete sample of 196 morphologically selected ETGs with $K < 22$, only 15 could provide a high-S/N spectrum suitable for the present study.

All the selected galaxies have the 14 bands GOODS-South survey coverage (Santini et al. 2009 [102]): deep optical images taken from four *Hubble Space Telescope*-Advance Camera for Surveys band-passes ($F435W$, $F606W$, $F775W$ and $F850LP$); photometric data provided by extensive observations of European Southern Observatory (ESO) telescopes both in the optical (three U-band filters) and in the near-Infrared (J, H and K filters), and by the four *Spitzer-Infrared Array Camera bands* (3.6, 4.5, 5.8 and 8.0μm).

Thanks to these multiwavelength data I was able to perform the global SED fitting of all the galaxies of the sample in order to extract the global stellar population properties. The SED fitting process was carried out assuming the stellar population synthesis model of Bruzual and Charlot (Sec. 3.3) with a Chabrier initial mass function (IMF). I adopted star formation histories with five exponentially declining star formation rates with e-folding time τ =[0.1, 0.3, 0.4, 0.6, 1.0] Gyr and assumed solar metallicity Z = 0.020. Dust extinction, following Calzetti et al. 2000 [8], was applied in the range $0 < A_v < 2$ mag. In Table 5.1, the stellar parameters obtained from the SED fitting of the 15 ETGs are reported: photometric ages Age_{phot} of the stellar populations, dust extinction A_v, stellar masses $\mathcal{M}_*$ and star formation time-scale τ.

For five objects out of the whole sample (those at the highest spectral resolution) the velocity dispersion measures are from the work of van der Wel et al. 2005 [128]. Furthermore, 7 out of the 15 target galaxies (those at $z > 0.9$) are included in the complete sample of the GOODS-South field ETGs at $z > 0.9$ of Saracco et al. 2010 [106].

5.1.1 Spectroscopic data

As already mentioned, this sample of ETGs was collected following the availability of high-S/N optical spectra in the GOODS-South field for galaxies morphologically confirmed as ETGs at $z \sim 1$. These high-quality spectra come from three different observing campaigns: one summarized in Mignoli et al. 2005 ([78], K20 survey), one in Popesso et al. 2009 [94] and one in van der Wel et al. 2005 [128]. I could not use spectra coming from the VLT/FORS2 spectroscopic campaign in the GOODS-South field reported in Vanzella et al. 2005, 2008 ([131], [132]), because observations have been made without the cut order filter OG590+32, so they have not a solid continuum shape calibration necessary for the measurement in particular of the D4000 index.

The K20 survey is a near-Infrared-selected redshift survey targeting galaxies ($K_s < 20$, Vega system) in two fields, one of which has been later included in the GOODS-South area. From this precious data base of public galaxy spectra, I have searched for the highest S/N spectra of $z \geq 0.7$ ETGs in the 4000Å break region rest frame. 8 ETGs have been finally extracted in the redshift range $0.73 < z < 1.2$. Spectroscopic observations of these objects come from VLT-FORS1 in MOS mode and VLT-FORS2 in MXU mode (multi-object spectroscopy with exchangeable masks),

Table 5.1: Sample of 15 ETGs. Data extracted from photometric analysis: stellar population age (A_{phot}), dust extinction (A_v), logarithm of the stellar mass ($\log(\mathcal{M}_*)$) and star formation time-scale (τ). σ is the velocity dispersion measured by van der Wel et al. 2005 [128]. Units of right ascension are hour, minutes and seconds, and unites of declination are degrees, arcminutes and arcseconds.

ID	RA	Dec	z_{spec}	Age_{phot} (Gyr)	Av (mag)	$\log(\mathcal{M}_*)$ ($M_\odot$)	τ (Gyr)	σ (km s^{-1})
1192^a	3:32:25.16	-27:54:50.1	1.089	0.7	1.0	11.01	0.1	231±15
1382^a	3:32:22.93	-27:54:34.3	0.964	1.4	0.4	11.08	0.1	200±9
1950^a	3:32:26.29	-27:54:05.0	1.044	1.9	0.3	10.75	0.3	300±30
1837^a	3:32:19.29	-27:54:06.1	0.964	3.0	0.4	11.40	0.4	336±18
2694^a	3:32:31.37	-27:53:19.1	1.135	2.5	0.3	11.40	0.3	232±19
9066^a	3:32:33.06	-27:48:07.5	1.188	2.0	0.6	10.58	0.3	-
11539^a	3:32:37.19	-27:46:08.1	1.096	2.3	0.5	11.42	0.3	-
10020	3:32:15.81	-27:47:13.6	0.738	1.8	0.5	10.85	0.3	-
10960	3:32:19.24	-27:46:32.2	0.737	2.4	0.3	10.76	0.3	-
11225	3:32:14.44	-27:46:24.5	0.736	1.4	0.2	10.22	0.1	-
9792	3:32:18.01	-27:47:18.6	0.734	3.25	0.5	11.58	0.4	-
13386	3:32:17.49	-27:44:36.7	0.734	1.7	0.3	10.31	0.3	-
9838	3:32:17.94	-27:47:21.5	0.732	3.25	0.2	11.08	0.4	-
17044	3:32:37.38	-27:41:26.2	0.672	3.25	0.1	11.21	0.4	-
7424	3:32:39.54	-27:49:28.4	0.669	2.6	0.2	10.54	0.4	-

^{a}objects belonging to 34 ETGs of Saracco et al. 2010 [106].

with a set of grisms 150*I*, 200*I* and 300*I* providing dispersion of 5.5, 3.9 and 2.6 Å/pixel and spectral resolution of R = 260, 380 and 660 respectively. The observation period of the K20 spectroscopic survey was confined in 20 nights during four years (1999-2000, 2002).

The next source of optical spectra was the second campaign of the ESO-GOODS spectroscopic programme operated with VLT-VIMOS (VIsible MultiObject Spectrograph) and reported in Popesso et al. 2009 [94]. From the thousands of available spectra I have looked for the ones with longer exposure time (exp-time > 5h) in order to reach the highest S/N for $z > 0.7$ ETGs. Moreover, my searching has been focused only on median resolution (MR - resolution R = 580, dispersion 2.5Å/pixel) grism data, necessary to perform the measurements of the spectrophotometric indices. I found only 2 suitable objects in the redshift range $z \sim 0.7 - 1.0$. Observations were carried on during the winter of 2004-2005 for both objects.

Finally, the last 5 objects of this sample were analysed by means of the optical spectra coming from observations performed by van der Wel et al. 2005 [128] with FORS2 in MXU mode on VLT telescope. They used the GRIS-600z grism together with the OG590 order separation filter, with a resolution of R ∼ 1390, that led to

Table 5.2: Information about the spectroscopic data used in this work: spectroscopic instrument, grism, dispersion, resolution and the observing run.

ID	Instrument	Grism	Dispersion (Å/pixel)	Resolution	Observing run
1192	VLT-FORS2	600z	1.6	1390	van der Wel et al. 2005 [128]
1382	VLT-FORS2	600z	1.6	1390	van der Wel et al. 2005 [128]
1950	VLT-FORS2	600z	1.6	1390	van der Wel et al. 2005 [128]
1837	VLT-FORS2	600z	1.6	1390	van der Wel et al. 2005 [128]
2694	VLT-FORS2	600z	1.6	1390	van der Wel et al. 2005 [128]
9066	VLT-FORS2	300I	2.6	660	Mignoli et al. 2005 [78]
11539	VLT-FORS2	200I	3.9	380	Mignoli et al. 2005 [78]
10020	VLT-FORS1	150I	5.5	260	Mignoli et al. 2005 [78]
10960	VLT-FORS2	150I	5.5	260	Mignoli et al. 2005 [78]
11225	VLT-FORS2	200I	3.9	380	Mignoli et al. 2005 [78]
9792	VLT-FORS1	150I	5.5	260	Mignoli et al. 2005 [78]
13386	VLT-FORS2	200I	3.9	380	Mignoli et al. 2005 [78]
9838	VLT-FORS1	150I	5.5	260	Mignoli et al. 2005 [78]
17044	VLT-VIMOS	MR	2.5	580	Popesso et al. 2009 [94]
7424	VLT-VIMOS	MR	2.5	580	Popesso et al. 2009 [94]

a binned spectral dispersion of 1.6 Å/pixel and a wavelength coverage from about 6500 to 11000Å (that means around the spectral region of the Balmer/4000Å break for galaxies at $z \sim 1$). The observations of the 5 objects were carried out in the period from 2002 September to 2003 March, with a mean exposure time of about 11 h for object.

All the details of the spectroscopic data are summarized in Table 5.2.

5.1.2 Data reduction

Spectra coming from Popesso et al. 2009 [94] and an der Wel et al. 2005 [128] have been reduced starting from raw observed data. For K20-survey spectra, I used directly the reduced online material (from Vizier: "K20 survey: spectroscopic catalogue Mignoli et al. 2005"). Standard spectral data reduction has been applied using `IRAF` software tools. Particular care has been devoted to the relative spectral flux calibration, which has been achieved using spectrophotometric standard stars observed in the same nights of the targets; in particular, for VLT-FORS2 data (an der Wel et al. 2005 [128]), I took the mean sensitivity function built with standard stars of different spectral type, which reveal small intrinsic differences in their shape. Moreover, still with the aim of obtaining the best continuum shape calibration necessary for a solid measure of spectral indices, I applied a further continuum calibration on the VLT-FORS2 spectra: indeed I noted a systematic distortion of the spectrum shape for objects whose slits are shifted with respect to the central position, along the dispersion direction. The amount of the flux distortion is proportional to the distance of the slit from the central position and, in the particular case of these VLT-FORS2 objects, the maximum offset slit position leads to a variation up to about 30% of the flux. I corrected for this further distortion using flat-field lamp spectra as standard spectral sources, available for all the slits. The ratio between the wavelength-calibrated flat-field spectrum obtained in a central position and the one obtained through each slit in offset position has been used for this further correction. The final check of the obtained continuum shape accuracy in the spectral region involved in the measure of the chosen spectrophotometric indices, was to overlap the final 1D spectra with the photometric points in the optical bands. The agreement is reached within 1-σ error from the photometric points.

Reduced monodimensional spectra of the whole sample are shown in Figure 5.1 together with the principal absorption lines in the region of 4000Å rest frame.

5.2 Analysis

As it can be seen in Figure 5.1, many absorption lines typical of the stellar atmospheres can be identified in the optical spectra of this selected sample: Balmer series, BL3580, CN, CaII(H,K), Gband. I have taken advantage of the quality of this sample of spectra of ETGs in order to analyse the main properties of their stellar populations, in particular the *age* of their stellar content.

I measured D4000 and H+K(CaII) indices (Sec. 2) on the spectra of this sample of ETGs, and results are reported in Table 5.3. The choice of measuring the values of these two spectrophotometric indices was supported by their intrinsic peculiarities as already discussed in Sec.2. In fact, these indices not only are strongly dependent on stellar population's age variations, mainly for ages less than 6-7 Gyr which is about the age of Universe at $z \sim 1$, but they also present precious differences which have made their combined measure very interesting. It is worthy to note that the measure of the H+K(CaII) index is sensitive to the spectral resolution of the spectral data (Longhetti et al. 1999 [59]), and I have taken this into account when comparing measures with models. Indeed, each measure performed on the spectra was corrected by the corresponding factor which brings the index value as it was measured on a spectrum with the higher resolution of models. In order to obtain these correction factors, I have degraded the spectrum of a reference template, with the original resolution full width at half-maximum (FWHM)= 3 Å (in the spectral range 3000 − 5000 Å rest frame), to the lower resolutions of the observed spectra. I derived the correction factors by dividing the index values measured on the degraded spectra by those measured on the reference template. These correction factors decrease the index values up to about 5% of their measured values in the case of the lower resolution grism (R= 260).

Furthermore, as already discussed in Sec. 2.4, the broadening of the absorption lines due to the intrinsic velocity dispersion of galaxies affects the measure of this index. I thus corrected the raw H+K(CaII) index measures obtained on the five

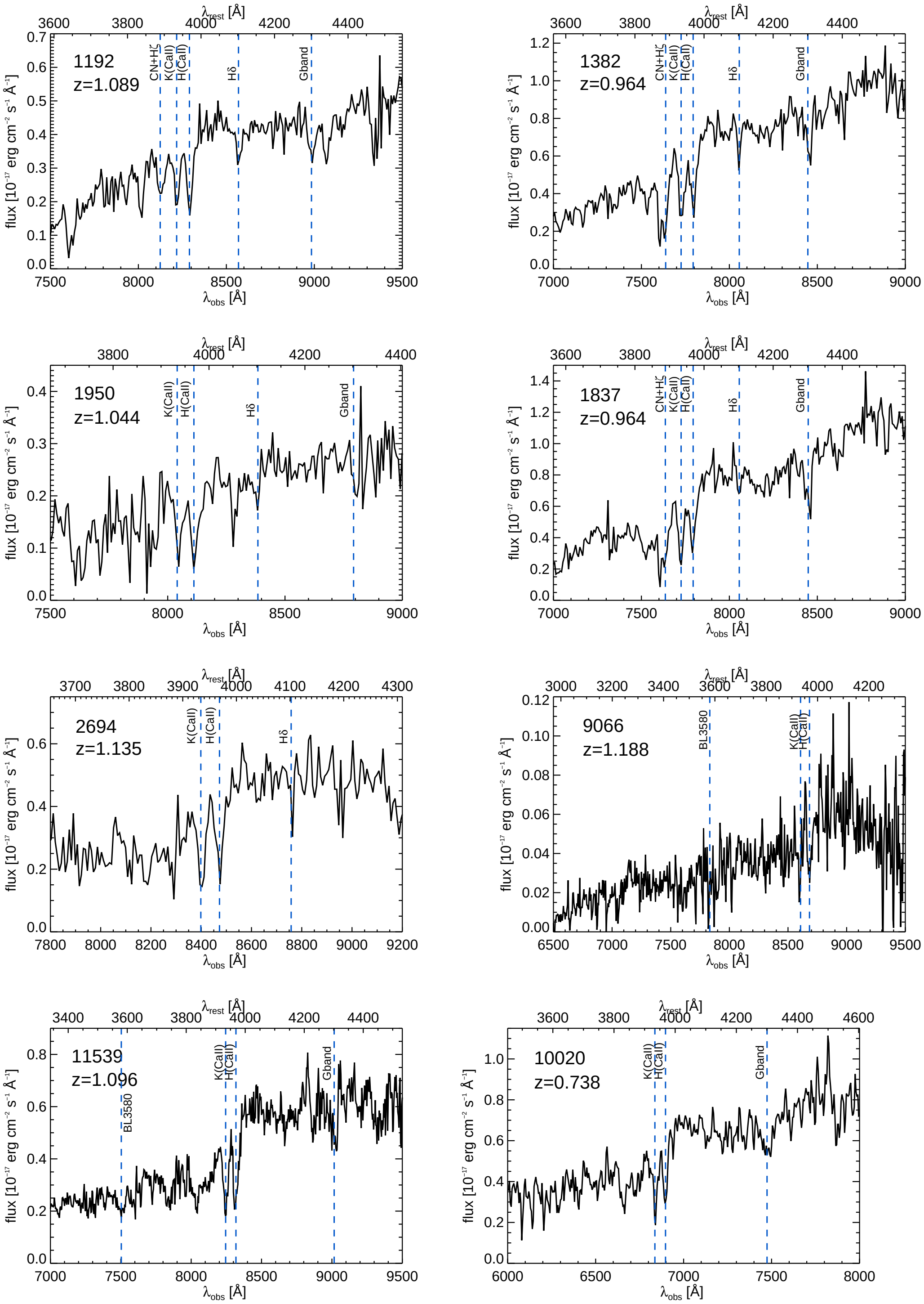

Figure 5.1: Spectra of the sample galaxies with the main absorption lines in the region of the Balmer/4000Å break. Information about the spectroscopic data is shown in Table 5.2. Spectra are shown in bins spanning from 2.5 to 8 Å.

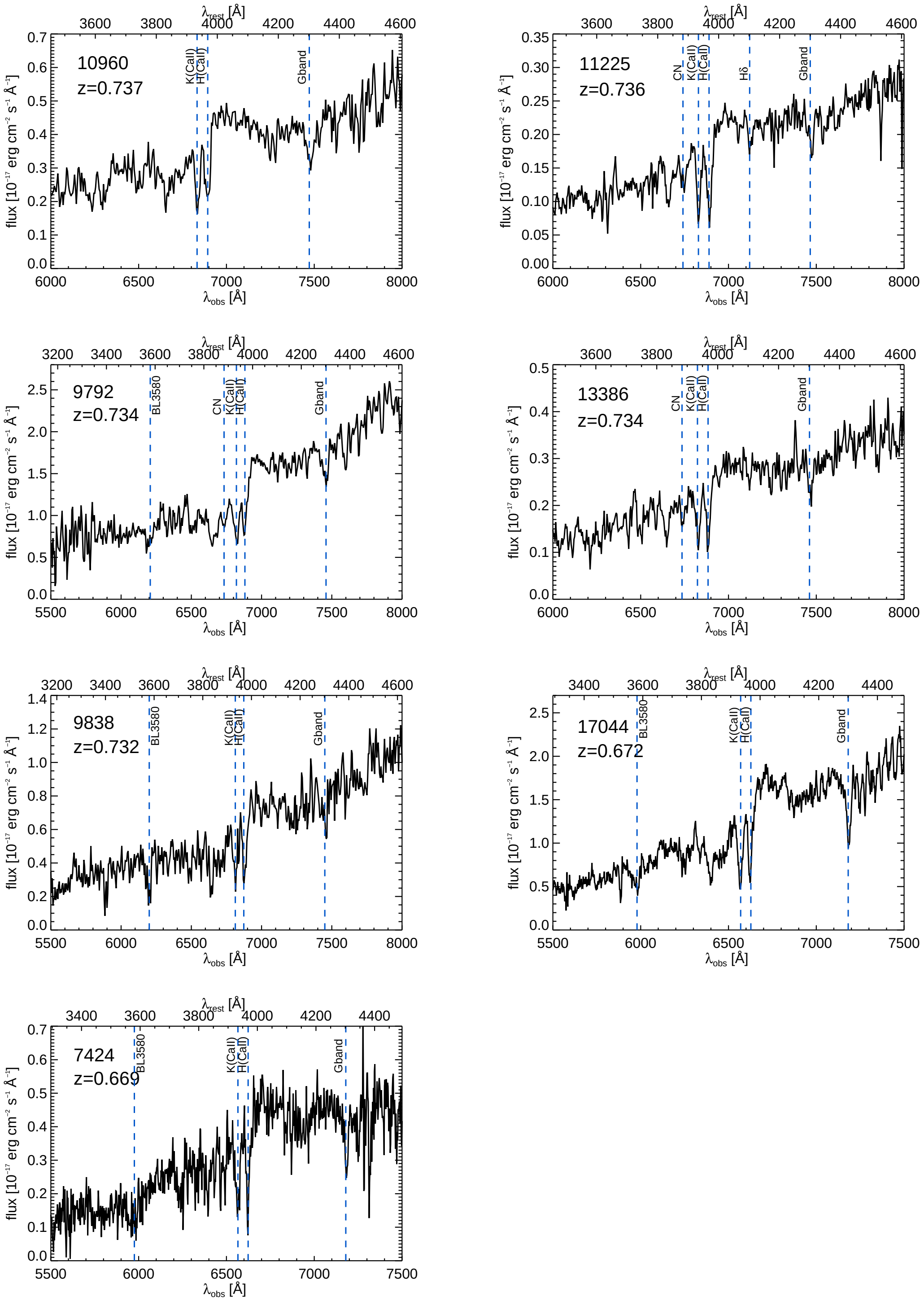

Figure 5.2: Continued.

ETGs observed at the highest spectral resolution (van der Wel et al. 2005 [128]) for this effect, reporting them to the case of null velocity dispersion. I followed the same procedure as for the resolution correction: taking a reference template spectrum which has the same spectral resolution of van der Wel et al. 2005 [128] data, I enlarged their spectral lines convolving them with a Gaussian curve with different σ in order to simulate the effect of the velocity dispersion. I measured the H+K(CaII) index values for each value of the applied velocity dispersion and derived the correction factors to be applied to the index measurements. The correction factors were found to be rather small and well within the error bars. In particular, for three objects the correction was within 2% of the measured value, and for the other two objects it was about 4%. For all the other 10 ETGs of the sample, the lower spectral resolution of their observations prevents to appreciate the latter effect, being much larger than the broadening caused by the resolution itself. Indeed, I have verified that for the medium-resolution spectra (Popesso et al. 2009 [94]), the corresponding correction factors, assuming a typical velocity dispersion of 250 km/s, would be less than 1% of the measured index values.

Errors have been computed from the uncertainties in the measures of fluxes and in the flux calibration (Sec. 2.4). In particular, I have estimated the values of S/N ratios in the two spectral regions involved in the indices definitions (i.e. $3750-4000$Å and $4050-4250$Å) which represent the statistical errors affecting the flux values. On the other hand, I took into account also the flux calibration uncertainties derived from both the standard flux calibration and from the further correction applied on the FORS-2 spectra which suffer for the shape distortion due to the CCD slit position. Obviously, the H+K(CaII) index, being the flux ratio at two very close wavelengths, is almost unaffected by these flux calibration uncertainties. The final errors are shown in Table 5.3.

The measured values of the indices have been compared with the expectations of the spectro-photometric synthesis models (BC03) assuming a Chabrier IMF and an exponentially declining star formation history with time-scale τ (with the same assumptions of the photometric analysis, i.e. $\tau = 0.1 - 1$ Gyr and solar metallicity; afterwards I will discuss the effects of varying these assumptions). Indeed, to start with the simpler evolutionary modelling of star formation typical of ETGs, it is assumed that the bulk of the star formation activity has happened in a confined initial episode with small time-scale τ ($\tau < 1$ Gyr, as it is the case of ETGs (Saracco et al. 2010 [106]).

In this scenario, the stellar content of galaxies is rather coeval, within τ, so if this evolutionary modelling is appropriate for the real star formation history of ETGs, it is expected that the stellar ages derived from the values of the two indices would be consistent with each other.

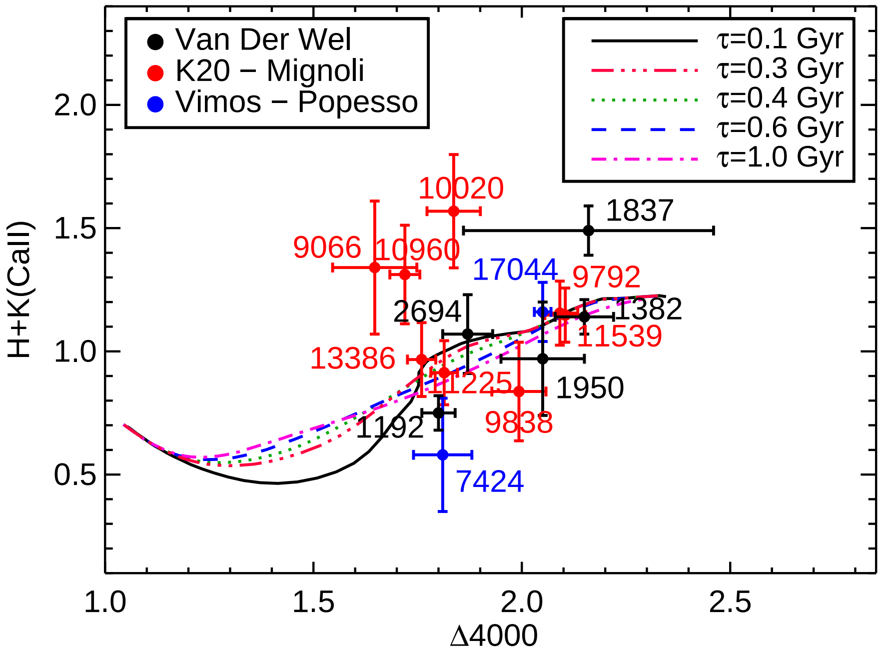

Figure 5.3: Data versus model comparison in the index index plane: measured values of the indices D4000 (x-axis) and H+K(CaII) (y-axis) from the spectroscopic sample of van der Wel et al. 2005 [128] (black dots), Mignoli et al. 2005 [78] (red dots) and Popesso et al. 2009 [94] (blue dots), compared with the expectations of BC03 models at different ages (from left to right, from about 10^8 to 10^{10} yr), fixed solar metallicity and for different *star formation time-scale parameters* τ (colored lines). With the exception of those from van der Wel et al. 2005 sample, shown data points have H+K(CaII) index values a bit underestimated (within error bars) with respect to those indicated by models due to the difference between the spectral resolutions of BC03 synthetic spectra (FWHM= 3Å) and that of the observed ones (see Table 5.2).

Table 5.3: Values of the measured H+K(CaII) and D4000 indices.

ID-MUSIC	H+K(CaII)	D4000
1192	0.75±0.07	1.80±0.04
1382	1.14±0.07	2.15±0.07
1950	0.97±0.23	2.05±0.1
1837	1.49±0.10	2.16±0.3
2694	1.07±0.16	1.87±0.06
9066	1.34±0.27	1.65±0.10
11539	1.15±0.11	2.10±0.05
10020	1.57±0.23	1.84±0.06
10960	1.31±0.20	1.72±0.04
11225	0.91±0.13	1.81±0.03
9792	1.15±0.13	2.09±0.04
13386	0.97±0.15	1.76±0.03
9838	0.84±0.20	1.99±0.06
17044	1.16±0.12	2.05±0.02
7424	0.58±0.23	1.81±0.07

Figure 5.3 shows the comparison between data and models in the D4000 versus H+K(CaII) plane. Black dots are galaxies from the spectroscopic sample of van der Wel et al. 2005 [128], red ones from Mignoli et al. 2005 [78] and blue ones from Popesso et al. 2009 [94]. Lines represent the trends of the values of the two indices of synthetic models at different ages, from younger ages (10^8 yr) at the bottom left to older ages (10^{10} yr) at the upper right (at fixed solar metallicity), and their colours show different star formation histories determined by the time-scale parameter τ. From Figure 5.3 it is possible to notice that: *i)* data points cover an extended area in the index index plane which corresponds to stellar populations older than ~ 2.5 Gyr; *ii)* different τ-models (coloured lines) are confined in a rather thin strip, while measured data are more widespread. While the majority of the data points are in agreement with models, I get the evidence that for 6 out of 15 objects both indices deviate at more than 1σ from models. In particular, starting from the measured values of the D4000 index, 7 out of 15 data points have: either too low values of the H+K(CaII) index (IDs: 1192, 7424 and 9838), suggesting possible stellar populations younger than what pointed out from the D4000 index (see Section 2), or so high values of the H+K(CaII) index (H+K(CaII)>1.2, IDs: 9066, 10960, 10020 and 1837) that they cannot find any correspondence with models within 2σ. It is important to notice that this sample of galaxies is not complete, so these percentages are just evidence that at least some of these high-redshift ETGs have a less homogeneous stellar population with respect to what is expected in a rigorous passive evolution.

Points that are not consistent with the proposed models at different star formation time-scales cannot be explained by using synthetic models with different *metallicities*. As an example, in Figure 5.4 the same diagram of Figure 5.3 is shown, but in this case the different coloured lines represent models with three distinct metallicities (Z = 0.008, Z = 0.020 and Z = 0.040), at fixed time-scale parameter ($\tau = 0.1$ Gyr). From Figure 5.4 it is clear that the not consistent points still remain without a satisfactory explanation on the basis of single-component star formation histories even at different metallicities.

Adding some amounts of dust ($A_v > 0.5$ mag) in the single component models would marginally help in explaining those data points which have low values of the H+K(CaII) index (IDs: 1192, 7424 and 9838). However, even this addition is not able to reproduce the index values of four objects with high H+K(CaII) (IDs: 9066, 10960, 10020 and 1837) because its main effect is to slightly increase the values of the D4000 index. Moreover, this choice should be supported by a physical motivation able to justify these quantities of dust in systems where globally the star formation activity should be quenched (age $>> \tau$).

I have also checked that the values of the two measured indices on synthetic models do not depend on the spectrophotometric models adopted in the analysis: comparing index values obtained from BC03 models with those obtained with the latest version of the same code (Charlot & Bruzual, in preparation), I do not find any difference, while the comparison with Maraston & Strömbäck 2011 [72] models reveals small differences but well within the observational errors (see Sec. 3).

The comparison between the measured indices and models has thus suggested that the star formation histories of these galaxies must have been more complex, eventually involving the presence of later star formation events superimposed on a rather old bulk of stars, causing a less homogeneous population than predicted by simple short τ models.

A further confirmation of this evidence comes from the discrepancy I found among ages derived from the values of the two indices and those extracted from the SED fitting analysis, as shown in Table 5.2: the D4000 index points towards generally more evolved stellar populations. Ages deduced from the indices values and reported in Table 5.2 have been derived assuming BC03 models, solar metallicity and $\tau = 0.1$ Gyr. Ages deriving from indices and from SED fitting are two different but complementary tools to study the stellar content of galaxies: the spectroscopic analysis is based on a small portion of the SED but it is able to give important details on their recent star formation history, while the photometric analysis can provide mean stellar parameters dealing with the whole SED. This first result thus suggests that in general the SED analysis is missing small pieces of information, revealed instead by the indices.

Moreover, for many objects (8 out of 15) the ages derived from the D4000 index tend to differ by more than 1σ from those derived from the H+K(CaII) index. In particular, in one case they differ by more than 2σ (ID-9838). Furthermore, even if possible, it appears unlikely that the age inconsistency arisen from the two

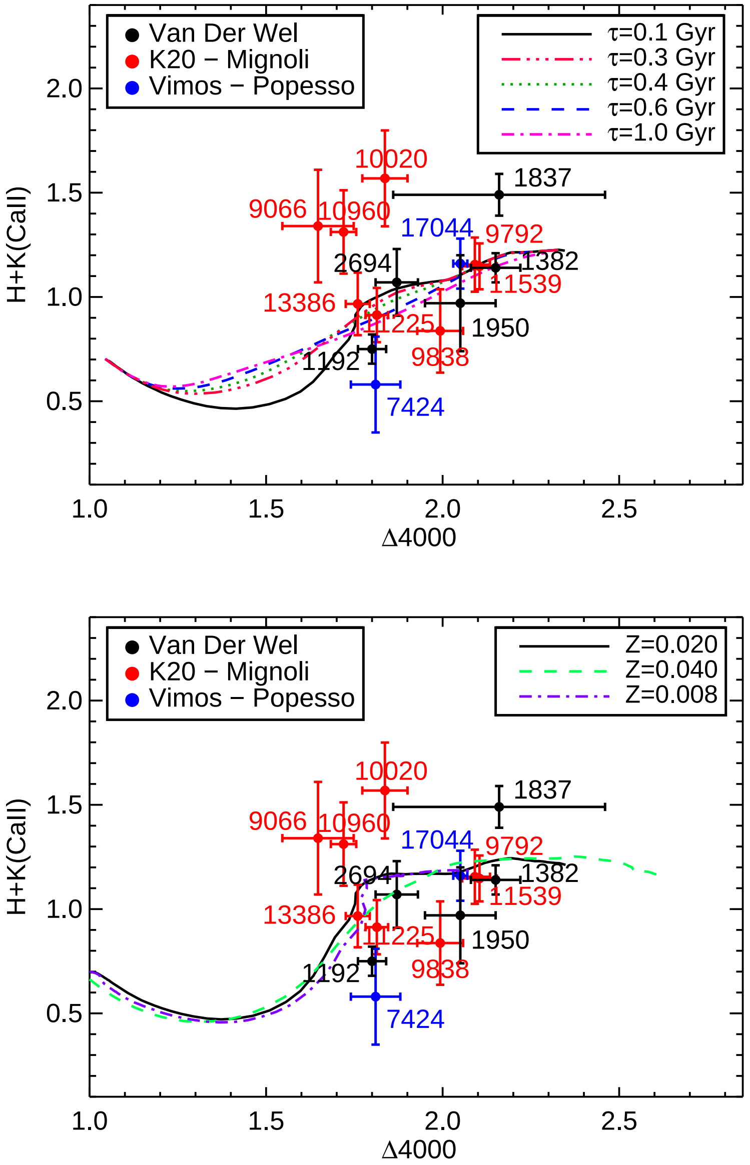

Figure 5.4: Data versus models comparison in the index index plane: measured values of the indices D4000 (x-axis) and H+K(CaII) (y-axis) from the spectroscopic sample of van der Wel et al. 2005 [128] (black dots), Mignoli et al. 2005 [78] (red dots) and Popesso et al. 2009 [94] (blue dots), compared with the expectations of BC03 models at different ages (from left to right, from about 10^8 to 10^{10} yr), fixed star formation time-scale parameter τ and for different *metallicities*: Z = 0.008, Z = 0.020 and Z = 0.040 (coloured lines). As in Figure 5.3, with the exception of those from van der Wel et al. 2005 sample, shown data points have H+K(CaII) index values a bit underestimated (within error bars) with respect to those indicated by models due to the difference between the spectral resolutions of BC03 synthetic spectra (FWHM= 3Å) and that of the observed ones (see Table 5.2).

Table 5.4: Age estimates derived from indices and photometric analysis (Gyr) obtained from the comparison with synthetic stellar populations models with $\tau = 0.1$ Gyr and solar metallicity.

ID-MUSIC	Age from H+K(CaII) (Gyr)	Age from D4000 (Gyr)	Age from photometry (Gyr)
1192	1±0.1	1.9±0.5	0.7
1382	4.5±1.5	5.5±1.5	1.4
1950	1.7±2	4±1	0.7
1837	-	5.75±3	0.9
2694	3±1.2	2.4±0.4	1.3
9066	-	0.9±0.4	1.3
11539	4.7±1.5	4.75±0.5	1.3
10020	-	2.2±0.5	1.3
10960	-	1.1±0.3	1.4
11225	1.2±0.5	1.9±0.4	1.4
9792	4.7±1.5	4.7±0.9	2.7
13386	1.4±0.6	1.5±0.4	0.6
9838	0.9±0.3	3.1±0.4	2.3
17044	1.9±1	3.75±0.4	2.3
7424	0.7±0.4	1.9±0.5	1.4

indices is due to measurement errors. Indeed, it would mean introducing a kind of systematicity which should always decrease the values of age derived from the H+K(CaII) index and at the same time always increase those derived from the D4000 index. In fact, ages from the D4000 index are older than those indicated from H+K(CaII) index (only for one object there is the opposite trend), in agreement with Onodera et al. 2012 [81] who found similar results for passive galaxies at $z > 1.4$. Furthermore, in some cases, ID-2694, ID-9066, ID-10020 and ID-10960 as displayed in Table 5.2, H+K(CaII) values do not find any age correspondence with models, as evident from Figure 5.3. As already hinted in Section 2, the missing matching of the ages derived from these two selected indices should be due to the sensitivity of H+K(CaII) index to very recent (or ongoing) star forming events, even if very weak. On the other hand, D4000 index is a good indicator of the age of the bulk of the stellar content of galaxies. Thus, in order to understand the nature of the discrepancy between the two indices values measured in some of the galaxies of my analyzed sample, I started a new analysis of their properties, assuming that a quite recent star-forming event has been superimposed on an otherwise homogeneous and old stellar population.

As a pure exercise, I have performed the analysis based on the assumption of a double age stellar component for all the galaxies of the sample. The real convenience of introducing the second component, as discussed in the following section, is found only for those objects for which the age values derived from the two indices were not in agreement. And this is the case for 9 out of 15 galaxies. For the remaining galaxies, values of $\tau \geq 0.1$ Gyr are sufficient to explain the inhomogeneity of their stellar content even though with some corrections to the mean ages derived from the SED fitting analysis.

5.2.1 Double-component analysis

To better reproduce the observed stellar populations properties of this sample galaxies and in particular to reproduce the measured indices, I thus hypothesized the presence of *composite* stellar populations, assuming that after the initial bulk of star formation, additional events have occurred also in the following few Gyr. For the sake of simplicity, I started introducing only *double* stellar components; it cannot be excluded that a more refined analysis which involves more than two spectral index measurements on higher quality spectra could eventually find the presence of triple and over stellar populations.

In Figure 5.5 (left-hand panel), the comparison of the measured indices with those obtained on synthetic double-component models is shown: models represent galaxies for which the bulk of the stellar mass belongs to a population whose age increases from left to right (from about 10^8 to 10^{10} yr) in the index index plane, and small mass fractions are taken into account by a younger component with fixed age 0.5 Gyr. Coloured lines represent the increasing intensity of the secondary burst, i.e. the fraction of the younger component, from the right (dark green line) with a fraction of 0.1% to the left (magenta line) with 2.5%. From this plot, it is clear that with only small mass fractions of a superimposed younger population, observed points with low H+K(CaII) index values can be fully explained.

A similar explanation can be possibly advanced also for points with higher H+K(CaII) index values, but with the addition of a further ingredient, as already discussed in Chapter 2. Considering the definition of the H+K(CaII) index, high index values would mean that the "H" absorption line must be very weak with respect to the K(CaII) line. I then hypothesized that the Balmer Hϵ line blended with the H(CaII) line is in *emission* rather than in absorption. As shown in Figure 5.6 in BC03 models, for stellar populations younger than < 0.2 Gyr, Balmer Hϵ emission is dominant over the absorption. So that the presence of a small mass fraction of very young stellar population (i.e., very recent weak burst) can be able to fill the depth of the whole H line, thus increasing the value of the H+K(CaII) index. I then introduced in this analysis BC03 models which include the nebular emission lines (Charlot & Longhetti 2001 [13]). In fact, as shown in Figure 5.7, differences between models with emission (cyan solid line) and without emission (black dashed line) are evident for ages smaller than 1 Gyr; for older ages these models coincide. As an example of this analysis, in Figure 5.5 (right-hand panel) the comparison of model prediction with the observed data in the case of double age component models is shown for a starburst age of 5 Myr. Given the very young age of the secondary component, I took into account the possible dust extinction that should be acting around

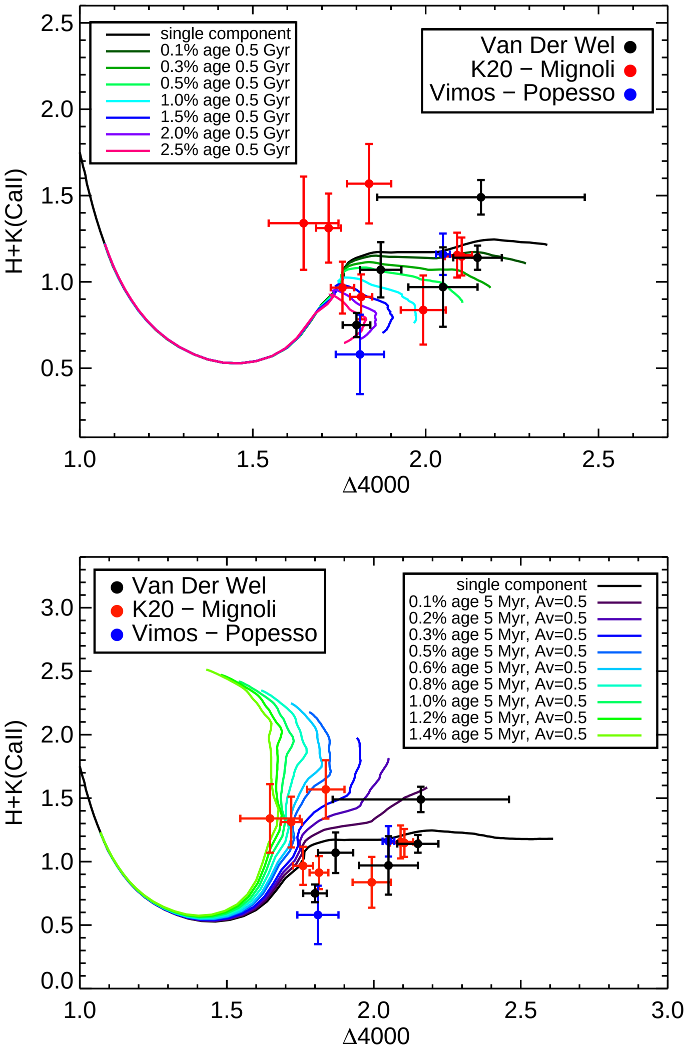

Figure 5.5: Index index plane: comparison with *double-component* models. Left-hand panel: observed points are the same as in Figure 5.3; lines represent the values of the indices on BC03 synthetic models composed of a main component whose age increases from left to right (from about 10^8 to 10^{10} yr), and by small mass fraction of a younger stellar component with age 0.5 Gyr. The fraction of the secondary component increases from 0.1% (dark green line) to 2.5% (magenta line). Right-hand panel: same as the left-hand panel; here the small and younger component has age 5 Myr and it has been reddened with a typical dust extinction of 0.5 mag. Mass fractions span from 0.1% (violet line) to 1.4% (green line). BC03 models are with fixed solar metallicity and $\tau = 0.1$ Gyr. As in Figure 5.3 and 5.4, with the exception of those from van der Wel et al. 2005 sample, shown data points have H+K(CaII) index values a bit underestimated (within error bars) with respect to those indicated by models due to the difference between the spectral resolutions of BC03 synthetic spectra (FWHM= 3Å) and that of the observed ones (see Table 5.2). Both plots show how those data points which were not consistent with *single-component* models can be explained.

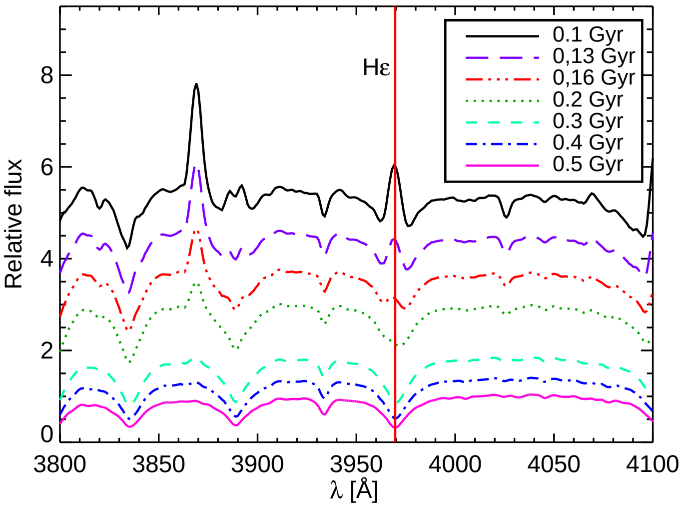

Figure 5.6: Synthetic spectra with Balmer Hϵ ($\lambda = 3969.65$ Å, red vertical line) emission line in models at different stellar population ages. Ages decrease from 0.5 Gyr (magenta line) to 0.1 Gyr (black line).

it, assuming $A_v = 0.5$; it is worthy to specify that the introduction of dust affects only the D4000 index, increasing its value in the same way as age. The intensity of the star formation burst increases from right (violet line), with a mass fraction of 0.1%, to left (green line), with a mass fraction of 1.4%. Both panels of Figure 5.5 are useful examples that show how the suggested presence of small mass fraction of younger stellar component is able to explain the observed data. Age and percentage of mass involved in the secondary component (i.e., age and strength of the recent burst) can be varied to exactly match each single observation. Below I will present the detailed analysis of the whole sample of galaxies and the obtained results.

Each galaxy has been analysed by means of a code that, spanning all the double-component possible models, extracts best-fitting solutions, following the analogue of the one-component photometric analysis. Assuming the BC03 models, including possible emission nebular components, with fixed $\tau = 0.1$ Gyr and solar metallicity, the code builds all the possible double-component combinations of spectra varying ages, mass fractions and dust extinction of the two stellar components. A maximum age limit has been imposed equal to the age of the Universe at the redshift of each galaxy. Recent burst strengths (i.e. the mass percentage involved in the young component) have been considered by means of 0.05% steps. Dust extinction has been applied both on the whole double-component spectrum and only on the younger component, in parallel distinct analysis, with a 0.1 mag pass.

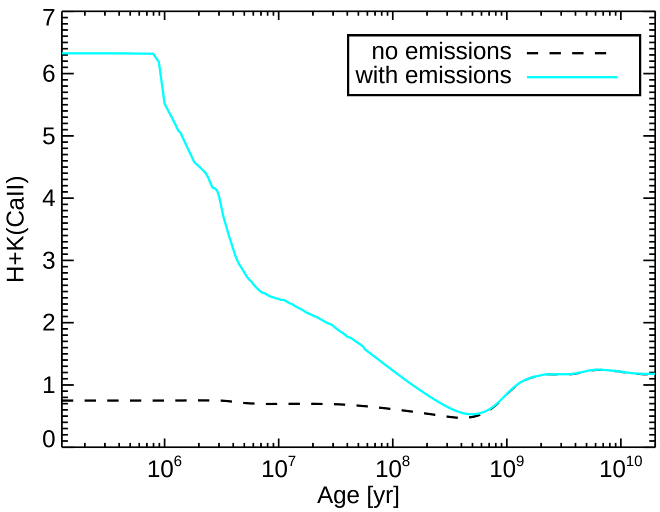

Figure 5.7: Trend of the H+K(CaII) index with age measured on BC03 models with Balmer lines emission (cyan solid line) and without emission (black dashed line). Differences between two models become important only for stellar population with age < 1 Gyr.

From the generated composed synthetic spectra my code selects the solutions which are consistent with the measured values of the two spectrophotometric indices within their observational errors. After this selection, the code starts the χ^2 minimization process of the composite synthetic SED on the observed photometric data. In this way not only the optical band is considered, but the whole spectral distribution of energy.

The results of the analysis are shown in Table 5.6. Mass fraction values expressed in Table 5.6 are indicative of the amount of mass for the solutions with lower χ^2 values. The sample objects are well described by two-component models, revealing the consistence of the found solutions with the presence of a younger stellar population for almost all the galaxies of the sample. Moreover, thanks to the procedure applied in my code, all the composite spectra are fully consistent with the measured indices, contrary to the single-component analysis from which this happens only for a couple of objects. Dust extinction in general becomes important, i.e. $A_v > 2$, only for objects whose young component is younger than the star formation time-scale parameter $\tau = 0.1$ Gyr, that means that the star formation is still ongoing.

The improvement in terms of probability $P(\chi^2)$ of the obtained double-component solutions with respect to the single component ones (with $\tau = 0.1$ Gyr, see Table 5.2) is illustrated in Table 5.5, where I report the comparison of the reduced-χ^2 (χ^2_ν). The estimation of the χ^2_ν includes both the contribution of the 14 photometric points which constitute the global SED and the values of the two analysed spectral indices. It is worth to remark that in this part of the analysis, for consistency, I have compared the double-component models with the single component ones obtained with fixed small $\tau = 0.1$ Gyr. Accordingly, the χ^2_ν values and the corresponding probabilities shown in Table 5.5 are referred to these particular SED fitting solutions.

As can be seen from Table 5.5, the double-component solutions are preferable over the single component ones for almost all the galaxies of the sample. More in details, for 9 out of 15 galaxies (60% of the sample) (IDs: 1192, 1950, 1837, 9066, 10020, 10960, 9838, 17044 and 7424), which have the age values derived from indices not in agreement with each other (see Table 5.2), the double-component solutions with age differences > 1.5 Gyr are clearly more representative of their inhomogeneous stellar contents. For the other six objects, even if providing statistically more probable solutions for four out of six cases, the double-component analysis appears not significantly necessary. Indeed, for these six galaxies the ages derived from the two indices result all in agreement with each other pointing to the same generally older age with respect to the ages extracted from the SED fitting analysis (see Table 5.2). In particular, for three galaxies (IDs: 1382, 11539 and 9792), the double-component solutions are statistically more probable actually just because the bulk of the mass ($> 98\%$) matches the age indicated by the two indices (compare Table 5.2 with Table 5.6), while the single-component solutions miss this important information. Only for the remaining 3 cases (IDs: 2694, 11225 and 13386) both indices and $\tau \geq 0.1$ Gyr SED fitting analysis point to the same age, directly revealing a rather homogeneous stellar population.

Summarizing, the double-component analysis shows that in 60% of the galaxies of this sample there are two stellar components whose presence explains the different ages derived from the index values. Furthermore, thanks again to the index values, this analysis has confirmed or corrected the ages of the SED fitting solutions for the remaining objects.

In Figure 5.8, I present two examples of the analysis that I performed on two opposite cases which are not consistent with a single component description: object ID-9066 (top panels) which has a high H+K(CaII) value (> 1.2), and object ID-7424 (bottom panels) which has a low value of the H+K(CaII) index. In the caption of Figure 5.8, I report, as example, the detailed discussion of these two representative cases. Left-hand panels of Figure 5.8 show the comparison between the single-component (black) and double-component (red) best-fitting solutions on the observed SED (blue points): both the presented double-component models fit better the spectral distributions. Focusing on the 4000Å rest frame region (right-hand panels), it can be seen that the double-component spectrum (red) reproduces better the observed spectrum (black) than the single component model (green), in particular the features involved in the H+K(CaII) index definition (i.e. the H and K absorption lines).

5.2.2 The ages of the two stellar components

As it can be seen from the analysis of this sample, based on both the spectral indices and the photometric SED fitting, I found evidence that at least 60% of the selected ETGs have the bulk of the mass composed of rather old stars and a small percentage

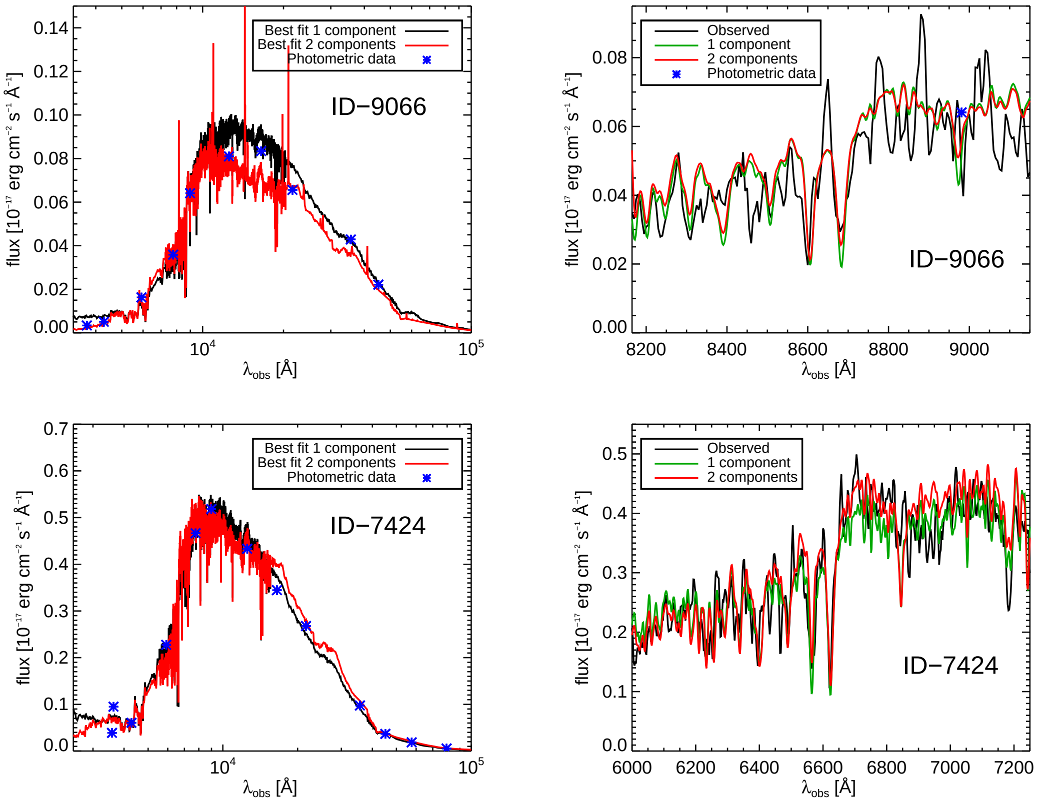

Figure 5.8: Left-hand panels: comparison between single-component solutions (red line) and double-component models (black line) on the observed SED (blue points). Right-hand panels: comparison between single-component spectrum (green) and double-component spectrum (red) on the observed spectrum (black) in the region of the 4000Å rest frame. Upper panels: galaxy ID-9066. Analysis: the corresponding stellar age of this object from the SED fitting analysis was 2 Gyr (with $\tau = 0.3$ Gyr and $A_v = 0.6$, see Table 5.1); instead, from the index measurements it is obtained an age estimate of about 0.9 Gyr from the D4000 index and none from the H+K(CaII) index because its value is above the critical value (i.e. 1.2). I thus proceeded with the double-component analysis on models with gas emission lines. The result is a composite stellar population with a 6 Myr younger component (with signs of recent star formation) reddened with $A_v = 2.8$, superimposed on the bulk of the stellar mass ($> 99.3\%$) with an older age of 1.7 Gyr. The value of the older component age is similar to the photometric age, but the single-component solution was not consistent with the measured indices. Instead the double-component solution, with the adding of small amounts of very young stellar population has been able to adjust the fit of the spectral features, and taking into account at the same time the trend of the whole SED. Bottom panels: galaxy ID-7424. Analysis: from the SED fitting analysis this object was described by a 2.6 Gyr old stellar population with $\tau = 0.4$ Gyr and $A_v = 0.2$, on the other hand, H+K(CaII) and D4000 indices pointed to ages of 0.7 and 1.9 Gyr respectively (see Table 5.2). Moreover, the single-component solution was not consistent with the measure of the H+K(CaII) index. The double-component analysis found a consistent solution composed by a main component with old age 6.25 Gyr and a relative high fraction (about 15%) of a young component with age 0.7 Gyr, reddened with $A_v = 0.5$.

Table 5.5: Comparison of the reduced-χ^2 and corresponding probabilities between the single and double-component solutions. The χ^2_ν estimations include the comparison among the photometric points and the analysed spectral indices.

ID	χ^2_ν single component	Probability (%)	χ^2_ν double component	Probability (%)
1192	5.01	0.7	1.14	32
1382	13.6	0	3.7	16
1950	7.5	0.06	2.94	5
1837	19.94	0	1.31	27
2694	1.56	21	1.8	16
9066	3.31	4	0.66	52
11539	12.66	0	1.16	31
10020	5.02	0.7	0.844	43
10960	3.85	2	1.74	17
11225	0.59	55	0.77	46
9792	9.05	0.01	1.64	19
13386	4.89	0.7	1.16	31
9838	3.43	3	1.26	28
17044	9.87	0.01	1.31	27
7424	2.038	13	1.01	36

of younger stars. In the following, I include also the three objects (IDs: 1382, 11539 and 9792) for which I have corrected the age of the bulk of stars by means of the index values; indeed, the amounts of younger component, although not necessary, are found to be very small. In this 80% of the sample, which I remark again is not complete, with the exception of object ID-7424, I find that the mass fractions of the younger component are small, less than 10%, with the smallest being 0.05%, while the bulk of the mass belongs to the older component. The distributions of the ages of the old (left-hand panel) and young (right-hand panel) components of this part of the sample, are shown in Figure 5.9. White data represent the whole 80% of the sample, while blue and green shaded data represent subsamples at respectively $z \sim 0.7$ and $z \sim 1$. Considering the old component age distribution (left-hand panel), it appears bimodal with a younger sample with a mean age of 2.25 Gyr and with an older one of 5.3 Gyr. This means that the bulk of their stars formed at $1 < z_{form} < 3$ and $z > 5$, as it can be seen in Figure 5.10 which clearly shows that both the two subsamples of galaxies at $z_{spec} \sim 0.7$ and $z_{spec} \sim 1$ have a z_{form} of their main stellar component bimodally distributed, without any dependence on redshift. I stress that this result is evidence coming from a casually selected sample of ETGs and hence it cannot be interpreted as a general bimodality in the distribution of the star formation episodes in ETGs.

On the contrary, in the young component histogram (Figure 5.9, right-hand

Table 5.6: Results obtained from the double-component analysis on the sample of galaxies extracted from the composition of BC03 models, with fixed $\tau = 0.1$ Gyr and solar metallicity. Mass fractions are the indicative values for the solutions with lower χ^2 values.

ID	Age younger (Gyr)	Mass fraction (%)	Age older (Gyr)	Mass fraction (%)	A_v (mag)	Age differences (Gyr)	z_{form}
1192	0.64	6.5	2.4	93.5	0	1.76	2.15
1382	0.1	0.05	5	99.95	0.9^a	4.9	6.1
1950	0.45	1	5.5	99	0	5.05	>6
1837	0.015	0.95	5.5	99.05	2.8^a	5.485	>6
2694	0.5	0.65	2.3	99.35	0.1	1.8	2.2
9066	0.006	0.75	1.7	99.25	2.8^a	1.694	1.95
11539	0.3	0.1	4.75	99.9	0.2^a	4.45	>6
10020	0.03	1.5	2.6	98.5	2.3^a	2.57	1.45
10960	0.015	1.65	2.3	98.35	2.6^a	2.285	1.32
11225	0.9	20	6.25	80	0.2	5.35	>6
9792	0.8	1.65	4.75	98.35	0.3	3.95	2.86
13386	0.1	0.1	1	99.9	0.3	0.9	1
9838	0.5	2.6	4	97.4	0.8^a	3.5	2.16
17044	1	5.3	7	96.5	0.2	6	>6
7424	0.7	16.7	6.25	83.3	0.5^a	5.55	5.5

[a] A_v applied only on the young component.

panel), the distribution is homogeneous with a mean age of 0.4 Gyr. From both histograms, it is clear that there is no dependence on redshift in the obtained results, so it cannot be identified a single confined cosmic period for the formation of the stars neither of the old nor of the younger components.

It is worthy to note that the ages of the bulk components are generally older than the ages derived from the photometric analysis. Indeed, the main components generally reveal the same stellar ages predicted from the values of the D4000 index, which, as already discussed, is a measure of the global stellar population (see Table 5.6 in comparison with Table 5.2). In Figure 5.11 I report the comparison between the ages estimated from the SED analysis (with fixed $\tau = 0.1$ Gyr) with respect to both those of the young components (light blue squares) and those of the old components (dark blue triangles). It can be seen that ages derived from the SED analysis are all younger than 2.7 Gyr, while in this double-component analysis, the ages of the old components reach 7 Gyr. This figure demonstrates that the photometric analysis, without the constraints imposed by the spectrophotometric indices, clearly underestimates the age of the bulk of stars in ETGs at $z \sim 1$. As a consequence, it results that also the stellar mass derived from the SED fitting is on average underestimated with respect to the value that can be derived from the double-component analysis. Indeed, I estimated that the mean correction factor for the stellar mass of

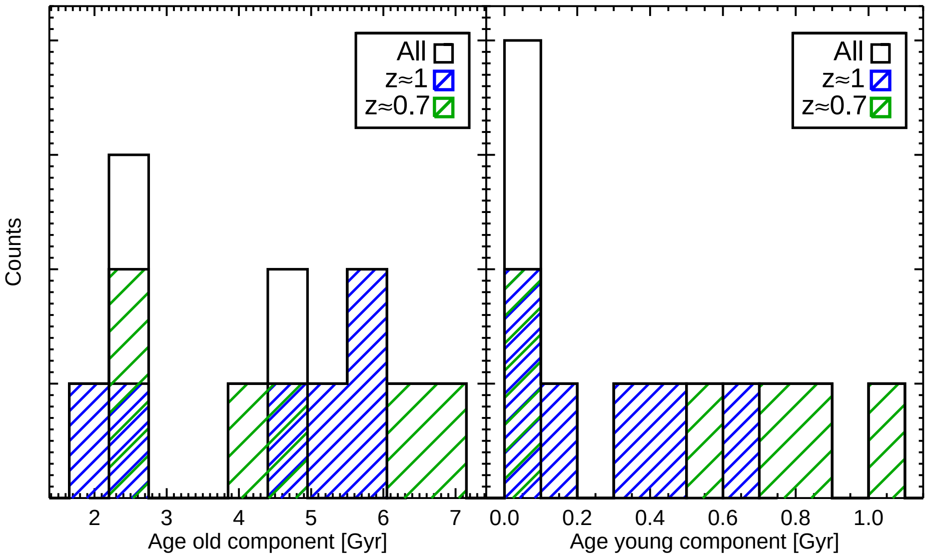

Figure 5.9: Histograms of the double-component analysis results on the 80% of the sample (see Section 5.2.2). White: data from all the 80% of the sample; blue shaded: data from the subsample of galaxies at $z \sim 0.7$; green shaded: data from the subsample of galaxies at $z \sim 1$. Left-hand panel: distribution of the ages of the old components in bins of 0.55 Gyr. There are two visible subsets with mean age of about 2.25 Gyr and 5.3 Gyr. Right-hand panel: distribution of the ages of the young components in bins of 0.1 Gyr. The mean age is about 0.4 Gyr.

the sample galaxies is on average 1.2 with peaks up to a factor of 2, and the more is the difference between the age extracted from the SED fitting and the age of the older component, the higher is the value of this correction.

In conclusion, these results suggest that the bulk of the star formation in this sample of ETGs at $z \sim 1$ happened in two indicative cosmic periods: one at $z_{form} > 5$ and the other more recent at $1 < z_{form} < 3$. New and minor events of star formation occurred in these galaxies within 1 Gyr (upper limit) from their observation, i.e. $z \sim 1$ and $z \sim 0.7$.

It is worthy to note that the obtained results are strictly related to the peculiarities of the two spectrophotometric measured indices. In particular, the H+K(CaII) index has been of fundamental importance to detect the presence of small fractions of young stellar populations also when the bulk of the mass ($> 98 - 99\%$) belonged to the older main component. Indeed, as it appears evident from Figure 5.5, the H+K(CaII) index experiences large variations even when only a small percentage of stellar mass younger than 1 Gyr is added to the old bulk of stars.

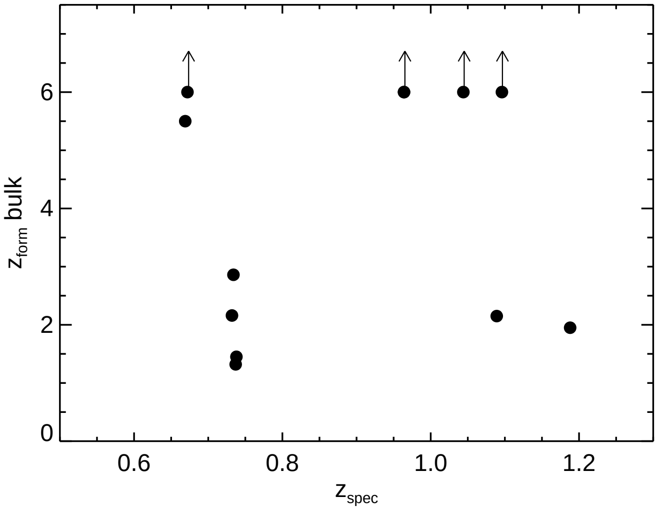

Figure 5.10: z_{form} of the main component as a function of the z_{spec} of the 80% of the sample of galaxies. Arrows mean that the values can be higher than what indicated by the respective points.

5.3 Discussion

In the last years, only two works based on high-redshift ETG optical spectra reported a similar spectroscopic analysis based on spectrophotometric indices. In this section, I try to compare the obtained results with the finding of these two works.

The first one is a work by Onodera et al. 2012 [81] where the authors present a spectral analysis of a sample of 18 passive elliptical galaxies at $1.4 < z < 1.8$ in the *Cosmological Evolution Survey* field. In particular, based on near-IR *Subaru/Multi-Object Infrared Camera and Spectrograph* spectra (resolution R $\simeq$ 500), they performed the measurements of two spectrophotometric indices in the same region of our analysis: the Hδ index (defined as Hδ_F by Worthey & Ottaviani 1997 [136]) and D$_n$4000, a 4000Å break index definition by Balogh et al. 1999 [2], not coincident with the one adopted in the present analysis.

To compare our sample with that of Onodera et al. 2012, I have measured the values of the Hδ_F and D$_n$4000 indices on the spectra of our sample. Results are listed in Table 5.7.

In their Figure 17, Onodera and collaborators showed the comparison of their measurements with the predictions of synthetic models (Charlot & Bruzual, in preparation) assuming four different star formation histories and most of their objects are not consistent with any of the displayed models. I add my lower redshift sample in the same Hδ_F versus D$_n$4000 plane, and the result is shown in Figure 5.12 (top panels). Indeed, on average, at fixed D$_n$4000 index value, the Hδ_F index value is either higher than expected from models or too low to find any correspondence with

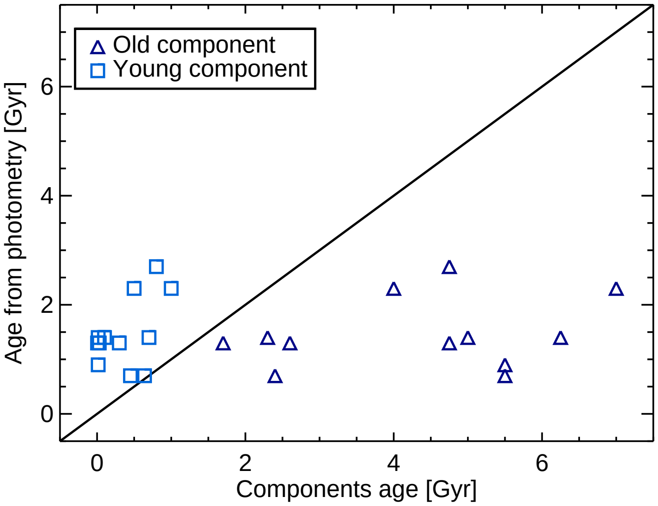

Figure 5.11: Comparison between the ages derived from the SED fitting photometric analysis (from Table 5.2) and the ages of the main component (dark blue triangles) and the young component (light blue squares) extracted from the double-component analysis (from Table 5.6). Data concern the 80% of the sample.

models (with $\tau = 0.1$ Gyr and solar metallicity, black line in Figure 5.12, top panels). I then proceeded with the same arguments followed in the previous sections, considering double stellar components models. The top-left panel of Figure 5.12 presents composite models with the younger component at fixed age 0.7 Gyr, while in the top-right panel the minor component is so young, 5 Myr, to present emission lines and to produce negative values of the Hδ_F index. Double-component models with the adding of gas emission are successful in explaining many of the data points of both samples, in particular those with lower values of both indices. Unfortunately, those points with extreme high values of Hδ_F (and relative high values of D$_n$4000 index) remain still unexplained with any combinations of stellar component ages, as already noticed by Onodera et al. 2012.

Focusing only on my sample data (red points in Figure 5.12, top panels), it is worth to stress that the obtained spread in the Hδ_F versus D$_n$4000 index plane is more restrained than that in the H+K(CaII) versus D4000 index plane discussed in this analysis (see Figure 5.3). This is due to the lower sensitivity of the Hδ_F index respect to that of the H+K(CaII) index to the presence of very small amounts of young stars. As explained in Section 2, indeed, the measure of the H line depth and its ratio with the K line is influenced almost only by the blended Hϵ line depth, making the values of their ratio (i.e. H+K(CaII) index) a very sensible tools for detecting young stellar populations. The larger effectiveness of the H+K(CaII) index with respect to the Hδ_F index in finding the younger component is easily verified looking at the synthetic models. Colored lines in Figure 5.12 (top left panel) indicate the

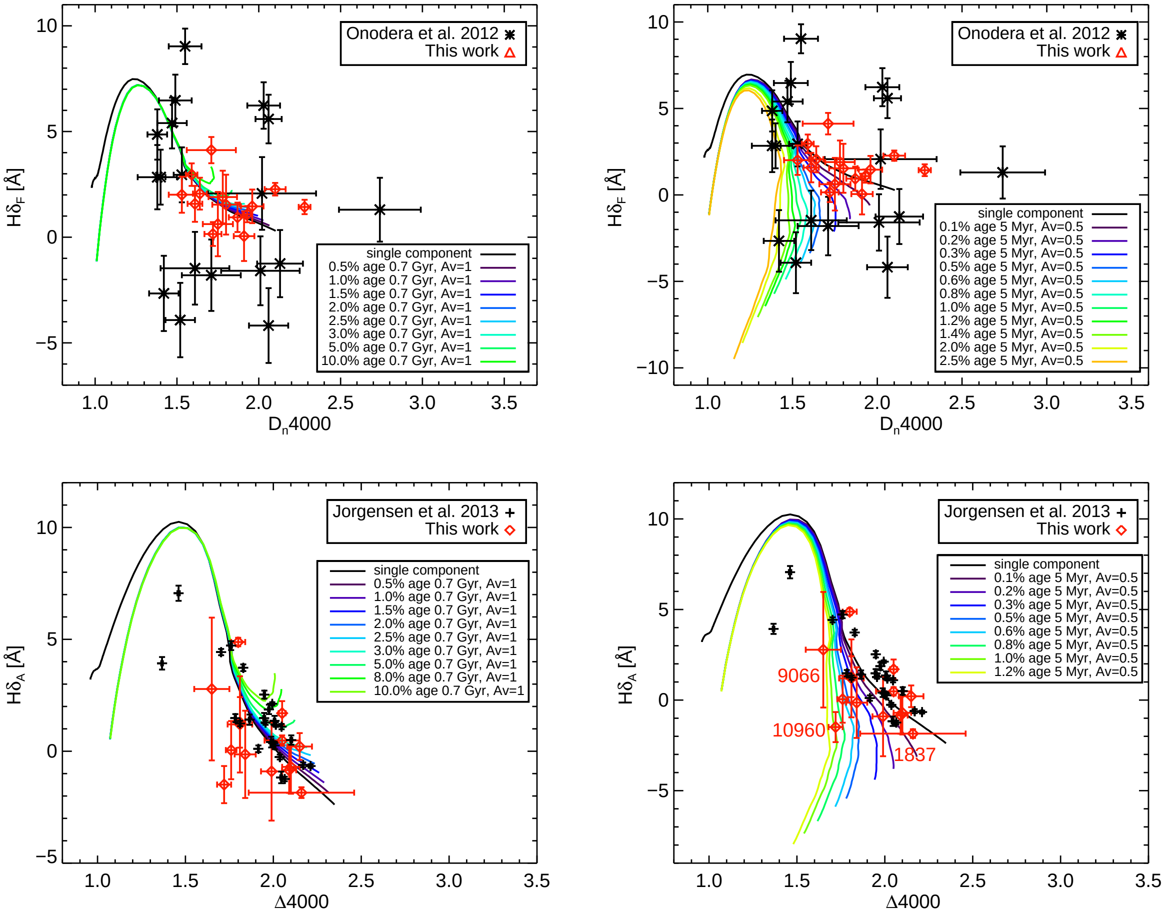

Figure 5.12: Same plots as Figure 5.5 in the Hδ_F versus D$_n$4000 plane, for both the Onodera et al. 2012 [81] sample (black points) and this analysis sample (red points)(top panels), and in the Hδ_A versus D4000 plane for both the Jorgensen & Chiboucas 2013 [40] sample (black points) and this analysis sample (red points)(bottom panels). Double-component models (coloured lines) are composed of the bulk of the mass whose ages increase from left to right (from about 10^8 to 10^{10} yr), and by increasing mass fractions of young component with age 0.7 Gyr with A$_v$ = 1 (left-hand panels), and with age 5 Myr, reddened with A$_v$ = 0.5 (right-hand panels). Double-component models in the right-hand panels are shown with the adding of gas emission lines. In all panels, Hδ_F values of synthetic models (coloured lines) and data points have been properly corrected to take care of their different spectral resolutions.

Table 5.7: Values of the D_n4000 and $H\delta_F$ indices (used in Onodera et al. 2012 [81]) and $H\delta_A$ index (used in Jorgensen & Chiboucas 2013 [40]) measured on this sample spectra.

ID	z	D_n4000	$H\delta_F$	$H\delta_A$
1192	1.089	1.59±0.03	2.44±0.53	4.88±0.19
1382	0.964	2.10±0.06	2.15±0.30	0.21±0.60
1950	1.044	1.53±0.08	2.16±0.85	0.48±0.23
1837	0.964	2.28±0.04	1.54±0.34	-1.85±0.24
2694	1.135	1.96±0.07	1.57±0.79	1.13±0.53
9066	1.188	1.71±0.15	4.12±0.62	2.78±3.19
11539	1.096	1.91±0.06	0.05±1.18	-0.70±1.20
10020	0.738	1.78±0.09	1.90±1.25	-0.14±1.95
10960	0.737	1.72±0.05	0.15±0.56	-1.49±0.83
11225	0.736	1.64±0.04	2.06±0.75	1.29±1.13
9792	0.734	1.87±0.05	0.94±0.69	-0.85±1.01
13386	0.734	1.61±0.04	1.58±0.85	0.05±1.30
9838	0.732	1.80±0.08	1.54±1.42	-0.90±2.20
17044	0.672	1.93±0.03	1.09±0.38	1.70±0.54
7424	0.669	1.75±0.09	0.62±1.52	1.20±2.15

values of the $H\delta_F$ and D_n4000 indices of double-component models with increasing fractions of the younger component, and it can be noticed that the detachment from the single-component model (black line) is limited with respect to what obtained in Figure 5.5 in the case of H+K(CaII) index.

Interestingly, from both top panels of Figure 5.12, it can be noticed that data points of this analysis sample (red points) stay closer to models than those of Onodera et al. 2012. Since my points refer to lower z galaxies, I thus looked for a correlation of this spreading with redshift. I separated the entire sample of galaxies in five subsets with different range of redshift: $z \sim 0.7$, ~ 1, ~ 1.4, ~ 1.6 and ~ 1.8. In Figure 5.13, I present the same plot of Figure 5.12, but with only a representative single-component model (black line, with $\tau = 0.1$ Gyr and solar metallicity). Colours of the data points go from yellow, low-redshift objects ($z \sim 0.7$), to dark red, the highest redshift ($z \sim 1.8$). From this plot, it is clear that low-z data stay closer to the model than those with high z and that the more the redshift increases, the more the data are widespread in the index index plane, i.e. more distant from models. Furthermore, in Figure 17 in Onodera et al. 2012, the authors present the comparison of their high-z data with local SDSS passive galaxies, and the trend seems to be confirmed: local objects are generally well represented by single-component models with respect to high-z data. In high-redshift objects, differences of ages among possible multiple stellar components are easier to be detected thanks to the younger mean ages, for which even small age differences produce strong signatures (e.g. Balmer lines depth), while in the local Universe the same age differences are

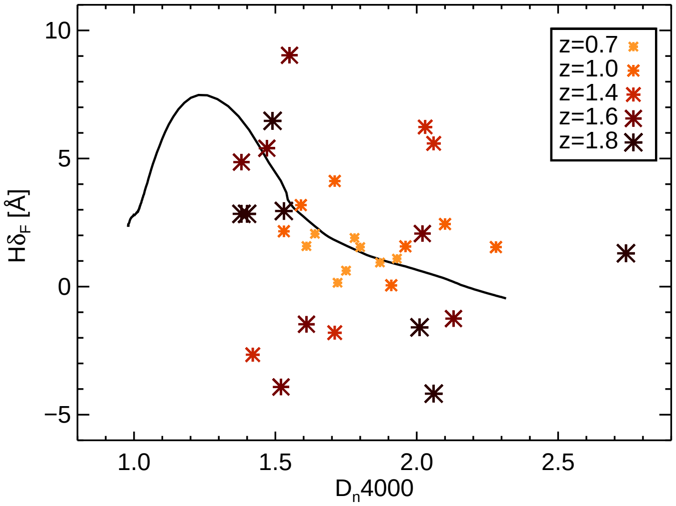

Figure 5.13: Hδ_F versus D$_n$4000 plot. Black line is the single-component model with $\tau = 0.1$ Gyr and solar metallicity. Data from the sample of Onodera et al. 2012 [81] and this work galaxies. Data points are divided into five redshift bins (from yellow to dark red crosses): $z \sim 0.7$, ~ 1, ~ 1.4, ~ 1.6 and ~ 1.8. Errors bars are omitted for simplicity; they would be the same as in Figure 5.12.

almost impossible to be detected for the stellar population ageing, thus vanishing the opportunity of observing the presence of double components. Indeed, two stellar populations with 8 and 12 Gyr, respectively, have almost the same Balmer lines depth. This strengthens the advantage of dealing with direct spectral measurements of higher redshift ETGs in order to study their star formation history.

The second interesting comparison is with the work by Jorgensen & Chiboucas 2013 [40]. Their analysis is based on high-S/N optical spectroscopy of the early-type members of three galaxy clusters at $z > 0.5$ in the framework of the "The Gemini/HST Galaxy Cluster Project". I limited the comparison to the highest z clusters which are the RXJ0152.7-1357 at $z = 0.83$ and RXJ1226.9+3332 at $z = 0.89$, because they match the average redshift of my sample. For these galaxy clusters, in particular, the authors make available the measurements of some spectrophotometric indices obtained from the GMOS-N instrument (R = 1918). They adopt the same definition of the D4000 index as I adopted, and the definition of the Hδ_A by Worthey & Ottaviani 1997 [136], different from that of Onodera et al. 2012. In order to perform the comparison, I thus measured the values of the Hδ_A of my sample galaxies, and the results are listed in column 5 of Table 5.7.

Once again I compared the results with the expectation of the single-component BC03 models (black line, with $\tau = 0.1$ Gyr and solar metallicity), in Figure 5.12, bottom panels. Data points from Jorgensen & Chiboucas 2013 (black points) remain relative close to the single-component model predictions (black line), in agreement with the measure of our sample, supporting the previous finding that the secondary younger component is more evident at increasing z. In order to preserve the graphic clearness, in Figure 5.12 only data points belonging to RXJ1226.9+3332 galaxy cluster are shown. In Figure 5.12, bottom-left panel, I report the comparison of both the two sample data with the double-component models (colored lines), the same as in the top-left panel: points with higher values of Hδ_A index at fixed D4000 index value result fully explained by adding a small mass fraction of young stars. On the other hand, only some of our sample data points (red points) have lower values of Hδ_A index at fixed D4000 index and they can be again explained with double-component models adding very young stellar components displaying Balmer emission lines. In particular, it is interesting to note that the three objects ID-9066, ID-10960 and ID-1837 of my sample, highlighted with labels in Figure 5.12 (bottom-right panel), have Hδ_A and D4000 indices which are consistent with double-component models displaying emission lines in agreement with the results found using the H+K(CaII) index with respect to the Hδ_A one in this analysis (see Figure 5.5, right-hand panel).

Finally, I remark that in the bottom panels of Figure 5.12, I am comparing in the same plots data coming from two samples of galaxies at about the same mean redshift but in different environments: my sample (red points) is composed of field galaxies, i.e. low-density environment (with mean $z = 0.83$), while Jorgensen & Chiboucas 2013 sample (black points) is composed exclusively of galaxies belonging to the cluster RXJ1226.9+3332 at $z = 0.89$. The fact that the galaxies of the sample of Jorgensen & Chiboucas 2013 do not need on average the presence of a second stellar component modelled with Balmer emission lines, means that in general their stellar populations are homogeneous, i.e. formed in a single or very short burst with no secondary bursts, in agreement with the well-known results of Thomas et al. 2005 [116], where high-density environment galaxies are expected to form their star earlier than low-density counterparts and in a shorter time-scale. Supposedly, many cluster objects have experienced the same mechanism of star formation and assembling of this sample of ETGs that led to the presence of stellar components with different properties, but these events must have occurred earlier in the cosmic time and are less appreciable at the observation redshift.

5.4 Conclusions

Having revealed the presence of small young stellar components in many galaxies in a wide redshift range ($0.7 < z < 1.8$, thanks to the enlarged sample) implies that there must be a common mechanism by which ETGs at any cosmic time either accrete new amounts of young stellar mass by means of minor merging events, or activate new events of star formation almost constantly over time. Minor merger-induced star formation is the most widely accredited hypothesis to explain the presence of ongoing star formation in ETGs, since it has been also found in the local Universe (Kaviraj et al. 2012 [44]). Minor mergers are those with mass ratio (M/m) in the range $1/10 < M/m < 1/4$, and my findings on the younger components mass fractions are consistent with this scenario. Indeed, adopting the assumption of "dry" minor merging, which in general involves a maximum value of gas fraction of 10% of the total accreted mass (stars+gas), the very small fractions of the second components observed in this work, i.e. $\sim 0.1\%$, result in agreement with this description. On the other hand, obviously, also wet minor merging events are able to explain the origin of the observed younger component, with the accretion of external gas being the driver of new star formation activity. However, minor merging events do not seem to be so frequent in the cosmic epoch from $z \sim 1$ to now. Indeed, Lopez-Sanjuan et al. 2012 [65] have found that from $z \sim 1$ to $z \sim 0$ the number of minor merging per red galaxy is 0.46 ± 0.06; thus, it seems rather unlikely that in an albeit small sample of 15 galaxies, I found that at least 9 objects (i.e. 60%) have recently experienced a minor merging event. In addition, it must be considered that all these objects have been classified as ETGs and their morphology appear all regular; thus, if merger events have happened in the cosmic histories of these galaxies, they must have taken place at least few Gyr earlier with respect to their observation in order to resettle the elliptical morphology. But this is not in agreement with our findings where the younger component is always observed with age < 1 Gyr.

Moreover, other independent works, such that by Gargiulo et al. 2012 [31], not only have demonstrated the inhomogeneities of stars in ETGs at $z > 1$, but they have also localized the younger component in the inner part of the galaxies. This naturally leads to the question of what is the physical mechanism which, after the external mass accretion by means of hypothetical merging events, is able to bring only the younger stars to the centre of galaxies at least in the case of dry merger event.

On the other hand, the finding of a second younger component also in other high-z samples suggests that the presence of a small percentage of young stars at any epoch which coexist with the passively evolving older stellar bulk of the galaxy could be common in ETGs. In fact, it is known that ETGs contain small fraction of cold molecular gas that could be converted in star formation activity and its presence has been observationally detected in the local Universe (Lees et al. 1991 [57], Crocker et al. 2011 [19], Panuzzo et al. 2011 [85]). This minimal gas reservoir, besides having a presumed external origin, could also be due to the stellar mass loss or may be left over from the initial star formation major burst in the earlier epochs. The favoured scenario is that of the cold accretion: it has been shown (Fardal et al. 2001 [27], Keres et al. 2005 [45], Dekel et al. 2006 [22]) that a cold gas mode could be responsible for the star formation in the cosmic history of galaxies and that it can be present, with its filamentary nature and in small quantities, also in spheroidal passive systems where the hot gas mode is dominant. In fact, Keres et al. 2005 show that, from $z \sim 3$ to $z \sim 0$ hot gas mode dominated galaxies, i.e. passive and massive spheroids, can form new stars thanks to small amounts of cold gas, and the involved mass fractions, $< 20\%$ for stellar masses $\log(M_*) > 10.5$, are fully consistent with the detected mass fractions of the younger component in the analyzed sample. In addition, this scenario could be in agreement with the observed inner position of the younger component, as the cold gas stream is assumed to infall towards the centre of galaxy attracted by the main potential well.

Thus, the detected young stellar component in the sample of ETGs analysed in the present work suggests that a star formation activity took place steadily over time during the secular evolution of these galaxies, activated by small gas quantities since $z > 1$.

Chapter 6

Very high stellar metallicity in a massive $z = 1.4$ ETG

In this chapter I present the first determination of *stellar* metallicity and chemical abundance ratios for an individual ETG at high-redshift ($z = 1.426$) in the COSMOS field.

It is known that the chemical composition of the stellar populations is related to their star formation time-scale (Thomas et al. 2005 [116]). Indeed, the abundance of heavy metals with respect to α-elements of the stellar population is tightly correlated with the time delay between Type `I` and Type `II` supernovae, giving a direct probe of the time-scale within which star formation has occurred.

Up to now, this kind of estimate has been attempted only for samples of local galaxies, because at high redshift the available S/N are not high enough for this analysis. Indeed, only few works have experimented a spectral analysis on ETGs at $z > 1$ (Onodera et al. 2012 [81], Jorgensen & Chiboucas 2013 [41]) and they are mostly dedicated to age estimates. In particular, the spectral analysis have been done mostly in the UV band (Cimatti et al. 2008 [17]) and what is still lacking is the analysis in the restframe optical region. Furthermore, measures are usually performed on stacked spectra (that means that all the individual spectra are added together in order to increase the S/N), thus deleting the peculiarities of the single objects. A single-object measurement of the stellar metallicity and chemical abundance of $z > 1.2$ ETGs is missing at the present time. With this work I fill this gap, presenting the first attempt to measure the chemical composition of a $z \sim 1.4$ ETG that is in the early stages of its evolution.

This analysis is based on observations obtained with the X-Shooter instrument at the VLT, which, as described in Sec. 4.3, provides a spectrum at high (R > 5000) spectral resolution, covering from the UV to the near-IR wavelength range; and the used method to derive the metallicity estimate, is the measurement of the values of several spectral absorptions tracing chemical species, in particular Magnesium and Iron, besides determining the D4000. In particular, the most solid indication of the stellar metallicity is derived by the value of the metallicity-dependent index Mg_b (see

Table 6.1: COSMOS-307881. Data derived from the analysis of Onodera et al. 2012 [81]: K-band magnitude in Vega system (K_s); spectroscopic redshift (z_{spec}^{ONOD}); stellar population age (Age_{phot}) and logarithm of the stellar mass ($\log\mathcal{M}_*$) derived from SED fitting assuming a Chabrier IMF [12]; effective radius (R_e); degree of compactness ($C=R_e/R_{e,z=0}$). Units of right ascension are hour, minutes and seconds, and unites of declination are degrees, arcminutes and arcseconds.

ID	RA	DEC	K_s (Vega)	z_{spec}^{ONOD}(*)	Age_{phot} (Gyr)	$\log\mathcal{M}_*$ ($M_\odot$)	R_e (kpc)	C
307881	10:02:35.64	02:09:14.36	17.59	1.4290±0.0009	3.50	11.50	2.68±0.12	0.32

(*)This work: $z_{spec} = 1.426 \pm 0.001$

Sec. 2), whose strong depth, together with the relatively strong Hβ absorption, is reproduced only assuming models at high metallicity and characterized by [α/Fe]> 0.

The global analysis of all the measured indices, as described in the following sections, reveals a $4^{+0.5}_{-0.8}$ Gyr old stellar population, with a stellar metallicity of [Z/H]= $0.61^{+0.06}_{-0.05}$ and [α/Fe]= $0.45^{+0.05}_{-0.19}$. These properties suggest that this galaxy formed its stars at $z_{form} > 5$ within a short time scale ~ 0.1 Gyr, passively evolving at least in the first 4 Gyr of life.

6.1 The target and the spectroscopic data

The target of this analysis is COSMOS-307881, a bright and massive ($> 10^{11}$ $M_\odot$) ETG from the K-selected galaxy catalog in the COSMOS (Cosmological Evolution Survey) field (McCracken et al. 2010 [76]). It is one of the 12 galaxies with K_s(Vega) < 17.7 selected on the basis of three criteria (Mancini et al. 2010 [66]): *(i)* non-detection at 24 μm in the *Spitzer*+MIPS data; *(ii)* visual elliptical morphology (see Fig. 6.1, top panel); *(iii)* multicolor Spectral Energy Distribution (SED) consistent with old and passive stellar populations with no dust reddening. All the available information on this object are shown in Table 6.1. Further details can be found in the works of Mancini et al. 2010 [66] and Onodera et al. 2012 [81].

From these two studies it can be inferred that the target is an old and slightly compact ($R_e \sim 0.3\ R_e^{z=0}$, w.r.t. the local size-mass relation) ETG, and most of its mass is composed by a passively evolving stellar population.

The spectroscopic observations were carried out with the X-Shooter spectrograph on the VLT/UT2 in Italian guaranteed time during the nights $9-10$ February 2011, (program: 086.A-0088(A)). The target has been observed under bad sky condition (seeing $> 2''$) during the first night (about 1.7h for the VIS and UVB arms and about 1.9h for the NIR arm), while during the second night more than 4 hours of target exposure have been collected under good sky conditions (seeing $\sim 0.8''$). Only the latter set of observations were considered for the analysis. The use of the $1''.0$ slit in the UVB arm and $0''.9$ slit in the VIS and NIR arms, resulted in a spectral resolution of 5100, 8800 and 5600 in the UV, VIS and NIR respectively.

The data reduction has been performed taking advantage of the ESO pipeline (Goldoni et al. 2006 [34]) regarding the first steps of the process, and completed by means of `IRAF` tools. In Fig. 6.1 the reduced monodimensional spectrum of 307881 (black line) is shown in comparison with the photometric points (cyan diamonds) and with an example of the stellar population model of Maraston and Strömbäck 2011 [72] based on MILES (Sanchez-Blazquez et al. 2006 [100]) stellar library (as described in Sec. 3.4) of a 4 Gyr Simple Stellar Population (SSP) with super-solar metallicity (Z= 0.04) (red line). Note that this model is the most similar one to the best-fit solution obtained in the following sections for which the SED is available. The original high resolution of the spectrum (e.g. ~ 1 Å in the VIS) has been decreased to match the lower resolution of the models (i.e. ~ 6 Å at $z= 1.4$), that has been used to perform the analysis of spectral indices, that are based on the the MILES stellar library instead of a higher resolution one (e.g. MARCS) to take advantage of the increasing S/N in downgrading the observed resolution. The value of the signal to noise ratio (S/N) obtained in the spectral region around 5000 Å restframe is ~ 7 per pixel.

In order to accustom the reader's eye to the expected appearance of the main spectral absorption lines when observed at a redshift so high as that of the here analyzed galaxy, in Figure 6.2 a synthetic template (upper first panels) that broadly reproduces the observed one (bottom panels) which is adapted to the measured velocity dispersion (second panels), then downgraded to be noisy as the observed spectrum (third panels) and finally compared with the observed (bottom panels). The similarity between the expected and observed absorption features is quite evident.

6.2 Analysis

As a first step, I measured the redshift of 307881 fitting the Mg_b line region, which in the spectrum is the cleanest from the background residuals, as it can be seen in Fig. 6.1 (bottom panel), finding $z= 1.426\pm0.001$. The Mg_b line region has been also used to find a best fitting velocity dispersion estimate, that resulted to be $\sigma = 385 \pm 85$ km/s. The procedure for determining z and σ was a χ^2 minimization process in which the observed spectral region is compared with different models downgraded to different resolutions corresponding to different velocity dispersions ([$120 - 615$ km/s with step 5 km/s), and redshifted in the range [$1.423 - 1.430$] with step 0.0001. The stability of the result has been proved also changing the age and the metallicity of the template used in the fitting procedure.

I then selected some spectral indices (see Sec. 2) whose absorption features are clearly visible in the observed spectrum of 307881, to try to simultaneously derive both the mean age and the metallicity of its stellar population. The selected indices are: D4000 index (Hamilton 1985 [36]), $\mathrm{H}\gamma_F$ (Worthey & Ottaviani 1997 [136]), G4300, Fe4383, Ca4455, Fe4531, $\mathrm{H}\beta$, Fe5015 and Mg_b (Lick/IDS system, Worthey et al. 1994 [135]). In particular, I have already discussed in Sec. 2.2 that the

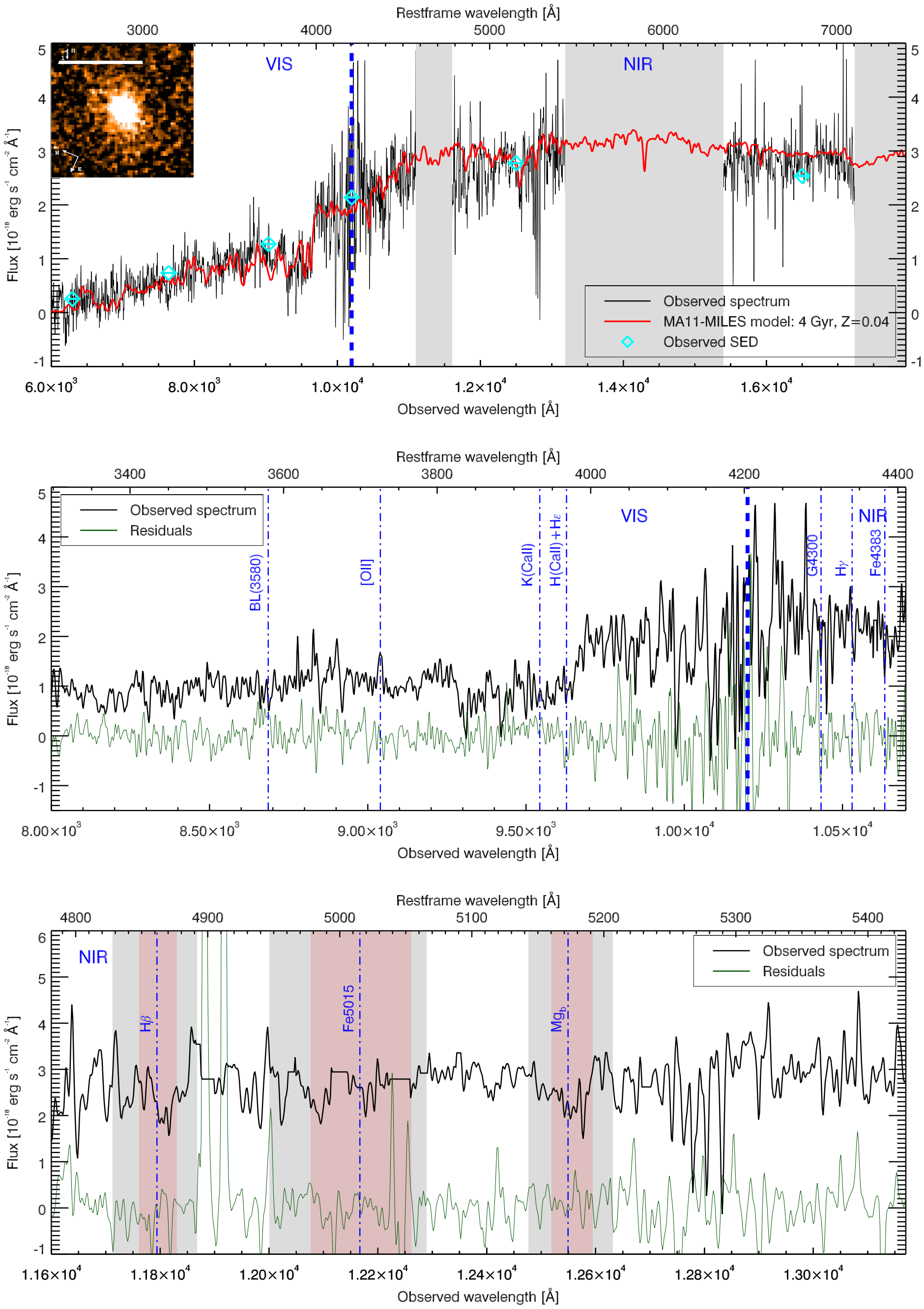

Figure 6.1: COSMOS 307881. The observed spectrum (black line) is shown in comparison with an example of synthetic model of Maraston and Strömbäck 2011 [72] with age of 4 Gyr and super-solar metallicity (Z= 0.04), and with the observed photometric data (cyan diamond). Top panel: VIS and NIR spectral region together with the HST/ACS I-band image of the target. Middle panel: zoom of the 4000 Å restframe region. Bottom panel: zoom of the 5000 Å restframe region. The main absorption (and one emission) lines in each spectral region are highlighted. Dark green lines indicate the residual spectrum.

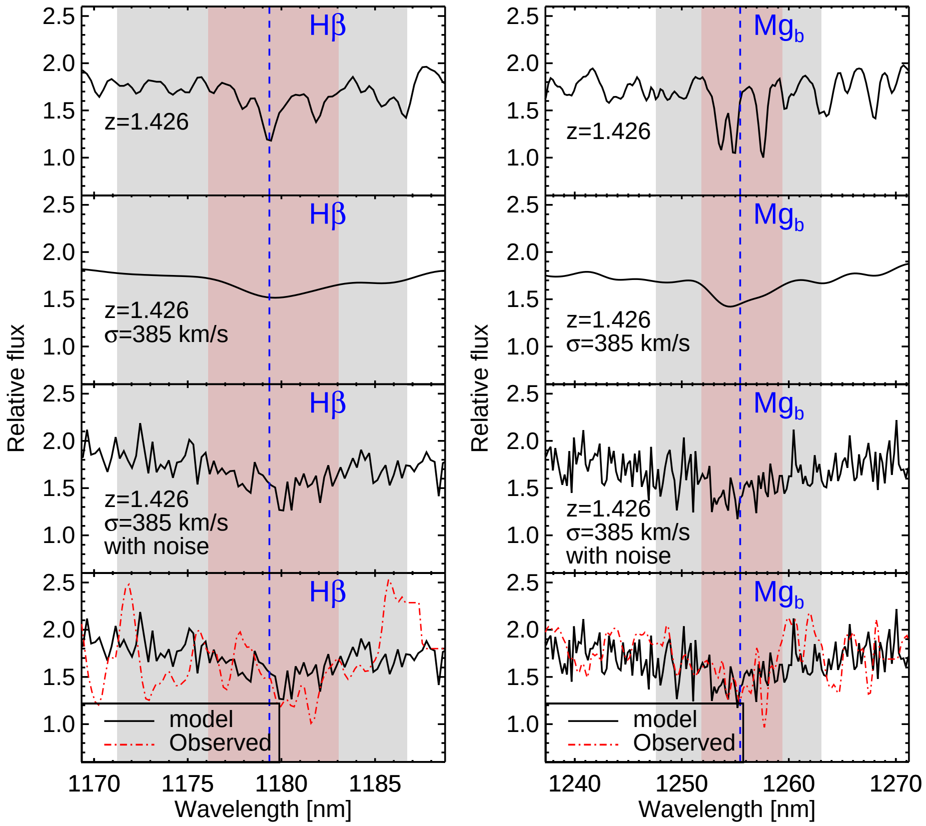

Figure 6.2: Hβ (left panels) and Mg$_b$ (right panels) features in a template of 4 Gyr and 2Z$\odot$ metallicity. First panels: template at $z \sim 1.4$; second panels: template corrected for $\sigma = 385$ km/s; third panels: template downgraded for the observed poissonian noise; fourth panels: comparison with the observed spectrum (point-dashed red line).

Mg$_b$ index is the best *metallicity* and *chemical abundance* dependent index in the region around 5000 Å restframe. In Table 6.2 I report the measured values of the indices together with their errors derived by means of *MonteCarlo* simulations set on the uncertainties in the flux measurements (see Sec.2.4.1 for details on MonteCarlo approach).

Before going on in the analysis, I want to point out the presence of the [OII]3727 emission line (Fig. 6.1, middle panel). It can be excluded that its origin is due to an active AGN, since I do not see any other AGN signature in the observed wide spectral window. Indeed, as it can be noticed from Fig. 6.2 left panels, it is highly unlikely that the Hβ feature is affected by emission as it should be if some residual star formation was on-going in the galaxy, considering also that its value suggests a stellar population age in good agreement with that derived by the Hγ and D4000 index. The most probable explanation of such an emission, is that it is caused by

Table 6.2: Measured indices values.

Index	value
D4000	2.44 ± 0.12
D_n4000	2.42 ± 0.17
$H\gamma_F$	-1.56 ± 0.92
G4300	6.52 ± 1.12
Fe4383	7.40 ± 1.74
Ca4455	1.06 ± 0.83
Fe4531	3.20 ± 1.40
$H\beta$	2.52 ± 0.93
Fe5015	3.89 ± 1.91
Mg_b	5.75 ± 0.81

the UV ionizing emission of old stars in post main-sequence phases (Yi & Yoon 2004 [138]), as confirmed by UV indices. Furthermore, a strong contribution from SF can be excluded.

In Fig. 6.3 I show the Hβ index as a function of the Mg$_b$ index, that is a metallicity indicator as I discussed in the previous sections. I compare it with the predictions of the SSP of TMJ models (Thomas et al. 2011 [118]) based on the MILES library for a wide range of ages (from 0.1 Gyr to 4 Gyr, considering the age of the Universe at $z\sim$ 1.4), for super-solar metallicities [Z/H]= 0.35 (red lines) and [Z/H]= 0.67 (cyan lines), assuming a Salpeter initial mass function (IMF), and corrected for the measured velocity dispersion value of $\sigma = 385 \pm 85$ km/s. As it can be seen, the extreme value of the Mg$_b$ index fully requires high metallicity models up to [Z/H]= 0.67. In particular, in Fig. 6.3 the model expectations for these indices are reported also in case of non-solar values of the α-enhancement [α/Fe], from 0.3 to 0.5 (dashed and dotted lines respectively). Models corresponding to abundances characterized by extreme values of [α/Fe]> 0.5 better reproduce the observed feature with respect to those with solar abundances.

Hints on such extreme values of metallicity, come also from considering the values of all the other Lick indices measured on the spectrum. Indeed, as it can be noticed in Fig. 6.4 where G3400, Hβ and Fe4383 (upper, middle and bottom panel respectively) as a function of D4000, all the measured indices are in agreement pointing toward very-high metallicity values ([Z/H] $\sim$ 0.67, cyan lines) being only marginally consistent with the 2Z$_\odot$ values ([Z/H] $\sim$ 0.35, red lines).

Notice that the highest metallicity models in Thomas et al 2011 [118] are partly in extrapolation, as they are sampling the edge of the parameter space in terms of the available empirical fitting functions for such extreme stellar parameters (see Johansson et al. 2010 [39]). At the same time, the underlying stellar tracks are based on real calculations (see Maraston et al. 2003 [68] for details).

More quantitatively, I have computed the best fitting solution obtained compar-

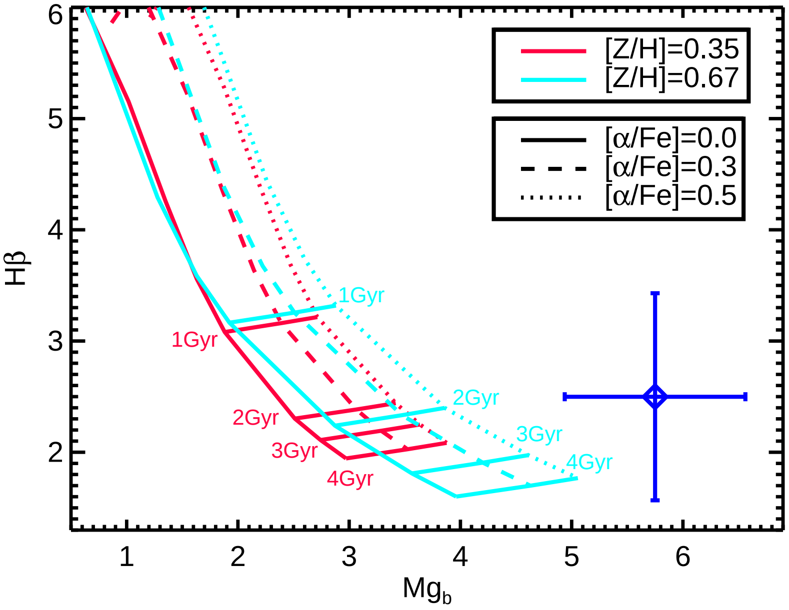

Figure 6.3: Hβ versus Mg$_b$ plot. Comparison between the measured indices and TMJ models. Ages run from 0.1 − 4 Gyr; super-solar metallicities: [Z/H]= 0.35, 0.67 (red, cyan lines); α-element abundances: [α/Fe]= 0.0, 0.3, 0.5 (solid, dashed, dotted lines). The measured values are shown with a blue diamond. Indices values of models are corrected for the measured value of $\sigma = 385$ km/s.

ing all the 9 observed indices values (Table 6.2) with models. The free parameters were the age (0.1 − 4.5, truncated at the age of Universe, with step 0.1 Gyr)[1], the total metallicity (from [Z/H]= −2.25 to [Z/H]= 0.67, with step 0.01) and the α-enhancement (from [α/Fe]= −0.3 to [α/Fe]= 0.5, with step 0.01). The minimum χ^2 value resulted for a stellar population with age of $4.0^{+0.5}_{-0.8}$ Gyr, metallicity [Z/H]= $0.61^{+0.06}_{-0.05}$ and [α/Fe]= $0.45^{+0.05}_{-0.19}$, with $\chi^2 = 0.7$ and an associated probability $\sim 70\%$. Errors indicate the range values of these parameters over all the solutions associated to probabilities larger than 65%. The distributions of the 3 fitting parameters, displayed in different χ^2 ranges, are shown in Fig. 6.5, top panel. A global picture of the χ^2 values can be seen in Figure 6.6 where the minimum χ^2 trends of the 3 parameters of all solutions are shown. It is easy to notice that ages < 2 Gyr can be completely excluded due to the rapid increasing of their χ^2 values toward younger ages. Instead for ages > 4.5 (limit of the Universe age, not shown here) the χ^2 values remains practically constant.

Furthermore, it is found that all models with $Z \leq Z_\odot$ provide a fit of the free

---

[1] Note that I have performed the analysis using all available model ages (up to 15 Gyr) thereby ignoring the age of the Universe as a constrain. However, as no particular improvement was noticed in the derived quantities, I decided to focus on ages within the age of the Universe at $z \sim 1.4$

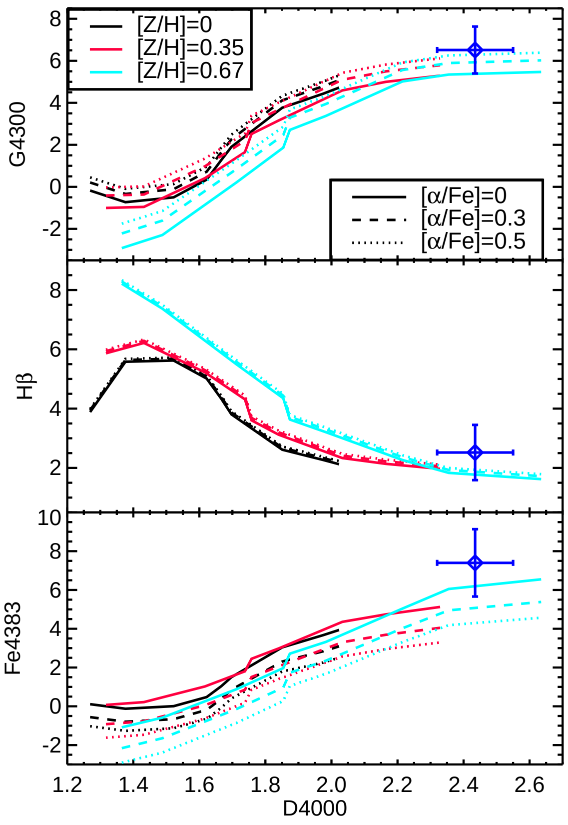

Figure 6.4: Comparison between 4 measured indices (G4300, Hβ and Fe4383 versus D4000) and TMJ models. Ages run from $0.1-4$ Gyr, metallicities from [Z/H]= 0, 0.35, 0.67 (black, red, cyan lines), and α-element abundances from [α/Fe]= 0, 0.3, 0.5 (solid, dashed, dotted lines). The measured values are shown with a blue diamond. Indices values of models are corrected for the measured value of $\sigma = 385$ km/s.

parameters with a probability less than 0.1%.

I also verified the strength of this result by repeating the same fitting process selecting smaller and different set of indices, finding very similar solutions with respect to the previous ones based on the whole set of indices. Two examples are shown in Fig. 6.5, middle and bottom panels: the distributions of the fitting solutions are obtained from two sub-sets of indices *(i)* D4000, G4300, Hγ, Fe4383, Hβ, Fe5015 and Mg$_b$ and *ii)* D4000, Hγ, Hβ and Mg$_b$) which lead to a best-fit solution of *i)* age= 4.0 Gyr, [Z/H]= 0.61 and [α/Fe]= 0.44 with $\chi^2 = 0.9$, and *ii)* age= 4.0 Gyr, [Z/H]= 0.60 and [α/Fe]= 0.5 with $\chi^2 = 0.5$, both totally consistent with the all-indices one.

I also evaluated the feasibility of this analysis on this low S/N spectrum, in particular as far as the metallicity and α-enhancement estimates, by repeating it on a set of 500 mock spectra built on a model spectrum characterized by the obtained best-

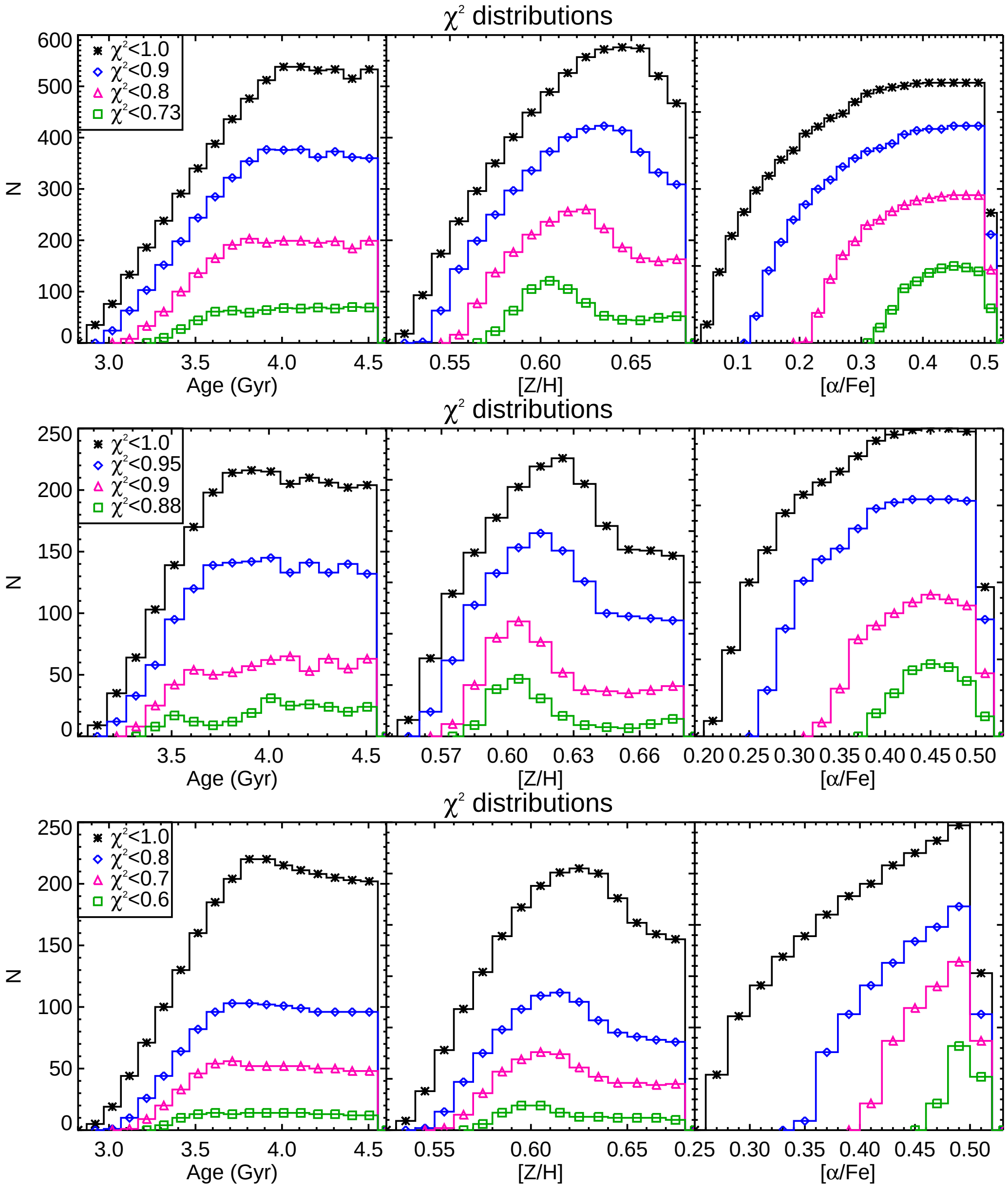

Figure 6.5: Fitting-solutions distributions of age, metallicity and α-enhancement. Colours and symbols indicate solutions in different χ^2 ranges, e.g. green squares include the most probable solutions. Top panel: distributions obtained from the all-indices analysis; middle panel: distributions obtained from a sub-set of indices: D4000, G4300, Hγ, Fe4383, Hβ, Fe5015 and Mg$_b$; bottom panel: distributions obtained from a sub-set of indices: D4000, Hγ, Hβ and Mg$_b$.

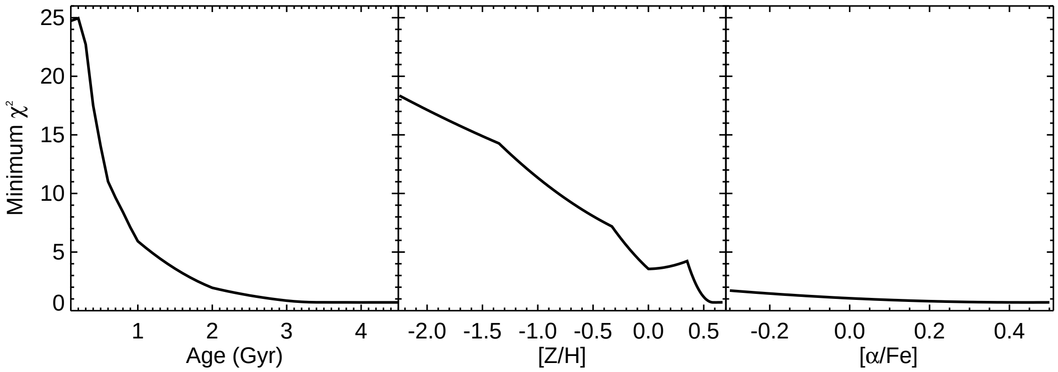

Figure 6.6: Trends of minimum χ^2 for age, [Z/H] and [α/Fe] of all obtained solutions. In particular, ages < 2 Gyr can be completely excluded due to the rapid degrade of χ^2 towards younger ages.

fit parameters (Table 6.3) of the observed one and downgraded with the poissonian observed noise. The obtained distributions of [Z/H] and [α/Fe] are shown in Fig. 6.7. They all peak around the true original values (red vertical lines) demonstrating that within the declared errors the obtained values are solid.

Furthermore I tested if the large error on the velocity dispersion could affect these results by performing the same analysis assuming $\sigma = 300$ km/s, and I found the same best-fit solution (4.1 Gyr, [Z/H]= 0.6, [α/Fe]= 0.41 with $\chi^2 = 0.6$).

Finally, in order to test the model dependence of this result, I repeated the same analysis adopting the Bruzual & Charlot 2003 [7] models (BC03). These models do not include the [α/Fe] parameter, hence I shall use them to constrain age and total metallicity solely. The BC03 models cover a slightly lower Z range with respect to TMJ models, and are based on different stellar evolutionary tracks. The BC03 best-fit corresponds to age 4.5 Gyr and metallicity [Z/H]= 0.4 that is in fact the maximum available value in this set of models. Hence the result of a high-age and high-Z is not model dependent.

It is important to note the high metallicity is mainly derived as a consequence of the maximum allowed age of 4.5 *Gyr. Should one allow the age to be older than the age of the Universe, the metallicity will decrease, as a result of age/metallicity degeneracy.* Actually, the large error bar of both the indices and of σ prevents a real precise measure of the metallicity, but the peculiarity of such a strong Mg_b absorption band combined with the narrow range of possible ages (due to its redshift), make necessary the assumption of a very high value of the stellar metallicity.

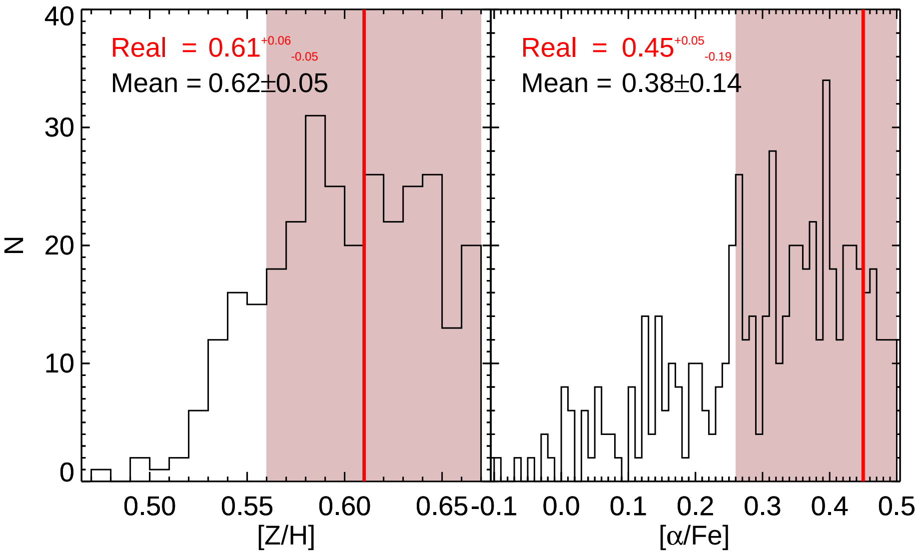

Figure 6.7: Distributions of [Z/H] and [α/Fe] derived for a set of 500 mock spectra built on a model spectrum characterized by the obtained best-fit parameters (Table 6.3) of the observed one and downgraded with the poissonian noise. The 2 distributions are well peaked around the true original values (red vertical lines).

Table 6.3: Results: spectroscopic redshift (z_{spec}) and velocity dispersion (σ) obtained from this spectroscopic analysis; best-fit values of age (Gyr), [Z/H] and [α/Fe].

z_{spec}	σ (km/s)	Age (Gyr)	[Z/H]	[α/Fe]
1.426 ± 0.001	385 ± 85	$4.0^{+0.5}_{-0.8}$	$0.61^{+0.06}_{-0.05}$	$0.45^{+0.05}_{-0.19}$

6.3 Discussion and conclusions

In this chapter I have described a detailed spectroscopic analysis of a z=1.426 ETG, showing strong evidence of its very high stellar metallicity, α-enhancement and age (Table 6.3). All these quantities bring information on the past star formation history experienced by this galaxy. In particular, [α/Fe] is strictly related to the time-scale Δt of the galaxies star formation histories (Thomas et al. 2005 [116]) quantifying the time delay elapsed between the Type II supernovae events, responsible of the formation of α-elements, and the Type I supernovae related to the formation of Fe peak elements. The high value [α/Fe]$\sim$ 0.4 obtained for 307881 is a direct signature that its star formation time-scale must have been short. In particular, adopting the simple theoretical modelling of Thomas et al. 2005 [116], where the star formation is modelled with a Gaussian function, I calculated a star formation time-scale Δt $\sim$ 0.1

Gyr covering the interval within which 95% of the stars were formed. Considering also the old age of its stellar content, this suggests that 307881 formed the bulk of its stars at $z_{form} > 5$ within a short time-scale of Δt $\sim$ 0.1 Gyr and then passively evolved over the following 4 Gyr.

With the high [α/Fe] value suggesting a short star formation time scale of 307881, the clear indication of its extremely high metallicity opens new issues on the gas enrichment history of the Universe. It is worth emphasising that the global integrated metallicity of the local ETGs never reaches values higher than $1 - 2$ $Z_{\odot}$. Indeed, I considered the local sample analysed in Thomas et al. 2010 [117] and quickly verified that the metallicity and [α/Fe] values of 307881 together with its velocity dispersion estimate, are not included in the local distribution of values, even if such high values of Z and [α/Fe] are expected for dense ETGs as suggested by these scaling relations (see a more detailed argumentation of this in Chapter 7). Thus, this indicates that this galaxy must experience mass accretion events (minor merging) from z= 1.4 to z= 0 which will move it on the observed local scaling relations towards lower values of both Z and σ, diluting the extreme metallicity stars and confining them in the central part of the galaxy. Indeed, such extreme metallicity values are in some cases found in the inner core of local massive ETGs (Thomas et al. 2005 [116], Trager et al. 2000 [120], Martin-Navarro et al. 2015 [73]) which are known to show metallicity gradients (La Barbera et al. 2012 [53]). I calculated that adding e.g. 15% of a sub-solar metallicity component, as in the case of dwarf galaxies, to 307881 would decrease the measure of its average metallicity to the local observed values. On the other hand, the gas metallicities up to now measured in z> 3 star forming galaxies result to be solar or subsolar, and do not match at all the high stellar value measured in this target galaxy (Mannucci et al. 2009 [67]) and in the centers of local ETGs (Spolaor et al. 2008 [110]). It is out of the aims of this thesis to suggest a possible explanation of this missing detection of high-z high metallicity gas. A possibility is that the lower gas metallicity comes from dilution through infalling primeval gas, or selective mass loss of metals in galactic winds. At the same time, the estimate of the metallicity of the Broad Line Regions in quasars at z> 4 reveals gaseous metallicities even higher than the stellar one reported here (Juarez et al. 2009 [42]), suggesting the possibility that their enriched gas is involved in the initial star formation events of (at least some) high-z massive proto-elliptical galaxies.

Chapter 7

Individual stellar metallicity measure in $z > 1.4$ ETGs

The stellar population properties, such as age and metallicity, enclose precious information to derive the past formation and evolution of early-type galaxies (ETGs) at each cosmic epoch, from the local Universe to high redshift. The closer we approach the epoch of their early phases of evolution, the more we complete the puzzle of their star formation history, obtaining more direct probes on the precursors of the well known local ellipticals.

Indeed, in the local Universe, where data are easily obtained and analyzed, the stellar properties of old ETGs could have been mixed up by any possible evolutionary event, preventing the possibility to derive their detailed star formation histories. On the other hand, dealing with high redshift data, harder to be obtained and treated, allows to get focused details on the evolutionary status of young ETGs and uniquely permits to cover the gap between their formation and the beginning of later evolutionary events like minor and/or major merging. Moreover, the considerable younger ages of the high-redshift systems (age < 2 Gyr) gives the important advantage of greatly reducing the well-known age-metallicity degeneracy, making the measurements of these two parameters possible even if with low S/N ratios spectroscopic data.

The chemical content of stellar systems is strictly connected with their formation mechanisms from the primordial gas and with the time-scale on which the star formation has taken place (Thomas et al. 2005, 2010 [116], [117], Spolaor et al. 2010 [110], Lonoce et al. 2015 [64]). Moreover, the same information coupled with a precise estimate of the ages of the stellar component can be exploited to understand if natural ageing processes or other evolutionary paths drive the evolution of this class of galaxies.

The stellar population properties, in particular the metallicity, can be efficaciously derived by a detailed spectral analysis exploiting the measurements of spectral indices as it is usually done in the local Universe studies (Thomas et al. 2010 [117], Spolaor et al. 2010 [110]). Up to now, only few pioneering works (Cimatti et al. 2008 [16]; Onodera et al. 2012 [81]; Jorgensen & Chiboucas 2013 [40]; Lonoce et al. 2014 [63]; Gallazzi et al. 2014 [29]; Jorgensen et al. 2014 [41]) have been devoted to the analysis of spectral indices of high-z ETGs, and they are mostly based on the measure of few indices (age estimator), on low resolution data. A way to obtain a solid estimate of the age and metallicity of individual high-z ETGs is to derive the combined measure of many spectral indices on a wide spectral range in order to remove any residual age-metallicity degeneracy and to take into account the contributions from all the stars. In particular, beside the classical optical Lick/IDS system (i.e.: Hγ, Hβ, Mg$_b$, etc..), newly explored spectral indices in the UV region (i.e.: MgI, MgII, Mg$_{wide}$, BL3096, BL3580, etc...) can be exploited when studying high-z galaxies thanks also to the recent developing of high-resolution models in the UV region (Maraston et al. 2009).

In the work of Chapter 6 I estimated for the first time the stellar metallicity and the α/Fe abundance ratio of an individual ETG at $z > 1.4$ in the COSMOS field thanks to the measure of many spectral indices, in particular in the optical band (e.g. Mg$_b$). In this chapter I complete the analysis adding new clues on COSMOS-307881 by means of the UV indices, and I extend the determination of the metallicity to a total sample of 4 ETGs at $z > 1.4$.

7.1 The sample

The analyzed sample is composed by the only 4 ETGs in the redshift range $1.4 < z < 2$, selected on the basis of the availability of their X-Shooter spectroscopic data. As well explained in Sec. 4.3, X-Shooter provides wide spectral coverage data, from the UV band to the near-IR one, allowing to deal with many spectral indices. In particular, two objects are in the COSMOS (Cosmological Evolution Survey) field (McCracken et al. 2010 [76]), and the other two have been selected from the UKIDSS-UDS (Ultra Deep Survey) field (Lawrence et al. 2007 [55], Williams et al. 2009 [133]).

In particular, COSMOS-307881 has been already analyzed in the previous Chapter 6 by means of the same spectrum presented in this work, and the other 3 targets, COSMOS-7447, UDS-19627 and UDS-29410 have been already analyzed by means of the same spectroscopic data in the work of van de Sande et al. 2013 ([127] and references therein), where the authors performed the measurement of the velocity dispersion exploiting the high resolution of X-Shooter data. In this work, more detailed information on the spectral analysis of COSMOS-307881 will be discussed, in particular regarding the blue-UV spectral range, and a full description of the stellar population content of the other three galaxies, obtained from the analysis of a wide combination of spectral indices, will be given to complete the available knowledge on this rare and precious high-redshift sample of ETGs.

The 4 ETGs are all bright (K $\lesssim$ 20), massive ($M = 10^{11} M_{\odot}$) and dense objects ($\sigma > 270$ km/s), and their passivity has been checked thanks to the available broadband photometry (van de Sande et al. 2013 [127] and Fig. 7.1-7.4) and will be

Table 7.1: Main information about the sample of ETGs: K-band magnitude in AB system (K); spectroscopic redshift (z_{spec}); logarithm of the stellar mass ($\log\mathcal{M}_*$) derived from SED fitting assuming a Chabrier IMF [12]; effective radius (R_e); observed velocity dispersion (σ). Units of right ascension are hour, minutes and seconds, and unites of declination are degrees, arcminutes and arcseconds.

ID	RA	DEC	K (AB)	z_{spec}	$\log\mathcal{M}_*$ ($M_\odot$)	R_e (kpc)	σ (km/s)
307881	10:02:35.64	02:09:14.36	19.44	1.426	11.50	2.68±0.12	385 ± 85^a
7447	10:00:06.96	02:17:33.77	19.64	1.800	11.27	1.75±0.21	274 ± 51^b
19627	02:18:17.06	-5:21:38.83	20.19	2.036	11.24	1.32±0.17	287 ± 39^b
29410	02:17:51.22	-5:16:21.84	19.36	1.456	11.29	1.83±0.23	355 ± 98^b

^{a} measured by Lonoce et al. 2015.

^{b} measured by van de Sande et al. 2013.

confirmed by this spectroscopic analysis (Sec. 7.2). The regular elliptical morphology has been also carefully verified on the available HST (Hubble Space Telescope) (Szomoru et al. 2010 [112]) or UKIDSS-UDS (Lawrence et al. 2007 [55]) deep imaging. All the information about the sample are listed in Table 7.1: spectroscopic redshift, stellar mass, effective radius and velocity dispersion. For any further information I refer to the work of van de Sande et al. 2013 [127] and Lonoce et al. 2015 [64] (and all references therein).

7.1.1 Spectroscopic data

Observations exploited in this work have been all carried out with the X-Shooter spectrograph on the VLT (see Sec. 4.3). The great advantage of using X-Shooter is that it allows to obtain high-resolution spectra on a very wide spectral range with a single exposure; in particular, it consists of three arms: UVB, VIS and NIR, covering together a wide spectral window from 3000 Å to 24800 Å with a mean resolution $R \sim 6500$.

Recent papers, van de Sande et al. 2013 [127] and Lonoce et al. 2015 [64], have extensively presented the X-Shooter data on which this work is based. In Table 7.2 I just summarize their main characteristics.

The observing strategy for all the observations is the standard division in exposure blocks with an alternated ABA'B' dithering of the vertical source position in the slit. Close to the sources acquisitions, standard stars have been observed during the same nights.

The data reduction has been performed by means of the public `ESOREX` pipeline (Goldoni et al. 2006 [34]) as far as concerning the first steps of the process, while the main procedure has been carried on with the standard `IRAF` tools [140]. More

Table 7.2: .

ID	Period	Exposure time	slit	program ID
307881	February 9th, 2011	4.3h	0".9	086.A-0088(A)
7447	January 22th, 2010	1.8h	0".9	084.A-1082(A)
19627	October, 2009	1h+3h	0".6+0".9	084.A-0303(D)
29410	July, 2010	1.7h	0".9	085.A-0962(A)

[a] measured by Lonoce et al. 2015.
[b] measured by van de Sande et al. 2013.

in details, I relied on the pipeline for the standard calibration steps (correction for bias, dark, flat, etc...), checking the produced output of every single step. Particular care has been given to the identification of the spectral orders, their straightening and the wavelength calibration, where specific hand-made checks have been applied in order to control the pipeline outputs. Furthermore, in each reduction step where the position of the source was involved, I made use of an external code which identified its exact position along the slit with high precision; indeed, the faintness of our high-redshift objects makes difficult their identification over the noisy underlying sky, and the `ESOREX` tools fail to do this identification automatically. During all these first processes of the pipeline, I proceeded following the "stare" mode in order to obtain at the end a single, orders merged, wavelength calibrated, bidimensional spectrum for each observing block. I completed the data reduction by means of `IRAF` performing the sky subtraction, the monodimensional spectrum extraction and its flux calibration. Indeed I verified that the sky subtraction of all the targets was more accurately obtained by means of the `IRAF` tools combined with the possibility to exploit the A-B observing pattern with respect to the `ESOREX` pipeline. The construction of the sensitivity function has been performed starting from the reduced standard stars produced by `ESOREX`.

The reduced spectra of the 4 galaxies can be seen in Fig. 7.1-7.4 (black lines). The three spectral windows coming from the three X-Shooter arms (UVB, VIS and NIR) are connected at $\sim$ 5600Å and $\sim$ 10200Å (vertical dashed blue lines) with the help of the available photometric data (green diamonds). The UVB region of COSMOS-307881 and UDS 29410, due to their lower redshift, did not reveal any non-zero signal, thus it has not been included in the analysis and in Fig. 7.1, 7.4. In the NIR region, all the strong atmospheric absorptions have been masked by means of grey shading. For each galaxy, a representative MS11 model obtained from the analysis described in the following sections is shown (red lines).

In particular, in these figures the observed spectra (black lines) have been downgraded to match the spectral resolution of the models that will be used during the analysis (i.e. models based on the MILES stellar library with a restframe FWHM

= 2.55 Å). This correction is necessary also to gain a higher S/N ratio which is finally resulting within $4-7$ per dispersion element (i.e. 1.8 Å in the UV and VIS arms and 2.0 Å in the NIR arm), depending on the spectral range.

7.2 Analysis

The wide spectral extension of the X-Shooter data (see Sec. 4.3) allows the measurement of many spectral indices in different spectral regions which bring a lot of information about the stellar content of the stellar populations. In particular, thanks also to the high-redshift nature of the galaxies of the analyzed sample, the restframe UV region can be investigated to reveal further hints on their stellar population properties. Therefore, in this analysis, for the first time, it has been possible to put together the information extracted by all the indices not only in the usually analyzed optical restframe region, but also in the newly explored UV band.

All the measured indices values are shown in Table 7.3. Note that not all the indices have been measured for all the objects as the redshift and the spectrum quality (atmospheric absorption regions, telluric residuals, arms connections...) depends on the target. This fact will lead to a specific analysis of each galaxy of the sample, as it will be discussed below. Errors have been derived by means of a Monte-Carlo approach, in which starting from the observed spectrum I simulated many times (> 5000) the effect of the poissonian noise in each spectral region involved in each index, and measuring the corresponding index values to obtain a distribution whose width is identified as the statistical error.

Within the optical band (restframe) analysis, I measured most of the well-known Lick/IDS system indices (Worthey et al. 1994 [135]), following the band-passes definitions proposed by Trager et al. 2000 [120], together with the Hδ and Hγ index definitions by Worthey & Ottaviani 1997 [136]. This widely used set of indices has been revealed to be precious for the investigation of stellar population properties of ETGs both in the local (Longhetti et al. 2000 [60], Poggianti et al. 2001 [92], Thomas et al. 2010 [117]) and medium-z Universe (Jorgensen & Chiboucas 2013 [40], Gallazzi et al. 2014 [29]). Interestingly, thanks to new studies on the chemical abundance dependence of the Lick indices, it has been possible to derive information also on the α-enhancement value of elliptical galaxies stellar populations, that is connected with the time-scale within which the star formation has occurred. In particular, in this work I adopted the models of Thomas Maraston & Johannson 2011 [118] (hereafter TMJ) based on the MILES library (Sanchez-Blazquez et al. 2009 [100]), for the comparison of the measured Lick indices, in order to take advantage of this further element in the stellar population analysis.

Recently, because of the increasing number of available spectroscopic sample of high-redshift galaxies, new sets of spectral features in the blue-UV (restframe) part of the spectrum have been tested and calibrated (Ponder et al. 1998 [93], Maraston et al. 2009 [70]). The UV indices, historically defined by Fanelli et al. 1990 [26] and Davidge & Clark 1994 [21], are good indicators of the age and metallicity of

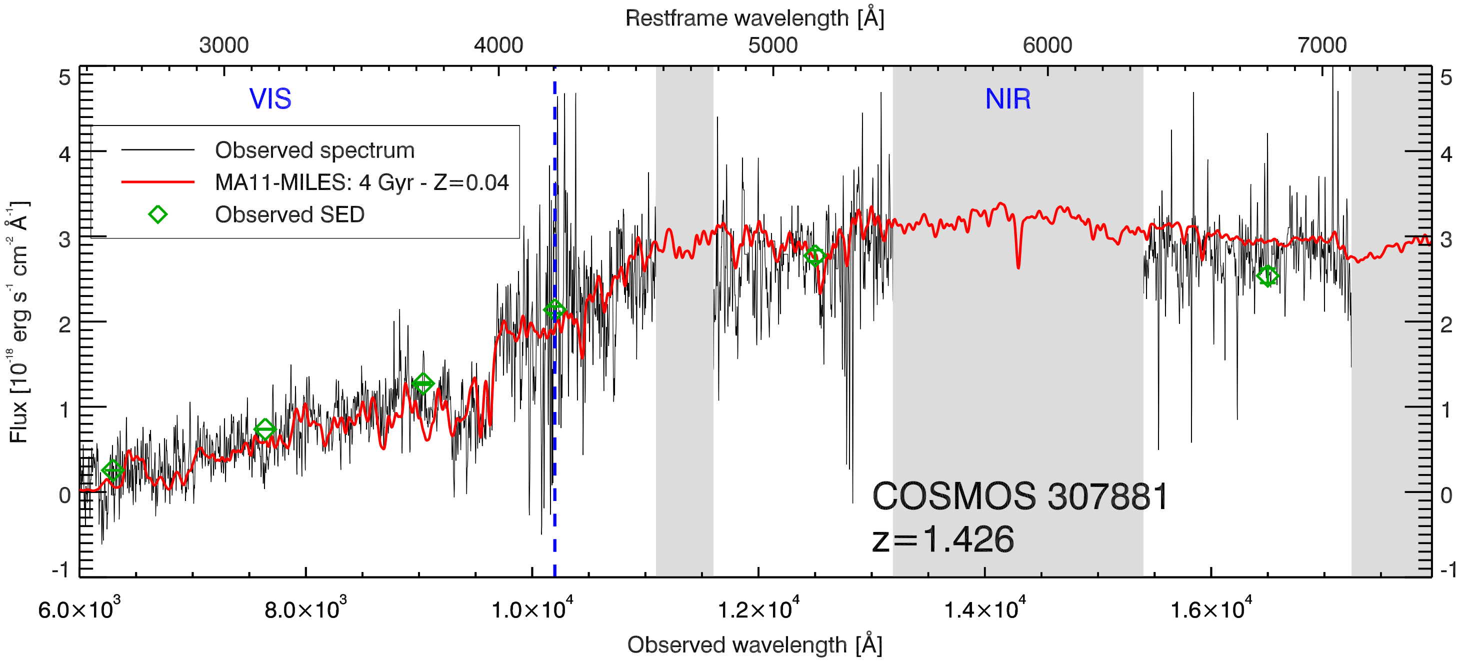

Figure 7.1: Observed spectrum of COSMOS-307881. The observed spectrum (black line) is compared with the available photometric data (green diamonds) and with the representative MS11 model (red lines). Vertical dashed blue lines indicate the connection between UVB-VIS and VIS-NIR arms at ∼ 5600Å and ∼ 10200Å. In the NIR band, the strong atmospheric absorptions have been covered. The spectral resolution of the observed spectrum has been downgraded to match the MS11 one, i.e. FWHM = 2.55 Å restframe.

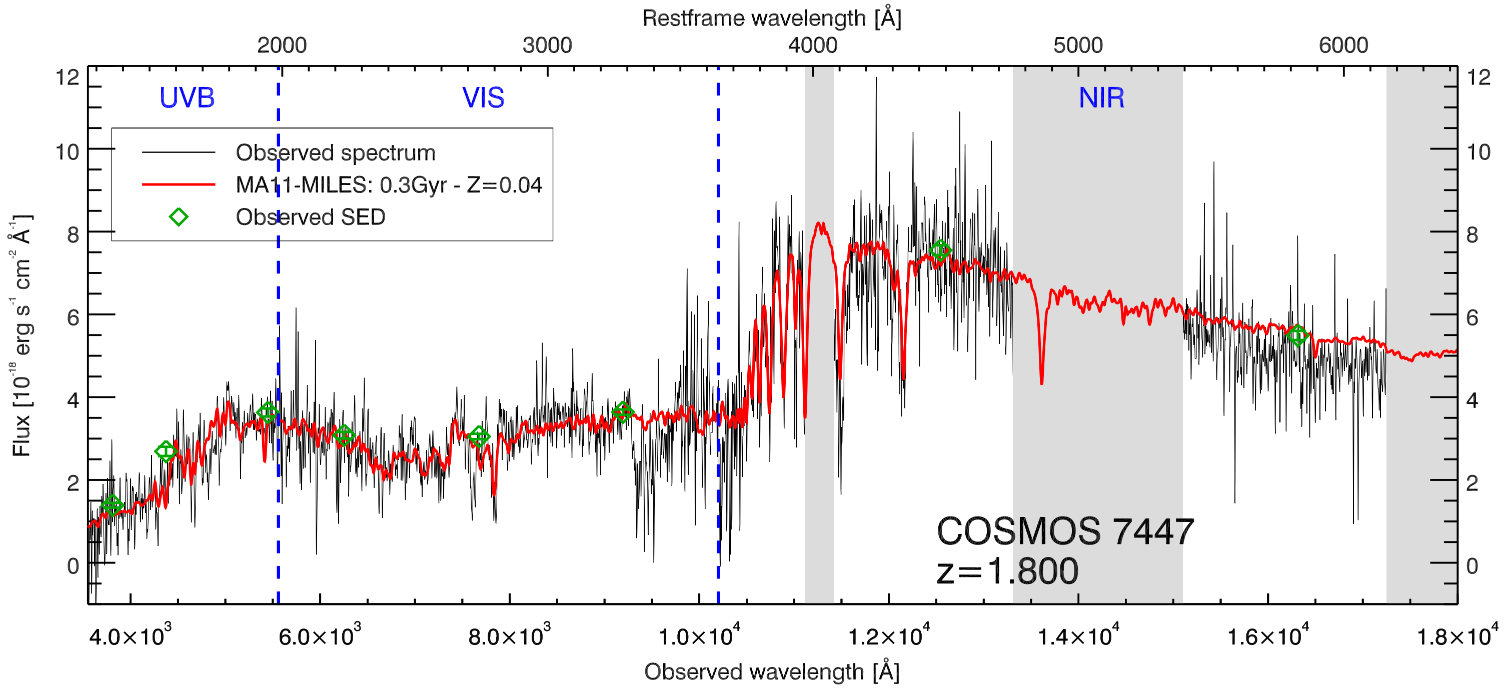

Figure 7.2: Observed spectrum of COSMOS-7447. The observed spectrum (black line) is compared with the available photometric data (green diamonds) and with the representative MS11 model (red lines). Vertical dashed blue lines indicate the connection between UVB-VIS and VIS-NIR arms at ~ 5600Å and ~ 10200Å. In the NIR band, the strong atmospheric absorptions have been covered. The spectral resolution of the observed spectrum has been downgraded to match the MS11 one, i.e. FWHM = 2.55 Å restframe.

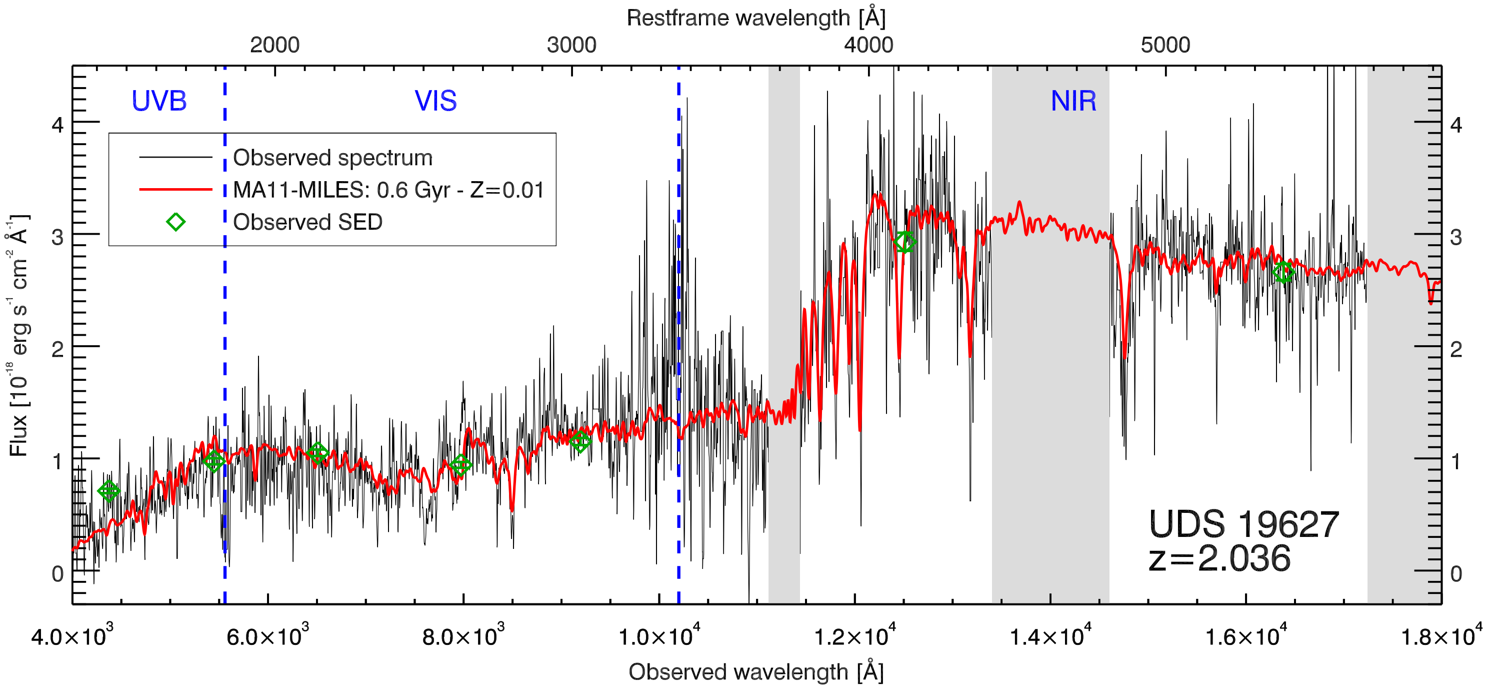

Figure 7.3: Observed spectrum of UDS-19627. The observed spectrum (black line) is compared with the available photometric data (green diamonds) and with the representative MS11 model (red lines). Vertical dashed blue lines indicate the connection between UVB-VIS and VIS-NIR arms at ∼ 5600Å and ∼ 10200Å. In the NIR band, the strong atmospheric absorptions have been covered. The spectral resolution of the observed spectrum has been downgraded to match the MS11 one, i.e. FWHM = 2.55 Å restframe.

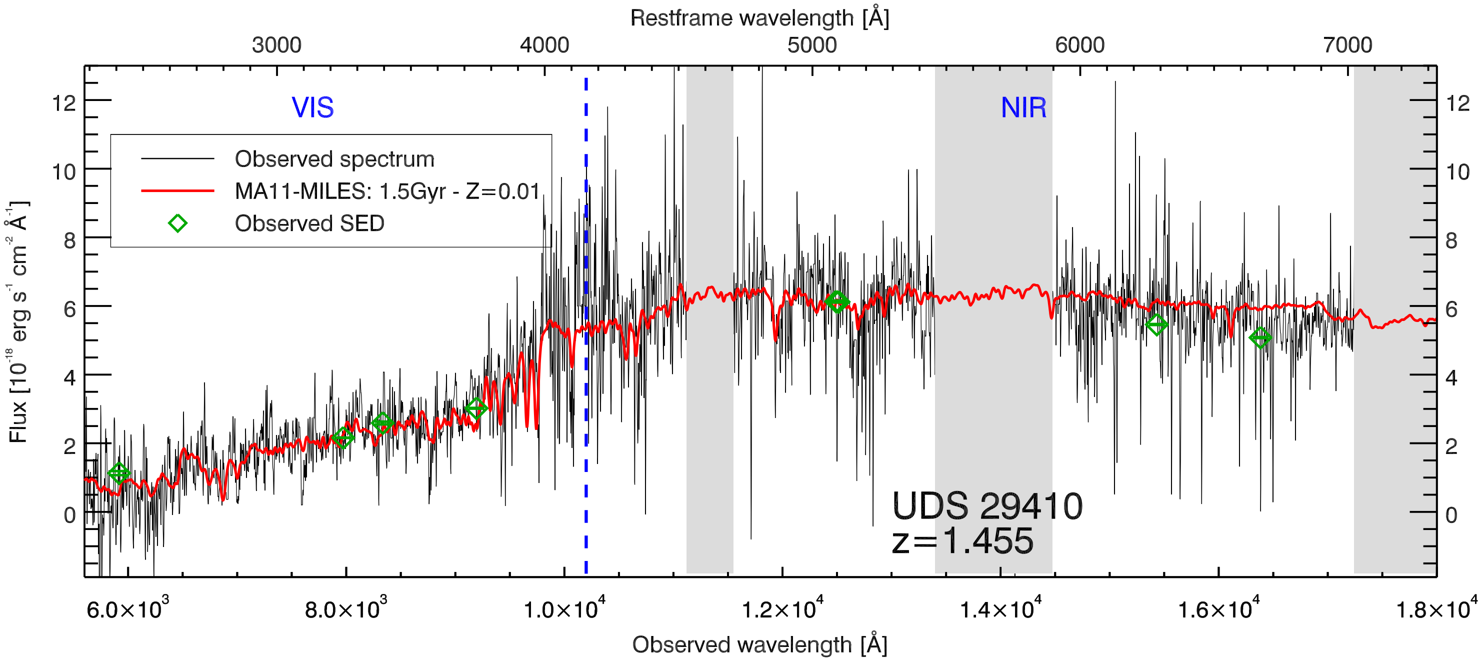

Figure 7.4: Observed spectrum of UDS-29410. The observed spectrum (black line) is compared with the available photometric data (green diamonds) and with the representative MS11 model (red lines). Vertical dashed blue lines indicate the connection between UVB-VIS and VIS-NIR arms at ∼ 5600Å and ∼ 10200Å. In the NIR band, the strong atmospheric absorptions have been covered. The spectral resolution of the observed spectrum has been downgraded to match the MS11 one, i.e. FWHM = 2.55 Å restframe.

Table 7.3: Values of all the measured indices, from the UV to the NIR region, for the 4 ETGs: COSMOS-307881, COSMOS-7447, UDS-19627 and UDS-29410. Blanks mean that the measure of those indices could not be done due to the spectrum quality in that spectral region.

Index	COSMOS-307881	COSMOS-7447	UDS-19627	UDS-29410
BL(1617)	-	-0.224±1.535	4.856±1.781	-
BL(1664)	-	5.112±1.326	4.105±1.880	-
BL(1719)	-	3.846±1.006	-1.071±1.761	-
BL(1853)	-	4.010±1.022	-	-
FeII(2402)	-	5.856±1.246	4.514±2.126	-
BL(2538)	-	4.353±1.301	10.540±1.656	-
FeII(2609)	-	5.460±0.865	6.918±1.259	1.648±3.072
MgII	13.997±2.793	12.397±0.788	13.024±1.283	13.616±2.267
MgI	13.177±2.062	2.501±0.822	3.429±1.278	10.406±1.832
Mg_{wide}	51.407±7.506	19.627±14.523	9.433±3.826	8.786±6.660
FeI(3000)	9.596±3.724	-	3.714±2.760	-
BL(3096)	0.714±1.903	-	-	-
NH(3360)	14.088±1.827	4.380±3.464	-	0.969±2.723
BL(3580)	8.988±1.797	-	-	11.099±2.102
CN(3883)	0.162±0.067	0.067±0.032	-	0.116±0.053
H+K(CaII)	-	0.994±0.370	0.289±0.087	-
D4000	2.435±0.115	1.449±0.063	1.695±0.036	1.747±0.038
D_n4000	2.420±0.117	-	1.434±0.040	1.379±0.042
CN(4170)	-	-0.333±0.034	-0.043±0.034	-
Hδ_A	-	-	4.927±1.263	7.856±1.138
Hδ_F	-	8.985±0.685	4.870±0.869	-
Ca(4227)	-	-0.073±0.566	-0.011±0.742	-
Hγ_A	-	10.675±0.861	8.3684±1.244	6.299±1.431
Hγ_F	-1.559±0.918	7.911±0.535	8.004±0.775	5.220±0.940
G4300	6.515±1.117	-3.916±1.153	0.703±1.310	3.435±1.382
Fe(4383)	7.398±1.737	-1.453±1.453	-	-
Ca(4455)	1.063±0.828	-0.475±0.748	-	-
Fe(4531)	3.199±1.396	1.865±1.194	-	-
Fe(4668)	-	-	-	-
Hβ	2.520±0.931	-	-	2.781±1.176
Fe(5015)	3.886±1.909	-	-5.628±1.676	2.456±2.370
Mg_b	5.750±0.812	-	4.063±0.675	1.624±1.548
Fe(5270)	-	-	1.614±0.762	1.733±1.367
Fe(5335)	-	-	-2.629±1.046	0.855±1.478
Fe(5406)	-	-	-1.156±0.861	-
Fe(5709)	-	0.820±0.775	0.970±0.582	-
Fe(5782)	-	0.923±0.720	-	-

the underlying stellar population, being related to various elements absorptions and blends. However, up to now a complete modelling of the UV indices including also the α-enhancement dependence of each index is not yet available. Consequently, from this set of indices we are able only to give constraints on age and metallicity assuming a solar chemical composition. As far as the UV indices measured in this work I assumed the modelling of Maraston and Strömbäck 2011 [72] (hereafter MS11) based again on the MILES library.

Summarizing the adopted models, I merged the TMJ models with the MS11 models, adopting the former to derive the expectation of Lick indices in the optical band and MS11 for all the other bluer indices. In particular, TMJ models directly provide the indices values at the MILES spectral resolution (i.e. 2.5 Å restframe), while MS11 models provide the whole template SEDs (at the same MILES resolution) on which the measure of the indices can be performed. The consistency of the two models has been already discussed in Maraston and Strömbäck 2011 [72].

The analysis of spectral indices of high-z ETGs must be carefully treated. Indeed, $z > 1.4$ ETGs contain rather young stellar populations (age $\sim 1-2$ Gyr), and at these ages the spectral indices trends with age and metallicity have particular behaviours due to the quick changes in the spectral features of young stars. This is not the case for example of local ETGs analysis, which are old (age $>> 5$ Gyr) and for which indices trends are very stable in their dependence with stellar parameters.

Thus, with the aim of deriving constraints on the stellar age and metallicity of the sample galaxies, a separation between *age*-dependent and *metallicity*-dependent indices must be done, even if, as just stated, these dependences depend on the age of the analyzed stellar population. Indeed, the same index (both UV or optical) can change its sensitivity on stellar parameters depending on the explored ages range.

As an example of this behaviour, in Fig. 7.5, the trends of two indices, one UV index, FeI(3000), and one Lick index, $\mathrm{Mg}_b(5175)$, are shown as a function of the age of the stellar population for 3 different stellar metallicities, subsolar (blue lines), solar (black lines) and supersolar (red lines). From Fig. 7.5 it can be noticed that for ages < 1 Gyr both indices are solid *age*-indicators since the 3 metallicity lines are almost coincident and show an increasing trend with age, while for older ages they become good *metallicity*-indicators.

Moreover, also the measured value of the index itself can be helpful in some cases to discriminate the age or the metallicity of a stellar population, as happened for example in the case of COSMOS-307881 described in Chapter 6 (Lonoce et al. 2015 [64]), where the extremely deep Mg_b absorption feature could be explained only assuming high metallicity values and old ages of its stellar content.

Therefore, the most efficient way to extract information from the many spectral indices I could measure was to operate a single-case analysis for each index and for each object. In details, looking at the peculiar trends of an index, at its measured value and at the redshift of the galaxy, for each object I classified each index as *age*-indicator or *metallicity*-indicator. I have checked that if all the indices are analyzed

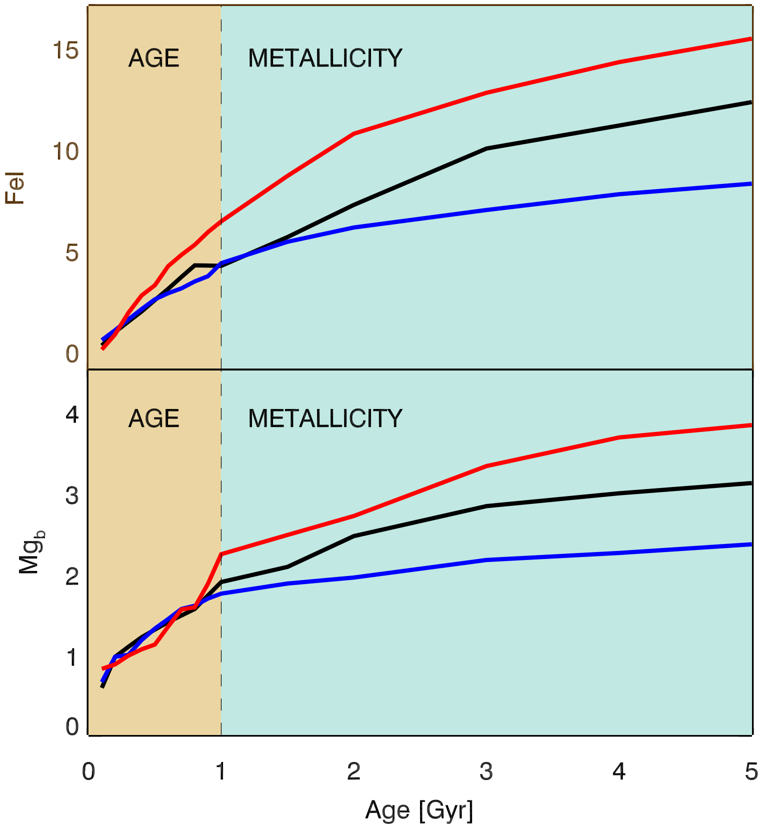

Figure 7.5: Examples of the different trends with age of two representative spectral indices, i.e. FeI(3000) and Mg_b, for MS11 and TMJ models respectively, for different stellar metallicities: subsolar (blue lines), solar (black lines) and supersolar (red lines). For ages < 1 Gyr both indices are solid *age*-indicators since the 3 metallicity lines are almost coincident, while for older ages they become good *metallicity*-indicators given the spreading of the lines.

together without taking into account their own peculiarities, the results would be less constrained (i.e. with larger uncertainties) since residuals of the age-metallicity degeneracy are left. A similar effect is also found if a separation between blue indices and Lick indices is adopted: the results point to the same parameters values but the degeneracy is more marked.

In Fig. 7.6-7.12 for each galaxy of the sample the values of only the indices (black cross) used in the final analysis are shown as a function of the most solid age-dependent index D4000 in comparison with the expectations of the stellar population models (coloured lines); MS11 models for blue-UV indices and TMJ models for Lick indices. Some of the measured indices presented in Table 7.3 have been not included in the final analysis because they have been considered not significant due to their large error bar or to their modelling that did not add any useful information.

For the analysis of each single object I proceeded as follows: I firstly compared by means of a χ^2 minimization process the values of the set of *age*-dependent indices with the merged MS11-TMJ models (described above) assuming age from 0.1 Gyr to the limit of the age of the Universe determined by each galaxy's redshift at step of 0.1 Gyr, and metallicity from $[Z/H] = -0.30$ to 0.30 at step of 0.01. The best-fit solution and the distribution of all the fitting-solutions with similar associated probabilities thus provided the indication of the age value of that stellar population with its error. The same process was then repeated with the set of *metallicity*-dependent indices but including the constraint imposed by the previous age analysis, i.e. with ages running only in the range indicated by the *age*-dependent indices, and thus deriving the best fitting metallicity values. All the results are summarized in Table 7.4.

I also repeated all the same procedure excluding the contribution of Balmer lines indices (e.g. Hβ, Hγ, Hδ) in order to verify that eventual residuals of star formation, which could affect these indices, or any younger minor stellar component would not alter the obtained results. As can be seen in Table 7.4, the results obtained in the two cases, with and without the Balmer lines indices, are consistent.

The information on the α-enhancement, characterizing the stellar content of the sample galaxies, can be derived only from the Lick indices using TMJ models. This measurement is still very competitive in the distant Universe and I am aware that with these spectroscopic data only an indicative estimate of this parameter can be obtained. Thus I tried this estimate comparing the set of Lick indices with TMJ models again through a χ^2 minimization process, with age running again from 0.1 Gyr to the limit of the age of the Universe at step of 0.1 Gyr, covering a wide range of metallicities (not explored by MS11 models) from $[Z/H] = -2.25$ to 0.67 at step of 0.01, and with $[\alpha/\mathrm{Fe}]$ values in the range from -0.30 to $+0.50$ at step of 0.01. The obtained results are shown in Table 7.5.

All the results appeared in Table 7.4 and 7.5 will be discussed in the next Sec. 7.3.

A special case is that of 307881 already discussed in Chapter 6 (Lonoce et al. 2015 [64]). In the previous work only the Lick indices have been analyzed and they

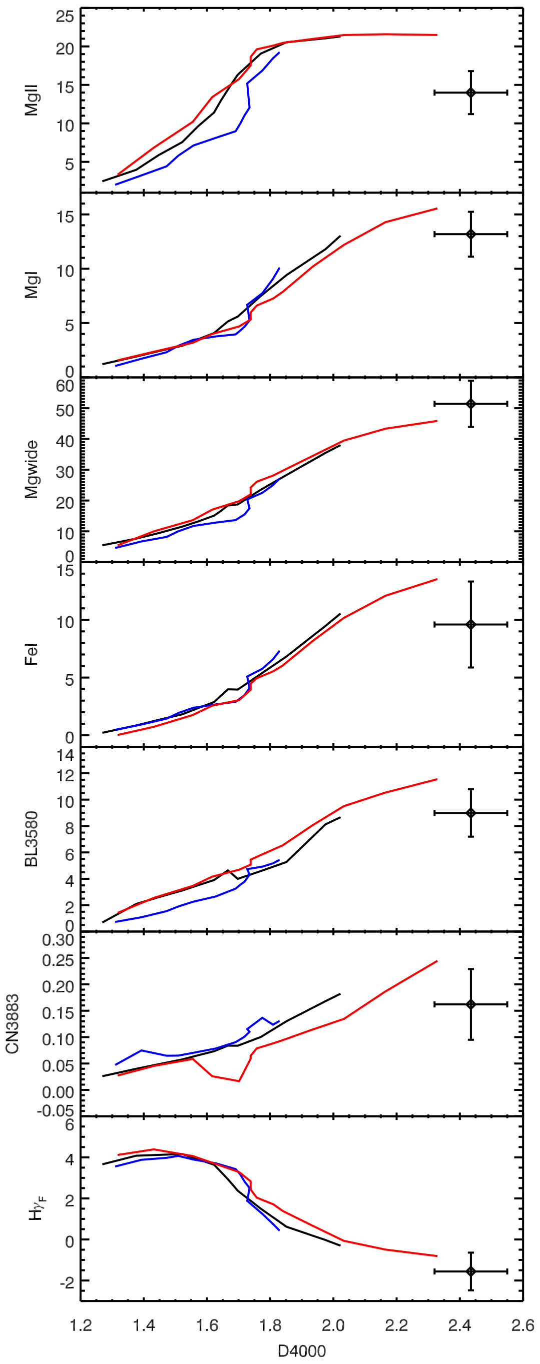

Figure 7.6: 307881. All the used indices (black crosses) as a function of the most solid age-dependent index D4000 in comparison with the expectations of the stellar population models; subsolar metallicity (blue lines), solar metallicity (black lines) and supersolar metallicity (red lines); MS11 models for blue-UV indices and TMJ models for Lick indices. Ages run from 0.1 to 5 Gyr (the limit of the Universe age at this redshift).

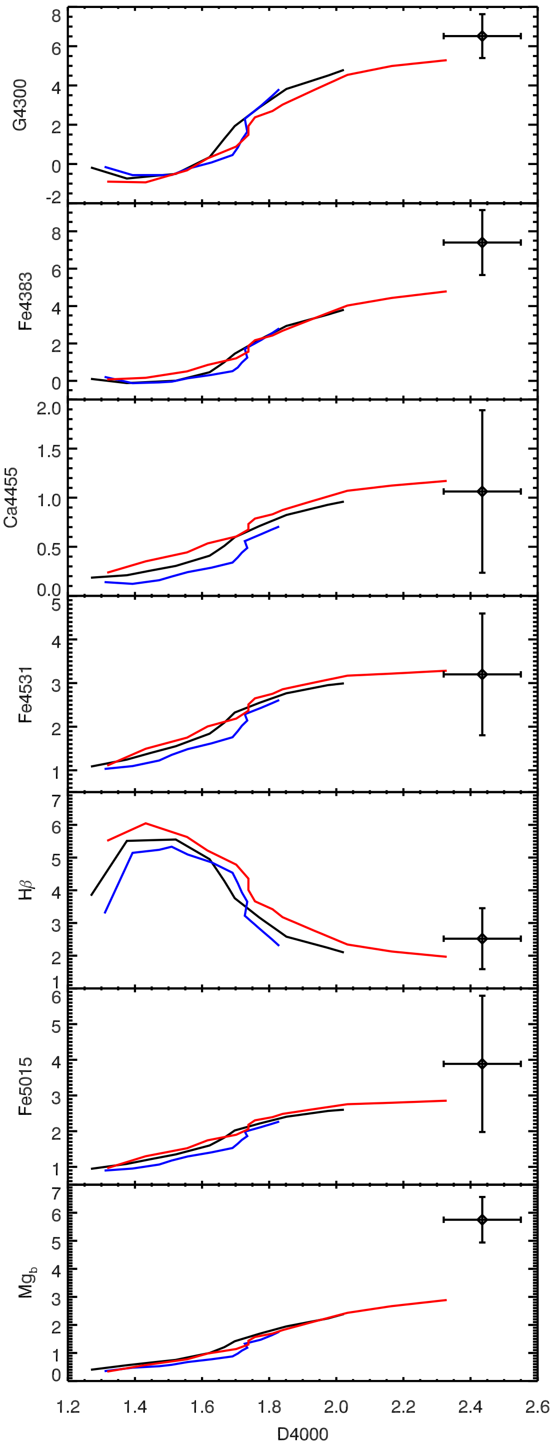

Figure 7.7: 307881. Continued.

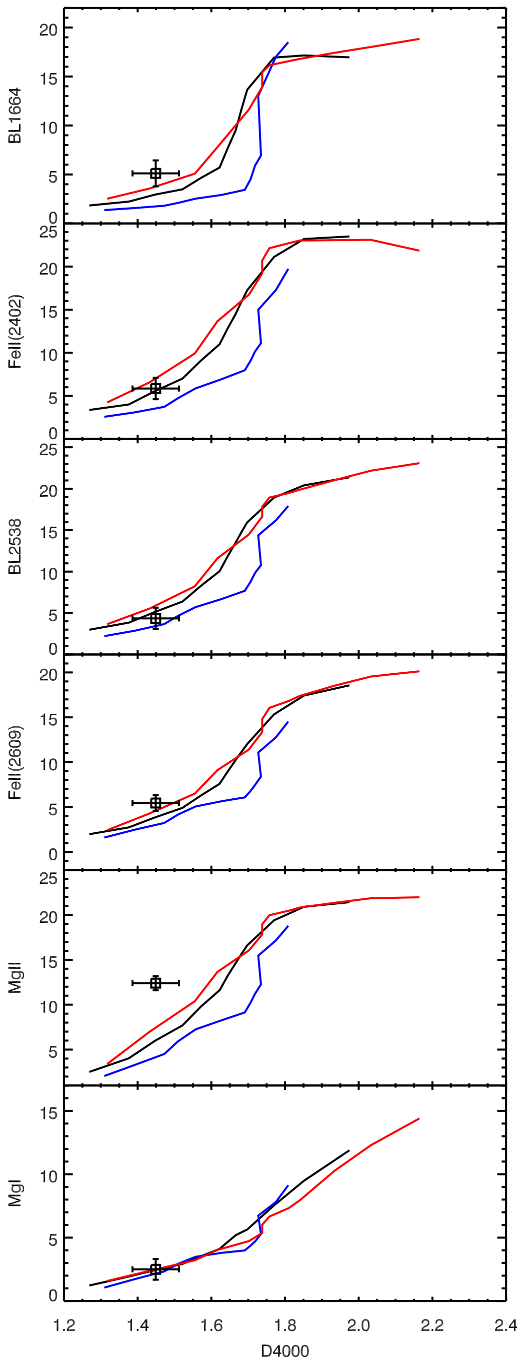

Figure 7.8: 7447. All the used indices (black crosses) as a function of the most solid age-dependent index D4000 in comparison with the expectations of the stellar population models; blue lines are for subsolar metallicity, black lines for solar metallicity and red lines for supersolar metallicity; MS11 models are adopted for blue-UV indices and TMJ models for Lick indices. Ages run from 0.1 to 4 Gyr (the limit of the Universe age at this redshift).

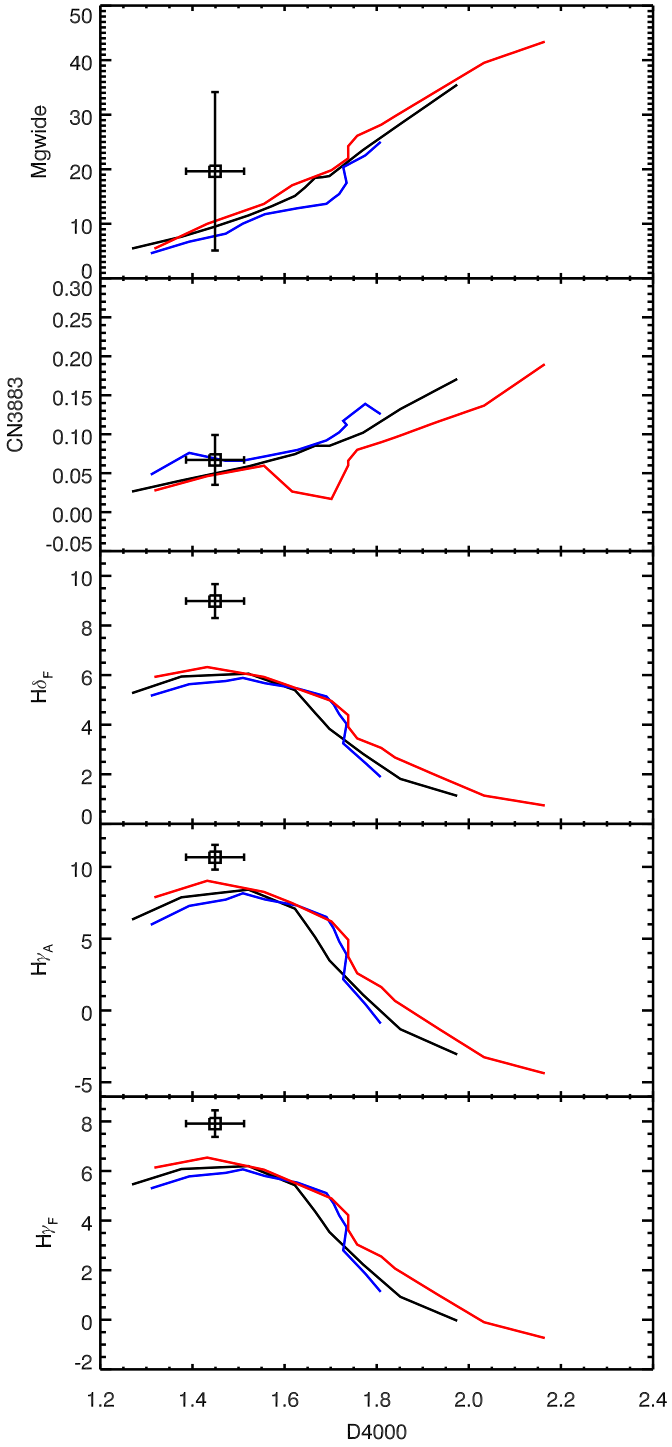

Figure 7.9: 7447. Continued.

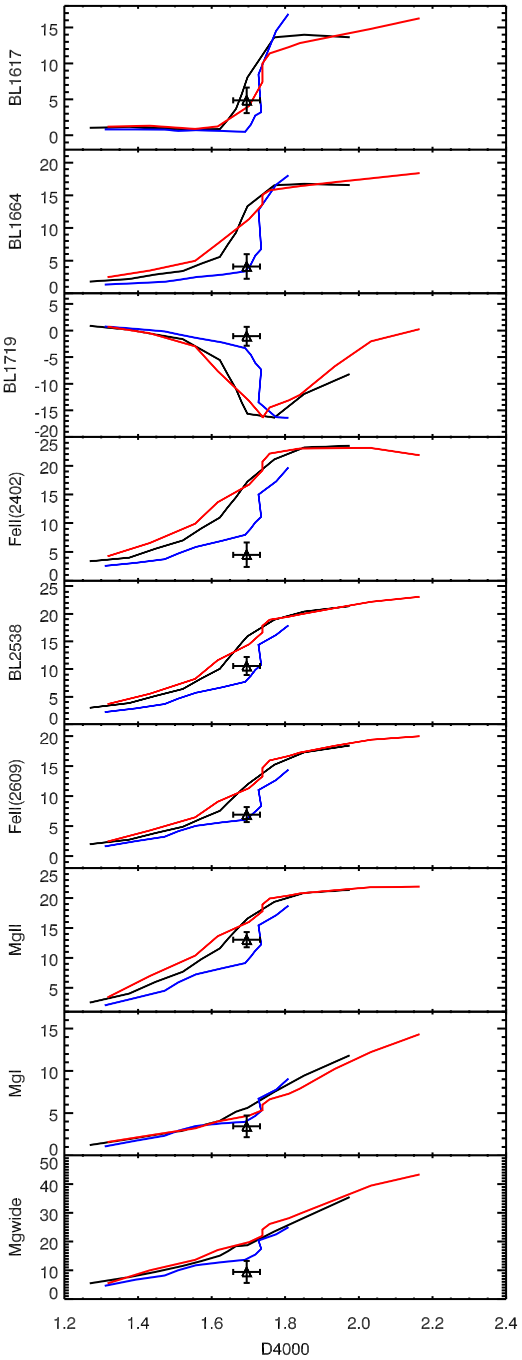

Figure 7.10: 19627. All the used indices (black crosses) as a function of the most solid age-dependent index D4000 in comparison with the expectations of the stellar population models; blue lines are for subsolar metallicity, black lines for solar metallicity and red lines for supersolar metallicity; MS11 models are adopted for blue-UV indices and TMJ models for Lick indices. Ages run from 0.1 to 4 Gyr (the limit of the Universe age at this redshift).

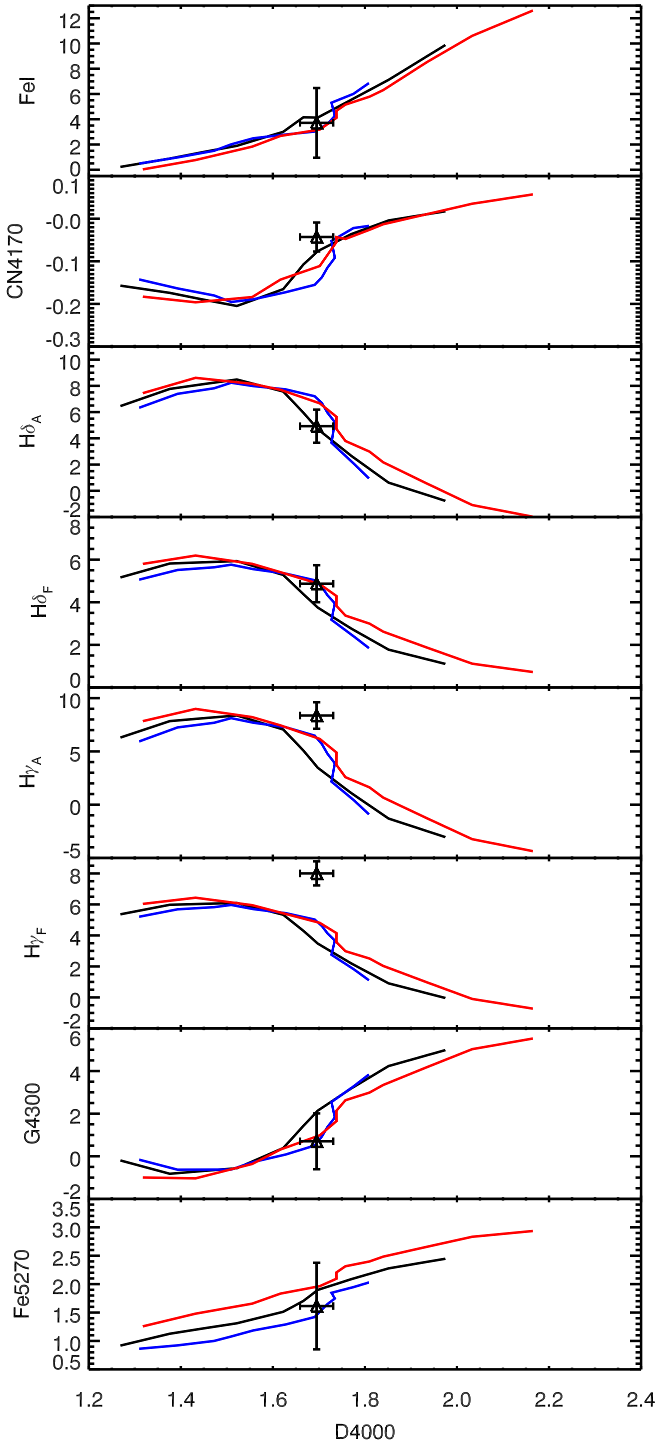

Figure 7.11: 19627. Continued.

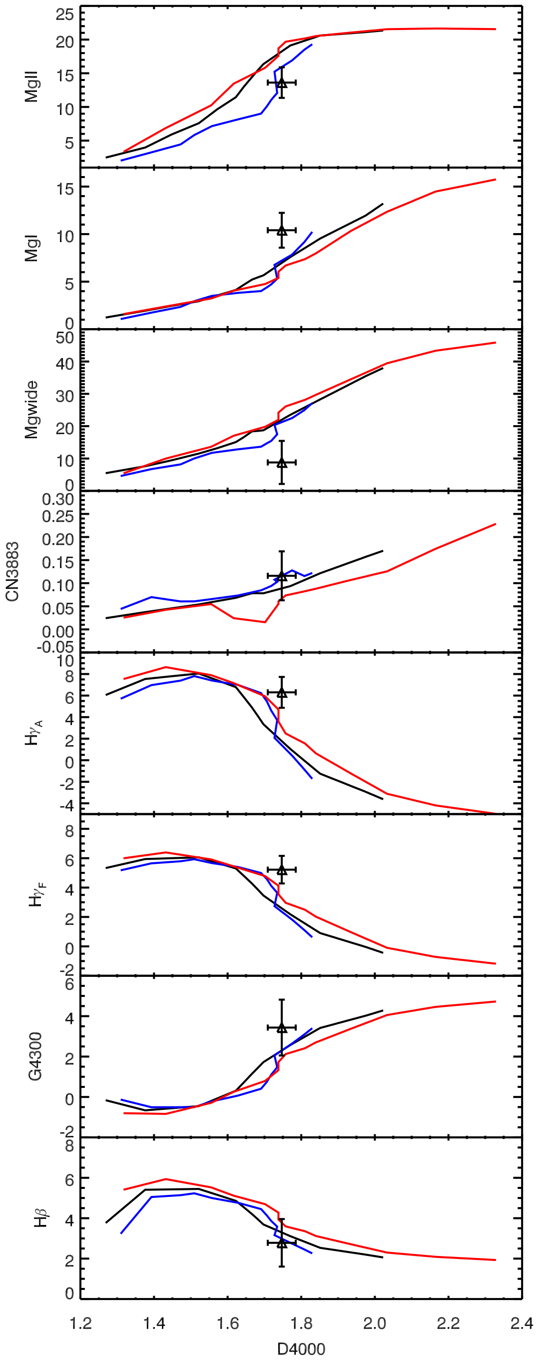

Figure 7.12: 29410. All the used indices (black crosses) as a function of the most solid age-dependent index D4000 in comparison with the expectations of the stellar population models; blue lines are for subsolar metallicity, black lines for solar metallicity and red lines for supersolar metallicity; MS11 models are adopted for blue-UV indices and TMJ models for Lick indices. Ages run from 0.1 to 5 Gyr (the limit of the Universe age at this redshift).

Table 7.4: Results obtained from the separated analysis of the set of *age*-dependent and *metallicity*-dependent indices: best-fit values of age and metallicity with their χ^2 values and associated probabilities. The “NO Balmer” columns refer to the same analysis performed excluding the Balmer lines indices (see text).

ID	Set of used indices	Age (Gyr)	[Z/H]	χ^2	Prob. (%)	Age (Gyr) NO Balmer	[Z/H] NO Balmer	χ^2	Prob. (%)
307881	[CN(3883), D4000, Hβ]	4.1±0.4		0.90	43.83	4.2±0.3		1.17	31.08
	[MgII, MgI, Mg$_{wide}$, FeI(3000), BL(3580), Hγ_F, Gband, Fe(4383), Ca(4455), Fe(4531), Fe(5015), Mg$_b$]		$0.26^{+0.04}_{-0.1}$	2.40	0.43		0.24	2.56	0.31
7447	[MgI, CN(3883), D4000, Hδ_F, Hγ_A, Hγ_F]	$0.2^{+0.2}_{-0.05}$		4.30	0.02	0.3±0.1		0.04	98.88
	[BL(1664), FeII(2402), BL(2538), FeII(2609), MgII, Mg$_{wide}$]		$0.26^{+0.04}_{-0.4}$	4.44	0.02				
19627	[MgI, Mg$_{wide}$, FeI(3000), D4000, Hδ_A, Hδ_F, Hγ_A, Hγ_F, Gband]	0.6±0.1		2.40	1.01	0.7±0.1		0.30	91.40
	[BL(1617), BL(1664), BL(1719), FeII(2402), BL(2538), FeII(2609), MgII, CN(4170), Fe(5270)]		$-0.30^{+0.1}_{-0.0}$	2.69	0.40				
29410	[D4000, Gband, Hβ]	1.8±0.3		0.21	89.20	1.8±0.4		0.30	73.81
	[MgII, MgI, Mg$_{wide}$, CN(3883), Hγ_A, Hγ_F]		$-0.30^{+0.2}_{-0.0}$	2.94	0.71		$-0.30^{+0.1}_{-0.0}$	1.87	11.19

Table 7.5: Results obtained from the analysis of only the Lick indices compared with TMJ models. Thanks to TMJ models, an indication of the [α/Fe] values can be hinted, together with again the age and metallicity.

ID	Set of used indices	Age (Gyr)	[Z/H]	[α/Fe]	Probability (%)
307881	[D4000, Hγ_F, Gband, Hβ, Fe(4383), Ca(4455), Fe(4531), Fe(5015), Mg$_b$]	$4.1^{+0.5}_{-0.8}$	$0.61^{+0.06}_{-0.05}$	$0.45^{+0.05}_{-0.19}$	> 70
7447	[D4000, Hδ_F, Hγ_A, Hγ_F]	$0.3^{+0.2}_{-0.1}$	$-1.92^{+0.3}_{-0.2}$	$0.50^{+0.0}_{-1.3}$	> 70
19627	[D4000, Hδ_A, Hδ_F, Hγ_A, Hγ_F,Gband, Fe(5270)]	$0.7^{+0.3}_{-0.2}$	$-0.82^{+0.3}_{-0.6}$	$-0.18^{+0.2}_{-0.12}$	> 1
29410	[D4000,Gband,Hβ, Hγ_A,Hγ_F]	$1.2^{+0.6}_{-0.7}$	$-0.70^{+0.2}_{-0.3}$	$0.42^{+0.08}_{-0.1}$	> 40

revealed a very metal rich and α-enhanced stellar population, as recalled in Table 7.5. The extended analysis presented here which includes the information brought from bluer indices, confirms the result concerning its old age and high metallicity. However, this wider analysis seems not to require so high values of the metallicity, even if the obtained bestfitting value is very close to the upper modelling limit. In fact, I noticed that some UV indices are not consistent with the proposed models, showing a systematic lower values that a higher metallicity cannot explain. I speculated that probably part of the UV indices are affected by the so-called UV up-turn phenomenon. This hypothesis will be discussed in the next dedicated Subsection 7.2.1.

7.2.1 COSMOS-307881: UV up-turn

It is well known that the emission in the UV region is principally dominated by the hot component of the stellar population contributing to the whole galaxy emission. Generally, the hot component is associated with young stars (age < 1 Gyr) in their early evolutionary phases. However, there is the possibility that also in old stellar populations (age > 1 Gyr) old stars can become UV-bright after a post main-sequence phase of sufficient mass loss (Greggio & Renzini 1990 [35]). This phenomenon is the so-called UV up-turn, recently reviewed by Yi & Yoon [138]. The effect of the UV up-turn on the spectrum shape is clearly visible in the extreme far UV (around $1000 - 2000$ Å), but also many spectral indices in the ~ 2500 Å region are affected by this peculiar emission (e.g. MgII(2800), MgI(2852) and FeI(3000)).

Up to now, this phenomenon is not yet fully understood and its origin is still under debate. One of the most accredited possibilities, proposed by Greggio & Renzini

1990 [35], is that post main-sequence stars with an enough high-metallicity content do increase significantly the opacity in their stellar atmospheres thus causing mass loss during their long horizontal branch phase. Consequently, the internal hotter shells become the responsible of the dominant emission.

Among the 4 analyzed sample, COSMOS-307881 is a good candidate where testing this hypothesis for the UV up-turn. Indeed from the previous analysis we know that this object has an old ($\sim$ 4 Gyr) and very metal-rich stellar population, and we could detect the signature of the UV up-turn within its measured UV indices (see Fig. 7.6 and Table 7.3): a discrepancy between the measured values of some UV indices (e.g. `MgII`(2800), `MgI`(2852) and `FeI`(3000)) and the models previsions has been found and it cannot be explained even assuming higher metallicity values.

Recently, the work of Le Cras et al., in preparation, has explored the population of UV up-turn galaxies (both late-type and ETGs) in a wide sample of galaxies up to $z \sim 0.6$, finding that a significant fraction of the sample (47%) shows the signatures of this phenomenon. In order to reveal the UV up-turn effect, the authors investigated the values of the principal UV spectral indices compared with particular stellar population models which include the mass loss effect in the evolutionary tracks. This modelling, built by the authors for this purpose, is based on the models of Maraston et al. 2009 [70] and the differences with the standard models raise at ages older than 1 Gyr (see Le Cras et al., in preparation, for further details), where the effect of the old stars UV emission starts dominating. I thus exploited this new modelling in the comparison with the 3 UV indices `MgII`(2800), `MgI`(2852) and `FeI`(3000), which are found to be the most sensitive to the UV up-turn effect and at the same time which are the most affected by the observed discrepancy with the standard models (Fig. 7.6).

The comparison is shown in Fig. 7.13, where it is clear that MS11 models are not able to cover the measured values of these 3 UV indices in COSMOS-307881, for any of the explored metallicities (subsolar are blue lines, solar are black lines and supersolar are red lines). In particular for `MgII`(2800) and `MgI`(2852), I also verified if a high value of the α/Fe ratio as the one that seems to characterize this galaxy could help explaining the detected discrepancy: dashed lines indeed are the previsions of an α-enhanced stellar population with $[\alpha/\text{Fe}]= 0.3$ derived applying to the indices values the expected variations due to α-enhancement as the ones calculated for the Mg optical values. Indeed, it is worthy to note that up to now models with the contribution of the α-enhancement in the UV region are not yet available. From both upper and middle panels of Fig. 7.13 it can be seen that the increasing of $[\alpha/\text{Fe}]$ value cannot contribute to explain the measured indices values. Only the UV up-turn models (with solar metallicity), green-crossed lines, are able to get closer in the direction of the observed values and to explain the stellar content of this object, even if their expected values do not totally cover the observed ones. This is due to the up to now lack of up-turn models with supersolar metallicity values, which we know they would be more suitable for this object.

Obviously, I cannot claim that this object certainly shows the UV up-turn ef-

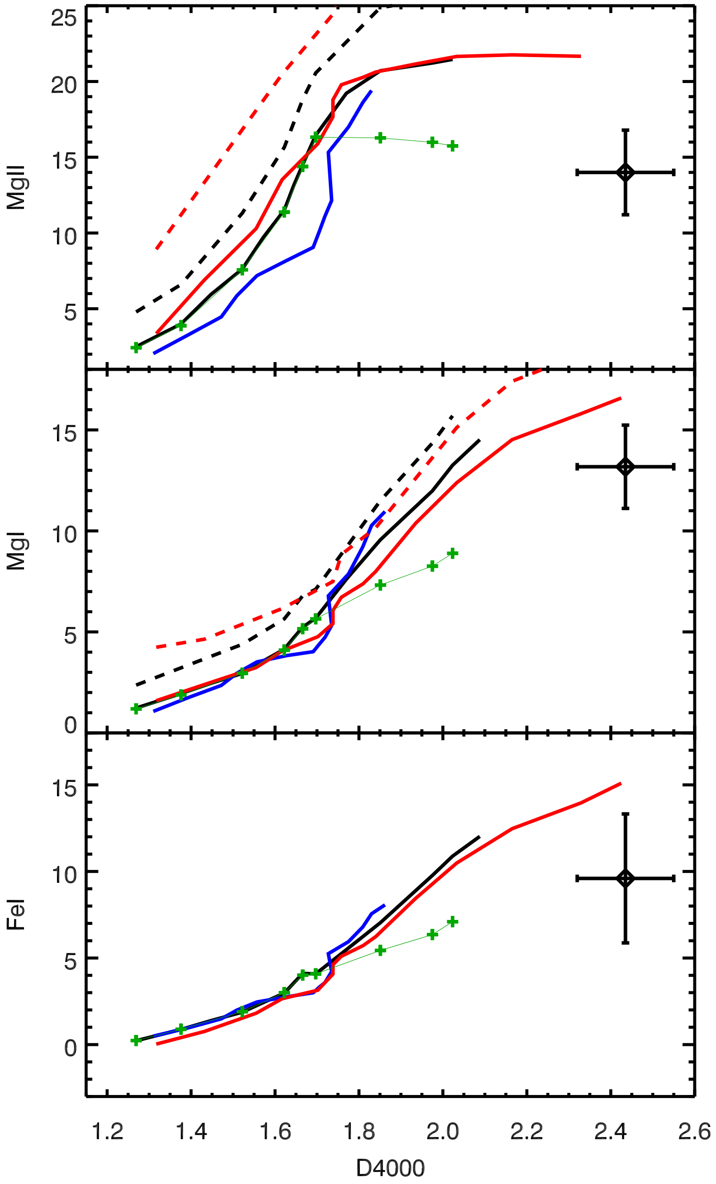

Figure 7.13: MgII, MgI and FeI(3000) vs D4000 for COSMOS-307881 (black crosses) in comparison with stellar population models (MS11) for different metallicities: subsolar metallicity (blue lines), solar metallicity (black lines) and supersolar metallicity (red lines). Solid lines are for solar value of [α/Fe] and dashed lines are for supersolar value of [α/Fe] derived as projections of Magnesium indices values from TMJ Mg_b(5175Å) index. The green-crossed lines are the solar metallicity values of MA09 models with the inclusion of the UV up-turn.

fect because it should be confirmed by exploring also the more extreme UV spectral region (around 1000 – 2000 Å) where this signature is more evident, but I am confident that this phenomenon is the only one that is able to explain the values of our UV indices without affecting those of all the other redder indices. Moreover, I speculated that the presence of a bright-UV old stellar population is also the responsible of the detected [OII](3727Å) weak emission, as already hinted in Lonoce et al. 2015. Indeed, locating COSMOS-307881 on a BPT diagram involving [OII](3727Å), [OIII](5007Å) (null flux) and Hβ (in absorption) as shown in Thomas et al. 2013 [119], I could classify this object as a LINER (Low-ionization nuclear emission-line region) galaxy. It is known from optical spectroscopic studies that a significant fraction of elliptical galaxies with their old stellar populations belong to the LINERs population (Yan et al. 2006 [137]), although the ionization mechanism in LINERs is still under debate (Annibali et al. 2010 [1]). One of the most accredited scenario is that photo-ionization by old post-asymptotic giant branch stars is the responsible of the atomic excitations since their radiation is able to reproduce the observed emission-line ratios in LINERs (Trinchieri & di Serego Alighieri 1991 [124]). My hypothesis is that the same old population responsible of the UV up-turn effect noticed in the altered values of UV indices, contributes also to the excitation of some residual gas in the interstellar medium of this ETG, thus causing the detected [OII] weak emission.

7.3 Discussion

In this section, all the results obtained from the indices analysis (Table 7.4 and 7.5) will be discussed. First of all, from this analysis we can learn that the stellar content among the galaxies of the sample is not homogeneous, both in terms of age and of metallicity. Indeed, the ages of their stellar population span a large range from < 1 Gyr (0.3 Gyr of COSMOS-7447) to 4 Gyr (of COSMOS-307881), and the metallicities are found to cover the range from the lower limit of the adopted models ([Z/H]$= -0.3$) to the very high values of again COSMOS-307881 ([Z/H]$= 0.61$]). Moreover these two stellar population properties are not correlated, with both younger and older galaxies having both high and low metallicity. This information tells us that also the star formation histories of these galaxies, their formation and evolution, are not homogeneous.

More in details, for COSMOS-307881 I found (following the indication of only Lick indices, Table 7.5, as explained in Sec. 7.2.1) an age of $4.0^{+0.5}_{-0.8}$ Gyr, a very high metallicity $[Z/H] = 0.61^{+0.06}_{-0.05}$ and a positive α-enhancement $[\alpha/Fe] = 0.45^{+0.05}_{-0.19}$. For COSMOS-7447 I well constrained the age of 0.3 ± 0.1 Gyr, I obtained an indication of a high metallicity $[Z/H] = +0.26^{+0.04}_{-0.4}$, but I could not estimate the α-enhancement, since indices are not fully consistent with a single well defined value of this parameter. I well constrained the age of the stellar population of UDS-19627, 0.7 ± 0.1 Gyr, and for this object I found a very low metallicity $[Z/H] = -0.30^{+0.2}_{-0.0}$ (at the limit of the used modelling) and a negative α-enhancement $[\alpha/Fe] = -0.18^{+0.2}_{-0.12}$. Finally, for

UDS-29410 I detected an age of 1.8 ± 0.3 Gyr slightly older than the other galaxies, again a very low metallicity $[\mathrm{Z/H}] = -0.30^{+0.2}_{-0.0}$, but a high value of α-enhancement $[\alpha/\mathrm{Fe}] = 0.42^{+0.08}_{-0.1}$.

The age estimates of the stellar content of the sample galaxies resulted to be the more solid and reliable measure of the present analysis. Indeed, they resulted very stable for any set of indices I have investigated. From the estimates of the age I could derive the relative epochs of stellar formation of these galaxies: with the only exception of the object COSMOS-307881 that has a redshift of formation $z_{form} > 5$, the other three galaxies have formed the bulk of their stars in the not so far cosmic epoch around $z_{form} \sim 2 - 2.5$.

The expected following evolution of these galaxies from the epochs of observation to $z \sim 0$, can be explored comparing the stellar population properties I derived from this analysis with the results that are found in the local Universe. This is usually done by means of the well known local scaling relations which involve the stellar parameters (age, metallicity and α-enhancement) and the velocity dispersion (Thomas et al. 2010 [117]). As a comparison set I adopted the sample of ~ 50 local ETGs analyzed in Spolaor et al. 2010 [111] in a similar way followed by the present work. In particular, in that work the stellar parameters are provided for the same galaxy as measured both in the inner core (within a radius of $\mathrm{r}_e/8$) and at the effective radius (r_e, considered as the mean values of the global stellar population, see Spolaor et al. 2010 [111]). This double information is precious because it not only provides an indication of the parameters gradients within the galaxies, but also gives us a tool to understand if the compact galaxies of our sample will become the centers of local elliptical (Naab et al. 2009 [80], Huang et al. 2013 [37]) or they will experience only an enlargement of their radius without affecting their stellar content.

The comparison is shown in Fig. 7.14. The stellar properties, age (top panel), metallicity (middle panel) and α-enhancement (bottom panel) are plotted as a function of the velocity dispersion at $\mathrm{r}_e/8$. The central ($\mathrm{r}_e/8$) values of σ for the galaxies of our sample have been derived from the global ones assuming the formula by Cappellari et al. 2006 [9]. Black crosses refer to the central values ($\mathrm{r}_e/8$) of the local sample of Spolaor et al. 2010, and solid black lines are the derived scaling relation; instead blue crosses and lines are the analogous referred to the mean values. Typical error bars are positioned at the upper left corner of each panel. Our objects are labelled with green diamonds.

Our points (green diamonds in Fig. 7.14) occupy the right region of all plots correspondent to the higher values of the velocity dispersion. This is not surprising because our sample is composed by compact ETGs which are typically found to be more dense than the local sample (Trujillo et al. 2009 [125]).

As far as the age scaling relation (Fig. 7.14, top panel), I have aged the stellar populations of our objects assuming a pure passive evolution, in order to compare the results obtained at $z > 1.4$ with the local Universe. The vertical green arrows indicate this assumed evolution toward the $z \sim 0$ values (small green diamonds). It can be noticed that these derived values are in a perfect agreement with the local

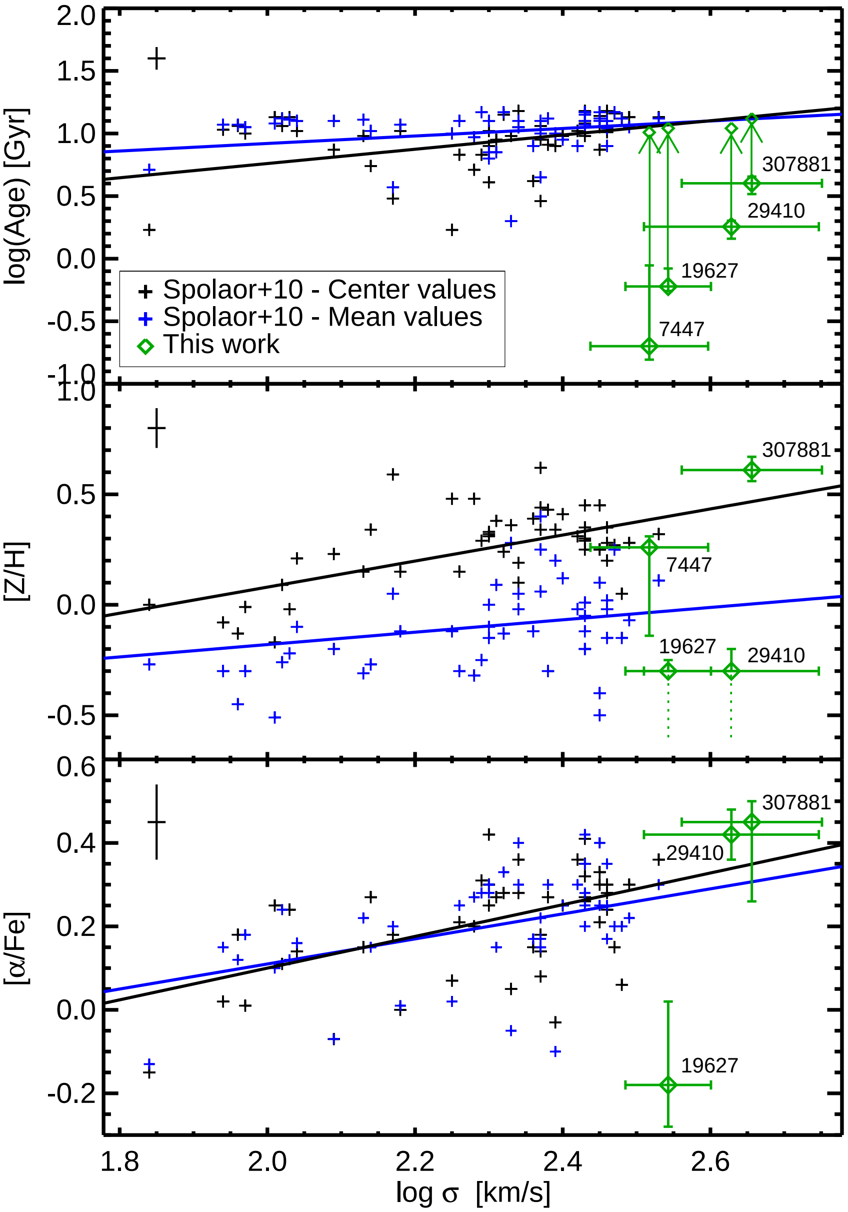

Figure 7.14: Comparison with the local scaling relations of age (top panel), metallicity (middle panel) and α-enhancement (bottom panel) as a function of the central velocity dispersion (at $r_e/8$). Black and blue crosses are respectively the central (at $r_e/8$) and mean values for the local sample of ETGs analyzed in Spolaor et al. 2010 [111] with the derived scaling relation (black and blue lines respectively). Typical error bars are positioned at the upper left corner of each panel. Green diamonds are the values of our sample of galaxies.

scaling relation, although I cannot discriminate whether they follow the inner or mean values scaling relation, since the two curves are degenerate in that range of σ. I could thus conclude that the star formation histories of the galaxies of the sample are consistent with a star formation happened at $z > 2$ (> 5 for COSMOS-307881) followed by a passive evolution of at least the bulk of their stellar population.

But we can learn more about the evolution of their stellar content looking at the metallicity scaling relation (Fig. 7.14, middle panel). First of all it can be seen a larger scatter of the values in the [Z/H] vs σ plane, even if it is of the order of the local sample scatter. Thus I could infer that this is probably not due to the difficulty of the metallicity measure at high-redshift. In particular, I remind that two objects, UDS-19627 and UDS-29410, are positioned at the lower limit of the modelling (i.e. [Z/H]$= -0.3$), but probably they have lower metallicity values if models at lower metallicities would have been available. The 4 galaxies follow two mainly distinct behaviours: COSMOS-307881 and COSMOS-7447 seem to lie on the local scaling relation built with the center values, while UDS-19627 and UDS-29410 on that one built with the mean values.

This framework suggests different possibilities for both the formation and evolution of the galaxies of the sample. As far as COSMOS-307881, as already claimed in the previous Chapter 6, its high metallicity value is expected from the local scaling relation which requires such values for high velocity dispersions. Indeed, a possible explanation proposed by the model of Pipino & Matteucci 2004 [90], is that high mass objects are found to have formed in a rapid star formation burst with the consequent increasing of the star formation efficiency and thus of the metals production. This scenario is supported also by the high value of the α/Fe ratio of this object (as shown in Fig. 7.14, bottom panel), which is strictly connected with the star formation timescale as modelled by Thomas et al. 2005 [116], which in this case results to be very short. Possible progenitors of this extreme object are quasars at $z > 4$ observed to contain supersolar gaseous metallicities (Juarez et al. 2009 [42]). Such metallicity values in the local Universe are not found in the global values of local ellipticals, but only in their centers as observed in many works focused on metallicity gradients of local ETGs (Trager et al. 2000 [120], Spolaor et al. 2008 [110], Martin-Navarro et al. 2015 [73]). This means that probably COSMOS-307881 will experience minor merging events with lower metallicity systems during its evolution toward $z = 0$, which are able to dilute both the velocity dispersion and the chemical content (Naab et al. 2009 [80]). Indeed, low-mass systems (as dwarf galaxies) are expected to contain low metallicity stars as it is observed in the local mass-metallicity relation (Thomas et al. 2005 [116]). This interpretation is shown in Fig. 7.15, upper panel: COSMOS-307881 probably comes from an even more metal rich situation (red arrow) and will probably evolve in the direction (cyan arrow) of the cores local scaling relation (black line), decreasing both its metal content and its velocity dispersion by means of mass accretion.

Different explanations must be found for the other 3 objects, which, although as massive and dense as COSMOS-307881, are consistent with a lower metallicity

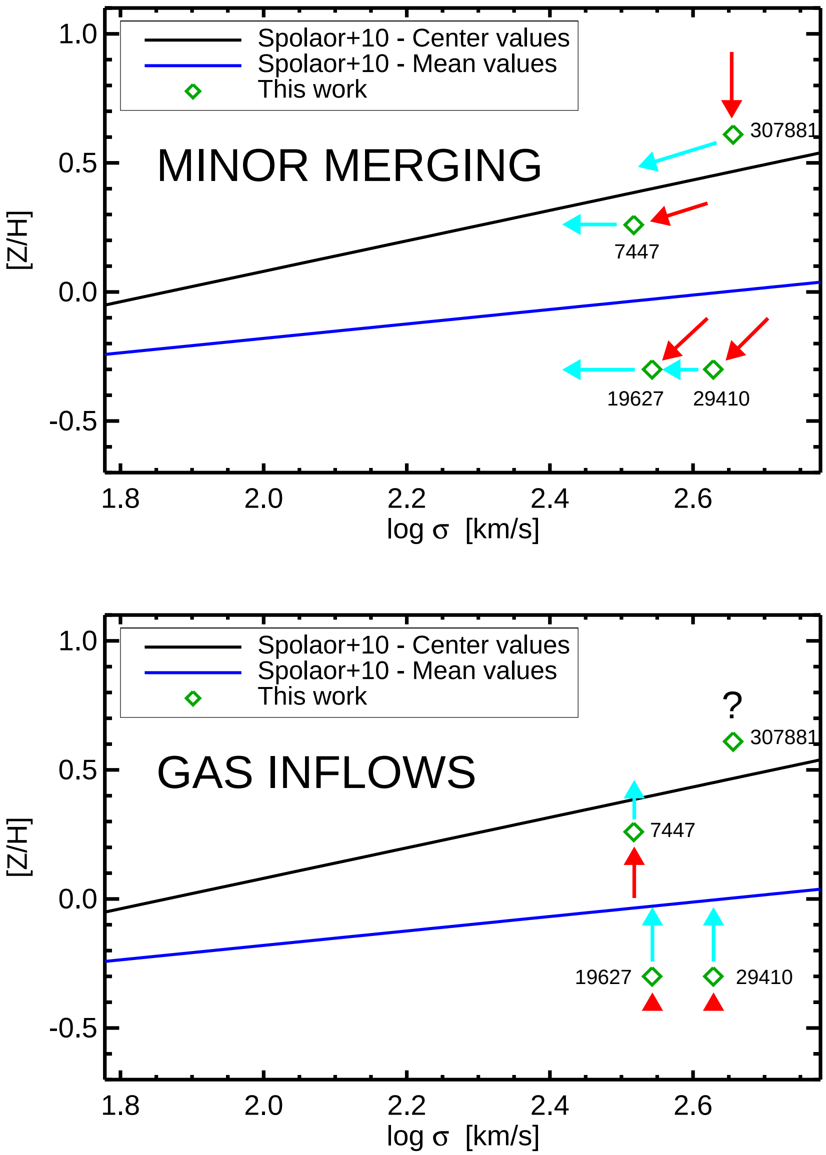

Figure 7.15: Mass-metallicity relation: two possible scenario for the evolution of the sample galaxies (green diamond) in comparison with the local relation of Spolaor et al. 2010 [111] (see Fig. 7.14). Upper panel: minor merging scenario. Bottom panel: gas inflow scenario. Red arrows for the formation and cyan arrows for the evolution.

stellar content. COSMOS-7447 shows a supersolar metallicity but its error bar makes it consistent also with subsolar values. A possibility similar to the previous one is that, given their high mass and the arguments previously exposed, also these galaxies have formed in a short burst at $z \sim 2 - 2.5$ from high-metallicity gas, but their metal content have been already diluted by merging events happened soon after the formation and that involved all the galaxy, not only its external regions. This possible scenario is outlined in Fig. 7.15, upper panel: red arrows show the direction from which the sample galaxies (green diamonds) are formed in the [Z/H] vs σ plane, and cyan arrows show their possible future evolution.

Still adopting the merging scenario, we can also suppose that these 3 ETGs have formed from a metal poor nebular gas as that of Lyman-break galaxies (LBG), observed at $z \sim 3$ as less metal enriched than local star forming galaxies (Mannucci et al. 2009 [67]). Indeed, LBGs could be the progenitors of $z \sim 1$ compact ETGs (Williams et al. 2014 [134]). In this case the sample ETGs are formed in the position as they are observed in the [Z/H] vs σ plane (Fig. 7.15, upper panel, not considering the red arrows), and their evolution will bring them toward the region of the less dense systems thanks to minor merging events with subsolar or at least solar metallicity systems (cyan arrows).

A second possible scenario is that of the cold gas accretion (Fig. 7.15, bottom panel): supposing again that these galaxies started their evolution from a metal poor stellar composition (and e.g. being the descendant of LBGs), cold gas streams reaching the inner part of ETGs would activate new star formation events prolonged in time, thus increasing the metal content of these galaxies centers. Indeed, it seems that field ETGs are able to retain gas coming from evolving stars which is able to form new generation of metal rich stars (Peebles 2002 [87]) . This is consistent with the results obtained in Chapter 5, where the constant presence of small amounts of young stars in $z \sim 1$ ETGs is observed. This process, as shown in Fig. 7.15 (bottom panel) with the same notation as before, would leave the galaxies with metallicity (and age) gradients, as it is observed in the local Universe (Spolaor et al. 2010 [111], La Barbera et al. 2012 [53]). This scenario however cannot explain the evolution of COSMOS-307881, as it is improbable that it will further increase its metallicity, as such extreme values are not observed in the local Universe.

Finally, from the bottom panel of Fig. 7.14, it is possible to give some indications on the star formation time-scale of the 3 galaxies for which it was possible to derive the values of the α/Fe abundance ratio, i.e.: COSMOS-307881, UDS-19627 and UDS-29410. As already mentioned, high values of [α/Fe] mean short star formation time-scales since the lack of Fe peak elements is a sign that supernovae type Ia had not enough time to explode before the star formation quenching. Massive systems are expected to show high values of α/Fe (i.e., short star formation time scale), as indicated by the local mass-[α/Fe] scaling relation. This is the case of COSMOS-307881 and UDS-29410, which are consistent with the local scaling relation (see Fig. 7.14, bottom panel), confirming the expectations of Thomas et al. 2002 [114] and

Pipino & Matteucci 2004 [90]. UDS-19627 instead shows a subsolar value of [α/Fe] in contrast with the expectations. However its value is consistent within the observed scatter of the local scaling relation, i.e. similar massive local ETGs with low [α/Fe] do exist.

7.4 Summary and conclusions

In the previous section I presented the first metallicity and α/Fe estimate in 4 individual ETGs at $z > 1.4$ in the COSMOS and UDS fields. These measures have been performed thanks to the unique possibility of analyzing many spectral indices from the UV to the near-IR band given by X-Shooter spectra, that cover a wide spectral range with high resolution. In particular, beside the optical Lick indices, I have measured the newly explored UV indices (down to ~ 1500 Å restframe). The large number of indices I could measure helped a lot in disentangling the residual age-metallicity degeneracy in the comparison with stellar population models. This has been done considering the value of each index and the stellar population characteristics of each object. I obtained the results summarized in Table 7.6. I constrained the age of the 4 galaxies with a mean error of $\sigma_{Age} \sim 0.3$ Gyr, the stellar metallicity with a mean $\sigma_{[Z/H]} \sim 0.12$ and I gave an indication of the α/Fe abundance ratio for 3 of the 4 objects.

All the 3 stellar parameters show an evident non-homogeneity within this sample of ETGs, with the age of their stellar populations running from 0.3 to 4 Gyr near the limit of the age of the Universe, and the metallicities covering the range from the lower limit of the adopted models ([Z/H]$= -0.3$) to the very high values of COSMOS-307881 ([Z/H]$= 0.61$]). I thus compared these stellar population properties of high-z galaxies with those measured in the local Universe as a function of the velocity dispersion, i.e. by means of local scaling relations. Local ellipticals show clear correlations with the velocity dispersion, while the 4 analyzed high-z ETGs are rather spread in the planes. An exception is the age-mass relation from which I found that our galaxies are fully consistent with a passive evolution of the bulk of their stars. From the mass-metallicity relation two possible scenarios can be inferred to explain the metal enrichment history of these galaxies: the minor merging scenario which decreases the global metallicity by means of the accretion of low-mass and low-metallicity systems, and the cold gas accretion which instead is able to increase the metallicity of their centers giving an explanation of the metallicity gradients observed in the local Universe. Finally, from the mass-α/Fe relation I confirmed that the star formation time-scale of massive ETGs is short (< 1 Gyr).

The results obtained in this work, given the large non-homogeneity of the stellar populations parameters I have found, make interesting the possibility to extend this analysis on a wider sample of high redshift ETGs. Indeed, it is of fundamental importance to understand if the different behaviours of the deduced metal enrichment histories of our 4 galaxies is confirmed and in which proportions. I am aware that only

Table 7.6: Results: best-fit values of age (Gyr), [Z/H] and [α/Fe].

ID	Age (Gyr)	[Z/H]	[α/Fe]
307881	$4.0^{+0.5}_{-0.8}$	$+0.61^{+0.06}_{-0.05}$	$+0.45^{+0.05}_{-0.19}$
7447	0.3 ± 0.1	$+0.26^{+0.04}_{-0.40}$	-
19627	0.7 ± 0.1	$-0.30^{+0.20}_{-0.00}$	$-0.18^{+0.20}_{-0.12}$
29410	1.8 ± 0.3	$-0.30^{+0.20}_{-0.00}$	$+0.42^{+0.08}_{-0.10}$

a statistical confirmation of these findings would significantly constrain the formation and evolutionary models proposed for ETGs, although the preliminary results of this work are telling us that probably there is not a unique evolutionary path for this class of objects transforming them in the local ellipticals population. Moreover, a clearer view of the relationship between the gaseous metallicity and the stellar metallicity during the initial star formation process of ETGs should be reached in order to match the observational evidences found from high-z ETGs analysis and star-forming galaxies studies at $z > 3$. Furthermore, it would be of great help for this kind of analysis to have a set of stellar population models with the complete dependence on the chemical properties, that means covering a wide range of metallicities and in particular of α-enhancement values, in a wide spectral range (e.g. from UV to near-IR) and not only for the Lick indices. This goal would allow to derive the α/Fe abundance ratio also from UV restframe spectra, which corresponds to the observed optical band for $z > 1$ objects. A wider parameters range of models would be useful also to strengthen analysis like the one described here based on X-Shooter spectra which include the measure of spectral indices from the UV to the optical restframe wavelength range.

In conclusion, obtaining X-Shooter spectroscopic data for a complete sample of $z > 1.4$ ETGs together with new models with the α/Fe dependence of UV spectral indices, would be the ideal tool to characterize the star formation histories of ETGs. Indeed, I have demonstrated that with a wide range of spectral indices, each with its peculiar dependence on age and metallicity, taking into account all the characteristics of each objects, we are able to disentangle the age-metallicity degeneracy and determine the metallicity and α/Fe abundance ratio for objects in an evolutionary phase very close to their formation and which is revealing the hidden complexity of the first Gyrs of life of ETGs.

Chapter 8

Conclusions

Early-type galaxies exhibit a sharp regularity of their morphological, structural and stellar population properties in the well-studied local Universe, making them a favoured tool to investigate the formation and the evolution of the stellar structures in the Universe. Observations of the last 20 years have confirmed the homogeneity of this class of objects at least up to $z \approx 0.5 - 0.6$, pushing the range of redshift where studying their formation towards $z > 1$ and beyond.

This thesis is focused on the analysis of stellar population properties of distant ETGs with the aim of putting new solid constraints on their past formation and on their possible following evolution toward the local Universe. The two mainly investigated stellar population properties in this work are the *age* (Section 1.4) and the *metallicity* (Section 1.5). Ages are essential to date the epoch of formation of the bulk of stars of ETGs, but also to understand, for example, if the stellar populations are coeval at any redshift. The stellar metallicity reveals informations on the past history of the Universe (when the metals involved in the star formation processes are created), and when compared with the local stellar metallicities can provide constraints on the ETGs evolution. More precise information on the metal content of ETGs is obtained by the estimate of α/Fe abundance ratio which gives a clear indication on the time-scale on which the star formation has occurred.

In the present work, all these properties have been derived thanks to high quality (S/N$\gtrsim$ 10) spectroscopic data obtained with the most high-performing spectrographs on the 8m VLT telescope, i.e. FORS2, VIMOS and X-Shooter, which with their high spectral resolution and wavelength coverage have allowed to perform for the first time a detailed spectral analysis of individual high-z ETGs (Chapter 4). Indeed, this kind of measure is still very challenging at $z > 1$ because of the faintness of the sources and the consequent difficulty in obtaining high-quality spectra.

The principal tool used in this analysis to derive the stellar properties is the measure of many spectral indices, solid indicators of both the age and the metal content of the stellar populations (Chapter 2). In particular, the combined measure of specific set of indices has been extremely efficacious in revealing also hidden peculiarities of the investigated stellar populations. All the relevant information on the age and metallicity of the analyzed ETGs have been extracted thanks to the comparison with the most up-to-date set of models, which accurately describe the spectral characteristics of the stellar populations (Chapter 3).

The work of this thesis has been carried out through three steps, each of on described in a single chapter of this thesis (Chapter 5, 6 and 7), and on the basis on different samples of ETGs from $z \sim 0.7$ to $z \sim 2$. The first work has been focused on the analysis of the age of the stellar populations on a lower redshift sample of ETGs, while in the other two, thanks to the availability of X-Shooter spectra which cover a wider spectral range, it has been possible to give constraints also on the chemical content of a higher redshift sample of galaxies.

The key question to which this thesis is addressed is the following: is the apparent homogeneity of early-type galaxies observed in the local Universe a natural consequence of a common formation process and thus always detectable at any redshift, or individual evolutionary histories have shaped them to form the homogeneous class of local ellipticals? In other words, have all ETGs formed in a single star formation event happened at high redshift ($z > 3$) and followed by the passive evolution of their stars, or later star formation and/or assembly events have occurred also at $z < 2$?

The results obtained in this work tell us that the homogeneity observed in the local and intermediate Universe is not confirmed at $z > 1$. Indeed, ETGs of the analyzed $z \gtrsim 1$ samples show a hidden complexity in their stellar population properties, despite of their morphology and colors which appear quite homogeneous.

In the analysis of a sample of ETGS at $0.6 < z < 1.2$, it has been found that, for most of the sample the presence of small mass fractions of young stars is detected. In some cases signs of recent star formation activity, superimposed on the bulk of stars which resulted to be old and passively ageing, are revealed. This means that some mechanism which is able to trigger small episodes of star formation must act in these early phases of evolution of ETGs and then progressively stop toward $z = 0$. Moreover, I found that the younger component is present in the stellar population of almost all the analyzed ETGs both at $z \sim 0.8$ and at $z \sim 1.1$, suggesting that such mechanism should operate constantly in time. Furthermore, these findings are also consistent with the results of color gradients studies at $z \sim 1$ which give indications that the detected younger stellar components are located in the center of the galaxies. All these elements point toward the scenario of the cold gas inflow in which a continuous infall of cold gas takes place towards the centers of ETGs after their main star formation event. Indeed, part of the gas responsible of the formation of the bulk of stars happened at $z > 3$, perhaps enriched by the metals of the main star formation event, can still be available and at disposal for very weak and confined star formation episodes at $z < 2$ falling toward the centers of these ellipticals. These new star formation episodes are necessarily connected with the gas reserve contained in each galaxy, thus, as I observed, not for all high-z ETGs this phenomenon occur with the same strength.

The second work is based on the analysis of a single very peculiar massive compact ETG at $z \sim 1.4$, COSMOS-307881. Indeed, the analysis of its stellar content revealed an old age, high velocity dispersion and very high metallicity ($Z \sim 5Z_{\odot}$) and α-enhancement. Its formation can thus be located in a very distant epoch, i.e. $z > 5$, and its high metal content suggest the possibility of the presence of very metal rich gas at high redshift, similar to that characterizing the gaseous disk of high redshift quasars. Its high velocity dispersion is consistent with its moderate compactness and high mass. Following the local scaling relations, its high velocity dispersion is also consistent with the observed high metallicity and high α-enhancement. Since objects with such extreme characteristics are rare to be observed in the local Universe, some processes able to dilute both its velocity dispersion and its metallicity must occur during its future evolution toward $z = 0$ in order to match the local scaling relations. A possible proposed mechanism consists of minor merging events with small and low-mass systems, in order to not increase the final stellar mass which is already high. This process is indeed able to decrease the global velocity dispersion thanks to the consequent redistribution of the stars, and the global metallicity, but leaving the center more metallic than the outskirts as generally observed in local ellipticals.

An other peculiarity of this galaxy comes from the analysis of the UV spectral indices, which shown a systematic deviation from the expected stellar population models prevision. I have attributed this discrepancy to the UV up-turn observed in many ETGs and which seems to be connected with old and metallic stellar populations. Up to now, models taking into account this phenomenon are incomplete, and my hypothesis needs to be confirmed. At the same time, if the UV upturn will be confirmed for this galaxy, the observed high metallicity of this galaxy would be fully confirmed also by UV indices; moreover, this could also explain the presence of the detected weak emission of the [OII] that cannot be ascribed to residual star formation.

Finally, the investigation of the metal content of high redshift ETGs has been extended to a wider sample of 4 massive and compact ETGs at $z > 1.4$. The analysis of many spectral indices from the UV to the optical band (restframe) has revealed a non homogeneous distribution of the metallicity and α/Fe abundance among the galaxies of the sample. In details, in addition to the extreme high value of COSMOS-307881, I found a solar metallicity object and two very low metallicity objects. The different metal content of these 4 ETGs suggests that they have formed and evolved since $z \sim 1.4$ under the action of different processes. I have thus proposed two possible different metal enrichment scenarios for the 3 lower metallicity galaxies: the minor merging scenario which could be the responsible of the decreasing of the metallicity thanks to the accretion of low-metallicity systems, and the cold gas inflow that will act mainly in the centers of these ETGs causing the increasing of their metallicity thanks to the processing of enriched gas. Indeed, without disturbing the bulk of stars which evolves passively, there is the possibility for ETGs to form new stars in prolonged periods of their evolution thanks to small amounts of inflowing cold gas in their centers, thus rejuvenating and metal enriching the inner part of these systems. The latter hypothesis would be consistent with what I have inferred from the work on the lower redshift sample, i.e. with a continuous weak star formation triggering combined with a bulk of stars passively evolving.

Unfortunately, at the moment the two scenarios cannot be discriminated, and the possibility that both the evolutionary scenarios have taken place in producing the local ETGs remain the most probable.

In conclusion, with this PhD thesis I have demonstrated firstly the feasibility of this kind of spectral analysis on $z > 1$ ETGs, and I have put some important constraints on their evolution: *i*) there is a secondary younger component in most of $0.8 < z < 1.1$ ETGs and *ii*) that the chemical characterization of $z > 1.4$ ETGs is non homogeneous and not consistent with the distribution of local ETGs values. Moreover, the presence of a dense, old, high-metallicity and high-α/Fe ETG at $z \sim 1.4$ open new possibilities also regarding the origin of this class of galaxies.

In the future many improvements could help in completing the puzzle of the galaxy formation and evolution processes:

- The availability of spectroscopic data with high S/N ratio (> 10) both in the optical and near-IR band, of a large number of high redshift ETGs to be obtained for example by means of large observative programs conducted with $8 - 10$m telescope.

- The identification of complete samples of field ETGs at $z > 1.5$ on which a statistical analysis can be performed. This would allow to know for example the number distribution of ETGs with (very) high/low metallicity and to understand how the extreme values I have observed in my analysis are common in the distant Universe.

- The extension of the stellar population models to cover a wider range of metallicity values in order to better investigate the extreme cases as observed in this work in a more precise and reliable way than from simple extrapolation as used in this work. Moreover, models should be improved with the adding of the α-enhancement dependence also in the UV band that will be particularly useful in the high redshift Universe.

- A deeper investigation of the UV up-turn phenomenon with local data in order to shed light on its physical nature and dependence. In particular, it should be probed the connection between this phenomenon and the population of LINERs in the local Universe.

- The investigation of the possible dependence of the obtained results from the environment. Is the non-homogeneity of the stellar population properties, in particular metallicity, of field high-z ETGs observed also in clusters? Does the environment play a role in the chemical histories of ETGs? Since it seems that cluster ETGs have formed earlier in the cosmic time, is the observed scenario expected to be similar but shifted at even higher-z in denser environment?

- The study of the possible influence of the obtained results on the IMF assumed to model the observed features.
- The possibility to obtain of spatially resolved spectroscopic data of high-redshift ETGs when the instrumentation technology will allow to reach this important goal. This huge improvement would permit to investigate the spatial distribution of the stellar population properties and thus to confirm or reject the hypothesis made about the formation and evolution scenarios of this class of galaxies.

As far as I am concerned, the first concrete step to continue this study of the origin and evolution of the ETGs, is the observing time request for the observation of a sample of cluster ETGs at $z \sim 1.2$ consistent with the already analyzed sample of field counterparts. These observations would be carried out with the X-Shooter spectrograph on the VLT, in order to follow the same kind of analysis of this work, but with higher S/N. With these data, I wish to verify the environment dependence of the previous results, that means to understand if the non-homogeneity of the metallicity values observed in field ETGs is a consequence of the low density environment.

Bibliography

[1] Annibali F., Bressan A., Rampazzo R., Zeilinger W. W., Vega O. and Panuzzo P., *Nearby early-type galaxies with ionized gas. IV. Origin and powering mechanism of the ionized gas*, Astronomy and Astrophysics, 2010, 519, 40

[2] Balogh M. L., Morris S. L., Yee H. K. C., Carlberg R. G., and Ellingson E., *Differential Galaxy Evolution in Cluster and Field Galaxies at* $z\sim 0.3$, The Astrophysical Journal, 1999, 527, 54

[3] Bastian N., Covey K.R., and Meyer M.R., *A Universal Stellar Initial Mass Function? A Critical Look at Variations*, Annual Review of Astronomy and Astrophysics, 2010, 48, 339

[4] Bell E.F. et el., *Nearly 5000 Distant Early-Type Galaxies in COMBO-17: A Red Sequence and Its Evolution since* $z \sim 1$, The Astrophysical Journal, 2004, 608, 752

[5] Bezanson R. et al., *The Relation Between Compact, Quiescent High-redshift Galaxies and Massive Nearby Elliptical Galaxies: Evidence for Hierarchical, Inside-Out Growth*, The Astrophysical Journal, 2009, 697, 1290

[6] Bruzual G., *Spectral evolution of galaxies. I - Early-type systems*, The Astrophysical Journal, 1983, 273, 105

[7] Bruzual B., and Charlot S., *Stellar population synthesis at the resolution of* 2003, Mon. Not. R. Astron. Soc., 2003, 344, 1000

[8] Calzetti D., Armus L., Bohlin R.C., Kinney A.L., Koornneef J., and Storchi-Bergmann T., *The Dust Content and Opacity of Actively Star-forming Galaxies*, The Astrophysical Journal, 2000, 533, 682

[9] Cappellari M. et al., *The SAURON project - IV. The mass-to-light ratio, the virial mass estimator and the Fundamental Plane of elliptical and lenticular galaxies*, Mon. Not. R. Astron. Soc., 2006, 366, 1126

[10] Carollo C.M., Danziger I.J., and Buson L., *Metallicity Gradients in Early Type Galaxies*, Mon. Not. R. Astron. Soc., 1993, 265, 553

[11] Cassisi S., Castellani M., and Castellani V., *Intermediate-age metal deficient stellar populations: the case of metallicity* $Z = 0.00001$, Astronomy and Astrophysics, 1997, 317, 108

[12] Chabrier G., *Galactic Stellar and Substellar Initial Mass Function*, The Publications of the Astronomical Society of the Pacific, 2003, 115, 763

[13] Charlot S., and Longhetti M., *Nebular emission from star-forming galaxies*, Mon. Not. R. Astron. Soc., 2001, 323, 887

[14] Cimatti A. et al., *Old galaxies in the young Universe*, Nature, 2004, 430, 184

[15] Cimatti A., Daddi E., and Renzini A., *Mass downsizing and "top-down" assembly of early-type galaxies*, Astronomy and Astrophysics, 2006, 453, L29

[16] Cimatti A., *The formation and evolution of early-type galaxies: solid results and open questions*, CP1111, Probing Stellar Population Out to the Distant Universe, Cefalù 2008, Proceedings of the International Conference.

[17] Cimatti A. et al., *GMASS ultradeep spectroscopy of galaxies at* $z \sim 2$. *II. Superdense passive galaxies: how did they form and evolve?*, Astronomy and Astrophysics, 2008, 482, 21

[18] Coccato L., Gerhard O., and Arnaboldi M., *Distinct core and halo stellar populations and the formation history of the bright Coma cluster early-type galaxy NGC 4889*, Mon. Not. R. Astron. Soc., 2010, 407, L26

[19] Crocker A.F., Bureau M., Young L.M., and Combes F., *Molecular gas and star formation in early-type galaxies*, Mon. Not. R. Astron. Soc., 2011, 410, 1197

[20] Daddi E. et al., *Passively evolving early-type galaxies at* $1.4 \lesssim z \lesssim 2.5$ *in the hubble ultra deep field*, The Astrophysical Journal, 2005, 626, 680

[21] Davidge T.J., and Clark C.C., *Absorption line gradients in the blue and near-ultraviolet spectra of bright elliptical galaxies, and implications for studies of intermediate redshift objects*, The Astrophysical Journal, 1994, 107, 946

[22] Dekel A., and Birnboim Y., *Galaxy bimodality due to cold flows and shock heating*, Mon. Not. R. Astron. Soc., 2006, 368, 2

[23] De Lucia G. et al., *The formation history of elliptical galaxies*, Mon. Not. R. Astron. Soc., 2006, 366, 499

[24] Eggen O.J., Lynden-Bell D., and Sandage A.R., *Evidence from the motions of old stars that the galaxy collapsed*, Astrophysical Journal, 1962, 136, 748

[25] Faber S.M., Worthey G., and Gonzalez J.J, *Absorption-Line Spectra of Elliptical Galaxies and Their Relation to Elliptical Formation*, IAU Symposium 149, 1992, The Stellar Population of Galaxies. Kluwer, Dordrecht, 255

[26] Fanelli M.N., O'Connell R.W., Burstein D., and Wu C.C., *Spectral synthesis in the ultraviolet. III - The spectral morphology of normal stars in the mid-ultraviolet*, Astrophysical Journal, 1990, 364, 272

[27] Fardal M.A., Kats N., Gardner J.P., Hernquist L., Weinberg D.H., and Dave' R., *Cooling Radiation and the Lyalpha Luminosity of Forming Galaxies*, The Astronomical Journal, 2001, 562, 605

[28] Fontana A. et al., *The K20 survey. VI. The distribution of the stellar masses in galaxies up to* $z \simeq 2$, Astronomy and Astrophysics, 2004, 424, 23

[29] Gallazzi A., Bell E.F., Zibetti S., Brinchmann J., and Kelson D.D., *Charting the Evolution of the Ages and Metallicities of Massive Galaxies since* $z = 0.7$ The Astrophysical Journal, 2014, 788, 72

[30] Gargiulo A., Saracco P., and Longhetti M., *Colour gradients in normal and compact early-type galaxies at* $1 < z < 2$, Mon. Not. R. Astron. Soc., 2011, 412, 1804

[31] Gargiulo A., Saracco P., Longhetti M., La Barbera F., and Tamburri S., *Spatially resolved colours and stellar population properties in early-type galaxies at* $z \sim 1.5$, Mon. Not. R. Astron. Soc., 2012, 425, 2698

[32] Girardi L. et al., *Evolutionary tracks and isochrones for low- and intermediate-mass stars: From* 0.15 *to* $7\ M_{sun}$*, and from* $Z = 0.0004$ *to* 0.03, Astronomy and Astrophysics Supplement, 2000, 141, 371

[33] Glazebrook K. et al., *Cosmic Star Formation History to* $z = 1$ *from a Narrow Emission Line-selected Tunable-Filter Survey*, The Astronomical Journal, 2004, 128, 2652

[34] Goldoni P. et al., *Data reduction software of the X-shooter spectrograph*, Proc.SPIE, 2006, 6269, 626933

[35] Greggio L., and Renzini A., *Clues on the hot star content and the ultraviolet output of elliptical galaxies*, The Astrophysical Journal, 1990, 364, 35

[36] Hamilton D., *The spectral evolution of galaxies. I. An observational approach*, The Astrophysical Journal, 1985, 297, 371

[37] Huang S., Ho L.C., Peng C.Y., Li Z., and Barth A.J., *The Carnegie-Irvine Galaxy Survey. III. The Three-component Structure of Nearby Elliptical Galaxies*, The Astrophysical Journal, 2013, 766, 47

[38] Im M. et al., *Luminosity Functions of Elliptical Galaxies at* $z < 1.2$, Astrophysical Journal Letters, 1996, 461, L79

[39] Johansson J., Thomas D. and Maraston C., *Empirical calibrations of optical absorption-line indices based on the stellar library MILES*, Mon. Not. R. Astron. Soc., 2010, 406, 165

[40] Jorgensen I., and Chiboucas K., *Stellar Populations and Evolution of Early-type Cluster Galaxies: Constraints from Optical Imaging and Spectroscopy of z* $= 0.5 - 0.9$ *Galaxy Clusters*, Astrophysical Journal, 2013, 145, 77

[41] Jorgensen I., Chiboucas K., Toft S., Bergmann M., Zirm A., Schiavon R., and Grutzbauch R., *RX J0848.6+4453: The Evolution of Galaxy Sizes and Stellar Populations in a* $z = 1.27$ *Cluster*, Astrophysical Journal, 2014, 148, 117

[42] Juarez Y. et al., *The metallicity of the most distant quasars*, Astronomy and Astrophysics, 2009, 494, L25

[43] Kauffmann G. et al., *The Formation and Evolution of Galaxies Within Merging Dark Matter Haloes*, Mon. Not. R. Astron. Soc., 1993, 264, 201

[44] Kaviraj S. et al., *Galaxy Zoo: dust and molecular gas in early-type galaxies with prominent dust lanes*, Mon. Not. R. Astron. Soc., 2012, 423, 49

[45] Keres D., Kats N., Weinberg D.H., and Dave' R., *How do galaxies get their gas?*, Mon. Not. R. Astron. Soc., 2005, 363, 2

[46] Kobayashi C., *GRAPE-SPH chemodynamical simulation of elliptical galaxies - I. Evolution of metallicity gradients*, Mon. Not. R. Astron. Soc., 2004, 347, 740

[47] Kodama T. et al., *Evolution of the colour-magnitude relation of early-type galaxies in distant clusters*, Astronomy and Astrophysics, 1998, 334, 99

[48] Koppen J., Weidner C., and Kroupa P., *A possible origin of the mass-metallicity relation of galaxies*, Mon. Not. R. Astron. Soc., 2007, 375, 673

[49] Korn A., Maraston C., and Thomas D., *The sensitivity of Lick indices to abundance variations*, Astronomy and Astrophysics, 2005, 438, 685

[50] Kroupa P., *On the variation of the initial mass function*, Mon. Not. R. Astron. Soc., 2001, 228, 187

[51] Kroupa P., Weidner C., Pflamm-Altenburg J., Thies I., Dabringhausen J., Marks M., and Maschberger T., *The Stellar and Sub-Stellar Initial Mass Function of Simple and Composite Populations*, Planets, Stars and Stellar Systems, 2013, 5, 115

[52] Kurucz R.L., *Stellar populations of galaxies*, eds. Barbuy & Renzini, Dordrecht: Kluwer Academic Publishers, 1992, 225

[53] La Barbera F., Ferreras I., de Carvalho R.R., Bruzual G., Charlot S., Pasquali A., and Merlin E., *SPIDER - VII. Revealing the stellar population content of massive early-type galaxies out to* $8R_e$, Mon. Not. R. Astron. Soc., 2012, 426, 2300

[54] Larson R.B., *Models for the formation of elliptical galaxies*, Mon. Not. R. Astron. Soc., 1975, 173, 671

[55] Lawrence A., Warren S.J., Almaini O., et al., *The UKIRT Infrared Deep Sky Survey (UKIDSS)*, Mon. Not. R. Astron. Soc., 2007, 379, 1599

[56] Le Borgne J.F. et al., *STELIB: A library of stellar spectra at* $R \sim 2000$, Astronomy and Astrophysics, 2003, 402, 433

[57] Lees J.F., Knapp G.R., Rupen M.P. and Phillips T.G., *Molecular gas in elliptical galaxies*, The Astrophysical Journal, 1991, 379, 177

[58] Lequeux J., Peimbert M., Rayo J.F., Serrano A., and Torres-Peimbert S., *Chemical composition and evolution of irregular and blue compact galaxies*, Astronomy and Astrophysics, 1979, 80, 155

[59] Longhetti M., Bressan A., Chiosi C., and Rampazzo R., *Star formation history of early-type galaxies in low density environments. V. Blue line-strength indices for the nuclear region*, Astronomy and Astrophysics, 1999, 345, 419

[60] Longhetti M., Bressan A., Chiosi C., and Rampazzo R., *Star formation history of early-type galaxies in low density environments. IV. What do we learn from nuclear line-strength indices?*, Astronomy and Astrophysics, 2000, 353, 917

[61] Longhetti M. et al., *Dating the stellar population in massive early-type galaxies at* $z \sim 1.5$, Mon. Not. R. Astron. Soc., 2005, 361, 897

[62] Longhetti M. et al., *The Kormendy relation of massive elliptical galaxies at* $z \sim 1.5$*: evidence of size evolution*, Mon. Not. R. Astron. Soc., 2007, 374, 614

[63] Lonoce I., Longhetti M., Saracco P., Gargiulo A., and Tamburri S, *Spectral detection of multiple stellar populations in* $z \sim 1$ *early-type galaxies*, Mon. Not. R. Astron. Soc., 2014, 444, 2048

[64] Lonoce I. et al., *Old age and super-solar metallicity in a massive* $z \sim 1.4$ *early-type galaxy from VLT/X-Shooter spectroscopy*, Mon. Not. R. Astron. Soc., 2015, in press, preprint (arXiv:1509.04000)

[65] Lopez-Sanjuan C. et al., *The dominant role of mergers in the size evolution of massive early-type galaxies since* $z \sim 1$, Astronomy and Astrophysics, 2012, 548, A7

[66] Mancini C. et al., *High-redshift elliptical galaxies: are they (all) really compact?*, Mon. Not. R. Astron. Soc., 2010, 401, 933

[67] Mannucci F. et al., *LSD: Lyman-break galaxies Stellar populations and Dynamics - I. Mass, metallicity and gas at* $z \sim 3.1$, Mon. Not. R. Astron. Soc., 2009, 398, 1915

[68] Maraston C., Greggio L., Renzini A., Ortolani S., Saglia R.P., Puzia T.H., and Kissler-Patig M., *Integrated spectroscopy of bulge globular clusters and fields. II. Implications for population synthesis models and elliptical galaxies*, Astronomy and Astrophysics, 2003, 400, 823

[69] Maraston C., *Evolutionary population synthesis: models, analysis of the ingredients and application to high-z galaxies*, Mon. Not. R. Astron. Soc., 2005, 362, 799

[70] Maraston C., Nieves Colmenarez L., Bender R., and Thomas D., *I. Empirical and theoretical stellar population models*, Astronomy and Astrophysics, 2009, 493, 425

[71] Maraston C. et al., *Star formation rates and masses of* $z \sim 2$ *galaxies from multicolour photometry*, Mon. Not. R. Astron. Soc., 2010, 407, 830

[72] Maraston C., and Strömbäck G., *Stellar population models at high spectral resolution*, Mon. Not. R. Astron. Soc., 2011, 418, 2785

[73] Martin-Navarro I., La Barbera F., Vazdekis A., Ferre-Mateu A., Trujillo I., and Beasley M., *The initial mass function of a massive relic galaxy*, Mon. Not. R. Astron. Soc., 2015, 451, 1081

[74] Matteucci F., Ponzone R., and Gibson B.K., *On the trend of [Mg/Fe] among giant elliptical galaxies*, Astronomy and Astrophysics, 1998, 335, 855

[75] Matteucci F., *The chemical evolution of the Galaxy*, Kluwer Academic Publisher, Dordrecht, 2001

[76] McCracken H.J. et al., *The COSMOS-WIRCam Near-Infrared Imaging Survey. I. BzK-Selected Passive and Star-Forming Galaxy Candidates at* $z > 1.4$, The Astrophysical Journal, 2010, 708, 202

[77] de Mello D.F., Daddi E., Renzini A., Cimatti A., di Serego Alighieri S., Pozzetti L., and Zamorani G., *Metal Enrichment in Near-Infrared Luminous Galaxies at* $z \sim 2$*: Signatures of Proto-elliptical Galaxies?*, The Astrophysical Journal, 2004, 608, 29

[78] Mignoli M. et al., *The K20 survey. VII. The spectroscopic catalogue: Spectral properties and evolution of the galaxy population*, Astronomy and Astrophysics, 2005, 437, 883

[79] Naab T., Khochfar S., and Burkert A., *Properties of Early-Type, Dry Galaxy Mergers and the Origin of Massive Elliptical Galaxies*, The Astrophysical Journal, 2006, 636, L81

[80] Naab T., Johansson P.H., and Ostriker J.P., *Minor mergers and the size evolution of elliptical galaxies*, The Astrophysical Journal, 2009, 699, L178

[81] Onodera M. et al., *Deep Near-infrared Spectroscopy of Passively Evolving Galaxies at* $z > 1.4$, Astrophysical Journal, 2012, 755, 26

[82] Onodera M. et al., *The Ages, Metallicities, and Element Abundance Ratios of Massive Quenched Galaxies at* $z = 1.6$, Astrophysical Journal, 2015, 808, 161

[83] Oser L., Ostriker J.P., Naab T., Johansson P.H., and Burkert A., *The Two Phases of Galaxy Formation*, The Astrophysical Journal, 2010, 725, 2312

[84] Oser L., Ostriker J.P., Naab T., and Johansson P.H., *The Cosmological Size and Velocity Dispersion Evolution of Massive Early-type Galaxies*, The Astrophysical Journal, 2012, 744, 630

[85] Panuzzo P., Rampazzo R., Bressan A., Vega O., Annibali F., Buson L.M., Clemens M.S., and Zeilinger W.W., *Nearby early-type galaxies with ionized gas. VI. The Spitzer-IRS view. Basic data set analysis and empirical spectral classification*, Astronomy and Astrophysics, 2011, 528, A28

[86] Patton D.R. et al., *Close Pairs of Field Galaxies in the CNOC1 Redshift Survey*, Astrophysical Journal, 1997, 475, 29

[87] Peebles P.J.E., *When did the large elliptical galaxies form?*, Astronomical Society of the Pacific, 2002, 351

[88] Pettini M. et al., *The Rest-Frame Optical Spectra of Lyman Break Galaxies: Star Formation, Extinction, Abundances, and Kinematics*, Astrophysical Journal, 2001, 554, 981

[89] Pettini M. et al., *New Observations of the Interstellar Medium in the Lyman Break Galaxy MS 1512-cB58*, Astrophysical Journal, 2002, 569, 742

[90] Pipino A., and Matteucci F., *Photochemical evolution of elliptical galaxies - I. The high-redshift formation scenario*, Mon. Not. R. Astron. Soc., 2004, 347, 968

[91] Pipino A., D'Ercole A., Chiappini C., and Matteucci F., *Abundance gradient slopes versus mass in spheroids: predictions by monolithic models*, Mon. Not. R. Astron. Soc., 2010, 407, 1347

[92] Poggianti B.M. et al., *Ages of S0 and Elliptical Galaxies in the Coma Cluster* Astrophysical Journal, 2001, 563, 118

[93] Ponder J.M. et al., *Integrated ultraviolet spectra and line indices of M31 globular clusters and the cores of elliptical galaxies*, The Astronomical Journal, 1998, 116, 2297

[94] Popesso P. et al., *The great observatories origins deep survey. VLT/VIMOS spectroscopy in the GOODS-south field*, Astronomy and Astrophysics, 2009, 494, 443

[95] Prugniel P., and Soubiran C., *A database of high and medium-resolution stellar spectra*, Astronomy and Astrophysics, 2001, 369, 1048

[96] Renzini A., *Stellar Population Diagnostics of Elliptical Galaxy Formation*, Annu.Rev.Astro.Astrophys., 2006, 44, 141

[97] Rocca-Volmerange B. et al., *Starburst and old stellar populations in the* $z \sim 3.8$ *radio galaxies 4C 41.17 and TN J2007-1316*, Mon. Not. R. Astron. Soc., 2013, 429, 2780

[98] Rose J.A., *Constraints on stellar populations in elliptical galaxies*, The Astronomical Journal, 1985, 90, 1927

[99] Salpeter E.E., *The Luminosity Function and Stellar Evolution*, Astrophysical Journal, 1955, 121, 161

[100] Sanchez-Blazquez P. et al., *Medium-resolution Isaac Newton Telescope library of empirical spectra*, Mon. Not. R. Astron. Soc., 2006, 371, 703

[101] Sanchez-Blazquez P. et al., *Evolution of red-sequence cluster galaxies from redshift 0.8 to 0.4: ages, metallicities, and morphologies*, Astronomy and Astrophysics, 2009, 499, 47

[102] Santini P. et al., *Star formation and mass assembly in high redshift galaxies*, Astronomy and Astrophysics, 2009, 504, 751

[103] Saracco P. et al., *The density of very massive evolved galaxies to* $z \simeq 1.7$, Mon. Not. R. Astron. Soc., 2005, 357, L40

[104] Saracco P. et al., *Probing the evolution of the near-infrared luminosity function of galaxies to* $z \simeq 3$ *in the Hubble Deep Field-South*, Mon. Not. R. Astron. Soc., 2006, 367, 349

[105] Saracco P., Longhetti M., and S. Andreon, *The population of early-type galaxies at* $1 < z < 2$ *- new clues on their formation and evolution*, Mon. Not. R. Astron. Soc., 2009, 392, 718

[106] Saracco P., Longhetti M., and Gargiulo A., *The number density of superdense early-type galaxies at* $1 < z < 2$ *and the local cluster galaxies*, Mon. Not. R. Astron. Soc., 2010, 408, L21

[107] Saracco P. et al., *Constraining the star formation and the assembly histories of normal and compact early-type galaxies at* $1 < z < 2$, Mon. Not. R. Astron. Soc., 2011, 412, 2707

[108] Schaller G., Schaerer D., Meynet G., and Maeder A., *New grids of stellar models from 0.8 to 120 solar masses at Z = 0.020 and Z = 0.001* Astronomy and Astrophysics Supplement Series, 1992, 96, 269

[109] Schiavon R.P. et al., *The DEEP2 Galaxy Redshift Survey: Mean Ages and Metallicities of Red Field Galaxies at* $z \sim 0.9$ *from Stacked Keck DEIMOS Spectra*, The Astrophysical Journal, 2006, 651, L93

[110] Spolaor M., Forbes D.A., Proctor R.N., Hau G.K.T., and Brough S., *The early-type galaxies NGC 1407 and NGC 1400 - II. Star formation and chemical evolutionary history*, Mon. Not. R. Astron. Soc., 2008, 385, 675

[111] Spolaor M., Kobayashi C., Forbes D.A., Couch W.J., and Hau G.K.T., *Early-type galaxies at large galactocentric radii - II. Metallicity gradients and the [Z/H]-mass, [alpha/Fe]-mass relations*, Mon. Not. R. Astron. Soc., 2010, 408, 272

[112] Szomoru D. et al., *Confirmation of the Compactness of a* $z = 1.91$ *Quiescent Galaxy with Hubble Space Telescope's Wide Field Camera 3*, The Astrophysical Journal, 2010, 714, L244

[113] Tamburri S., Saracco P., Longhetti M., Gargiulo A., Lonoce I., and Ciocca, F. *The population of early-type galaxies: how it evolves with time and how it differs from passive and late-type galaxies*, Astronomy and Astrophysics, 2014, 570, 102

[114] Thomas D., Maraston C., and Bender R., *The Epochs of Early-Type Galaxy Formation*, Astrophysics and Space Science, 2002, 281, 371

[115] Thomas D., Maraston C., and Korn A., *Higher-order Balmer line indices in alpha/Fe-enhanced stellar population models*, Mon. Not. R. Astron. Soc., 2004, 351, L19

[116] Thomas D. et al., *The epochs of early-type galaxy formation as a function of environment*, The Astrophysical Journal, 2005, 621, 673

[117] Thomas D., Maraston C., Schawinski K., Sarzi M., and Silk J., *Environment and self-regulation in galaxy formation*, Mon. Not. R. Astron. Soc., 2010, 404, 1775

[118] Thomas D., Maraston C., and Johansson J., *Flux-calibrated stellar population models of Lick absorption-line indices with variable element abundance ratios*, Mon. Not. R. Astron. Soc., 2011, 412, 2183

[119] Thomas D. et al., *Stellar velocity dispersions and emission line properties of SDSS-III/BOSS galaxies*, Mon. Not. R. Astron. Soc., 2013, 431, 1383

[120] Trager S.C., Faber S.M., Worthey G., and González J.J., *The Stellar Population Histories of Local Early-Type Galaxies. I. Population Parameters*, The Astrophysical Journal, 2000, 119, 1654

[121] Treu T. et al., *The properties of field elliptical galaxies at intermediate redshift - III. The Fundamental Plane and the evolution of stellar population from* $z \approx 0.4$ *to* $z = 0$, Mon. Not. R. Astron. Soc., 2001, 326, 237

[122] Treu T. et al., *The evolution of field early-type galaxies to* $z \sim 0.7$, The Astrophysical Journal, 2002, 564, L13

[123] Treu T. et al., *The assembly history of field spheroidals: evolution of mass-to-light ratios and signature of recent star formation*, The Astrophysical Journal, 2005, 633, 174

[124] Trinchieri G. and di Serego Alighieri S., *H-alpha images of early type galaxies with hot gas*, The Astronomical Journal, 1991, 101, 1647

[125] Trujillo I. et al., *Superdense Massive Galaxies in the Nearby Universe*, The Astrophysical Journal Letters, 2009, 692, L118

[126] van Albada T.S., *Dissipationless galaxy formation and the* $r^{1/4}$ *law*, Mon. Not. R. Astron. Soc., 1982, 201, 939

[127] van de Sande J. et al., *Stellar kinematics of* $z \sim 2$ *galaxies and the inside-out growth of quiescent galaxies*, The Astrophysical Journal, 2013, 771, 85

[128] van der Wel A. et al., *Mass-to-light ratios of field early-type galaxies at* $z \sim 1$ *from ultradeep spectroscopy: evidence for mass-dependent evolution*, The Astrophysical Journal, 2005, 631, 145

[129] van Dokkum P.G. et al., *Hubble Space Telescope Photometry and Keck Spectroscopy of the Rich Cluster MS 1054-03: Morphologies, Butcher-Oemler Effect, and the Color-Magnitude Relation at* $z = 0.83$, The Astrophysical Journal, 2000, 541, 95

[130] van Dokkum P.G. et al., *The fundamental plane at* $z = 1.27$*: first calibration of the mass scale of red galaxies at redshift* $z > 1$, The Astrophysical Journal, 2003, 585, 78

[131] Vanzella E. et al., *The Great Observatories Origins Deep Survey. VLT/FORS2 spectroscopy in the GOODS-South Field*, Astronomy and Astrophysics, 2005, 434, 53

[132] Vanzella E. et al., *The great observatories origins deep survey. VLT/FORS2 spectroscopy in the GOODS-South field: Part III*, Astronomy and Astrophysics, 2008, 478, 83

[133] Williams R.J., Quadri R.F., Franx M., van Dokkum P., and Labbé I., *Detection of Quiescent Galaxies in a Bicolor Sequence from* $z = 0 - 2$, The Astrophysical Journal, 2009, 691, 1879

[134] Williams C.C. et al., *The Progenitors of the Compact Early-type Galaxies at High Redshift*, The Astrophysical Journal, 2014, 780, 1

[135] Worthey G., Faber S.M., González J.J., and Burstein D., *Old stellar populations. 5: Absorption feature indices for the complete LICK/IDS sample of stars*, The Astrophysical Journal Supplement Series, 1994, 94, 687

[136] Worthey G., and Ottaviani D., *Hgamma and Hdelta Absorption Features in Stars and Stellar Populations*, The Astrophysical Journal Supplement Series, 1997, 111, 377

[137] Yan, R., Newman J.A., Faber S.M., Konidaris N., Koo D., and Davis M., *On the Origin of [OII] Emission in Red-Sequence and Poststarburst Galaxies*, The Astrophysical Journal, 2006, 648, 281

[138] Yi S.K., and Yoon S., *UV Upturn in Elliptical Galaxies: Theory*, The Astrophysical Journal Supplement Series, 2004, 291, 205

[139] Ziegler B.L., Thomas D., Böhm A., Bender R., Fritz A., and Maraston C., *Kinematic and chemical evolution of early-type galaxies*, Astronomy and Astrophysics, 2005, 433, 519

[140] http://iraf.noao.edu

Monthly Notices
of the
ROYAL ASTRONOMICAL SOCIETY

MNRAS **444,** 2048–2064 (2014) doi:10.1093/mnras/stu1593

Spectral detection of multiple stellar populations in $z \sim 1$ early-type galaxies

I. Lonoce,[1,2★] M. Longhetti,[1] P. Saracco,[1] A. Gargiulo[1] and S. Tamburri[1,2]

[1] *INAF–Osservatorio Astronomico di Brera, via Brera 28, I-20121 Milano, Italy*
[2] *Dipartimento di Scienza e Alta Tecnologia, Università degli Studi dell'Insubria, via Valleggio 11, I-22100 Como, Italy*

Accepted 2014 August 5. Received 2014 July 4; in original form 2014 January 24

ABSTRACT

We present a spectroscopic analysis based on measurements of two mainly age-dependent spectrophotometric indices in the 4000 Å rest-frame region, i.e. H+K(Ca II) and Δ4000, for a sample of 15 early-type galaxies (ETGs) at $0.7 < z_{\rm spec} < 1.1$, morphologically selected in the GOODS-South field. Ages derived from the two different indices by means of the comparison with stellar population synthesis models are not consistent with each other for at least nine galaxies (60 per cent of the sample), while for the remaining six galaxies, the ages derived from their global spectral energy distribution (SED) fitting are not consistent with those derived from the two indices. We then hypothesized that the stellar content of many galaxies is made of two stellar components with different ages. The double-component analysis, performed by taking into account both the index values and the observed SED, fully explains the observational data and improves the results of the standard one-component SED fitting in 9 out of the 15 objects, i.e. those for which the two indices point towards two different ages. In all of them, the bulk of the mass belongs to rather evolved stars, while a small mass fraction is many Gyr younger. In some cases, thanks to the sensitivity of the H+K(Ca II) index, we find that the minor younger component reveals signs of recent star formation. The distribution of the ages of the younger stellar components appears uniformly in time and this suggests that small amounts of star formation could be common during the evolution of high-z ETGs. We argue the possibility that these new star formation episodes could be frequently triggered by internal causes due to the presence of small gas reservoir.

Key words: galaxies: elliptical and lenticular, cD – galaxies: evolution – galaxies: formation – galaxies: high-redshift – galaxies: stellar content.

1 INTRODUCTION

Early-type galaxies (elliptical and lenticular, hereafter ETGs) are well-known precious high-redshift candidates to trace observationally the formation and evolution of the main structures in the Universe, since they are the most massive and so the brightest galaxies and contain most of the local observed stars and baryons (Renzini 2006, and references therein). Also the homogeneous properties of their stellar content put them in a privileged position to explore the history of their stellar mass assembly.

Despite the lower quality and quantity of high-redshift data, direct measurements on the stellar populations of high-z galaxies still remain the best solid way to constrain the earlier evolution of ETGs (Van der Wel et al. 2005; Cappellari et al. 2009; Guo et al. 2011; Strazzullo et al. 2013). In fact, the possibility of detecting pieces of direct evidence of stellar evolution, both through photometric and spectroscopic data, is almost unique in a redshift range, i.e. $1 < z < 2$, where most of the ETG evolution is expected (Cimatti et al. 2004; Glazebrook et al. 2004). A second convenience of dealing with high-z data is the more reliable use of the synthetic modelling which, thanks to the relative young ages of high-z sources, is significantly less affected by degeneracy effects, e.g. age–metallicity degeneracy which is dominant in the local ETGs.

Up to now, the most used method to explore the stellar population properties of high-z ETGs is the analysis of the spectral energy distribution (SED) by means of multiband photometry (Daddi et al. 2005; Longhetti & Saracco 2009; Santini et al. 2009; Sanchez et al. 2011). However, the physical parameters extracted from the SED fitting process on synthetic models, like in particular age, are actually only indicative mean values; thus, this method misses the detection of the possible presence of inhomogeneities in the stellar content. In contrast, a restricted but more detailed spectroscopic analysis would be an interesting challenge to unveil that information lost in the whole SED analysis.

★ E-mail: ilaria.lonoce@brera.inaf.it

Published by Oxford University Press on behalf of the Royal Astronomical Society

The important goal to be reached through the analysis of the stellar population properties of galaxies observed at $z \sim 1$ in their critical state of evolution is to understand if all of their stars are coeval and still passively evolving, as they are usually modelled with $z_{\rm form} > 2$–3 (Renzini 2006), or there are some pieces of evidence of later star-forming episodes or minor merging events which led to composite stellar populations already at $z \sim 1$.

The hidden complexity of the star formation history of ETGs has been revealed by many works on local ETGs (Coccato, Gerhard & Arnaboldi 2010; Panuzzo et al. 2011; Kaviraj et al. 2012; Rocca-Volmerange et al. 2013), and at intermediate redshift (Treu et al. 2002), where different kinds of signature suggest that elliptical galaxies have possibly undergone rejuvenation episodes in their recent history. Also at high redshift, with both archaeological and direct measurements, the necessity of introducing multiple stellar populations, with different stellar properties, in the used modelling has been found (Gargiulo et al. 2012; Huang et al. 2013). The main stellar properties involved in the differentiation of stellar components are age and metallicity. However, age is surely the first stellar parameter which should be investigated on high-z ETGs. In fact, direct spectroscopic measurements of stellar metallicity on high-z ETGs are still a hard issue; moreover, Gargiulo et al. (2012) found that age gradients are necessary to reproduce the majority of the observed high-z colour gradients.

Coexistent different stellar populations in ETGs are expected from the theoretical models on galaxy formation and evolution: minor mergers and small accretion events instead of major mergers, in fact, are predicted to be frequent until $z = 0$ (Naab, Johansson & Ostriker 2009; Oser et al. 2010, 2012). This inside-out formation scenario, however, predicts that for high-mass galaxies, accreted stars have been formed in the same epoch of '*in situ*' stars (Oser et al. 2010), assembling thus composite stellar populations of rather coeval stellar content, though the minor mergers have occurred at different times.

So the attention now should be focused on finding some observables which allow one to understand how homogeneous are the stellar populations of elliptical galaxies and how important are the mass fraction and the age of the accreted stars. A spectroscopic analysis on a sample of high-z ETGs can surely reveal precious details on their stellar properties, to shed light on the composition of the stellar populations of galaxies in their earlier phases of evolution. Previously, other pioneer works (Onodera et al. 2012; Jørgensen & Chiboucas 2013) have been devoted to the analysis of spectroscopic high-z data, revealing many differences in the stellar properties of $z > 1$ objects with respect to local ETGs, such as the presence of extreme values of spectral indices not foreseen by models (Onodera et al. 2012). In this paper, we present our spectroscopic analysis of a small sample of ETGs based on some of the first high-quality optical spectroscopic data at $z \sim 1$ in the GOODS-South field, which, thanks to the measurements of reliable age-dependent spectrophotometric indices in the 4000 Å rest-frame region, i.e. the H+K(Ca II) and $\Delta4000$, has led to interesting results on this topic.

The paper is organized as follows: in Section 2 we introduce our sample and describe the spectroscopic data with the main passes of the data reduction. In Section 3, we present the definition and the measurements of the spectrophotometric indices which are the basis of our spectral analysis. The comparison of the obtained results with synthetic stellar population models is widely discussed in Section 4, together with the description of our proposed double-component models. In Section 5, we discuss our results through the comparison with other works based on high-z spectral analysis. We propose the summary and our conclusion in Section 6.

Throughout this paper, we assume a standard cosmology with $H_0 = 70\,{\rm km\,s^{-1}\,Mpc^{-1}}$, $\Omega_{\rm m} = 0.3$ and $\Omega_\Lambda = 0.7$. All photometric magnitudes are expressed in the AB system.

2 THE SAMPLE

The sample consists of 15 ETGs at $0.7 < z_{\rm spec} < 1.1$ morphologically selected from a catalogue complete to $K \simeq 22$ (Tamburri et al., in preparation), in the southern field of the Great Observatories Origins Deep Survey (GOODS-South v2; Giavalisco et al. 2004). The selection criterion of this sample was basically the availability of sufficient high-quality (S/N > 5) spectroscopic data to perform the measurements of the main spectrophotometric indices in the 4000 Å break region, which is the aim of this work. Thus, starting from the complete sample of 196 morphologically selected ETGs with $K < 22$, only 15 could provide a high-S/N spectrum suitable for the present study (see Section 2.1 for details).

All the selected galaxies have the 14-band GOODS-South survey coverage (Santini et al. 2009): deep optical images taken from four *Hubble Space Telescope*-Advance Camera for Surveys bandpasses (*F*435*W*, *F*606*W*, *F*775*W* and *F*850*LP*); photometric data provided by extensive observations of European Southern Observatory (ESO) telescopes both in the optical (three *U*-band filters) and in the near-infrared (*J*, *H* and *K* filters), and by the four *Spitzer*-Infrared Array Camera (IRAC) bands (3.6, 4.5, 5.8 and 8.0 μm).

Thanks to these multiwavelength data, we were able to perform the global SED fitting of all the galaxies of the sample in order to extract the global stellar population properties. The SED fitting process was carried out assuming the stellar population synthesis model of Bruzual and Charlot (Bruzual & Charlot 2003, hereafter BC03) with a Chabrier initial mass function (IMF; Chabrier 2003). We adopted star formation histories with five exponentially declining star formation rates with *e*-folding time $\tau = [0.1, 0.3, 0.4, 0.6, 1.0]$ Gyr and assumed solar metallicity $Z = 0.020$. Dust extinction, following Calzetti et al. (2000), was applied in the range $0 < A_v < 2$ mag. In Table 1, we report the stellar parameters obtained from the SED fitting of the 15 ETGs: photometric ages ${\rm Age}_{\rm phot}$ of the stellar populations, dust extinction A_v, stellar masses $\mathcal{M}_*$ and star formation time-scale τ.

For five objects out of the whole sample (those at the highest spectral resolution), the velocity dispersion measures are available (Van der Wel et al. 2005). Furthermore, 7 out of the 15 target galaxies (those at $z > 0.9$) are included in the complete sample of the GOODS-South field ETGs at $z > 0.9$ (Saracco, Longhetti & Gargiulo 2010).

2.1 Spectroscopic data

As already mentioned, our sample of ETGs was collected following the disponibility of high-S/N optical spectra in the GOODS-South field for galaxies morphologically confirmed as ETGs with $z \sim 1$. High-quality spectra come from three different observing campaigns: one summarized in Mignoli et al. (2005, K20 survey), one in Popesso et al. (2009) and in Van der Wel et al. (2005). We could not use spectra coming from the campaign VLT/FORS2 (FOcal Reducer and low dispersion Spectrograph for the Very Large Telescope) spectroscopy in the GOODS-South field reported in Vanzella et al. (2005, 2008), because observations have been made without the cut order filter OG590+32, so they have not a solid continuum shape calibration necessary for the measurement in particular of the $\Delta4000$ index.

Table 1. Sample of 15 ETGs. Data extracted from photometric analysis: stellar population age ($A_{\rm phot}$), dust extinction (A_v), logarithm of the stellar mass ($\log(\mathcal{M}_*)$) and star formation time-scale (τ). σ is the velocity dispersion measured by Van der Wel et al. (2005). Units of right ascension are hour, minutes and seconds, and units of declination are degrees, arcminutes and arcseconds.

ID-MUSIC	RA	Dec.	$z_{\rm spec}$	Age$_{\rm phot}$ (Gyr)	A_v (mag)	$\log(\mathcal{M}_*)$ ($M_\odot$)	τ (Gyr)	σ (km s^{-1})
1192[a]	3:32:25.16	−27:54:50.1	1.089	0.7	1.0	11.01	0.1	231 ± 15
1382[a]	3:32:22.93	−27:54:34.3	0.964	1.4	0.4	11.08	0.1	200 ± 9
1950[a]	3:32:26.29	−27:54:05.0	1.044	1.9	0.3	10.75	0.3	300 ± 30
1837[a]	3:32:19.29	−27:54:06.1	0.964	3.0	0.4	11.40	0.4	336 ± 18
2694[a]	3:32:31.37	−27:53:19.1	1.135	2.5	0.3	11.40	0.3	232 ± 19
9066[a]	3:32:33.06	−27:48:07.5	1.188	2.0	0.6	10.58	0.3	–
11539[a]	3:32:37.19	−27:46:08.1	1.096	2.3	0.5	11.42	0.3	–
10020	3:32:15.81	−27:47:13.6	0.738	1.8	0.5	10.85	0.3	–
10960	3:32:19.24	−27:46:32.2	0.737	2.4	0.3	10.76	0.3	–
11225	3:32:14.44	−27:46:24.5	0.736	1.4	0.2	10.22	0.1	–
9792	3:32:18.01	−27:47:18.6	0.734	3.25	0.5	11.58	0.4	–
13386	3:32:17.49	−27:44:36.7	0.734	1.7	0.3	10.31	0.3	–
9838	3:32:17.94	−27:47:21.5	0.732	3.25	0.2	11.08	0.4	–
17044	3:32:37.38	−27:41:26.2	0.672	3.25	0.1	11.21	0.4	–
7424	3:32:39.54	−27:49:28.4	0.669	2.6	0.2	10.54	0.4	–

[a] Objects belonging to 34 ETGs of Saracco et al. (2010).

The K20 survey is a near-infrared-selected redshift survey targeting galaxies ($K_s < 20$, Vega system) in two fields, one of which has been later included in the GOODS-South area. From this precious data base of public galaxy spectra (http://vizier.u-strasbg.fr/viz-bin/VizieR?-source=J/A%2BA/437/883), we have searched for the highest S/N spectra of $z \geq 0.7$ ETGs in the 4000 Å break region rest frame. We finally extracted eight ETGs in the redshift range $0.73 < z < 1.2$. Spectroscopic observations of these objects come from VLT-FORS1 in MOS mode and VLT-FORS2 in MXU mode (multi-object spectroscopy with exchangeable masks), with a set of grisms 150*I*, 200*I* and 300*I* providing dispersion of 5.5, 3.9 and 2.6 Å pixel^{-1} and spectral resolution of $R = 260$, 380 and 660, respectively. The observation period of the K20 spectroscopic survey was confined in 20 nights during four years (1999–2000, 2002). For more details, see Mignoli et al. (2005).

Our next source of optical spectra was the second campaign of the ESO-GOODS spectroscopic programme operated with VLT-VIMOS (VIsible MultiObject Spectrograph) and reported in Popesso et al. (2009). From the thousands of available spectra, we have looked for the ones with longer exposure time (exp-time >5 h) in order to reach the highest S/N for $z > 0.7$ ETGs. Moreover, our searching has been focused only on median resolution (MR – resolution $R = 580$, dispersion 2.5 Å pixel^{-1}) grism data, necessary to perform the measurements of the spectrophotometric indices. We found only two suitable objects in the redshift range $z \sim 0.7$–1.0. Observations were carried on during the winter of 2004–2005 for both objects. For deeper details, see Popesso et al. (2009).

Finally, the last five objects of our sample were analysed by means of the optical spectra coming from observations performed by Van der Wel et al. (2005) with FORS2 in MXU mode on VLT telescope. They used the GRIS-600z grism together with the OG590 order separation filter, with a resolution of $R \sim 1390$, that led to a binned spectral dispersion of 1.6 Å pixel^{-1} and a wavelength coverage from about 6500 to 11 000 Å (that means around the spectral region of the Balmer/4000 Å break for galaxies at $z \sim 1$). The observations of the five objects were carried out in the period from 2002 September to 2003 March, with a mean exposure time of about 11 h for object (for details , see Van der Wel et al. 2005).

All the details of the spectroscopic data are summarized in Table 2.

2.2 Data reduction

Spectra coming from Popesso et al. (2009) and Van der Wel et al. (2005) have been reduced starting from raw observed data. For K20-survey spectra, we used directly the online material (from Vizier: ‘K20 survey: spectroscopic catalogue (Mignoli et al. 2005)’). Standard spectral data reduction has been applied using IRAF software tools. Particular care has been devoted to the relative spectral flux calibration, which has been achieved using spectrophotometric standard stars observed in the same nights of the targets; in particular, for VLT-FORS2 data (Van der Wel et al. 2005), we took the mean sensitivity function built with standard stars of different spectral type, which reveal small intrinsic differences in their shape. Moreover, still with the aim of obtaining the best continuum shape calibration necessary for a solid measure of spectral indices, we applied a further continuum calibration on the VLT-FORS2 spectra: indeed we noted a systematic distortion of the spectrum shape for objects whose slits are shifted with respect to the central position, along the dispersion direction (see details in Longhetti et al., in preparation). The amount of the flux distortion is proportional to the distance of the slit from the central position and, in the particular case of our VLT-FORS2 objects, the maximum offset slit position leads to a variation up to about 30 per cent of the flux. We corrected for this further distortion using flat-field lamp spectra as standard spectral sources, available for all the slits. The ratio between the wavelength-calibrated flat-field spectrum obtained in a central position and the one obtained through each slit in offset position has been used for this further correction. The final check of the obtained continuum shape accuracy in the spectral region involved in the measure of the chosen spectrophotometric indices was to overlap the final 1D spectra with the photometric points in the optical bands. The agreement is reached within 1σ error from the photometric points.

Table 2. Information about the spectroscopic data used in this work: spectroscopic instrument, grism, dispersion, resolution and the observing run.

ID-MUSIC	Instrument	Grism	Dispersion (Å pixel^{-1})	Resolution	Observing run
1192	VLT-FORS2	600z	1.6	1390	Van der Wel et al. (2005)
1382	VLT-FORS2	600z	1.6	1390	Van der Wel et al. (2005)
1950	VLT-FORS2	600z	1.6	1390	Van der Wel et al. (2005)
1837	VLT-FORS2	600z	1.6	1390	Van der Wel et al. (2005)
2694	VLT-FORS2	600z	1.6	1390	Van der Wel et al. (2005)
9066	VLT-FORS2	300I	2.6	660	Mignoli et al. (2005)
11539	VLT-FORS2	200I	3.9	380	Mignoli et al. (2005)
10020	VLT-FORS1	150I	5.5	260	Mignoli et al. (2005)
10960	VLT-FORS2	150I	5.5	260	Mignoli et al. (2005)
11225	VLT-FORS2	200I	3.9	380	Mignoli et al. (2005)
9792	VLT-FORS1	150I	5.5	260	Mignoli et al. (2005)
13386	VLT-FORS2	200I	3.9	380	Mignoli et al. (2005)
9838	VLT-FORS1	150I	5.5	260	Mignoli et al. (2005)
17044	VLT-VIMOS	MR	2.5	580	Popesso et al. (2009)
7424	VLT-VIMOS	MR	2.5	580	Popesso et al. (2009)

Reduced monodimensional spectra of the whole sample are shown in Fig. 1 together with the principal absorption lines in the region of 4000 Å rest frame.

3 SPECTRAL INDEX MEASURES

As can be seen in Fig. 1, many absorption lines typical of the stellar atmospheres can be identified in the optical spectra of our selected sample: Balmer series, BL3580, CN, Ca II(H,K), *G* band. We have taken advantage of the quality of our sample spectra of ETGs in order to analyse the main properties of their stellar populations, in particular the *age* of their stellar content.

The most important age-dependent spectrophotometric indices in the observed optical region are the Δ4000 index, defined by Bruzual (1983) and Hamilton (1985) as the ratio between mean fluxes in two different wide spectral ranges around the 4000 Å rest frame

$$\Delta 4000 = \frac{\bar{F}_\nu(\lambda_1 - \lambda_2)}{\bar{F}_\nu(\lambda_3 - \lambda_4)} \qquad (1)$$

with $\lambda_1 - \lambda_2 = [4050\text{–}4250\,\text{Å}]$, $\lambda_3 - \lambda_4 = [3750\text{–}3950\,\text{Å}]$; and the H+K(Ca II) index, defined by Rose (1985) as the ratio between minimum fluxes of the two Ca II absorption lines H and K

$$\mathrm{H+K(Ca\,II)} = \frac{F_{\min}(\lambda_3, \lambda_4)}{F_{\min}(\lambda_1, \lambda_2)} \qquad (2)$$

with $\lambda_1 = 3926$, $\lambda_2 = 3940$, $\lambda_3 = 3961$, $\lambda_4 = 3975$. In particular, the Ca II(H) absorption line is blended with the Balmer Hϵ at $\lambda = 3969.65$ Å (see details in Longhetti et al. 1999).

The choice of measuring the values of these two spectrophotometric indices was supported by their intrinsic peculiarities. In fact, these indices not only are strongly dependent on stellar population's age variations, mainly for ages less than 6–7 Gyr which is about the age of Universe at $z \sim 1$, but they also present precious differences which have made their combined measure very interesting.

The Δ4000 index provides a measure of the age of the global stellar population: in fact, according with its definition, this index evaluates the ratio of the old and red stars flux with respect to the UV flux emission of the younger population. Higher is its value, older is the stellar content. The effect of the metallicity goes in the same direction of ageing, but this degeneracy is minimal for stellar populations younger than 6–7 Gyr (the upper limit of the age of our high-z galaxies sample). On the other hand, the H+K(Ca II) index is deeply dependent on the presence of young stellar populations: in fact, the ratio between H and K(Ca II) lines would be constant if it was not for the blend of H(Ca II) with Balmer Hϵ, which actually determines the index value. In particular, the effective ratio between H(Ca II)+Hϵ and K(Ca II) becomes <1 only for hot stars of type earlier than F5 which have strong Balmer series absorptions, with a minimum value for A-type Balmer-dominated stars (Rose 1985).

We measured Δ4000 and H+K(Ca II) indices on the spectra of our sample of ETGs, and results are reported in Table 3. It is worthy to note that the measure of the H+K(Ca II) index is sensitive to the spectral resolution of the spectral data (see Longhetti et al. 1999), and we take this into account when comparing measures with models. Indeed, each measure performed on the spectra was corrected by the corresponding factor which brings the index value as it was measured on a spectrum with the higher resolution of models. In order to obtain these correction factors, we have degraded the spectrum of a reference template, with the original resolution full width at half-maximum (FWHM) = 3 Å (in the spectral range 3000–5000 Å rest frame), to the lower resolutions of the observed spectra. We derived the correction factors by dividing the index values measured on the degraded spectra by those measured on the reference template. In particular, these correction factors decrease the index values up to about 5 per cent of their measured values in the case of the lower resolution grism ($R = 260$).

Furthermore, the broadening of the absorption lines due to the intrinsic velocity dispersion of galaxies affects the measure of this index. We thus corrected the raw H+K(Ca II) index measures obtained on the five ETGs observed at the highest spectral resolution (Van der Wel et al. 2005) for this effect, reporting them to the case of null velocity dispersion. We followed the same procedure as for the resolution correction: taking a reference template spectrum which has the same spectral resolution of Van der Wel et al. (2005) data, we enlarged their spectral lines convolving them with a Gaussian curve with different σ in order to simulate the effect of the velocity dispersion. We measured the H+K(Ca II) index values for each value of the applied velocity dispersion and derived the correction factors to be applied to the index measurements. The correction

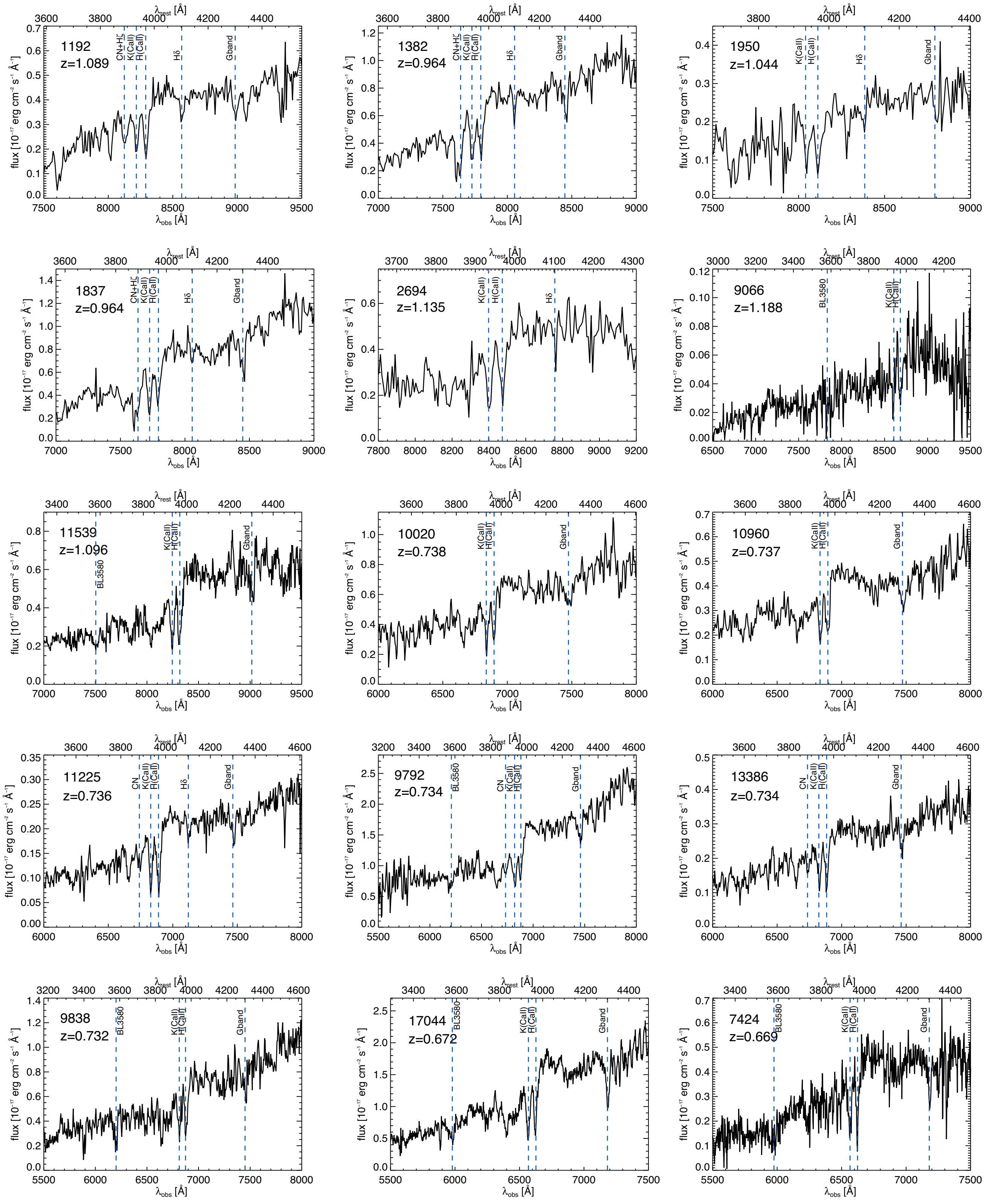

Figure 1. Spectra of the sample galaxies with the main absorption lines in the region of the Balmer/4000 Å break. Information about the spectroscopic data is shown in Table 2. Spectra are shown in bins spanning from 2.5 to 8 Å.

Table 3. Values of the measured H+K(Ca II) and Δ4000 indices.

ID-MUSIC	H+K(Ca II)	Δ4000
1192	0.75 ± 0.07	1.80 ± 0.04
1382	1.14 ± 0.07	2.15 ± 0.07
1950	0.97 ± 0.23	2.05 ± 0.1
1837	1.49 ± 0.10	2.16 ± 0.3
2694	1.07 ± 0.16	1.87 ± 0.06
9066	1.34 ± 0.27	1.65 ± 0.10
11539	1.15 ± 0.11	2.10 ± 0.05
10020	1.57 ± 0.23	1.84 ± 0.06
10960	1.31 ± 0.20	1.72 ± 0.04
11225	0.91 ± 0.13	1.81 ± 0.03
9792	1.15 ± 0.13	2.09 ± 0.04
13386	0.97 ± 0.15	1.76 ± 0.03
9838	0.84 ± 0.20	1.99 ± 0.06
17044	1.16 ± 0.12	2.05 ± 0.02
7424	0.58 ± 0.23	1.81 ± 0.07

factors were found to be rather small and well within the error bars. In particular, for three objects the correction was within 2 per cent of the measured value, and for the other two objects it was about 4 per cent. For all the other 10 ETGs of our sample, the lower spectral resolution of their observations prevents to appreciate the latter effect, being much larger than the broadening caused by the resolution itself. Indeed, we have verified that for the medium-resolution spectra (Popesso et al. 2009), the corresponding correction factors, assuming a typical velocity dispersion of 250 km s^{-1}, would be less than 1 per cent of the measured index values.

Errors have been computed from the uncertainties in the measures of fluxes and in the flux calibration. In particular, we have estimated the values of S/N ratios in the two spectral regions involved in the index definitions (i.e. 3750–4000 and 4050–4250 Å) which represent the statistical errors affecting the flux values. On the other hand, we took into account also the flux calibration uncertainties derived from both the standard flux calibration and from the further correction applied on the FORS-2 spectra which suffer for the shape distortion due to the CCD slit position (see Section 2.2). Obviously, the H+K(Ca II) index, being the flux ratio at two very close wavelengths, is almost unaffected by these flux calibration uncertainties. The final errors are shown in Table 3.

4 ANALYSIS

The measured values of the indices have been compared with the expectations of the spectrophotometric synthesis models (BC03) assuming a Chabrier IMF and an exponentially declining star formation history with time-scale τ (with the same assumptions of the photometric analysis, see Section 2, i.e. $\tau = 0.1-1$ Gyr and solar metallicity; afterwards we will discuss the effects of varying these assumptions). Indeed, to start with the simpler evolutionary modelling of star formation typical of ETGs, we assumed that the bulk of the star formation activity has happened in a confined initial episode with small time-scale τ ($\tau < 1$ Gyr, as it is the case of ETGs; see Saracco et al. 2010). In this scenario, the stellar content of galaxies is rather coeval, within τ, so if this evolutionary modelling is appropriate for the real star formation history of ETGs, we expected that the stellar ages derived from the values of the two indices would be consistent with each other.

Fig. 2 shows the comparison between data and models in the Δ4000 versus H+K(Ca II) plane. Black dots are galaxies from the spectroscopic sample of Van der Wel et al. (2005), red ones from Mignoli et al. (2005) and blue ones from Popesso et al. (2009). Lines represent the trends of the values of the two indices of synthetic models at different ages, from younger ages (10^8 yr) at the bottom left to older ages (10^{10} yr) at the upper right (at fixed solar metallicity), and their colours show different star formation histories determined by the time-scale parameter τ. From Fig. 2, it is possible to notice that (i) data points cover an extended area in the index–index plane which corresponds to stellar populations older than ∼2.5 Gyr; (ii) different τ-models (coloured lines) are confined in a rather thin strip, while measured data are more widespread. While the majority of the data points are in agreement with models, we get the evidence that for 6 out of 15 objects both indices deviate at more than 1σ from models. In particular, starting from the measured values of the Δ4000 index, 7 out of 15 data points have either too low values of the H+K(Ca II) index (IDs: 1192, 7424 and 9838), suggesting possible stellar populations younger than what pointed out from the Δ4000 index (see Section 3), or so high values of the H+K(Ca II) index (H+K(Ca II) > 1.2, IDs: 9066, 10960, 10020 and 1837) that they cannot find any correspondence with models within 2σ. It is important to notice that our sample of galaxies is not complete, so these percentages are just evidence that at least some of these high-redshift ETGs have a less homogeneous stellar population with respect to what is expected in a rigorous passive evolution.

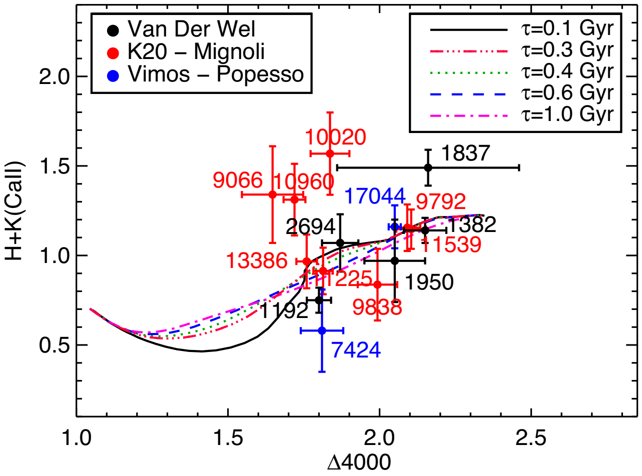

Figure 2. Data versus model comparison in the index–index plane: measured values of the indices Δ4000 (*x*-axis) and H+K(Ca II) (*y*-axis) from the spectroscopic sample of Van der Wel et al. (2005, black dots), Mignoli et al. (2005, red dots) and Popesso et al. (2009, blue dots), compared with the expectations of BC03 models at different ages (from left to right, from about 10^8 to 10^{10} yr), fixed solar metallicity and for different *star formation time-scale parameters* τ (coloured lines). With the exception of those from Van der Wel et al. (2005) sample, shown data points have H+K(Ca II) index values a bit underestimated (within error bars) with respect to those indicated by models due to the difference between the spectral resolutions of BC03 synthetic spectra (FWHM = 3 Å) and that of the observed ones (see Table 2).

Points that are not consistent with the proposed models at different star formation time-scales cannot be explained by using synthetic models with different *metallicities*. As an example, in Fig. 3 the same diagram of Fig. 2 is shown, but in this case the different coloured lines represent models with three distinct metallicities ($Z = 0.008$, 0.020 and 0.040), at fixed time-scale parameter ($\tau = 0.1$ Gyr). From Fig. 3, it is clear that the not consistent points still

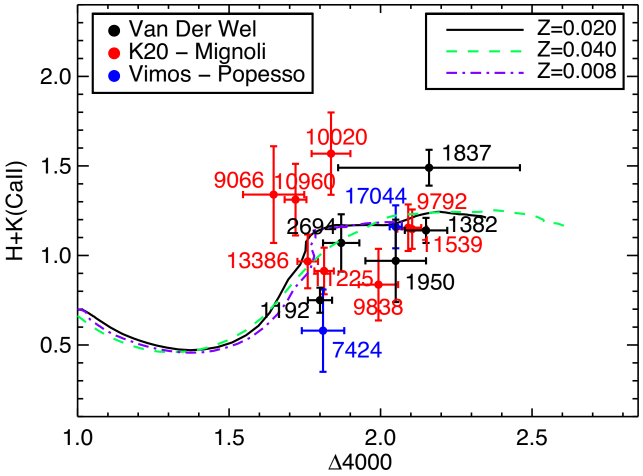

Figure 3. Data versus model comparison in the index–index plane: measured values of the indices Δ4000 (*x*-axis) and H+K(Ca II) (*y*-axis) from the spectroscopic sample of Van der Wel et al. (2005, black dots), Mignoli et al. (2005, red dots) and Popesso et al. (2009, blue dots), compared with the expectations of BC03 models at different ages (from left to right, from about 10^8 to 10^{10} yr), fixed star formation time-scale parameter τ and for different *metallicities*: $Z = 0.008$, 0.020 and 0.040 (coloured lines). As in Fig. 2, with the exception of those from the Van der Wel et al. (2005) sample, shown data points have H+K(Ca II) index values a bit underestimated (within error bars) with respect to those indicated by models due to the difference between the spectral resolutions of BC03 synthetic spectra (FWHM = 3 Å) and that of the observed ones (see Table 2).

remain without a satisfactory explanation on the basis of single-component star formation histories even at different metallicities.

Adding some amounts of dust ($A_v > 0.5$ mag) in the single-component models would marginally help in explaining those data points which have low values of the H+K(Ca II) index (IDs: 1192, 7424 and 9838). However, even this addition is not able to reproduce the index values of four objects with high H+K(Ca II) (IDs: 9066, 10960, 10020 and 1837) because its main effect is to little increase the values of the Δ4000 index. Moreover, this choice should be supported by a physical motivation able to justify these quantities of dust in systems where globally the star formation activity should be quenched (age $\gg \tau$).

We have also checked that the values of the two measured indices on synthetic models do not depend on the spectrophotometric models adopted in the analysis: comparing index values obtained from BC03 models with those obtained with the latest version of the same code (Charlot & Bruzual, in preparation), we do not find any difference, while the comparison with Maraston & Stromback (2011) models reveals small differences but well within the observational errors.

The comparison between the measured indices and models has thus suggested that the star formation histories of these galaxies must have been more complex, eventually involving the presence of later star formation events superimposed on a rather old bulk of stars, causing a less homogeneous population than predicted by simple short τ models.

A further confirmation of this evidence comes from the discrepancy we found among ages derived from the values of the two indices and those extracted from the SED fitting analysis, as shown in Table 4: the Δ4000 index points towards generally more evolved stellar populations. Ages deduced from the index values and reported in Table 4 have been derived assuming BC03 models, solar metallicity and $\tau = 0.1$ Gyr. Ages deriving from indices and from SED fitting are two different but complementary tools to study the stellar content of galaxies: the spectroscopic analysis is based on a small portion of the SED but it is able to give important details on their recent star formation history, while the photometric analysis can provide mean stellar parameters dealing with the whole SED. This first result thus suggests that in general the SED analysis is missing small pieces of information, revealed instead by the indices.

Moreover, for many objects (8 out of 15) the ages derived from the Δ4000 index tend to differ by more than 1σ from those derived from the H+K(Ca II) index. In particular, in one case they differ by more than 2σ (ID-9838). Furthermore, even if possible, it appears unlikely that the age inconsistency arisen from the two indices is due to measurement errors. Indeed, it would mean introducing a kind of systematicity which should always decrease the values of age derived from the H+K(Ca II) index and at the same time always increase those derived from the Δ4000 index. In fact, ages from the Δ4000 index are older than those indicated from H+K(Ca II)

Table 4. Age estimates derived from indices and photometric analysis (Gyr) obtained from the comparison with synthetic stellar populations models with $\tau = 0.1$ Gyr and solar metallicity.

ID-MUSIC	Age from H+K(Ca II) (Gyr)	Age from Δ4000 (Gyr)	Age from photometry (Gyr)
1192	1 ± 0.1	1.9 ± 0.5	0.7
1382	4.5 ± 1.5	5.5 ± 1.5	1.4
1950	1.7 ± 2	4 ± 1	0.7
1837	–	5.75 ± 3	0.9
2694	3 ± 1.2	2.4 ± 0.4	1.3
9066	–	0.9 ± 0.4	1.3
11539	4.7 ± 1.5	4.75 ± 0.5	1.3
10020	–	2.2 ± 0.5	1.3
10960	–	1.1 ± 0.3	1.4
11225	1.2 ± 0.5	1.9 ± 0.4	1.4
9792	4.7 ± 1.5	4.7 ± 0.9	2.7
13386	1.4 ± 0.6	1.5 ± 0.4	0.6
9838	0.9 ± 0.3	3.1 ± 0.4	2.3
17044	1.9 ± 1	3.75 ± 0.4	2.3
7424	0.7 ± 0.4	1.9 ± 0.5	1.4

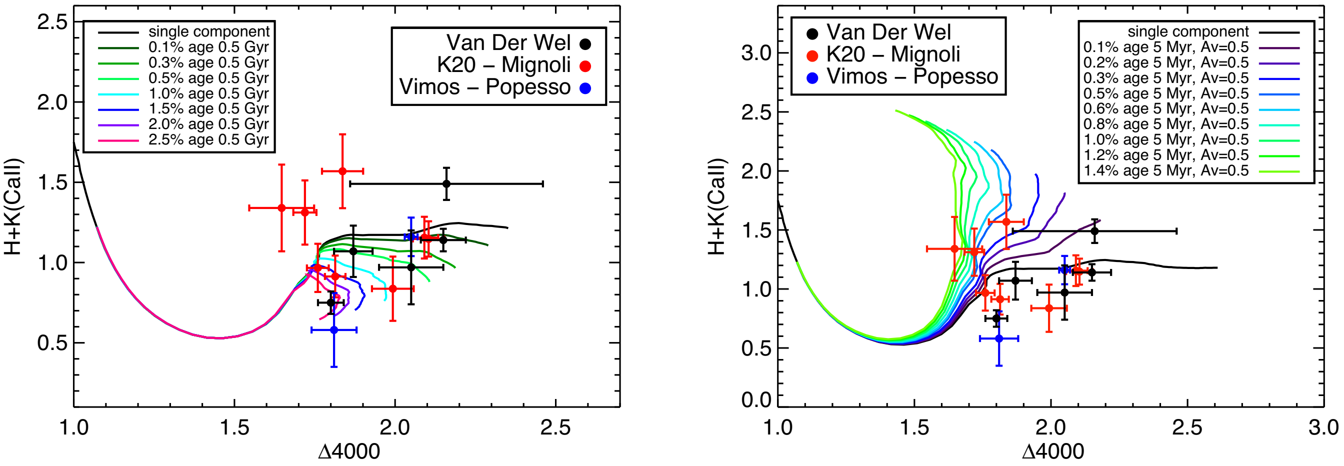

Figure 4. Index–index plane: comparison with *double-component* models. Left-hand panel: observed points are the same as in Fig. 2; lines represent the values of the indices on BC03 synthetic models composed of a main component whose age increases from left to right (from about 10^8 to 10^{10} yr), and by small mass fraction of a younger stellar component with age 0.5 Gyr. The fraction of the secondary component increases from 0.1 per cent (dark green line) to 2.5 per cent (magenta line). Right-hand panel: same as the left-hand panel; here the small and younger component has age 5 Myr and it has been reddened with a typical dust extinction of 0.5 mag. Mass fractions span from 0.1 per cent (violet line) to 1.4 per cent (green line). BC03 models are with fixed solar metallicity and $\tau = 0.1$ Gyr. As in Figs 2 and 3, with the exception of those from Van der Wel et al. (2005) sample; shown data points have H+K(Ca II) index values a bit underestimated (within error bars) with respect to those indicated by models due to the difference between the spectral resolutions of BC03 synthetic spectra (FWHM = 3 Å) and that of the observed ones (see Table 2). Both plots show how those data points which were not consistent with single-component models can be explained.

index (only for one object there is the opposite trend), in agreement with Onodera et al. (2012) who found similar results for passive galaxies at $z > 1.4$. Furthermore, in some cases, ID-2694, ID-9066, ID-10020 and ID-10960 as displayed in Table 4, H+K(Ca II) values do not find any age correspondence with models, as visible in Fig. 2. As discussed in Section 3, due to the nature of the two selected indices, we expect dissimilarity between them if the galaxy stellar content reveals non-homogeneous properties, especially age. For this reason, having found such a discrepancy in most cases, we started a new analysis of the star formation histories of our sample galaxies assuming that a quite recent star-forming event has been superimposed on an otherwise homogeneous and old stellar population.

As a pure exercise, we have performed the analysis based on the assumption of a double age stellar component for all the galaxies of the sample. The real convenience of introducing the second component, as discussed in the following section, is found only for those objects for which the age values derived from the two indices were not in agreement. And this is the case for 9 out of 15 galaxies. For the remaining galaxies, values of $\tau \geq 0.1$ Gyr are sufficient to explain the inhomogeneity of their stellar content even though with some corrections to the mean ages derived from the SED fitting analysis.

4.1 Double-component analysis

To better reproduce the observed stellar populations properties of our sample galaxies and in particular to reproduce the measured indices, we thus hypothesized the presence of *composite* stellar populations, assuming that after the initial bulk of star formation, additional events have occurred also in the following few Gyr. For the sake of simplicity, we started introducing only *double* stellar components; we cannot exclude that a more refined analysis which involves more than two spectral index measurements on higher quality spectra could eventually find the presence of triple and over stellar populations.

In Fig. 4 (left-hand panel), the comparison of the measured indices with those obtained on synthetic double-component models is shown: models represent galaxies for which the bulk of the stellar mass belongs to a population whose age increases from left to right (from about 10^8 to 10^{10} yr) in the index–index plane, and small mass fractions are taken into account by a younger component with fixed age 0.5 Gyr. Coloured lines represent the increasing intensity of the secondary burst, i.e. the fraction of the younger component, from the right (dark green line) with a fraction of 0.1 per cent to the left (magenta line) with 2.5 per cent. From this plot, it is clear that with only small mass fractions of a superimposed younger population, observed points with low H+K(Ca II) index values can be fully explained.

A similar explanation can be possibly advanced also for points with higher H+K(Ca II) index values, but with the addition of a further ingredient. Considering the definition of the H+K(Ca II) index, as discussed in Section 3, high index values would mean that the ‘H’ absorption line must be very weak with respect to the K(Ca II) line. We then hypothesized that the Balmer Hϵ line blended with the H(Ca II) line is in *emission* rather than in absorption. As shown in Fig. 5 in BC03 models, for stellar populations younger than <0.2 Gyr, Balmer Hϵ emission is dominant over the absorption. So that the presence of a small mass fraction of very young stellar population (i.e. very recent small burst) can be able to fill the depth of the whole H line, thus increasing the value of the H+K(Ca II) index. We then introduced in our analysis BC03 models which include the nebular emission lines (see Charlot & Longhetti 2001). In fact, as shown in Fig. 6, differences between models with emission (cyan solid line) and without emission (black dashed line) are evident for ages smaller than 1 Gyr; for older ages these models coincide. As an example of our analysis, in Fig. 4 (right-hand panel) the comparison of model prediction with the observed data in the case of double age component models is shown for a starburst age of

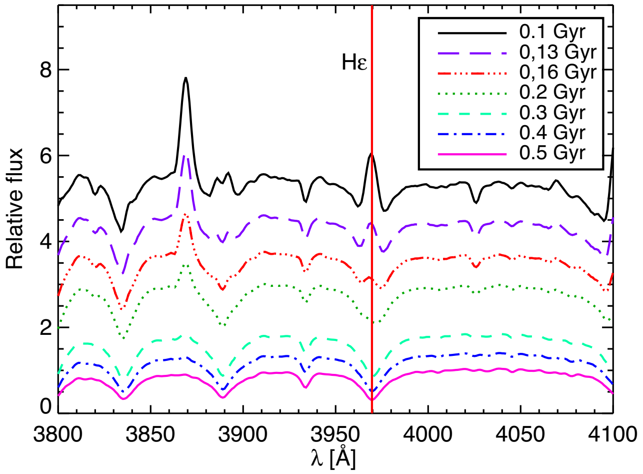

Figure 5. Synthetic spectra with Balmer Hϵ ($\lambda = 3969.65$ Å , red vertical line) emission line in models at different stellar population ages. Ages decrease from 0.5 Gyr (magenta line) to 0.1 Gyr (black line).

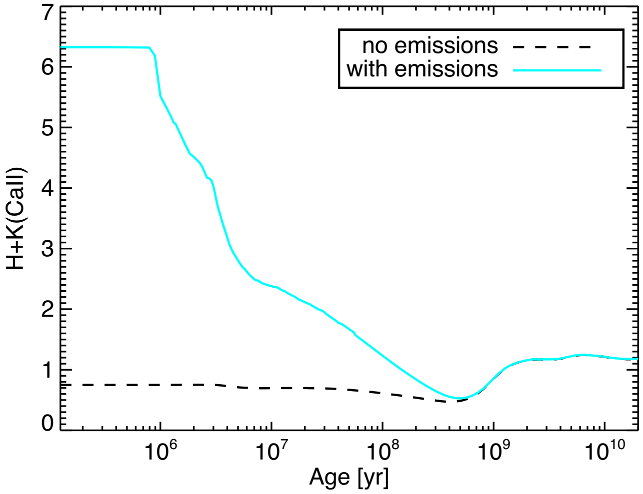

Figure 6. Trend of the H+K(Ca II) index with age measured on BC03 models with Balmer lines emission (cyan solid line) and without emission (black dashed line). Differences between two models become important only for stellar population with age <1 Gyr.

5 Myr. Given the very young age of the secondary component, we took into account the possible dust extinction that should be acting around it, assuming $A_v = 0.5$; we specify that the introduction of dust affects only the $\Delta 4000$ index, increasing its value in the same way as age. The intensity of the star formation burst increases from right (violet line), with a mass fraction of 0.1 per cent, to left (green line), with a mass fraction of 1.4 per cent. Both panels of Fig. 4 are useful examples that show how the suggested presence of small mass fraction of younger stellar component is able to explain the observed data. Age and percentage of mass involved in the secondary component (i.e. age and strength of the recent burst) can be varied to exactly match each single observation. Below we present the detailed analysis of the whole sample of galaxies and the obtained results.

Each galaxy has been analysed by means of a code that, spanning all the double-component possible models, extracts best-fitting solutions, following the analogue of the one-component photometric analysis. Assuming the BC03 models, including possible emission nebular components, with fixed $\tau = 0.1$ Gyr and solar metallicity, the code builds all the possible double-component combinations of spectra varying ages, mass fractions and dust extinction of the two stellar components. A maximum age limit has been imposed equal to the age of the Universe at the redshift of each galaxy. Recent burst strengths (i.e. the mass percentage involved in the young component) have been considered by means of 0.05 per cent steps. Dust extinction has been applied both on the whole double-component spectrum and only on the younger component, in parallel distinct analysis, with a 0.1 mag pass.

From the generated composed synthetic spectra, our code selects the solutions which are consistent with the measured values of the two spectrophotometric indices within their observational errors. After this selection, the code starts the χ^2 minimization process of the composite synthetic SED on the observed photometric data. In this way, not only the optical band is considered, but the whole spectral distribution.

The results of the analysis are shown in Table 6. Mass fraction values expressed in Table 6 are indicative of the amount of mass for the solutions with lower χ^2 values. The sample objects are well described by two-component models, revealing the consistence of the found solutions with the presence of a younger stellar population for almost all the galaxies of the sample. Moreover, thanks to the procedure applied in our code, all the composite spectra are fully consistent with the measured indices, contrary to the single-component analysis from which this happens only for a couple of objects. Dust extinction in general becomes important, i.e. $A_v > 2$, only for objects whose young component is younger than the star formation time-scale parameter $\tau = 0.1$ Gyr, that means that the star formation is still ongoing.

The improvement in terms of probability $P(\chi^2)$ of the obtained double-component solutions with respect to the single-component ones (with $\tau = 0.1$ Gyr, see Table 4) is illustrated in Table 5, where we report the comparison of the reduced-χ^2 (χ^2_ν). The estimation of the χ^2_ν includes both the contribution of the 14 photometric points which constitute the global SED and the values of the two analysed spectral indices. It is worth to remark that in this part of the analysis, for consistency, we have compared the double-component models with the single-component ones obtained with fixed small $\tau = 0.1$ Gyr. Accordingly, the χ^2_ν values and the corresponding probabilities shown in Table 5 are referred to these particular SED fitting solutions.

As can be seen from Table 5, the double-component solutions are preferable over the single-component ones for almost all the galaxies of the sample. More in details, for 9 out of 15 galaxies (60 per cent of the sample) (IDs: 1192, 1950, 1837, 9066, 10020, 10960, 9838, 17044 and 7424), which have the age values derived from indices not in agreement with each other (see Table 4), the double-component solutions with age differences >1.5 Gyr are clearly more representative of their inhomogeneous stellar contents. For the other six objects, even if providing statistically more probable solutions for four out of six cases, the double-component analysis appears not significantly necessary. Indeed, for these six galaxies the ages derived from the two indices result all in agreement with each other pointing to the same generally older age with respect to the ages extracted from the SED fitting analysis (see Table 4). In particular, for three galaxies (IDs: 1382, 11539 and 9792), the double-component solutions are statistically more probable actually just because the bulk of the mass (>98 per cent) matches the age indicated by the two indices (compare Table 4 with Table 6), while the single-component solutions miss this important information. Only for the remaining three cases (IDs: 2694, 11225 and 13386) both indices and

Table 5. Comparison of the reduced-χ^2 and corresponding probabilities between the single- and double-component solutions. The χ^2_ν estimations include the comparison among the photometric points and the analysed spectral indices.

ID	χ^2_ν single component	Associated probability (per cent)	χ^2_ν double component	Associated probability (per cent)
1192	5.01	0.7	1.14	32
1382	13.6	0	3.7	16
1950	7.5	0.06	2.94	5
1837	19.94	0	1.31	27
2694	1.56	21	1.8	16
9066	3.31	4	0.66	52
11539	12.66	0	1.16	31
10020	5.02	0.7	0.844	43
10960	3.85	2	1.74	17
11225	0.59	55	0.77	46
9792	9.05	0.01	1.64	19
13386	4.89	0.7	1.16	31
9838	3.43	3	1.26	28
17044	9.87	0.01	1.31	27
7424	2.038	13	1.01	36

Table 6. Results obtained from the double-component analysis on the sample of galaxies extracted from the composition of BC03 models, with fixed $\tau = 0.1$ Gyr and solar metallicity. Mass fractions are the indicative values for the solutions with lower χ^2 values.

ID	Age young component (Gyr)	Mass fraction (per cent)	Age old component (Gyr)	Mass fraction (per cent)	A_v (mag)	Age differences (Gyr)	$z_{\rm form}$ bulk
1192	0.64	6.5	2.4	93.5	0	1.76	2.15
1382	0.1	0.05	5	99.95	0.9^a	4.9	6.1
1950	0.45	1	5.5	99	0	5.05	>6
1837	0.015	0.95	5.5	99.05	2.8^a	5.485	>6
2694	0.5	0.65	2.3	99.35	0.1	1.8	2.2
9066	0.006	0.75	1.7	99.25	2.8^a	1.694	1.95
11539	0.3	0.1	4.75	99.9	0.2^a	4.45	>6
10020	0.03	1.5	2.6	98.5	2.3^a	2.57	1.45
10960	0.015	1.65	2.3	98.35	2.6^a	2.285	1.32
11225	0.9	20	6.25	80	0.2	5.35	>6
9792	0.8	1.65	4.75	98.35	0.3	3.95	2.86
13386	0.1	0.1	1	99.9	0.3	0.9	1
9838	0.5	2.6	4	97.4	0.8^a	3.5	2.16
17044	1	5.3	7	96.5	0.2	6	>6
7424	0.7	16.7	6.25	83.3	0.5^a	5.55	5.5

^{a} A_v applied only on the young component.

$\tau \geq 0.1$ Gyr SED fitting analysis point to the same age, directly revealing a rather homogeneous stellar population.

Summarizing, the double-component analysis shows that in 60 per cent of the galaxies of our sample there are two stellar components whose presence explains the different ages derived from the index values. Furthermore, thanks again to the index values, this analysis has confirmed or corrected the ages of the SED fitting solutions for the remaining objects.

In Fig. 7, we present two examples of the analysis that we performed on two opposite cases which are not consistent with a single-component description: object ID-9066 (top panels) which has a high H+K(Ca II) value (>1.2) and object ID-7424 (bottom panels) which has a low value of the H+K(Ca II) index. In the caption of Fig. 7, we report, as example, the detailed discussion of these two representative cases. Left-hand panels of Fig. 7 show the comparison between the single-component (black) and double-component (red) best-fitting solutions on the observed SED (blue points): both the presented double-component models fit better the spectral distributions. Focusing on the 4000 Å rest-frame region (right-hand panels), it can be seen that the double-component spectrum (red) reproduces better the observed spectrum (black) than the single-component model (green), in particular the features involved in the H+K(Ca II) index definition (i.e. the H and K absorption lines).

4.1.1 *The ages of the two stellar components*

As we have seen from the analysis of our sample, based on both the spectral indices and the photometric SED fitting, we found evidence that at least 60 per cent of the selected ETGs have the bulk of the mass composed of rather old stars and a small percentage of younger stars. In the following, we include also the three objects (IDs: 1382, 11539 and 9792) for which we have corrected the age of the bulk of stars by means of the index values; indeed, the amounts of younger component, although not necessary, are found to be very small. In this 80 per cent of our sample, which we remark here is not complete, with the exception of object ID-7424, we find that the mass fractions of the younger component are small, less than

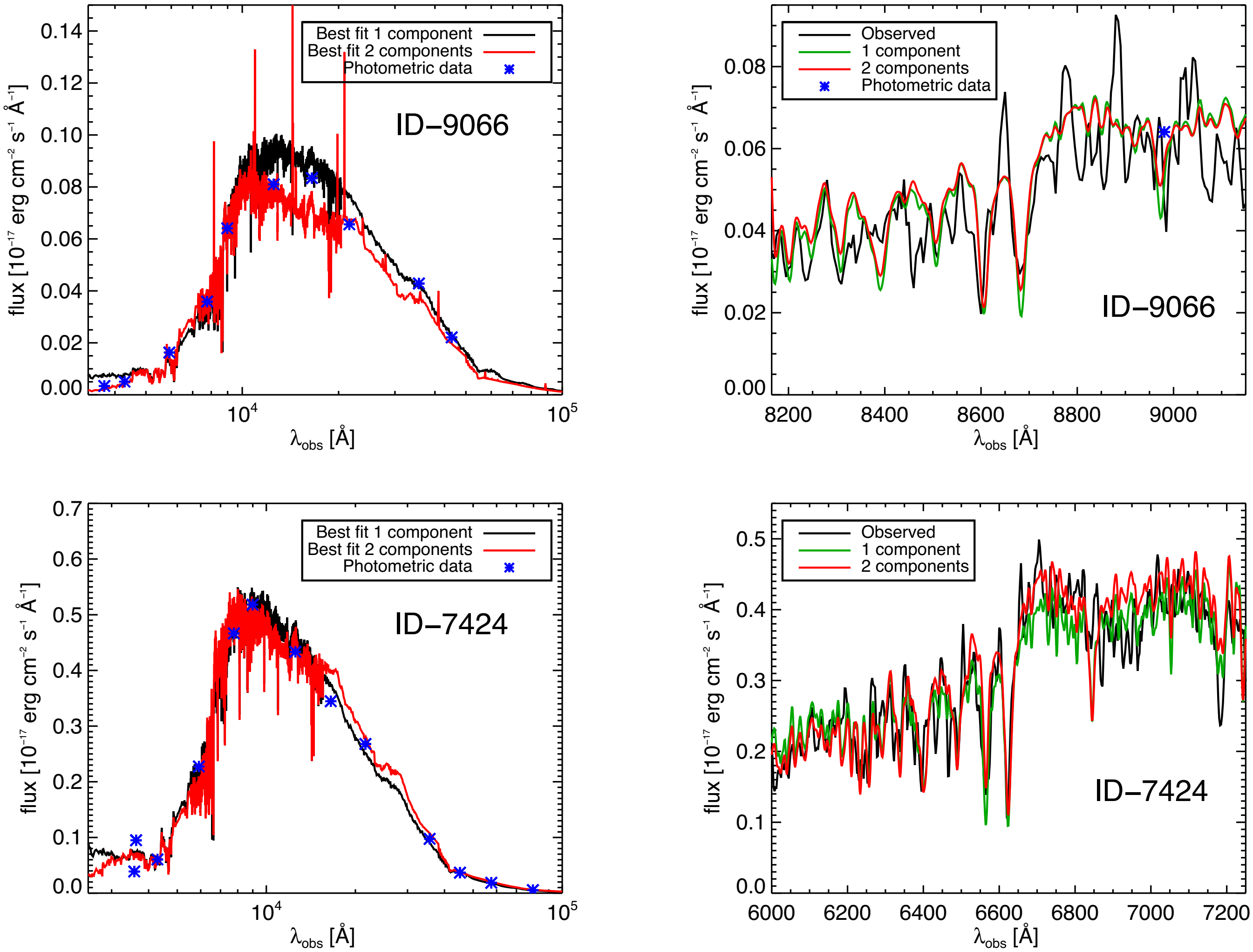

Figure 7. Left-hand panels: comparison between single-component solutions (red line) and double-component models (black line) on the observed SED (blue points). Right-hand panels: comparison between single-component spectrum (green) and double-component spectrum (red) on the observed spectrum (black) in the region of the 4000 Å rest frame. Upper panels: galaxy ID-9066. Analysis: the corresponding stellar age of this object from the SED fitting analysis was 2 Gyr (with $\tau = 0.3$ Gyr and $A_v = 0.6$, see Table 1); instead, from the index measurements we obtained an age estimate of about 0.9 Gyr from the Δ4000 index and none from the H+K(Ca II) index because its value is above the critical value (i.e. 1.2). We thus proceeded with the double-component analysis on models with gas emission lines. The result is a composite stellar population with a 6 Myr younger component (with signs of recent star formation) reddened with $A_v = 2.8$, superimposed on the bulk of the stellar mass (>99.3 per cent) with an older age of 1.7 Gyr. The value of the older component age is similar to the photometric age, but the single-component solution was not consistent with the measured indices. Instead the double-component solution, with the adding of small amounts of very young stellar population, has been able to adjust the fit of the spectral features, and taking into account at the same time the trend of the whole SED. Bottom panels: galaxy ID-7424. Analysis: from the SED fitting analysis this object was described by a 2.6 Gyr old stellar population with $\tau = 0.4$ Gyr and $A_v = 0.2$, on the other hand, H+K(Ca II) and Δ4000 indices pointed to ages of 0.7 and 1.9 Gyr, respectively (see Table 4). Moreover, the single-component solution was not consistent with the measure of the H+K(Ca II) index. The double-component analysis found a consistent solution composed by a main component with old age 6.25 Gyr and a relative high fraction (about 15 per cent) of a young component with age 0.7 Gyr, reddened with $A_v = 0.5$.

10 per cent, with the smallest being 0.05 per cent, while the bulk of the mass belongs to the older component. The distributions of the ages of the old (left-hand panel) and young (right-hand panel) components of this part of the sample are shown in Fig. 8. White data represent the whole 80 per cent of the sample, while blue and green shaded data represent subsamples at, respectively, $z \sim 0.7$ and $z \sim 1$. Considering the old component age distribution (left-hand panel), it appears bimodal with a younger sample with a mean age of 2.25 Gyr and with an older one of 5.3 Gyr. This means that the bulk of their stars formed at $1 < z_{\rm form} < 3$ and $z > 5$, as can be seen in Fig. 9 which clearly shows that both the two subsamples of galaxies at $z_{\rm spec} \sim 0.7$ and $z_{\rm spec} \sim 1$ have a $z_{\rm form}$ of their main stellar component bimodally distributed, without any dependence on redshift. We remark that this result is evidence coming from a casually selected sample of ETGs and hence it cannot be interpreted as a general bimodality in the distribution of the star formation episodes in ETGs.

In contrast, in the young component histogram (Fig. 8, right-hand panel), the distribution is homogeneous with a mean age of 0.4 Gyr. From both histograms, it is clear that there is no dependence on redshift in the obtained results, so we cannot identify a single confined cosmic period for the formation of the stars neither of the old nor of the younger components.

It is worthy to note that the ages of the bulk components are generally older than the ages derived from the photometric analysis. Indeed, the main components generally reveal the same stellar ages

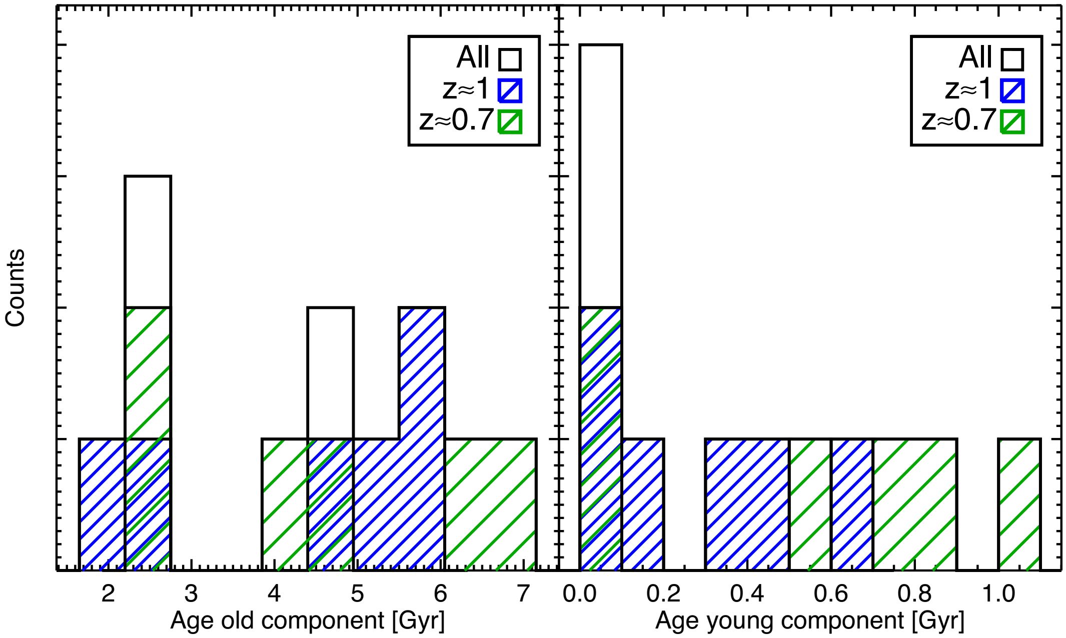

Figure 8. Histograms of the double-component analysis results on the 80 per cent of the sample (see Section 4.1.1). White: data from all the 80 per cent of the sample; blue shaded: data from the subsample of galaxies at $z \sim 0.7$; green shaded: data from the subsample of galaxies at $z \sim 1$. Left-hand panel: distribution of the ages of the old components in bins of 0.55 Gyr. There are two visible subsets with mean age of about 2.25 Gyr 5.3 Gyr. Right-hand panel: distribution of the ages of the young components in bins of 0.1 Gyr. The mean age is about 0.4 Gyr.

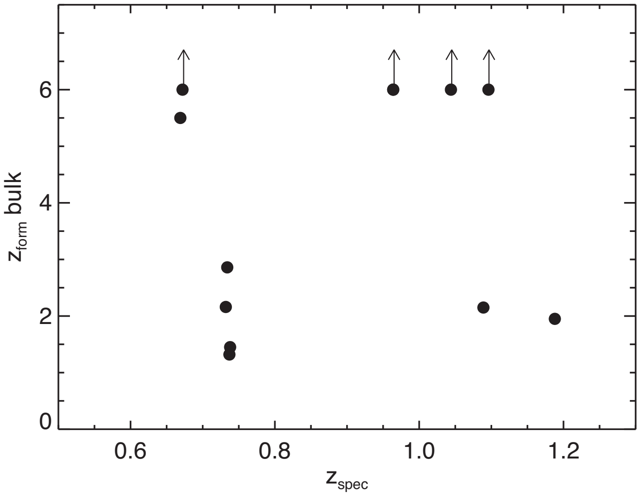

Figure 9. $z_{\rm form}$ of the main component as a function of the $z_{\rm spec}$ of the 80 per cent of the sample of galaxies. Arrows mean that the values can be higher than what indicated by the respective points.

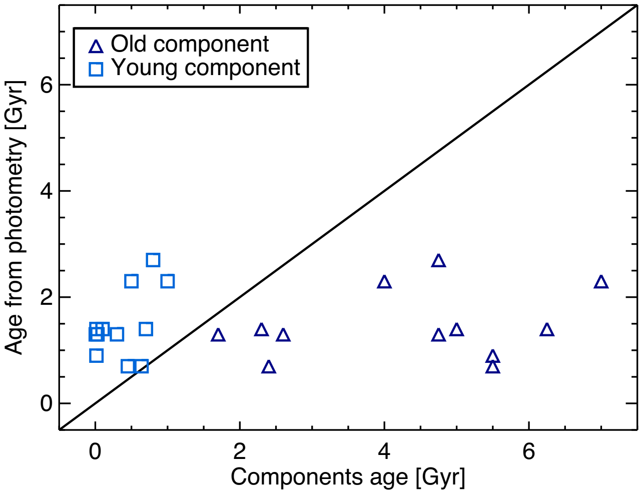

Figure 10. Comparison between the ages derived from the SED fitting photometric analysis (from Table 4) and the ages of the main component (dark blue triangles) and the young component (light blue squares) extracted from the double-component analysis (from Table 6). Data concern the 80 per cent of the sample.

predicted from the values of the Δ4000 index, which, as already discussed, is a measure of the global stellar population (see Table 6 in comparison with Table 4). In Fig. 10, we report the comparison between the ages estimated from the SED analysis (with fixed $\tau = 0.1$ Gyr) with respect to both those of the young components (light blue squares) and those of the old components (dark blue triangles). It can be seen that ages derived from the SED analysis are all younger than 2.7 Gyr, while in our double-component analysis, the ages of the old components reach 7 Gyr. This figure demonstrates that the photometric analysis, without the constraints imposed by the spectrophotometric indices, clearly underestimates the age of the bulk of stars in ETGs at $z \sim 1$. As a consequence, it results that also the stellar mass derived from the SED fitting is on average underestimated with respect to the value that can be derived from the double-component analysis. Indeed, we estimate that the mean correction factor for the stellar mass of our sample galaxies is on average 1.2 with peaks up to a factor of 2, and the more is the difference between the age extracted from the SED fitting and the age of the older component, the higher is the value of this correction.

In conclusion, our results suggest that the bulk of the star formation in our sample ETGs at $z \sim 1$ happened in two indicative cosmic periods: one at $z_{\rm form} > 5$ and the other more recent at $1 < z_{\rm form} < 3$. New and minor events of star formation occurred in these galaxies within 1 Gyr (upper limit) from their observation, i.e. $z \sim 1$ and

$z \sim 0.7$. Again, we point out that these results come from a limited sample without any statistics and completeness in z, so they should be consolidated by means of analysis on larger samples.

It is worthy to note that the obtained results are strictly related to the peculiarities of the two spectrophotometric measured indices. In particular, the H+K(Ca II) index has been of fundamental importance to detect the presence of small fractions of young stellar populations also when the bulk of the mass (>98−99 per cent) belonged to the older main component. Indeed, as it appears evident from Fig. 4, the H+K(Ca II) index experiences large variations even when only a small percentage of stellar mass younger than 1 Gyr is added to the old bulk of stars.

5 DISCUSSION

In the last years, only two works based on high-redshift ETG optical spectra reported a similar spectroscopic analysis based on spectrophotometric indices. In the following, we try to compare our results with the finding of these two works.

The first one is a work by Onodera et al. (2012) where the authors present a spectral analysis of a sample of 18 passive elliptical galaxies at $1.4 < z < 1.8$ in the Cosmological Evolution Survey (COSMOS) field. In particular, based on near-IR Subaru/Multi-Object Infrared Camera and Spectrograph (MOIRCS) spectra (resolution $R \simeq 500$), they performed the measurements of two spectrophotometric indices in the same region of our analysis: the Hδ index (defined as Hδ_F by Worthey & Ottaviani 1997) and D_n4000, a 4000 Å break index definition by Balogh et al. (1999), not coincident with the one adopted in our present work.

To compare our sample with that of Onodera et al. (2012), we have measured the values of the Hδ_F and D_n4000 indices on the spectra of our sample. Results are listed in Table 7.

In their fig. 17, Onodera and collaborators showed the comparison of their measurements with the predictions of synthetic models (Charlot & Bruzual, in preparation) assuming four different star formation histories and most of their objects are not consistent with any of the displayed models. We add our lower redshift sample in the same Hδ_F versus D_n4000 plane, and the result is shown in Fig. 11 (top panels). Indeed, on average, at fixed D_n4000 index value, the Hδ_F index value is either higher than expected from models or too low to find any correspondence with models (with $\tau = 0.1$ Gyr and solar metallicity, black line in Fig. 11, top panels). We then proceeded with the same arguments followed in the previous sections, considering double stellar components models. The top-left panel of Fig. 11 presents composite models with the younger component at fixed age 0.7 Gyr, while in the top-right panel the minor component is so young, 5 Myr, to present emission lines and to produce negative values of the Hδ_F index. Double-component models with the adding of gas emission are successful in explaining many of the data points of both samples, in particular those with lower values of both indices. Unfortunately, those points with extreme high values of Hδ_F (and relative high values of D_n4000 index) remain still unexplained with any combinations of stellar component ages, as already noticed by Onodera et al. (2012).

Table 7. Values of the D_n4000 and Hδ_F indices (used in Onodera et al. 2012) and Hδ_A index (used in Jørgensen & Chiboucas 2013) measured on our sample spectra.

ID-MUSIC	z	D_n4000	Hδ_F	Hδ_A
1192	1.089	1.59 ± 0.03	2.44 ± 0.53	4.88 ± 0.19
1382	0.964	2.10 ± 0.06	2.15 ± 0.30	0.21 ± 0.60
1950	1.044	1.53 ± 0.08	2.16 ± 0.85	0.48 ± 0.23
1837	0.964	2.28 ± 0.04	1.54 ± 0.34	− 1.85 ± 0.24
2694	1.135	1.96 ± 0.07	1.57 ± 0.79	1.13 ± 0.53
9066	1.188	1.71 ± 0.15	4.12 ± 0.62	2.78 ± 3.19
11539	1.096	1.91 ± 0.06	0.05 ± 1.18	− 0.70 ± 1.20
10020	0.738	1.78 ± 0.09	1.90 ± 1.25	− 0.14 ± 1.95
10960	0.737	1.72 ± 0.05	0.15 ± 0.56	− 1.49 ± 0.83
11225	0.736	1.64 ± 0.04	2.06 ± 0.75	1.29 ± 1.13
9792	0.734	1.87 ± 0.05	0.94 ± 0.69	− 0.85 ± 1.01
13386	0.734	1.61 ± 0.04	1.58 ± 0.85	0.05 ± 1.30
9838	0.732	1.80 ± 0.08	1.54 ± 1.42	− 0.90 ± 2.20
17044	0.672	1.93 ± 0.03	1.09 ± 0.38	1.70 ± 0.54
7424	0.669	1.75 ± 0.09	0.62 ± 1.52	1.20 ± 2.15

Focusing only on our sample data (red points in Fig. 11, top panels), it is worth to stress that the obtained spread in the Hδ_F versus D_n4000 index plane is more restrained than that in the H+K(Ca II) versus Δ4000 index plane discussed in this work (see Fig. 2). This is due to the lower sensitivity of the Hδ_F index with respect to that of the H+K(Ca II) index to the presence of very small amounts of young stars. As explained in Section 3, indeed, the measure of the H line depth and its ratio with the K line is influenced almost only by the blended Hϵ line depth, making the values of their ratio (i.e. H+K(Ca II) index) a very sensible tool for detecting young stellar populations. The larger effectiveness of the H+K(Ca II) index with respect to the Hδ_F index in finding the younger component is easily verified looking at the synthetic models. Coloured lines in Fig. 11 (top-left panel) indicate the values of the Hδ_F and D_n4000 indices of double-component models with increasing fractions of the younger component, and it can be noticed that the detachment from the single-component model (black line) is limited with respect to what obtained in Fig. 4 in the case of H+K(Ca II) index.

Interestingly, from both top panels of Fig. 11, it can be noticed that data points of our sample (red points) stay closer to models than those of Onodera et al. (2012). Since our points refer to lower z galaxies, we thus looked for a correlation of this spreading with redshift. We separated the entire sample of galaxies in five subsets with different range of redshift: $z \sim 0.7$, ∼1, ∼1.4, ∼1.6 and ∼1.8. In Fig. 12, we present the same plot of Fig. 11, but with only a representative single-component model (black line, with $\tau = 0.1$ Gyr and solar metallicity). Colours of the data points go from yellow, low-redshift objects ($z \sim 0.7$), to dark red, the highest redshift ($z \sim 1.8$). From this plot, it is clear that low-z data stay closer to the model than those with high z and that the more the redshift increases, the more the data are widespread in the index–index plane, i.e. more distant from models. Furthermore, in fig. 17 in Onodera et al. (2012), the authors present the comparison of their high-z data with local Sloan Digital Sky Survey (SDSS) passive galaxies, and the trend seems to be confirmed: local objects are generally well represented by single-component models with respect to high-z data. In high-redshift objects, differences of ages among possible multiple stellar components are easier to be detected thanks to the younger mean ages, for which even small age differences produce strong signatures (e.g. Balmer lines depth), while in the local Universe the same age differences are almost impossible to be detected for the stellar population ageing, thus vanishing the opportunity of observing the presence of double components. Indeed, two stellar populations with 8 and 12 Gyr, respectively, have almost the same Balmer lines depth. This strengthens the advantage of dealing with direct spectral measurements of higher redshift ETGs in order to study their star formation history.

The second interesting comparison is with the work by Jørgensen & Chiboucas (2013). Their analysis is based on high-S/N optical

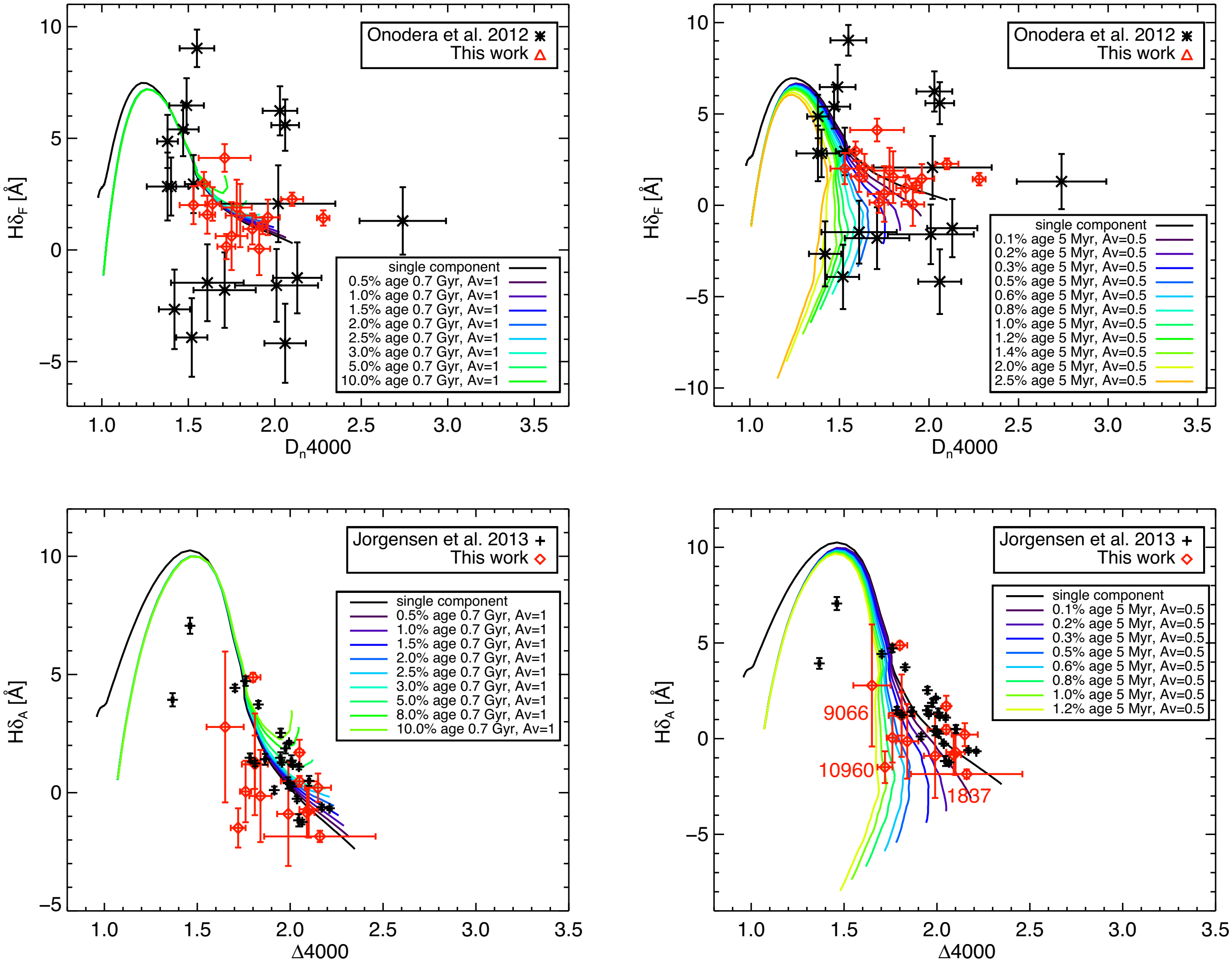

Figure 11. Same plots as Fig. 4 in the Hδ_F versus D_n4000 plane, for both the Onodera et al. (2012) sample (black points) and this work sample (red points) (top panels), and in the Hδ_A versus Δ4000 plane for both the Jørgensen & Chiboucas (2013) sample (black points) and this work sample (red points) (bottom panels). Double-component models (coloured lines) are composed of the bulk of the mass whose ages increase from left to right (from about 10^8 to 10^{10} yr), and by increasing mass fractions of young component with age 0.7 Gyr with $A_v = 1$ (left-hand panels), and with age 5 Myr, reddened with $A_v = 0.5$ (right-hand panels). Double-component models in the right-hand panels are shown with the adding of gas emission lines. In all panels, Hδ_F values of synthetic models (coloured lines) and data points have been properly corrected to take care of their different spectral resolutions.

spectroscopy of the early-type members of three galaxy clusters at $z > 0.5$ in the framework of the ‘The Gemini/HST Galaxy Cluster Project’ (Jørgensen et al. 2005). We limited our comparison to the highest z clusters which are the RX J0152.7−1357 at $z = 0.83$ and RX J1226.9+3332 at $z = 0.89$, because they match the average redshift of our sample. For these galaxy clusters, in particular, the authors make available the measurements of some spectrophotometric indices obtained from the GMOS-N instrument (R =1918). They adopt the same definition of the Δ4000 index as we adopted, and the definition of the Hδ_A by Worthey & Ottaviani (1997), different from that of Onodera et al. (2012). In order to perform the comparison, we thus measured the values of the Hδ_A of our sample galaxies, and the results are listed in column 5 of Table 7.

Once again we compared the results with the expectation of the single-component BC03 models (black line, with $\tau = 0.1$ Gyr and solar metallicity), in Fig. 11, bottom panels. Data points from Jørgensen & Chiboucas (2013, black points) remain relative close to the single-component model predictions (black line), in agreement with the measure of our sample, supporting the previous finding that the secondary younger component is more evident at increasing z. In order to preserve the graphic clearness, in Fig. 11 only data points belonging to RX J1226.9+3332 galaxy cluster are shown. In Fig. 11, bottom-left panel, we report the comparison of both the two sample data with the double-component models (coloured lines), the same as in the top-left panel: points with higher values of Hδ_A index at fixed Δ4000 index value result fully explained by adding a small mass fraction of young stars. On the other hand, only some of our sample data points (red points) have lower values of Hδ_A index at fixed Δ4000 index and they can be again explained with double-component models adding very young stellar components displaying Balmer emission lines. In particular, it is interesting to note that the three objects ID-9066, ID-10960 and ID-1837 of our sample, highlighted with labels in Fig. 11 (bottom-right panel), have Hδ_A and Δ4000 indices which are consistent with double-component models displaying emission lines in agreement with the

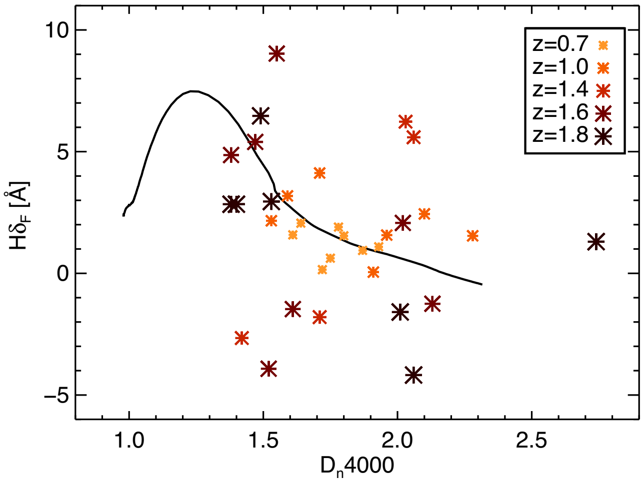

Figure 12. Hδ_F versus D_n4000 plot. Black line is the single-component model with $\tau = 0.1$ Gyr and solar metallicity. Data from the sample of Onodera et al. (2012) and this work galaxies. Data points are divided into five redshift bins (from yellow to dark red crosses): $z \sim 0.7$, ∼1, ∼1.4, ∼1.6 and ∼1.8. Errors bars are omitted for simplicity; they would be the same as in Fig. 11.

results found using the H+K(Ca II) index with respect to the Hδ_A one in this work (see Fig. 4, right-hand panel).

Finally, we remark that in the bottom panels of Fig. 11, we are comparing in the same plots data coming from two samples of galaxies at about the same mean redshift but in different environments: our sample (red points) is composed of field galaxies, i.e. low-density environment (with mean $z = 0.83$), while Jørgensen & Chiboucas (2013) sample (black points) is composed exclusively of galaxies belonging to the cluster RX J1226.9+3332 at $z = 0.89$. The fact that the galaxies of the sample of Jørgensen & Chiboucas (2013) do not need on average the presence of a second stellar component modelled with Balmer emission lines, means that in general their stellar populations are homogeneous, i.e. formed in a single or very short burst with no secondary bursts, in agreement with the well-known results of Thomas et al. (2005), where high-density environment galaxies are expected to form their star earlier than low-density counterparts and in a shorter time-scale (see fig. 10 in Thomas et al. 2005). Supposedly, many cluster objects have experienced the same mechanism of star formation and assembling of our sample ETGs that led to the presence of stellar components with different properties, but these events must have occurred earlier in the cosmic time and are less appreciable at the observation redshift.

6 SUMMARY AND CONCLUSIONS

We presented a spectroscopic analysis based on the measurements of age-dependent specrophotometric indices in the region of 4000 Å rest frame on high-redshift ETGs. We based our analysis on all the up-to-now publicly available optical spectra of ETGs at $z \sim 1$ in the GOODS-South field, with ascertained morphological classification (see Tamburri et al., in preparation), and with sufficient high-S/N ratio in the region of 4000 Å break rest frame to allow a detailed spectral analysis. The sample was then composed of 15 ETGs at $0.7 < z < 1.1$, whose spectral data came from three observing campaigns performed by Van der Wel et al. (2005), Mignoli et al. (2005) and Popesso et al. (2009).

From the reduced monodimensional spectra, we have measured the values of the two age-dependent spectrophotometric indices: H+K(Ca II) and Δ4000. The choice of these indices was supported by their sensitivity to the presence of multiple stellar populations with different age. In particular, we have stressed the peculiarity of the H+K(Ca II) index of being very sensitive to age variations even in the case of small amounts of very young stellar content.

From the comparison of the index values with the expectations of single-component BC03 models, we found that many measured values deviate significantly from models. Nor synthetic models with different star formation time-scale τ neither those with different metallicity could explain the discrepancy from the ages indicated by the Δ4000 index (in general older) and those pointed out by the H+K(Ca II) index. Furthermore, particularly intriguing it was the finding of some values of the H+K(Ca II) index which were too high to find any correspondence with models.

Such a behaviour has thus been attributed to inhomogeneous properties of the stellar populations in the sample galaxies, in particular to age variations. Simple models where the bulk of the star formation happened in a dominant initial event (within a time-scale τ) are not able to explain our results: a further degree of complexity is necessary to understand the star formation history of our sample galaxies. To take into account these inhomogeneities, we then introduced in the modelling a second star formation event, thus considering the stellar population composed of two stellar components which differ from their ages. Adopting composite models, the result is that a small mass percentage of younger stellar component is enough to explain those index values that were not consistent with single-component models. In particular, those high values of the H+K(Ca II) index could be explained introducing the contribution of gas emission lines, due to the presence of star-forming regions. Indeed, small mass fractions of very young components (<0.1 Gyr), where the star formation is still ongoing and the Hϵ Balmer line is in emission, are able to fill the whole H line involved in the H+K(Ca II) index, thus increasing its expected value. From the fitting analysis, we obtained that for at least 60 per cent of the galaxies of our sample, there are pieces of evidence of the presence of small mass fractions of a younger population coexisting with a much older stellar bulk.

Data suggest that the ages of the *older* components follow two distinct distributions with mean ages of 2.25 and 5.3 Gyr without any correlation with z, which correspond to mean formation redshift for the bulk of stars at $1 < z_{\rm form} < 3$ and $z_{\rm form} > 5$. However, due to the limited number of galaxies of our sample (15) not uniformly distributed in redshift, these results could be only a selection effect. Moreover, we found that the main component ages tend to be older than what concluded from the standard SED fitting analysis [in agreement with (Fan et al. 2014) analysis on star-forming galaxies], with some implications on the stellar mass estimate, which results to be underestimated by a factor of ∼1.2 on average. The following star-forming events (i.e. the *younger* components) are detected at any redshift of the galaxies of our sample ($0.7 < z < 1.1$), so it cannot be outlined in a common cosmic period in which the younger component has been accreted. It appears more likely that the star formation is triggered steadily over the cosmic time within field ETGs.

We have supposed the presence of younger components also in higher z sample of passive elliptical (Onodera et al. 2012) up to $z = 1.8$, and in $z \sim 1$ cluster galaxies (Jørgensen & Chiboucas 2013) even if based on the Hδ index rather than the H+K(Ca II) index, the former less sensible to small amounts of young stellar content. We have found that, in general, the ages of the minor younger component are less young for galaxies belonging to cluster, and more extreme with the increasing of redshift.

Having revealed the presence of small young stellar components in many galaxies in a wide redshift range ($0.7 < z < 1.8$, thanks to the enlarged sample) implies that there must be a common mechanism by which ETGs at any cosmic time either accrete new amounts of young stellar mass by means of minor merging events or activate new events of star formation almost constantly over time. Minor merger-induced star formation is the most widely accredited hypothesis to explain the presence of ongoing star formation in ETGs, since it has been also found in the local Universe (Kaviraj et al. 2012). Minor mergers are those with mass ratio (M/m) in the range $1/10 < M/m < 1/4$, and our findings on the younger components' mass fractions are consistent with this scenario. Indeed, adopting the assumption of 'dry' minor merging, which in general involves a maximum value of gas fraction of 10 per cent of the total accreted mass (stars+gas), the very small fractions of the second components observed in this work, i.e. ~0.1 per cent, result in agreement with this description. On the other hand, obviously, also wet minor merging events are able to explain the origin of the observed younger component, with the accretion of external gas being the driver of new star formation activity. However, minor merging events do not seem to be so frequent in the cosmic epoch from $z \sim 1$ to now. Indeed, Lopez-Sanjuan et al. (2012) have found that from $z \sim 1$ to $z \sim 0$ the number of minor merging per red galaxy is 0.46 ± 0.06; thus, it seems rather unlikely that in an albeit small sample of 15 galaxies, we found that at least 9 objects (i.e. 60 per cent) have recently experienced a minor merging event. In addition, it must be considered that all these objects have been classified as ETGs and their morphology appear all regular; thus, if merger events have happened in the cosmic histories of these galaxies, they must have taken place at least few Gyr earlier with respect to their observation in order to resettle the elliptical morphology. But this is not in agreement with our findings where the younger component is always observed with age <1 Gyr.

Moreover, other independent works, such that by Gargiulo et al. (2012), not only have demonstrated the inhomogeneities of stars in ETGs at $z > 1$, but they have also localized the younger component in the inner part of the galaxies. This naturally leads to the question of what is the physical mechanism which, after the external mass accretion by means of hypothetical merging events, is able to bring only the younger stars to the centre of galaxies at least in the case of dry merger event.

On the other hand, our finding of a second younger component also in other high-z samples suggests that the presence of a small percentage of young stars at any epoch which coexist with the passively evolving older stellar bulk of the galaxy could be common in ETGs. In fact, it is known that ETGs contain small fraction of cold molecular gas that could be converted in star formation activity and its presence has been observationally detected in the local Universe (Lees et al. 1991; Crocker et al. 2011; Panuzzo et al. 2011). This minimal gas reservoir, besides having a presumed external origin, could also be due to the stellar mass-loss or may be left over from the initial star formation major burst in the earlier epochs. The favoured scenario is that of the cold accretion: it has been shown (Fardal et al. 2001; Keres et al. 2005; Dekel & Birnboim 2006) that a cold gas mode could be responsible for the star formation in the cosmic history of galaxies and that it can be present, with its filamentary nature and in small quantities, also in spheroidal passive systems where the hot gas mode is dominant. In fact, Keres et al. (2005) show that, from $z \sim 3$ to $z \sim 0$, hot gas mode-dominated galaxies, i.e. passive and massive spheroids, can form new stars thanks to small amounts of cold gas, and the involved mass fractions, <20 per cent for stellar masses $\log(M_*) > 10.5$, are fully consistent with the detected mass fractions of the younger component in our analysis sample. In addition, this scenario could be in agreement with the observed inner position of the younger component, as the cold gas stream is assumed to infall towards the centre of galaxy attracted by the main potential well.

Thus, the detected young stellar component in the sample of ETGs analysed in the present work suggests that a star formation activity took place steadily over time during the secular evolution of these galaxies, activated by small gas quantities since $z > 1$.

ACKNOWLEDGEMENTS

We thank the anonymous referee of this paper for providing constructive comments that improved the manuscript. This work has received financial support from PRIN-INAF (1.05.09.01.05).

REFERENCES

Balogh M. L., Morris S. L., Yee H. K. C., Carlberg R. G., Ellingson E., 1999, ApJ, 527, 54
Bruzual G., 1983, AJ, 273, 105
Bruzual G., Charlot S., 2003, MNRAS, 344, 1000 (BC03)
Calzetti D., Armus L., Bohlin R. C., Kinney A. L., Koornneef J., Storchi-Bergmann T., 2000, ApJ, 533, 682
Cappellari M. et al., 2009, ApJ, 704, L34
Chabrier G., 2003, PASP, 115, 763
Charlot S., Longhetti M., 2001, MNRAS, 323, 887
Cimatti A. et al., 2004, Nature, 430, 184
Coccato L., Gerhard O., Arnaboldi M., 2010, MNRAS, 407, L26
Crocker A. F., Bureau M., Young L. M., Combes F., 2011, MNRAS, 410, 1197
Daddi E. et al., 2005, ApJ, 626, 680
Dekel A., Birnboim Y., 2006, MNRAS, 368, 2
Fan L., Lapi A., Bressan A., Nonino M., De Zotti G., Danese L., 2014, Res. Astron. Astrophys., 14, 15
Fardal M. A., Kats N., Gardner J. P., Hernquist L., Weinberg D. H., Davé R., 2001, ApJ, 562, 605
Gargiulo A., Saracco P., Longhetti M., La Barbera F., Tamburri S., 2012, MNRAS, 425, 2698
Glazebrook K. et al., 2004, Nature, 430, 181
Guo Y. et al., 2011, ApJ, 735, 18
Hamilton D., 1985, AJ, 297
Huang S., Ho L. C., Peng C. Y., Li Z., Barth A. J., 2013, ApJ, 766, 47
Jørgensen I., Chiboucas K., 2013, AJ, 145, 77
Jørgensen I., Bergmann M., Davies R., Barr J., Takamiya M., Crampton D., 2005, AJ, 129, 1249
Kaviraj S. et al., 2012, MNRAS, 423, 49
Keres D., Kats N., Weinberg D. H., Davé R., 2005, MNRAS, 363, 2
Lees J. F., Knapp G. R., Rupen M. P., Phillips T. G., 1991, ApJ, 379, 177
Longhetti M., Saracco P., 2009, MNRAS, 394, 774
Longhetti M., Bressan A., Chiosi C., Rampazzo R., 1999, A&A, 345, 419
Lopez-Sanjuan C. et al., 2012, A&A, 548, A7
Maraston C., Stromback G., 2011, MNRAS, 418, 2785
Mignoli M. et al., 2005, A&A, 437, 883
Naab T., Johansson P. H., Ostriker J. P., 2009, ApJ, 699, L178
Onodera M. et al., 2012, ApJ, 755, 26
Oser L., Ostriker J. P., Naab T., Johansson P. H., Burkert A., 2010, ApJ, 725, 2312
Oser L., Ostriker J. P., Naab T., Johansson P. H., 2012, ApJ, 744, 630
Panuzzo P., Rampazzo R., Bressan A., Vega O., Annibali F., Buson L. M., Clemens M. S., Zeilinger W. W., 2011, A&A, 528, A28
Popesso P. et al., 2009, A&A, 494, 443
Renzini A., 2006, ARA&A, 44, 141
Rocca-Volmerange B. et al., 2013, MNRAS, 429, 2780

Rose J. A., 1985, AJ, 90

Sanchez H. D. et al., 2011, MNRAS, 417, 900

Santini P. et al., 2009, A&A, 504, 751

Saracco P., Longhetti M., Gargiulo A., 2010, MNRAS, 408, L21

Strazzullo V. et al., 2013, ApJ, 772, 118

Thomas D., Maraston C., Bender R., de Oliveira C. M., 2005, ApJ, 621, 673

Treu T., Stiavelli M., Casertano S., Møller P., Bertin G., 2002, ApJ, 564, L13

Van der Wel A., Franx M., van Dokkum P. G., Rix H.-W., Illingworth G. D., Rosati P., 2005, ApJ, 631, 162

Vanzella E. et al., 2005, A&A, 434, 43

Vanzella E. et al., 2008, A&A, 478, 83

Worthey G., Ottaviani D., 1997, ApJS, 111, 377

This paper has been typeset from a TEX/LATEX file prepared by the author.

Mon. Not. R. Astron. Soc. **000**, 1–8 (2015) Printed 26 October 2015 (MN LaTeX style file v2.2)

Old age and super-solar metallicity in a massive $z \sim 1.4$ early-type galaxy from VLT/X-Shooter spectroscopy*

I. Lonoce[1,2]†, M. Longhetti[1], C. Maraston[3], D. Thomas[3], C. Mancini[4], A. Cimatti[5], F. Ciocca[1,2], A. Citro[5], E. Daddi[6], S. di Serego Alighieri[7], A. Gargiulo[5], R. Maiolino[8], F. Mannucci[7], M. Moresco[5], L. Pozzetti[5], S. Quai[5], P. Saracco[1]

[1] *INAF-Osservatorio Astronomico di Brera, via Brera 28, I-20121 Milano, Italy*
[2] *Dipartimento di Scienza e Alta Tecnologia, Università degli Studi dell'Insubria, via Valleggio 11, I-22100 Como, Italy*
[3] *Institute of Cosmology and Gravitation, University of Portsmouth, Dennis Sciama Building, Burnaby Road, Portsmouth PO1 3FX, UK*
[4] *INAF - Osservatorio Astronomico di Padova, Vicolo dell'Osservatorio 5, I-35122 Padova, Italy*
[5] *Dipartimento di Fisica e Astronomia, Università di Bologna, Viale Berti Pichat 6/2, I-30127 Bologna, Italy*
[6] *CEA-Saclay, Service d'Astrophysique, F-91191 Gif-sur-Yvette, France*
[7] *INAF—Osservatorio Astrofisico di Arcetri, Largo Enrico Fermi 5, I-50125 Firenze, Italy*
[8] *Kavli Institute for Cosmology, University of Cambridge, Madingley Road, Cambridge CB3 0HA, UK*

Accepted 2015 September 15. Received 2015 September 07; in original form 2015 May 19.

ABSTRACT

We present the first estimate of age, *stellar* metallicity and chemical abundance ratios, for an individual early-type galaxy at high-redshift ($z = 1.426$) in the COSMOS field. Our analysis is based on observations obtained with the X-Shooter instrument at the VLT, which cover the visual and near infrared spectrum at high (R > 5000) spectral resolution. We measure the values of several spectral absorptions tracing chemical species, in particular Magnesium and Iron, besides determining the age-sensitive D4000 break. We compare the measured indices to stellar population models, finding good agreement. We find that our target is an old ($t > 3$ Gyr), high-metallicity ([Z/H] > 0.5) galaxy which formed its stars at $z_{form} > 5$ within a short time scale ~ 0.1 Gyr, as testified by the strong [α/Fe] ratio (> 0.4), and has passively evolved in the first $> 3 - 4$ Gyr of its life. We have verified that this result is robust against the choice and number of fitted spectral features, and stellar population model. The result of an old age and high-metallicity has important implications for galaxy formation and evolution confirming an early and rapid formation of the most massive galaxies in the Universe.

Key words: galaxies: elliptical and lenticular, cD – galaxies: high-redshift – galaxies: stellar content.

1 INTRODUCTION

The cosmic history of galaxy mass assembly represents one of the open key questions in cosmology. Early-type galaxies (ETGs) are the most effective probes to investigate this topic, as they are the most massive and oldest galaxies in the local Universe and most likely those whose stars formed earliest. Observations have shown that a population of massive and passive galaxies is already in place at high redshift, when the Universe was only a few Gyr old (Cimatti et al. 2004, Saracco et al. 2005). So far, the main physical parameters related to their formation and assembly have been mainly estimated on local ETGs, and their ageing and evolution can mix up and confuse the original properties when the bulk of their mass formed and assembled. Information on the star formation (SF) time-scale of high-z ETGs can be obtained from the detailed chemical abundance ratios of their stellar populations (Thomas et al. 2005), which can be derived by a detailed spectral analysis. Indeed, the abundance of Iron with respect to α-elements is tightly correlated with the time delay between Type I and Type II supernovae (SN), giving a direct probe of the time-scale within which SF has occurred.

Up to now, only few works have experimented a spectral analysis on ETGs at $z > 1$ (Lonoce et al. 2014, Onodera et al. 2012, Jørgensen et al. 2014) due to the low S/N of the available spectroscopic data, and they were mostly focused

---

* Based on observations collected at the European Organisation for Astronomical Research in the Southern Hemisphere, Chile (programme: 086.A-0088(A))

† E-mail: ilaria.lonoce@brera.inaf.it (OAB)

on age estimates, in particular using the *UV* region (Cimatti et al. 2008). The analysis of the rest-frame optical spectrum is still lacking.

Furthermore, measures are usually performed on stacked spectra (Onodera et al. 2015), thus deleting possible peculiarities of single objects.

A single-object measurement of age, stellar metallicity and chemical abundance ratios of $z > 1.2$ ETGs is missing at the present time. We fill this gap, presenting the first attempt to measure the detailed chemical composition, besides age, of a $z \sim 1.4$ ETG directly in the early stages of its evolution.

Throughout this paper, we assume a standard cosmology with $H_0 = 70$ km s^{-1} Mpc^{-1}, $\Omega_m = 0.3$ and $\Omega_\Lambda = 0.7$.

2 COSMOS-307881: SPECTROSCOPIC DATA

Our target is a bright and massive ($> 10^{11}$ M$_\odot$) ETG from the K-selected galaxy catalog in the COSMOS (Cosmological Evolution Survey) field (McCracken et al. 2010). It is one of the 12 galaxies with K$_s$(Vega) < 17.7 selected by Mancini et al. (2010) on the basis of three criteria: (i) non-detection at 24 μm in the *Spitzer*+MIPS data (Sanders et al. 2007); (ii) visual elliptical morphology (see Fig. 1, top panel); (iii) multicolor Spectral Energy Distribution (SED) consistent with old and passive stellar populations with no dust reddening. All available information are shown in Table 1. For further details see Mancini et al. (2010) and Onodera et al. (2012). From these studies we can infer that our target is an old and slightly compact (R$_e \sim 0.3$ R$_e^{z=0}$, w.r.t. the local size-mass relation) ETG, and most of its mass is composed by a passively evolving stellar population. In the following we present a new analysis of the stellar population properties of this ETG based on new spectroscopic data, which, thanks to the high resolution in a wide spectral range of the X-Shooter spectrograph, allows us to measure the stellar metallicity of this high-*z* target.

Spectroscopic observations were carried out with the X-Shooter spectrograph on the VLT/UT2 (Vernet et al. 2011) in Italian guaranteed time during the nights $9 - 10$ February 2011, (program: 086.A-0088(A)). The target has been observed under bad sky condition (seeing $> 2''$) during the first night (about 1.7h for the VIS and UVB arms and about 1.9h for the NIR arm), while during the second night more than 4 hours of exposure have been collected under good sky conditions (seeing $\sim 0.8''$). We decided to consider only the latter set of observations. The use of the $1''.0$ slit in the UVB arm and $0''.9$ slit in the VIS and NIR arms, resulted in a spectral resolution of 5100, 8800 and 5600 in the UV, VIS and NIR respectively.

The data reduction has been performed taking advantage of the ESO pipeline (Goldoni et al. 2006) regarding the first steps of the process, and completed by means of `IRAF` tools. In Fig. 1 the reduced mono-dimensional spectrum of 307881 (black line) is shown in comparison with the photometric points (cyan diamonds, from Muzzin et al. 2013, and McCracken et al. 2012). Overlaid is a 4 Gyr, supersolar metallicity (Z= 0.04) simple stellar population (SSP) model of Maraston & Strömbäck (2011) (M11) based on the MILES stellar library (Sánchez-Blázquez et al 2006) (red line). Note that this template is the most similar in term of age and total metallicity, to the best-fit solution that will be derived in the next section. The full spectral model, as known, does not include the α/Fe parameter (see Maraston & Strömbäck (2011)), which we shall derive using selected absorption-line models in the next section (see Thomas et al. (2011)).

The original high resolution of the spectrum (e.g. ~ 1 Å in the VIS) has been decreased to match the lower resolution of the models (i.e. ~ 2.54 Å at rest-frame, and ~ 6 Å in the VIS at z= 1.4), which are used to perform the analysis of spectral indices (for details see Lonoce et al., in preparation). Note that we adopted the MILES-based M11 models instead of the higher resolution ones (M11-ELODIE or M11-MARCS, see www.maraston.eu/M11) to take advantage of the increasing S/N in downgrading the observed resolution. The value of the signal to noise ratio (S/N) obtained in the spectral region around 5000 Å restframe is ~ 7 per pixel.

In Fig. 2 we show how the Hβ and Mg$_b$ are expected to appear on a synthetic template (upper first panel) that broadly reproduces the observed one. The model is firstly adapted to the measured velocity dispersion (upper second panel), then downgraded to be as noisy as the observed spectrum (upper third panel) and finally compared to the observed one (bottom panel). The similarity between expected and observed absorption features is quite evident.

3 SPECTRAL ANALYSIS

As a first step, we measured the redshift of 307881 fitting the Mg$_b$ line region, which is the cleanest from the background residuals, as it can be seen in Fig. 1 (bottom panel), finding z= 1.426 ± 0.001. The Mg$_b$ line region has been also used to find a best fitting velocity dispersion estimate, that resulted to be $\sigma = 385 \pm 85$ km/s. More details on the fitting procedure adopted to fix both z and σ will be described in the forthcoming paper.

We then selected some indices whose absorption features are clearly visible in the observed spectrum, to try to simultaneously derive both the mean age and the metallicity of its stellar population. The selected indices are: D4000 index (Hamilton 1985), Hγ_F (Worthey & Ottaviani 1997), G4300, Fe4383, Ca4455, Fe4531, Hβ, Fe5015 and Mg$_b$ (Lick/IDS system, Worthey et al. 1994). In particular, it is well known that the Mg$_b$ index is the best *metallicity* and *chemical abundance* dependent index in the region around 5000 Å restframe (Korn et al. 2005). In Table 2 we report the measured values of these indices together with their errors derived by means of *Monte Carlo* simulations set on the uncertainties in the flux measurements.

Finally, we want to point out the presence of the [OII]3727 emission line (Fig. 1, middle panel). We can exclude that its origin is due to an active AGN, since we do not see any other signature in the observed wide spectral window. There are reasonable possibilities that this emission is caused by the UV ionizing emission of old stars in post main-sequence phases (Yi & Yoon 2004), as confirmed by UV indices (Lonoce et al., in preparation), while a strong contribution from SF can be excluded. Indeed, as it can be noted from Fig. 2 (left panels), it is highly unlikely that the Hβ feature is affected by emission, considering also that its

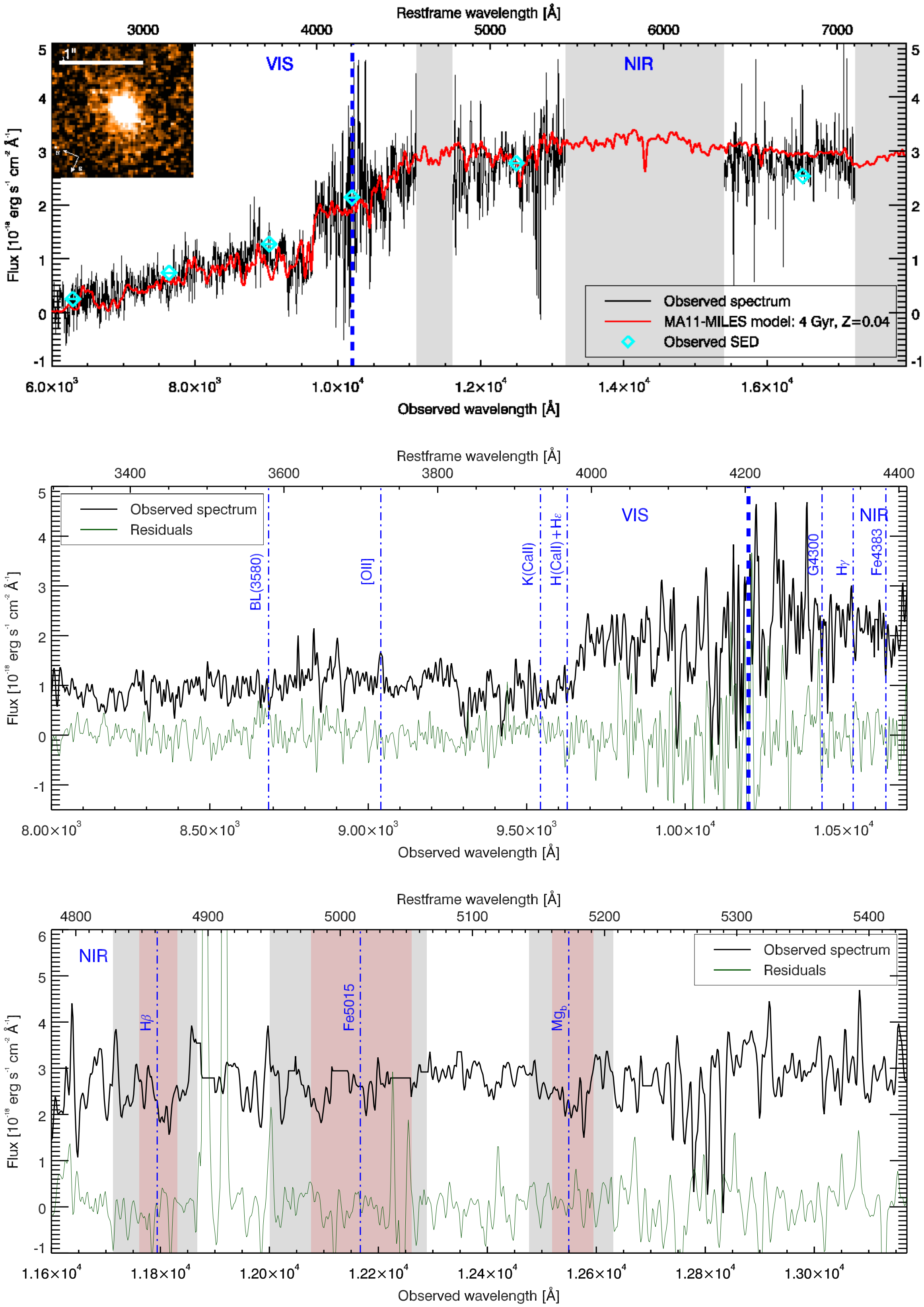

Figure 1. COSMOS 307881. The galaxy observed spectrum (black line) is compared to a model (Maraston & Strömbäck 2011) with age of 4 Gyr and super-solar metallicity (Z= 0.04), and to observed photometric data (cyan diamond). Top panel: VIS and NIR spectral region together with the HST/ACS I-band image of the target. Middle panel: zoom of the 4000 Å rest-frame region. Bottom panel: zoom of the 5000 Å restframe region. The main absorption (and one emission) lines in each spectral region are highlighted. Dark green lines indicate the residual spectrum.

Table 1. COSMOS-307881. Data derived from the analysis of Onodera et al. (2012): K-band magnitude in Vega system (K_s); spectroscopic redshift (z_{spec}^{ONOD}); stellar population age (Age_{phot}) and logarithm of the stellar mass ($\log\mathcal{M}_*$) derived from SED fitting assuming a Chabrier IMF (Chabrier 2003); effective radius (R_e); degree of compactness ($C=R_e/R_{e,z=0}$); Sersic index (n). Units of right ascension are hour, minutes and seconds, and unites of declination are degrees, arcminutes and arcseconds.

ID	RA	DEC	K_s (Vega)	z_{spec}^{ONOD}(*)	Age_{phot} (Gyr)	$\log\mathcal{M}_*$ ($M_\odot$)	R_e (kpc)	C	Sersic n
307881	10:02:35.64	02:09:14.36	17.59	1.4290±0.0009	3.50	11.50	2.68±0.12	0.32	2.29±0.10

(*)This work: $z_{spec} = 1.426 \pm 0.001$

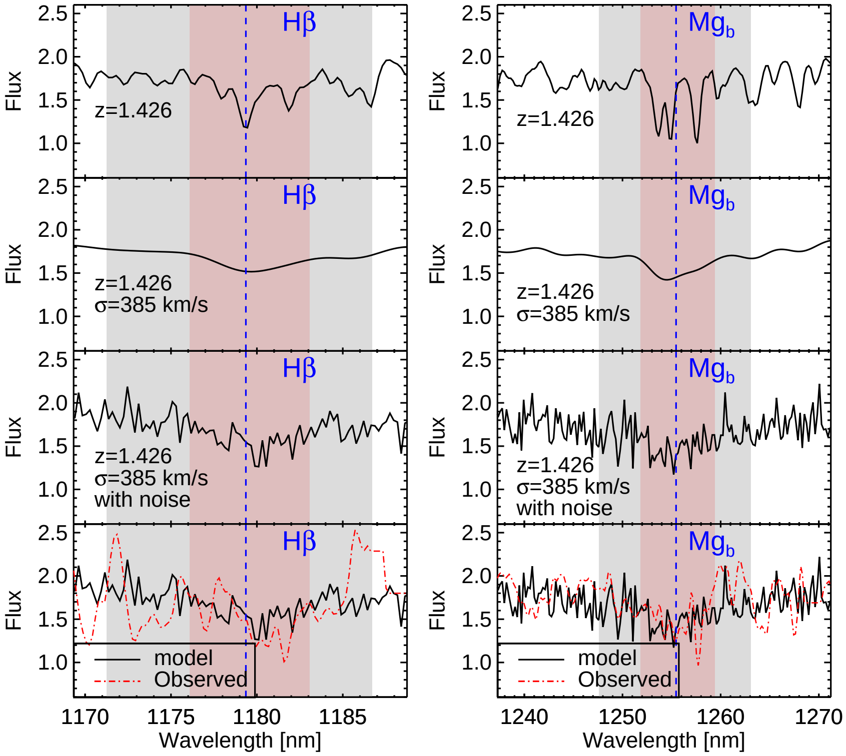

Figure 2. Hβ (left panels) and Mg$_b$ (right panels) features in the 4 Gyr, 2Z$\odot$ metallicity model shown in Figure 1. From top to bottom we show: model at $z \sim 1.4$; model corrected for $\sigma = 385$ km/s; model downgraded for the observed poissonian noise; model compared to the observed spectrum (point-dashed red line).

Table 2. Measured indices values.

Index	value
D4000	2.44 ± 0.12
D$_n$4000	2.42 ± 0.17
Hγ_F	-1.56 ± 0.92
G4300	6.52 ± 1.12
Fe4383	7.40 ± 1.74
Ca4455	1.06 ± 0.83
Fe4531	3.20 ± 1.40
Hβ	2.52 ± 0.93
Fe5015	3.89 ± 1.91
Mg$_b$	5.75 ± 0.81

value suggests a stellar population age in good agreement with that derived by the Hγ and D4000 index.

4 MODEL COMPARISON

In Fig. 3 we show the observed Mg$_b$ and Hβ indices (blue diamond), compared to the predictions of the SSP of Thomas et al. (2011) (hereafter TMJ models), based on the MILES library for a wide range of ages (from 0.1 Gyr shown up to the age of the Universe at $z \sim 1.4$, i.e. 4 Gyr); super-solar metallicities [Z/H]= 0.35 (red lines) and [Z/H]= 0.67 (cyan lines), and various α/Fe parameters, namely [α/Fe]= 0.0, 0.3, 0.5. Models assume a Salpeter (1955) initial mass function (IMF), and are corrected for the measured velocity dispersion value of $\sigma = 385 \pm 85$ km/s. As it can be seen, the extreme value of the Mg$_b$ index fully requires high metallicity models up to [Z/H]= 0.67. In particular, in Fig. 3 the model expectations for these indices are reported also in case of non-solar values of the α-enhancement [α/Fe], from 0.3 to 0.5 (dashed and dotted lines respectively).

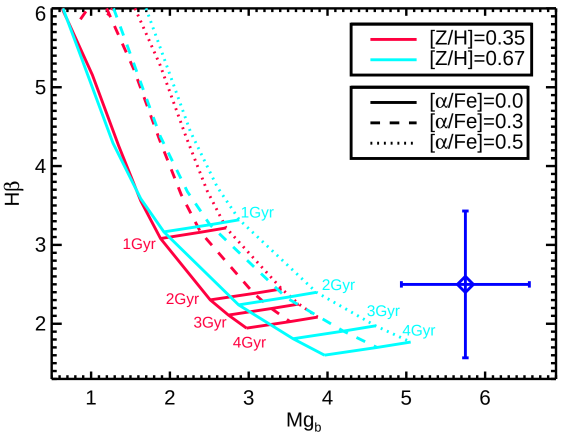

Figure 3. Hβ versus Mg$_b$ plot. Comparison between the measured indices (blue diamond) and models of Thomas et al. (2011) (lines). Ages run from 0.1 to 4 Gyr, for super solar metallicities of [Z/H]= 0.35, 0.67 (red, cyan lines), and α-element abundances: [α/Fe]= 0.0, 0.3, 0.5 (solid, dashed, dotted lines). The models are corrected for the measured value of $\sigma = 385$ km/s.

Models corresponding to extreme values of [α/Fe]> 0.5 seem to be required to match the observations.

The behaviour of the Mg$_b$ index, requiring such extreme values of Z, is confirmed also when considering the other absorption lines that we were able to measure on this X-Shooter spectrum. Indeed, as it can be noticed in Fig. 4 where we propose 3 examples of Lick indices (G3400, Hβ and Fe4383, upper, middle and bottom panel respectively) as a function of D4000, all measured indices consistently point towards a very-high metallicity ([Z/H] $\sim$ 0.67, cyan lines) being only marginally consistent with the 2Z$_\odot$ values ([Z/H] $\sim$ 0.35, red lines).

Notice that the highest metallicity models in Thomas et al. (2011) are partly in extrapolation, as they are sampling the edge of the parameter space in terms of the available empirical fitting functions for such extreme stellar parameters (see Johansson et al. (2010)). At the same time, the underlying stellar tracks are based on real calculations (see Maraston et al. (2003) for details).

More quantitatively, we have computed the best fitting solution obtained comparing all 9 observed indices values (Table 2) with models. The free parameters were age (0.1 $-$ 4.5, truncated at the age of Universe, with step 0.1 Gyr)[1], the total metallicity (from [Z/H]= -2.25 to [Z/H]= 0.67, with step 0.01) and the α/Fe-enhancement (from [α/Fe]= -0.3 to [α/Fe]= 0.5, with step 0.01). The minimum χ^2 value corresponds to an age of $4.0^{+0.5}_{-0.8}$ Gyr, metallicity [Z/H]= $0.61^{+0.06}_{-0.05}$ and [α/Fe]= $0.45^{+0.05}_{-0.19}$, with $\chi^2 = 0.7$ and an associated probability $\sim$ 70%. Errors indicate the range values of these parameters over all the solutions associated to probabilities larger than 65%. The distributions of the 3 fitting parameters, displayed in different χ^2 ranges, are shown in Fig. 5, top panel. A global picture of the χ^2 values can be seen in Figure 6 where the minimum χ^2 trends of the 3 parameters of all solutions are shown. It is easy to notice that ages $<$ 2 Gyr can be completely excluded due to the rapid increasing of their χ^2 values toward younger ages. Instead for ages $>$ 4.5 Gyr (limit of the Universe age, not shown here) the χ^2 values remains practically constant.

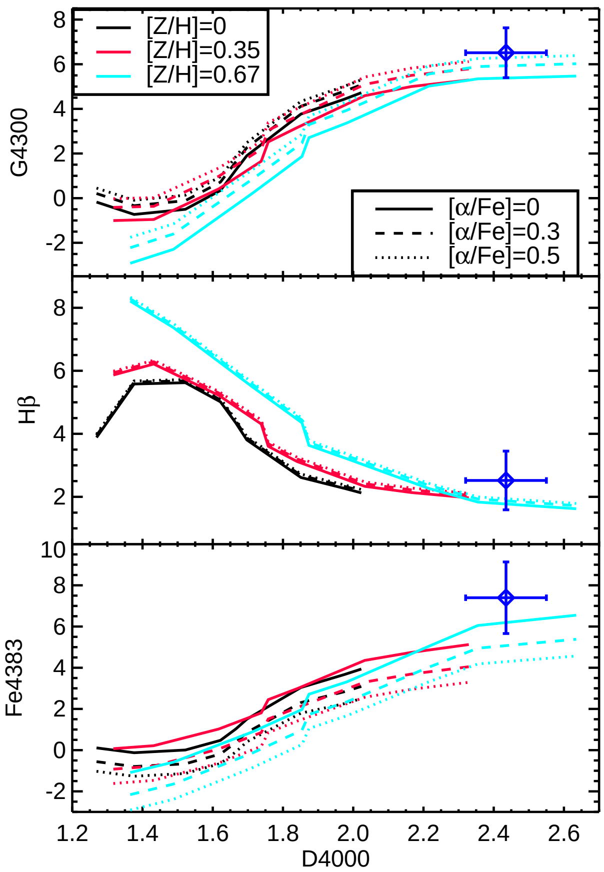

Figure 4. Comparison between four measured indices (G4300, Hβ and Fe4383 versus D4000) and the models of Thomas et al. (2011). Ages run from 0.1 $-$ 4 Gyr, metallicities from [Z/H]= 0, 0.35, 0.67 (black, red, cyan lines), and α-element abundances from [α/Fe]= 0, 0.3, 0.5 (solid, dashed, dotted lines). The measured values are shown with a blue diamond. Indices values of models are corrected for the measured value of $\sigma = 385$ km/s.

Furthermore, we found that models with Z$\leqslant$Z$_\odot$ provide a fit of the free parameters with a probability less than 0.1%.

We also verified the strength of this result by repeating the same fitting process selecting smaller and different set of indices, finding very similar solutions with respect to the previous ones based on the whole set of indices. Two examples are shown in Fig. 5 (middle and bottom panels): the distributions of the fitting solutions are obtained from two smaller sets of indices *(i)* D4000, G4300, Hγ, Fe4383, Hβ, Fe5015 and Mg$_b$ and *ii)* D4000, Hγ, Hβ and Mg$_b$) which lead to a best-fit solution of *i)* age= 4.0 Gyr, [Z/H]= 0.61 and [α/Fe]= 0.44 with $\chi^2 = 0.9$, and *ii)* age= 4.0 Gyr, [Z/H]= 0.60 and [α/Fe]= 0.5 with $\chi^2 = 0.5$, both totally consistent with the all-indices one.

---

[1] Note that we have performed the analysis using all available model ages (up to 15 Gyr) thereby ignoring the age of the Universe as a constrain. However, as no particular improvement was noticed in the derived quantities, we decided to focus on ages within the age of the Universe at $z \sim 1.4$

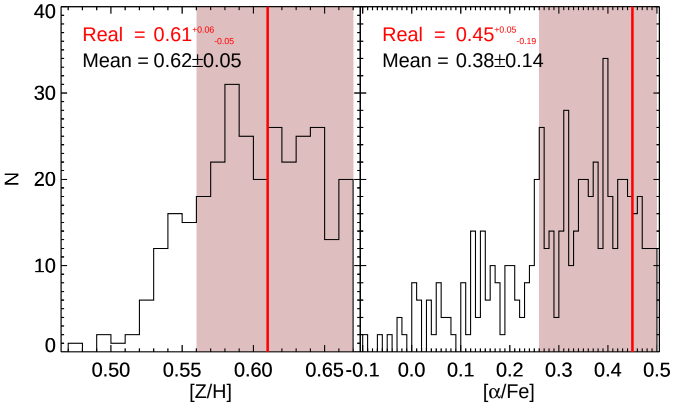

Figure 7. Distributions of [Z/H] and [α/Fe] derived for a set of 500 mock spectra built on a model spectrum with parameters (Table 3) as those of the best-fit to the observed spectrum and adding the poissonian noise. The two distributions are well peaked around the true original values (red vertical lines).

We also evaluated the feasibility of this analysis on this low S/N spectrum, in particular for metallicity and α-enhancement estimates, by repeating it on a set of 500 mock spectra built on a model spectrum with parameters as the best-fit to the observed one (cfr. Table 3) and downgraded with the poissonian observed noise. The obtained distributions of the measured [Z/H] and [α/Fe] are shown in Fig. 7. They all peak around the true original values (red vertical lines) demonstrating that within the declared errors the obtained values are solid.

Furthermore we tested if the large error on the velocity dispersion could affect the results by performing the same analysis assuming $\sigma = 300$ km/s. We found the same best-fit solution (4.1 Gyr, [Z/H]= 0.6, [α/Fe]= 0.41 with $\chi^2 = 0.6$).

Finally, in order to test the model dependence of this result, we repeated the same analysis adopting the Bruzual & Charlot (2003) models (BC03). These models do not include the [α/Fe] parameter, hence we shall use them to constrain age and total metallicity solely. The BC03 models cover a slightly lower Z range with respect to our fiducial TMJ models, and are based on different stellar evolutionary tracks. The BC03 best-fit corresponds to an age of 4.5 Gyr and a metallicity of [Z/H]= 0.4, which is the maximum available metallicity in these models. Hence our result of a high-age and high-Z is not model dependant.

It is important to note the high metallicity is mainly derived as a consequence of the maximum allowed age of 4.5 Gyr. Should we allow the age to be older than the age of the Universe, the metallicity will decrease, as a result of age/metallicity degeneracy. Actually, the large error bar of both the indices and of σ prevents a real precise measure of the metallicity, but the peculiarity of such a strong Mg$_b$ absorption band combined with the narrow range of possible ages (due to its redshift), make necessary the assumption of a very high value of the stellar metallicity.

Table 3. Results: spectroscopic redshift (z_{spec}) and velocity dispersion (σ) obtained from this spectroscopic analysis; best-fit values of age (Gyr), [Z/H] and [α/Fe].

z_{spec}	σ (km/s)	Age (Gyr)	[Z/H]	[α/Fe]
1.426 ± 0.001	385 ± 85	$4.0^{+0.5}_{-0.8}$	$0.61^{+0.06}_{-0.05}$	$0.45^{+0.05}_{-0.19}$

5 DISCUSSION AND CONCLUSIONS

We have performed a detailed spectroscopic analysis of a z=1.426, massive ($M^* \sim 10^{11} M_\odot$), early-type galaxy. We gain strong evidence of a high stellar metallicity and α-enhancement, and old (relative to its redshift) age (Table 3). These quantities constrain the past SF history experienced by the galaxy. In particular, the [α/Fe] ratio, quantifying the time delay between Type II SN events, responsible of the production of α-elements, and the Type Ia SNs, related to the formation of Fe-peak elements, allows to determine the SF time-scale (Thomas et al. 2005). The high value [α/Fe] $\sim$ 0.4 obtained for 307881 is a direct signature that its SF time-scale must have been short. In particular, adopting the simple theoretical modelling of Thomas et al. (2005), where the SF is modelled with a Gaussian function, we obtain a time-scale Δt $\sim$ 0.1 Gyr covering the interval within which 95% of the stars were formed. Considering also the old age of its stellar content, this suggests that 307881 formed the bulk of its stars at $z_{form} > 5$ within a short time-scale of Δt $\sim$ 0.1 Gyr and then passively evolved over the following 4 Gyr.

With the high [α/Fe] value suggesting a short SF time scale for 307881, the clear indication for an extremely high total metallicity opens new issues on the gas enrichment history of the Universe. It is worth emphasising that the global integrated metallicity of the local ETGs never reaches values higher than the $1-2$ Z$_\odot$. Indeed, we considered the local sample analysed in Thomas et al. (2010) and quickly verified that the metallicity and [α/Fe] values of 307881 together with its velocity dispersion estimate, are not included in the local distribution of values, even if such high values of Z and [α/Fe] are expected for dense ETGs as suggested by these scaling relations. Thus, this suggests that this galaxy must experience mass accretion events (minor merging) from z = 1.4 to z = 0 which will move it on the observed local scaling relations towards lower values of both Z and σ, diluting the extreme metallicity stars and confining them in the central part of the galaxy. Indeed, such extreme metallicity values are in some cases found in the inner core of local massive ETGs (Thomas et al. 2005, Trager et al. 2000, Martín-Navarro et al. 2015) which are known to show metallicity gradients (La Barbera et al. 2012). We calculated that adding e.g. 15% of a sub-solar metallicity component, as in the case of dwarf galaxies, to 307881 would decrease the measure of its average metallicity to the local observed values. On the other hand, the gas metallicities up to now measured in $z > 3$ star forming galaxies result to be solar or sub-solar, and do not match at all the high stellar value measured in our target galaxy (Mannucci et al. 2009) and in the centers of local ETGs (Spolaor et al. 2008). It is out of the aims of the present paper to suggest a possible explanation of this missing detection of high-z high metallicity gas. A possibility is that the lower gas metallicity comes from dilution

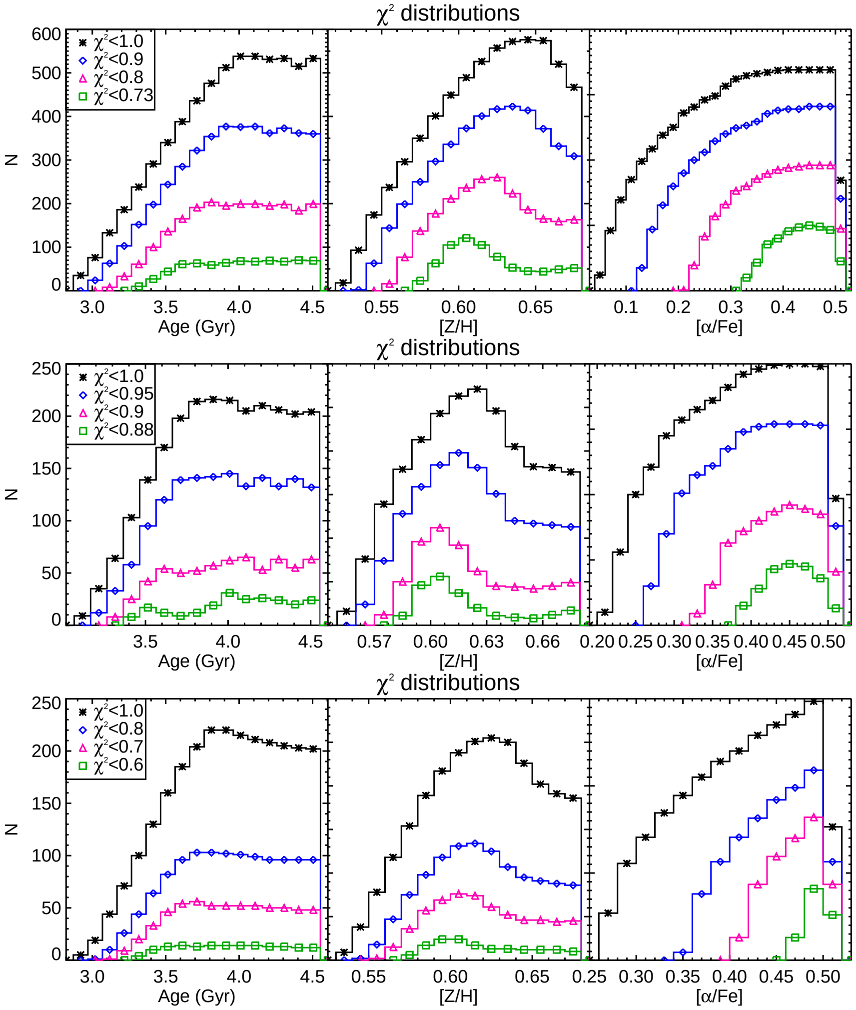

Figure 5. Distributions of the fitting-solutions: age, metallicity and α-enhancement. Colours and symbols indicate solutions in different χ^2 ranges, e.g. green squares include the most probable solutions. Top panel: distributions obtained from the all-indices analysis; middle panel: distributions obtained from a smaller set of indices: D4000, G4300, Hγ, Fe4383, Hβ, Fe5015 and Mg$_b$; bottom panel: distributions obtained from a smaller set of indices: D4000, Hγ, Hβ and Mg$_b$.

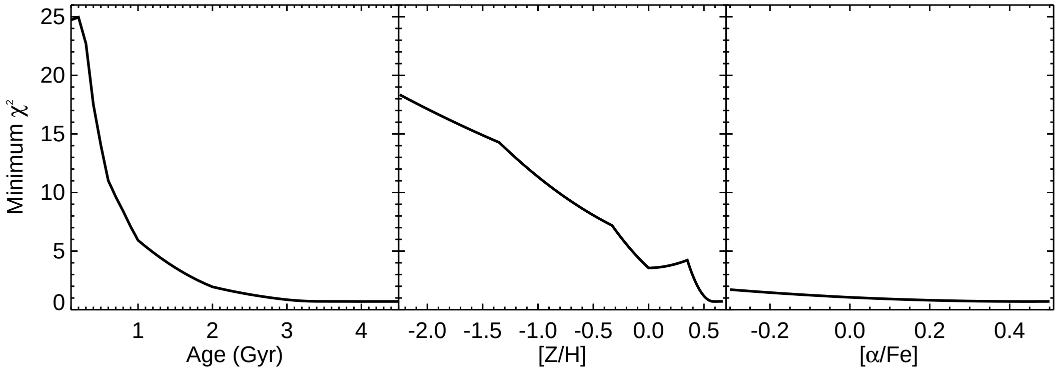

Figure 6. Trends of minimum χ^2 for age, [Z/H] and [α/Fe] of all obtained solutions. In particular, ages < 2 Gyr can be completely excluded due to the rapid degrade of χ^2 towards younger ages.

through infalling primeval gas, or selective mass loss of metals in galactic winds. At the same time, the estimate of the metallicity of the Broad Line Regions in quasars at $z > 4$ reveals gaseous metallicities even higher than the stellar one reported here (Juarez et al. 2009), suggesting the possibility that their enriched gas is involved in the initial SF events of (at least some) high-z massive proto-elliptical galaxies.

ACKNOWLEDGMENTS

We are grateful to the anonymous referee for helpful comments on our manuscript. We kindly thank Francesco La Barbera for his precious help in the data reduction and Kyle Westfall for helpful discussions. IL acknowledges the institute of Cosmology and Gravitation of the University of Portsmouth for a brilliant research visit during which a larger part of this project was worked out. IL, ML, AG and PS acknowledge the support from grant Prin-INAF 2012-2013 1.05.09.01.05. AC, LP, MM acknowledge the support from grant PRIN MIUR 2010-2011. CM and DT acknowledge The Science, Technology and Facilities Council for support through the Survey Cosmology and Astrophysics consolidated grant, ST/I001204/1.

REFERENCES

Bruzual G., and Charlot S., 2003, MNRAS, 344, 1000
Chabrier G., 2003, PASP, 115, 763
Cimatti A. et al., 2004, Nature, 430, 184
Cimatti A. et al., 2008, A&A, 482, 21
Goldoni P. et al., 2006, Proc.SPIE, 6269, 626933
Hamilton D., 1985, AJ, 297, 371
Korn A., Maraston C., and Thomas D., 2005, A&A, 438, 685
La Barbera F., Ferreras I., de Carvalho R.R., Bruzual G., Charlot S., Pasquali A., and Merlin E., 2012, MNRAS, 426, 2300
Lonoce I., Longhetti M., Saracco P., Gargiulo A., and Tamburri S., 2014, MNRAS, 444, 2048
Johansson J,, Thomas D. and Maraston C., 2010, MNRAS, 406, 165
Jørgensen I., Chiboucas K., Toft S., Bergmann M., Zirm A., Schiavon R., and Grutzbauch R., 2014, AJ, 148, 117
Juarez Y. et al., 2009, A&A, 494, L25
Mancini C. et al., 2010, MNRAS, 401, 933
Mannucci F. et al., 2009, MNRAS, 398, 1915
Maraston C., Greggio L., Renzini A., Ortolani S., Saglia R.P., Puzia T.H. and Kissler-Patig M., 2003, MNRAS, 400, 823
Maraston C., and Strömbäck, G., 2011, MNRAS, 418, 2785
Martín-Navarro I., La Barbera F., Vazdekis A., Ferré-Mateu A., Trujillo I., and Beasley, M. A., 2015, MNRAS, 451, 5600
McCracken H.J. et al., 2010, ApJ, 708, 202
McCracken H.J. et al., 2012, A&A, 544, 156
Muzzin A. et al., (2013), ApJS, 206, 8
Onodera M., et al., 2012, ApJ, 755, 26
Onodera M., et al., 2015, ApJ, 808, 161
Salpeter E.E., 1955, ApJ, 121, 161
Sánchez-Blázquez P., et al., 2006, MNRAS, 371, 703
Sanders D. B. et al., 2007, ApJS, 172, 86
Saracco P. et al., 2005, MNRAS, 357, 40
Spolaor M., Forbes D.A., Proctor R.N., Hau G.K.T., and Brough S., 2008, MNRAS, 385, 675
Thomas D., Maraston C., and Bender R., 2005, ApJ, 621, 673
Thomas D., Maraston C., Schawinski K., Sarzi M., and Silk J., 2010, MNRAS, 404, 1775
Thomas D., Maraston C., Johansson J., 2011, MNRAS, 412, 2183
Trager S.C., Faber S.M., Worthey G., and González J.J., 2000, ApJ, 119, 1654
Vernet J. et al., 2011, A&A, 536A, 105
Worthey G., Faber S.M., González J.J., and Burstein D., 1994, ApJS, 94, 687
Worthey G., and Ottaviani D., 1997, ApJS, 111, 377
Yi S.K., and Yoon S., 2004, Ap&SS, 291, 205